Structural and Spectroscopic Studies into Spin Crossover Complexes and Anils

HELEN MASON

Structural and Spectroscopic Studies into Spin Crossover Complexes and Anils

Helen E. Mason

A candidate for the degree of Doctor of Philosophy

Department of Chemistry, Durham University

2021

Foreword

By Dr Hazel A. Sparkes

This thesis is composed of a series of papers arising from data collected by Helen Mason during her PhD studies. She produced a significant volume of high quality data, which to date have resulted in nine peer reviewed papers being published, eight of these are combined here to form her thesis. Sadly, Helen died on the 6th of December 2019, after a break from writing up due to illness, so was unable to complete her thesis herself. She was a very patient, diligent and talented scientist who produced a significant amount of data in her short scientific career - more than sufficient data for her to have written a high quality thesis. Thanks to the sections she had already written up alongside her detailed experimental notes and well organised data it has been possible to write the papers and put this thesis by papers together for consideration for a posthumous PhD. To that end, I would like to thank all of the co-authors on the papers included in this thesis for agreeing to their use.

In all of the chapters, unless stated otherwise the crystallographic data were collected by Helen. The structures had all been refined by Helen normally to completion but in the majority of cases new cifs have been created either due to renumbering compounds for consistency in a paper or to include the hkl file in the cif, a relatively recent requirement. All of the compounds studied were synthesised by Helen, apart from a few in Chapter 7, and all of the diffuse reflectance and UV spectroscopic data were also collected by Helen. Although Helen had carried out a significant amount of analysis of the data in her preparation of her thesis, the selection of compounds included in the various papers prepared meant that the wording of papers from 2020 was for the main part written by myself. In the papers prior to 2020, Helen was heavily involved in writing and preparing them.

The as accepted papers have been reformatted here to produce a consistently formatted thesis but are essentially as published. Chapters 1 and 6 are literature reviews that Helen had written either for her final thesis or her first year PhD report respectively. They are essentially included as she wrote them and hence the references are not the most recent in the respective fields. A summary of any relevant points for all of the chapters and details of any sections not carried out directly by Helen is provided below along with details of the publication:

Chapter 1 - Spin Crossover Complexes Literature Review

Helen E. Mason

Prepared by Helen towards her thesis. The only section I have added is the 'Conclusions from the literature review' as it was not finished.

Chapter 2 - Structural and spectroscopic characterisation of the spin crossover in $[Fe(abpt)_2(NCS)_2]$ polymorph A

Helen E. Mason, Wei Li, Michael A. Carpenter, Michelle L. Hamilton, Judith A. K. Howard and Hazel A. Sparkes, *New Journal of Chemistry*, 2016, **40(3),** 2466-2478, doi 10.1039/C5NJ02359A. Reproduced with permission for the Royal Society of Chemistry.

The Resonant Ultrasound Spectroscopy in this chapter were collected in collaboration with Wei Li and Michael A. Carpenter. Helen carried out all of the rest of the experimental and was fully involved in the analysis and paper writing.

Chapter 3 - Structural Studies into the Spin Crossover Behaviour of $Fe(abpt)_2(NCS)_2$ Polymorphs B and D

Helen E. Mason, Jake R. C. Musselle-Sexton, Judith A. K. Howard, Michael R. Probert and Hazel A. Sparkes, *New Journal of Chemistry*, 2021, **45(31)**, 14014-14023, doi 10.1039/D1NJ02607K. Reproduced with permission for the Royal Society of Chemistry.

The high pressure crystallographic data in this chapter were recollected by Jake Musselle-Sexton and Michael Probert to clarify the position of the various transitions.

Chapter 4 - $[Fe(abpt)_2(NCSe)_2]$ polymorph A: Structural studies into the spin crossover behaviour

Helen E. Mason, Michelle L. Hamilton, Judith A. K. Howard and Hazel A. Sparkes, *New Journal of Chemistry*, 2018, **42(22)**, 18028-18037, doi 10.1039/C8NJ03627F. Reproduced with permission for the Royal Society of Chemistry.

Helen carried out all of the experimental and was fully involved in the analysis and paper writing.

Chapter 5 - $Co(abpt)_2(NCS)_2$ and $Ni(abpt)_2(NCS)_2$: Structural Characterisation of Polymorphs A and B

Helen E. Mason, Judith A. K. Howard and Hazel A. Sparkes, *Acta Crystallographica C*, 2021, in publication, doi.org/10.1107/S2053229621010251. Reproduced with permission of the International Union of Crystallography.

The data were all collected by Helen during her PhD.

Chapter 6 - Selected structural studies of photochromic systems

Helen E. Mason, Submitted as the literature review for her first year PhD report.

This chapter was fully written by Helen.

Chapter 7 - Structural studies of *N*-(methoxysalicylidene)-fluoroaniline, *N*-(methoxysalicylidene)-chloroaniline and *N*-(methoxysalicylidene)-bromoaniline derivatives

Helen E. Mason, Jane L. R. Yates, Rachael J. Potts, Matthias J. Gutmann, Judith A. K. Howard and Hazel A. Sparkes, *Acta Crystallographica B*, 2021 in publication, doi.org/10.1107/S2052520621009835. Reproduced with permission of the International Union of Crystallography.

Data on a few of the anils were collected by either Jane Yates or Rachael Potts as part of their final year projects. The neutron diffraction data were processed by Matthias Gutmann.

Chapter 8 - Selected solid state behaviour of three di-tertiary butyl substituted *N*-salicylideneaniline derivatives: temperature induced phase transitions and chromic behaviour

Helen E. Mason, Judith A. K. Howard and Hazel A. Sparkes, *Acta Crystallographica*, 2021, **C77**, 659-667, doi.org/10.1107/S2053229621008780. Reproduced with permission of the International Union of Crystallography.

All of the data were collected by Helen.

Chapter 9 - Synthesis and structures of three isoxazole containing Schiff bases

Helen E. Mason, Judith A. K. Howard and Hazel A. Sparkes, *Acta Crystallographica*, 2020, **C76**, 927-931, doi.org/10.1107/S2053229620010530. Reproduced with permission of the International Union of Crystallography.

All of the data were collected by Helen.

Chapter 10 - (*E*)-4-bromo-2-((phenylimino)methyl)phenol: A New Polymorph and Thermochromism

Helen E. Mason, Judith A. K. Howard and Hazel A. Sparkes, *Acta Crystallographica*, 2020, **76(11)**, 1001-1004, doi.org/10.1107/S2053229620011560. Reproduced with permission of the International Union of Crystallography.

All of the data were collected by Helen.

Abstract

This posthumous thesis combines two literature reviews written by Helen Mason and eight papers arising from data collected by Helen during her PhD studies. Helen also synthesised most of the compounds she studied and which are reported herein. The thesis uses single crystal X-ray diffraction data combined with spectroscopic data to study spin crossover complexes and anils, Schiff bases of salicylaldehyde derivatives with aniline derivatives. The thesis is divided into two main sections.

The first section examines spin crossover complexes initially through a summary of the reported literature (Chapter 1). The remainder of the section focuses on experimental studies into complexes containing (abpt = 4-amino-3,5-bis(pyridin-2-yl)-1,2,4-triazole) ligands. Chapters 2 and 3 examine the spin crossover behaviour of $Fe(abpt)_2(NCS)_2$ polymorphs **A**, **B** and **D**. The spin crossover behaviour of the three polymorphs is significantly different, which is particularly interesting given that their structures are very similar. Polymorph **A** has a thermal spin crossover, displays LIESST (Light Induced Excited Spin-State Trapping) and undergoes pressure induced spin crossover. Polymorph **B** does not undergo a thermal spin crossover at ambient pressure, however under pressure it undergoes a phase transition followed by a spin crossover. Polymorph **D** contains two unique Fe(II) centres in the asymmetric unit one of which undergoes a thermal spin crossover and displayed LIESST, upon the application of pressure a stepped spin crossover was observed at both unique Fe(II) centres. Structural and spectroscopic data are reported. The differences in structure and intermolecular interactions are examined and set in the context of similar structures in the literature. The thermal spin crossover and LIESST behaviour of $Fe(abpt)_2(NCSe)_2$ polymorph **A**, which is isostructural with $Fe(abpt)_2(NCS)_2$ polymorph **A**, is also reported and examined both structurally and spectroscopically (Chapter 4). The concluding chapter in this section, Chapter 5, reports the structures of two polymorphs $Co(abpt)_2(NCS)_2$ and $Ni(abpt)_2(NCS)_2$ polymorph **A** and **B**, which are isostructural with the corresponding $Fe(abpt)_2(NCS)_2$ polymorphs **A** or **B** respectively.

The second section begins with a literature review of selected photochromic systems which have been structurally characterised, Chapter 6. The rest of the section reports experimental studies into some anil compounds. Twenty seven *N*-(methoxysalicylidene)-haloaniline (halo = F, Cl or Br) derivatives were synthesised and their crystal structures determined, Chapter 7. New polymorphs were identified for two of the compounds, 4-(methoxysalicylidene)-4-fluroaniline and 3-(methoxysalicylidene)-4-chloroaniline and a temperature induced phase transition for 5-(methoxysalicylidene)-4-bromoaniline. Visual observations of their thermochromism alongside diffuse reflectance spectra are reported and linked to the observed structure, with those showing smaller interplanar angles between the ring generally tending to be more strongly thermochromic. Neutron diffraction data are also reported for two of the strongly thermochromic compounds, 5-(methoxysalicylidene)-2-chloroaniline and 5-(methoxysalicylidene)-2-bromoaniline. In Chapter 8, the structures of three di-tertiary butyl substituted anils, E)-2,4-di-tert-butyl-6-(((4-fluorophenyl)imino)methyl)phenol, (E)-2,4-di-tert-butyl-6-(((4-chlorophenyl)imino)methyl)phenol, and (E)-2,4-di-tert-butyl-6-(((4-bromophenyl)imino)methyl)phenol, are reported. Two polymorphs were identified for (E)-2,4-di-tert-butyl-6-(((4-fluorophenyl)imino)methyl)phenol, while the other two structures underwent a thermally induced phase transition. The thermochromic and photochromic behaviour of the compounds were examined using diffuse reflectance and Raman spectroscopy. In Chapter 9, the synthesis and structures of three isoxazole containing Schiff bases, (E)-2-((isoxazol-3-ylimino)methyl)phenol, (E)-2-(((5-methylisoxazol-3-yl)imino)methyl)phenol and (E)-2,4-di-tert-butyl-6-((isoxazol-3-ylimino)methyl)phenol, are reported. None of these were found to be strongly thermochromic but all three were found to be photochromic. Finally, Chapter 10 reports the structure of a new polymorph of (*E*)-4-bromo-2-((phenylimino)methyl)phenol. The colours of the two polymorphs at room temperature were found to be different, and both polymorphs were found to display thermochromism.

Contents

Chapter 2 26

Structural and spectroscopic characterisation of the spin crossover in $[Fe(abpt)_2(NCS)_2]$ polymorph A

Helen E. Mason, Wei Li, Michael A. Carpenter, Michelle L. Hamilton, Judith A. K. Howard and Hazel A. Sparkes, *New Journal of Chemistry*, 2016, **40(3)**, 2466-2478. Reproduced with permission for the Royal Society of Chemistry.

Chapter 4 70

$[Fe(abpt)_2(NCSe)_2]$ polymorph A: Structural studies into the spin crossover behaviour

Helen E. Mason, Michelle L. Hamilton, Judith A. K. Howard and Hazel A. Sparkes, *New Journal of Chemistry*, 2018, **42(22)**, 18028-18037. Reproduced with permission for the Royal Society of Chemistry.

Chapter 1

Spin Crossover Complexes Literature Review

Helen E. Mason

Prepared by Helen towards her thesis.

1.1 Introduction

Spin crossover (SCO) was first observed in the 1930s,[1] since then it has been extensively studied and there are many excellent recent review articles[2] and books[3] providing insight into this expanding multidisciplinary field of research. This literature review will therefore only provide a brief introduction to spin crossover from a ligand field perspective[4] and mainly focus on structural studies[5] and the importance of understanding structure-property relationships in SCO systems.[6]

SCO systems display a reversible low spin (LS) to high spin (HS) molecular spin state transition induced by external stimuli, including temperature, pressure,[7] magnetic field[8] and light irradiation.[9] Properties influenced by the electronic structure, including molecular structure, colour and magnetism, are altered during the transition providing the opportunity for the development of multifunctional systems. SCO materials also display remarkable bistability in the solid state, which can be extended into thin films, gels, liquid crystals[10] and nanoparticles,[11] giving great potential for externally triggered switching applications including data storage, display systems and molecular electronic devices.[3] Iron(II) systems, in particular those with six nitrogen donor ligands [Fe-N_6], are the most studied SCO materials[12] but SCO has also been observed in iron(III),[13] cobalt(II),[14] chromium(II) and manganese(III) complexes.[3b, 15] Although many systems have been studied, the cooperative propagation and spatio-temporal development of the spin transition in the solid state is not fully understood[16] and further development is needed before applications are fully realized.

1.2 Origin of spin crossover

SCO may be observed for first row transition metal ions and most commonly octahedral coordinate d^4 - d^7 electronic configurations. In a regular octahedral ligand field the valence *d*-orbitals split into non-bonding t_{2g} (d_{xy}, d_{yz}, d_{zx}) and antibonding e_g (d_{z^2}, $d_{x^2-y^2}$) sets, with an energy difference (ligand field splitting) symbolized by Δ. The nature of the metal ion, including its oxidation state, the ligands and their geometry around the central ion all affect the magnitude of Δ and for octahedral (O_h) symmetry Δ = 10Dq, where Dq corresponds to a semi-empirical parameter related to crystal field force (Figure 1.1).[4a, 17] The electronic ground state configuration adopted by the valence *d*-electrons, either LS or HS, depends on which of two conflicting factors which influence the e_g and t_{2g} occupancies is energetically favourable in a particular system:[4b] (1) The Aufbau principle - electrons will occupy lowest energy orbitals first. (2) Hund's rule - electrons align with parallel spins in different orbitals before antiparallel spin pairing in the same orbital. This reduces interelectronic (Coulombic) repulsion energy, π_c, and increases the quantum mechanical exchange energy, π_e, which provides stabilization to the system. π_e stabilizes the HS state, which contains fewer antiparallel paired electrons, more than the corresponding LS state. The crystal field splitting diagram shown in Figure 1.1 provides a very simplistic model for SCO valid only for regular octahedral symmetry and neglects any additional *d*-orbital splitting caused by spin-orbit coupling or interelectronic repulsion (also known as spin pairing energy, π).[4a]

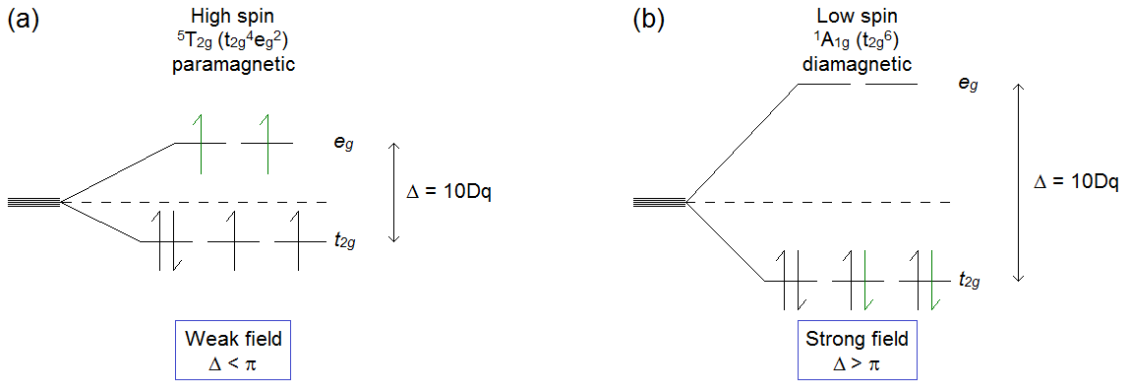

Figure 1.1 - Simple crystal field splitting diagram for a d^6 iron complex depicting the *d*-orbital splitting in a regular octahedral ligand field (barycentre illustrated as a dashed line). The electronic occupancies in a (a) weak and (b) strong ligand field are shown.[4a]

In d^4 and d^7 configurations a LS to HS transition causes an increase in orbital energy, +Δ, and decrease in Coulombic repulsion, $-\pi_c$, but in d^5 and d^6 systems this transition promotes two electrons from t_{2g} to e_g causing an energy change of $+2\Delta$ and $-2\pi_c$. The spin pairing energy, $\pi = \pi_c + \pi_e$, is the mean energy (per unit of Δ) required for spin pairing of *d* electrons.[4b] The LS state, where spin pairing in the lower energy t_{2g} orbitals is favoured prior to e_g orbital occupancy [minimum spin multiplicity, Figure 1.1(b)], is stabilized in a strong ligand field when $\Delta > \pi$, for example in $[Fe(CN)_6]^{4-}$. Whereas the HS state, where t_{2g} and e_g orbitals are both singularly occupied before antiparallel spin pairing [maximum spin multiplicity, Figure 1.1(a), is stabilized in a weak ligand field when $\Delta < \pi$, for example in $[Fe(H_2O)_6]^{2+}$.[4] Transition metal complexes with ligand field strengths that satisfy $\Delta(10Dq^{HS}) < \pi < \Delta(10Dq^{LS})$ can be strongly influenced by sample environment including temperature, light irradiation, magnetic field and pressure to undergo reversible HS to LS transitions (SCO). Tanabe Sugano diagrams,[18] calculated with Racah parameters[19] to include interelectronic repulsion contributions, are commonly used to illustrate how the energies of excited and ground ligand field states of a coordinated metal ion vary with increasing Δ.[4a]

In a LS→HS transition a characteristic elongation of metal ligand (M-L) bond lengths (r) is observed due to increased occupancy of the antibonding e_g orbitals in the HS state. Δ is affected by changes in the M-L bond lengths because $\Delta \approx \mu/r^n$ (μ is the ligand dipole moment and n = 5-6) therefore abrupt changes in M-L bond lengths cause abrupt changes in Δ.[12b] In iron(II) complexes with nitrogen or oxygen donor (N- or O-donor) ligands, M-L bond lengths in the LS state (r_{LS}) are generally 1.95 – 2.00 Å, whereas in the HS state (r_{HS}) they are 0.14-0.24 Å longer, lying in the range 2.12 – 2.18 Å.[4a, 20] For iron(III) and cobalt(II) systems smaller bond length changes of ~0.15 Å and ~0.1 Å respectively are observed.[13-14] From a thermodynamic perspective a SCO transition can be thought of as an entropy driven unimolecular LS↔HS reaction, with $\Delta H_{HL} > 0$ and $\Delta S_{HL} > 0$. Above a critical temperature ($T_c = T_{1/2}$) the reaction is spontaneous ($\Delta G_{HL} < 0$) with the LS or HS states enthalpically or entropically favoured respectively.[3b, 20a]

Iron(II), a d^6 metal ion, displays particularly favourable characteristics for SCO with maximum ligand field stabilization energy (LFSE) providing an easily accessible LS state and a lower spin pairing energy than for other ions. Octahedral SCO iron(II) systems generally exhibit larger structural changes than other complexes therefore the abrupt transitions with hysteresis desirable for applications are more commonly observed. These complexes are therefore the most studied SCO systems with mononuclear, polynuclear, polymeric networks, gels, porous cage-like systems, liquid crystals, films and nanomaterials prevalent in the research literature.[3] Ligands containing tris(diimine), bis(terimine),[21] pyrazolyl,[22] azole[22a, 23] and Schiff base[24] derivatives provide an appropriate ligand field strength for SCO in iron(II) systems to be observed and have all been extensively reviewed (Figure 1.2).

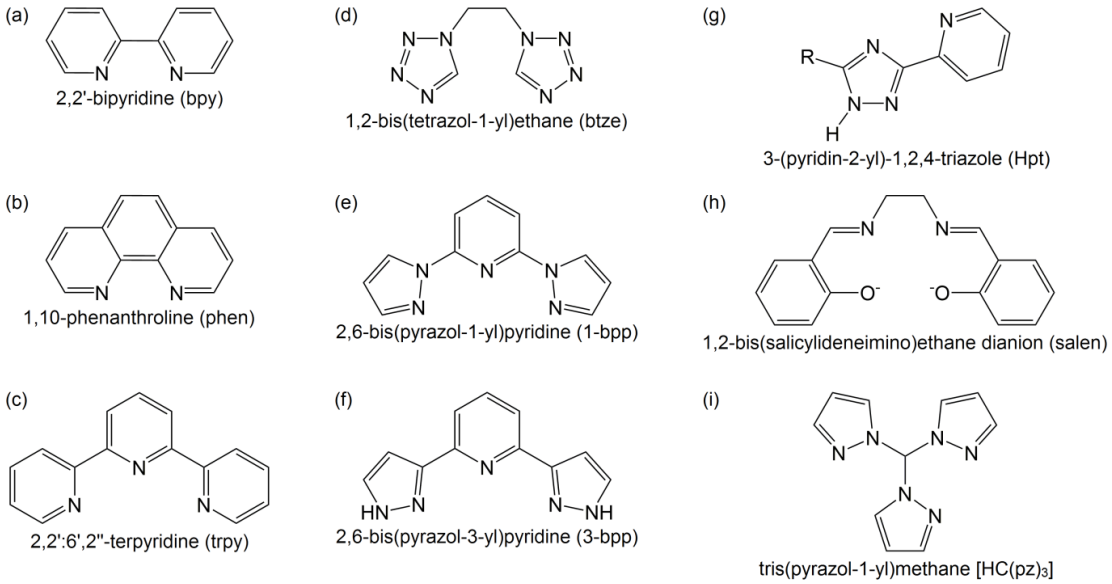

Figure 1.2 - Common ligands which have derivatives used to create SCO complexes.

1.3 Spin crossover transition profiles

SCO is observed in solution,[25] amorphous and crystalline solids but it is the cooperative nature of solid state spin transitions that attracts the greatest interest for applications.[26]. In a concentrated crystal lattice *inter*molecular interactions, including π-π, van der Waals (vdW), hydrogen and halogen bonding in discrete molecular systems and covalent interactions in polymeric systems, are known to propagate structural and electronic changes throughout the crystal bulk via strong communication between spin-changing molecules.[6a, 26b, 27] As a solid is diluted, either in a solvent or non-interacting matrix, the spin transition becomes more gradual or may be completely quenched.[25] This highlights that, rather than geometry changes in individual molecules, cooperative propagation throughout the crystal lattice via long range intermolecular interactions can help to explain the diverse range of solid state SCO behaviour observed (Figure 1.3).

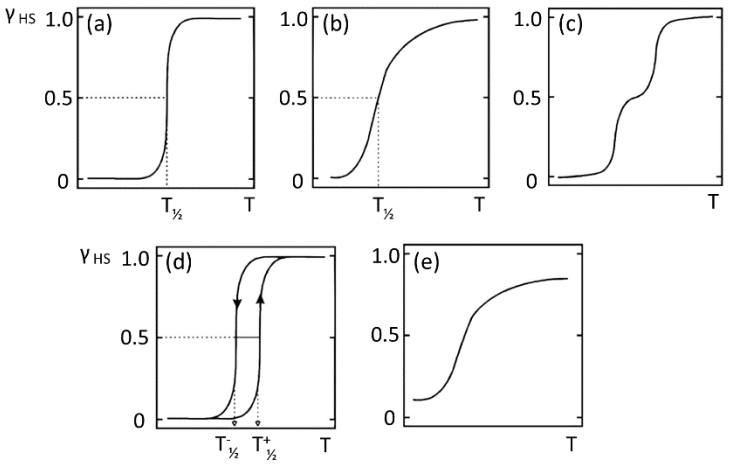

Figure 1.3 - Spin transition curve profiles (γ_{HS}, molar fraction of HS species): (a) abrupt, (b) gradual, (c) two-stepped, (d) transition with hysteresis where HS→LS and LS→HS transitions occur at different temperatures; $T_{1/2}^{\downarrow}$ and $T_{1/2}^{\uparrow}$, and (e) incomplete transition with a residual HS fraction, $\gamma_{HS} > 0$, at low temperature.[28]

The temperature where 50% of SCO active molecules are converted is defined as the spin transition temperature, $T_{1/2}$ and for complete transitions [Figure 1.3(a), (b), (d)] this occurs when the molar fractions of HS (γ_{HS}) and LS (γ_{LS}) species exist in a 1:1 ratio.[28] Abrupt transitions [Figure 1.3(a)], often accompanied by large hysteresis loops [Figure 1.3(d)], or gradual transitions [Figure 1.3(b)] are indicative of either strong or weak cooperativity respectively. SCO systems displaying abrupt, complete thermal transitions with a wide hysteresis loop in the room temperature region[20a] show unique bistability making them suitable for applications in information recording, switching and memory systems.[29] The origin and propagation mechanism of cooperative communication and hysteresis effects in the crystal lattice are therefore of fundamental importance. It is thought hysteresis may be caused by:

1. A structural phase change driving or occurring due to the spin transition.
2. Strong communication in a highly cooperative system.
3. A disorder-order transition, possibly in an anion or solvate molecule, occurring concurrently with a spin transition.

Enhancing cooperative effects in SCO systems is an active research topic and the formation of hydrogen bonded networks, incorporation of bridging ligands to create polymeric systems and inclusion of π-π stacking moieties have all been successful at increasing communication between metal centres.[2-3, 27]

1.4 Control of spin crossover properties

SCO behaviour can be modified by influences of a chemical or physical nature. Ligand substitution/replacement alters the molecular electronics and can introduce steric effects including *inter*-ligand repulsion; for example, $[Fe(phen)_3]^{2+}$ is LS at all temperatures whereas $[Fe(2\text{-methyl-phen})_3]^{2+}$ has a weaker Δ and displays SCO due to steric effects elongating the Fe-N bond adjacent to the methyl group.[30] SCO may also be prohibited in the solid state if the HS and LS structures differ by a large amount or if high density crystal packing creates a rigid environment; for example, some $[Fe(1\text{-bpp})_2]^{2+}$ complexes are trapped in a twisted HS structure due to a Jahn-Teller distortion favoured by the narrow ligand bite angle.[6a, 31] The ligand spectrochemical series ranks ligands according to their influence on Δ when complexed; strong field π-acceptors increase Δ and weak field π-donors decrease Δ. Tuning Δ by substitution of different field strength ligands is frequently used to modify SCO complexes and an example is given in Table 1.1.[28]

Table 1.1 - An example of the changes in magnetic behaviour observed upon sequential ligand substitution. The ligands with increasing field strength are ordered $Cl^- < NCS^- <$ py < phen < CN^-.[28]

Metal complex	Spin state	$T_{1/2}$ (K)
$[Fe(py)_4(NCS)_2]$	HS	×
$[Fe(phen)(py)_2(NCS)_2]$	Spin crossover observed	106
$[Fe(phen)_2(NCS)_2]$	Spin crossover observed	176
$[Fe(phen)_3]^{2+}$	LS	×
$[Fe(phen)_2(CN)_2]$	LS	×
$[Fe(phen)_2Cl_2]$	HS	×

Diluting SCO complexes by systematic doping with non-SCO active metal ions, for example Mn, Co, Zn, gradually decreases the abruptness of the transition and has provided new information about cooperative interactions in various materials. $T_{1/2}$ shifts to either lower or higher temperature depending on whether

the volume is increased or decreased by doping due to an effective decrease or increase in pressure respectively.[2, 12b]

Non-coordinated counter-anions and solvent molecules in the crystal lattice also influence the SCO properties. Different magnetic behaviour is observed for seven alcohol solvates of $[Fe(2\text{-pic})_3]Cl_2$[1] despite similar layered packing structures being observed in the HS state (at 200 K) and the fact that no direct structure-property correlations have currently been identified.[32] The individual ethanol (EtOH) or 2-propanol (2-PrOH) solvates display two-stepped spin transitions associated with two re-entrant structural phase transformations and changing ratios of solvent disorder, whereas the mixed solvate $[(EtOH)_{0.744}(2\text{-}PrOH)_{0.256}]$ displays a gradual transition without hysteresis indicating that even subtle changes in vdW interactions influence the SCO behaviour.[32d] Structure-property relationships in anion dependent SCO systems are complex, differing for each system and difficult to differentiate from, for example, solvent and steric packing effects.[6a] In some systems a correlation between magnetic properties and cation····anion hydrogen bonding strength has been identified; for example, in $[Fe(trim)_2]X_2$ increased stability of the HS state in the order $X = F^- > Cl^- > Br^- > I^-$ is attributed to stronger N_{ligand}-H····X bond strengths for the smaller anions causing weakening of the Fe-N bonds through inductive effects [Figure 1.4(a)].[33] In $[FeH_3L^{Me}]Cl\cdot Y$ or $\cdot Y_2$ systems[2] the magnetic properties are reported to correlate with the size and shape of the counterion[34] but there are many other examples where relationships could not be identified.[6a] Disorder-order transitions in counter anions or solvent molecules can mediate solid state spin transitions where direct communication between metal centres is negligible[35] and can create additional features including stepped transitions in some systems.[32]

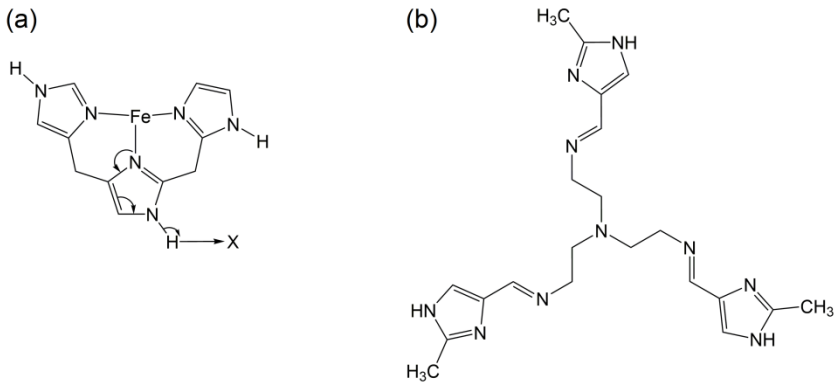

Figure 1.4 - (a) Inductive effect in $[Fe(trim)_2]X_2$ illustrated for the $[Fe_{1/2}(trim)]X$ asymmetric unit. (b) H_3L^{Me} ligand.

SCO behaviour is dependent on the sample preparation technique and any post synthetic processing. Care needs to be taken with processed samples, for example ground samples for powder diffraction, to ensure they display the same properties as the original sample before structure-property relationships are identified. $[Fe(L)_2(NCS)_2]$ (L= phen[36] or bpy)[37] was originally thought to be polymorphic because the abruptness and residual γ_{HS} and γ_{LS} fractions were strongly dependent on whether synthesis by precipitation or extraction was chosen.[38] It is now thought that differing sample quality with crystal defects induced either through sample treatment (grinding or milling) or the preparation technique produces the more gradual and incomplete spin transition.[39] The effect of temperature, pressure and light irradiation on SCO samples will be discussed in following sections.

[1] pic = picolylamine

[2] H_3L^{Me} is shown in Figure (b) and Y = BF_4^-, ClO_4^-, PF_6^-, AsF_6^-, SbF_6^-, $CF_3SO_3^-$, I_3^-

1.5 Thermal and pressure induced spin crossover

Thermal SCO is observed when the zero point energy difference between the lowest vibronic LS and HS states is approximately equal to thermal energy; $\Delta E^0_{HL} = E^0_{HS} - E^0_{LS} \approx k_BT$. At low temperature the complex is in the lower energy $^1A_{1g}$ LS state and occupancy of the $^5T_{2g}$ HS state occurs with increasing temperature. The crossover point of the LS and HS potential wells (Figure 1.5), which occurs when $\Delta(10Dq) = \pi$, does not correspond to an energy minimum and $\Delta(10Dq^{HS}) < \pi < \Delta(10Dq^{LS})$ should be used to determine the values of ΔE^0_{HL} where SCO may be observed.[4a] The limited range of ligand field strengths for which an [Fe(II)-N_6] complex may display thermal SCO has been estimated from spectroscopic studies of $[Fe(ptz)_6](BF_4)_2$[3] (Table 1.2).[4a, 12b] Cooperative spin state interactions influence Boltzmann statistics therefore real solid state systems do not fit simplistic models and complex models, simulations and calculations are needed to accurately study thermal SCO behaviour.[40]

Table 1.2 - Spin states observed for transition metal complexes with different ligand field strengths and the corresponding zero-point energy differences between lowest vibronic HS and LS spin states.[4a, 12b]

Ligand field strength, $\Delta(10Dq)$ (cm^{-1})	ΔE^0_{HL} (cm^{-1})	Spin state
<10000	<0	HS complex only
≈11000 - 12500	≈0 - 2000	SCO complex, HS state
≈19000 - 22000	≈0 - 2000	SCO complex, LS state
>23000	>2000	LS complex only

At constant temperature, applying pressure strongly influences the energy of a vibrational state and alters the LS↔HS equilibrium in SCO systems. Pressure induced SCO is observed due to the large increase in M-L bond lengths in a LS→HS transition giving a unit cell volume increase of ΔV^0_{HL} per SCO complex (~20 $Å^3$/Fe centre in a [Fe(II)-N_6] complex).[41] The work done on the system by increasing the pressure (p) at constant temperature increases the zero-point energy of the HS state by $p\Delta V^0_{HL}$ and the zero-point energy difference between LS and HS states such that $\Delta E^0_{HL}(p_2) > \Delta E^0_{HL}(p_1)$ when $p_2 > p_1$. The activation energy, ΔW^0_{HL}, required for a HS→LS transition is decreased and the LS state is favoured.[7, 42] A configurational coordinate diagram for an O_h iron(II) complex along the M-L bond coordinate, r(Fe-L), is shown in Figure 1.5, illustrating the influence of temperature and pressure on the adiabatic potentials of LS and HS ground states.[4a, 12]

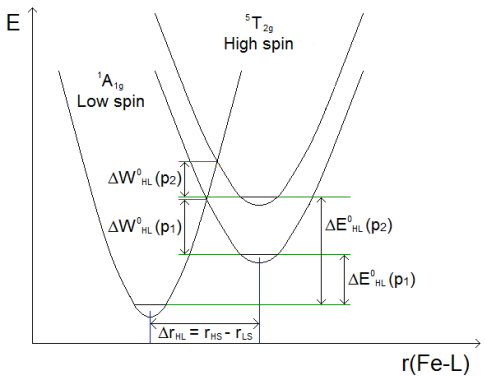

Figure 1.5 - Pictorial representation of the LS and HS potential wells for an octahedral d^6 iron complex along the M-L bond coordinate, r(Fe-L),[4a, 12] where $p_2 > p_1$ [reproduced with permission from reference].[7b]

[3] ptz = 1-propyltetrazole

Pressure induced SCO, which was first reported in the 1960s for substituted iron(III) dithiocarbamate complexes,[43] plays a fundamental role in biological molecules, for example haemoglobin,[44] and also processes in the Earth's mantle[45] therefore has attracted research interest from a broad audience. New hydrostatic pressure cells have recently been developed allowing combined variable temperature and pressure solid state[7] or solution studies in crystallographic, magnetic susceptibility, EXAFS, optical reflectivity, vibrational or Raman spectroscopy experiments.[7] This provides unique insight into the SCO mechanism; for example, if systematic variable temperature and pressure magnetic and crystallographic studies are carried out the influence of pressure on $T_{1/2}$ can be modelled using mean field approximation (Equation 1).[7a, 41] $T_{1/2}$ is typically found to shift 15 K/kbar for a [Fe(II)-N_6] complex.[41]

$$\partial \mathrm{T}_{1/2}/\partial \mathrm{p} = \Delta \mathrm{V}_{\mathrm{HL}}/\Delta \mathrm{S}_{\mathrm{HL}}$$

Equation 1: Clausius-Clapeyron relation modelling $T_{1/2}$ with respect to hydrostatic pressure, p, obtained using an Ising-like model with mean-field approximation. $\Delta \boldsymbol{V_{HL}}$ and $\Delta \boldsymbol{S_{HL}}$ are the changes in volume and entropy respectively occurring in a HS→LS transition.[7a, 41]

Often a residual low temperature HS fraction remains after a thermal HS→LS transition whereas under pressure a complete transition usually occurs.[7] $T_{1/2}$ is shifted to higher temperature (as seen by positive values of $\Delta \mathrm{V}_{\mathrm{HL}}$ and ΔS_{HL} in Equation 1) under hydrostatic pressure and a more gradual profile and reduced hysteresis loop are predicted[41] although some experimental studies contradict these expectations.[42] Low temperature high pressure experiments are very challenging and only a limited number of combined studies have been carried out. A nice example is [$Fe(phen)_2(NCS)_2$] polymorph II for which magnetic, crystallographic and EXAFS data have been used to estimate a value of $P_{1/2} \approx 0.6$-0.7 GPa[27, 46] and other important thermodynamic terms related to the spin transition.[27]

1.6 Light induced excited state spin trapping (LIESST)

In the 1980s the discovery of a new metastable photoinduced effect in SCO complexes called "Light induced excited state spin trapping" (LIESST) opened up exciting new prospects for SCO research. Short lived population of the HS state was detected upon pulsed laser irradiation of iron complexes in solution[47] and then in 1984[48] quantitative "trapping" of the metastable HS state was observed upon visible light irradiation at low temperature for crystalline $[Fe(ptz)_6](BF_4)_2$ (a thermochromic compound with $T_{1/2}^{\uparrow}$ = 135 K and $T_{1/2}^{\downarrow}$ = 128 K).[49] The 300 K (HS state, colourless crystal) and 80 K (LS state, purple crystal) optical spectra, shown in Figure 1.6(a), are indicative of a thermal HS→LS transition; at 300 K the spin allowed, parity forbidden $^5T_2 \rightarrow {}^5E$ transition is seen as a weak absorption band and at 80 K two absorption bands assigned to spin allowed $^1A_1 \rightarrow {}^1T_1$ and $^1A_1 \rightarrow {}^1T_2$ transitions are observed. Irradiation with 514.5 nm light at 10 K causes bleaching of the crystal colour as the metastable HS state is populated [similar spectrum to the thermal HS state at 300 K, Figure 1.6(a)].[2, 48, 50] Thermal relaxation at 10 K takes ~40 days but at 50 K it is much faster occurring within ~15 minutes. [5-6, 20]

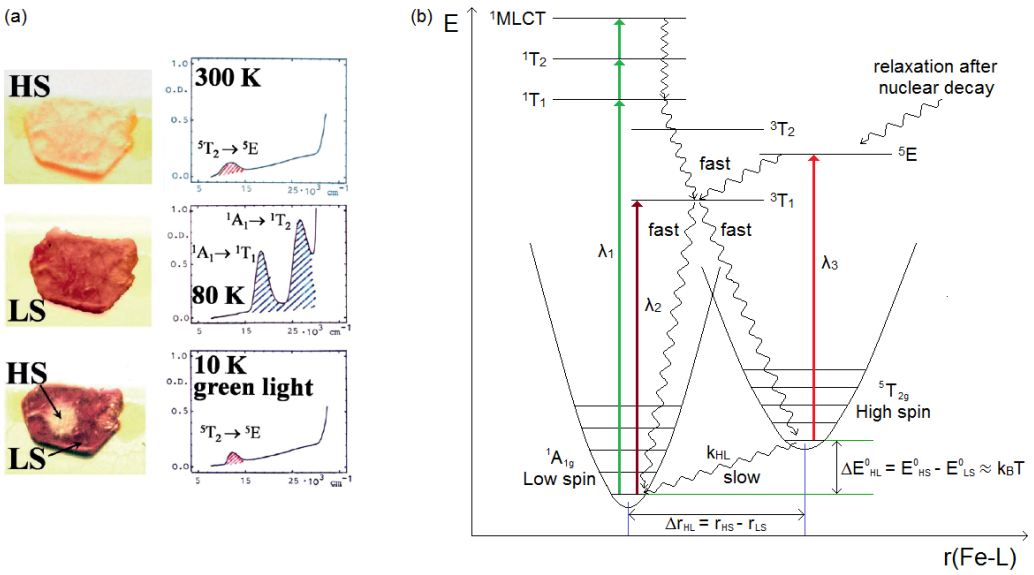

Figure 1.6 - (a) Single crystal UV-Vis spectra and photographs of $[Fe(ptz)_6](BF_4)_2$ at (from top to bottom) 300 K (HS state), 80 K (LS state) and after green light irradiation at 10 K (metastable HS state) [reproduced with permission][50]. (b) Jablonski diagram for a d^6 iron complex showing possible spin allowed *d-d* transitions (straight lines) and relaxation processes (wiggly lines) to illustrate the processes of LIESST and reverse LIESST [adapted from reference].[9, 12b]

The Jablonski diagram in Figure 1.6(b) shows transitions thought to be involved in LIESST and reverse LIESST processes for an octahedral iron(II) complex. The LS $^1A_{1g}(t_{2g})^6$ state, populated at low temperature, undergoes a spin allowed parity forbidden transition to the $^1T_1$,$^1T_2$ states upon irradiation with an appropriate wavelength (normally green), fast relaxation occurs via non-adiabatic intersystem crossing (ISC) to the $^3T_2$,$^3T_1$ states and then to the metastable HS $^5T_{2g}(t_{2g}^4e_g^2)$ state. The MLCT bands can also be populated upon exciting the $^1A_{1g}$ LS state because the shorter M-L bonds in the LS state mean greater overlap of metal and ligand orbitals and MLCT bands that are often lying at similar energy to the ligand field bands. The $^5T_{2g} \rightarrow {}^1A_{1g}$ transition is both spin and parity forbidden and the system is effectively "trapped" in the $^5T_{2g}$ state. Relaxation can only occur via radiationless thermal lattice vibrations therefore explaining the increased lifetime of this state with decreasing temperature. LIESST is enhanced if the double ISC ($^1T_1$,$^1T_{,2} \rightarrow {}^3T_1$,$^3T_2 \rightarrow {}^5T_{2g}$) occurs faster than direct $^1T_{1,2} \rightarrow {}^1A_{1g}$ relaxation and also the $^3T_2$, $^3T_1$ states lie at lower energy than the $^1T_1$, $^1T_2$ states. This process is not fully understood and ultrafast solution state studies have suggested an alternative mechanism of excitation into the ^{1}MLCT band and relaxation via ^{3}MLCT directly to the $^5T_{2g}$ state. The unit quantum efficiency for population of the $^5T_{2g}$ state on a <200 fs timescale and the lack of spectroscopic evidence for relaxation via intermediate $^3T_1$,$^3T_2$ states support this proposed direct relaxation process.[51] Reverse LIESST is observed when excitation from the metastable HS state, $^5T_{2g}$, to the ^5E_g state occurs upon light irradiation (normally red light) followed by fast ISC from $^5E_g \rightarrow {}^3T_1$,$^3T_2 \rightarrow {}^1A_{1g}$ through favourable spin-orbit coupling. Unlike LIESST, this is a non-quantitative process which reaches steady state equilibrium because individual excitation of the HS $^5T_{2g} \rightarrow {}^5E_g$ band is impossible due to overlap with the LS $^1A_1 \rightarrow {}^3T_1$ and $^1A_1 \rightarrow {}^3T_2$ bands.[9]

Classical thermal relaxation of the metastable HS species in the solid state would require enough thermal energy to overcome the energy barrier (E^a_{class}) between HS $^5T_{2g}$ and LS $^1A_{1g}$ potential wells. E^a_{class} = 2500-3000 cm^{-1} for iron(II) complexes (with small ΔE_{HL}) therefore as T→0 K the rate constant for HS→LS relaxation (k_{HL}) should go to zero if relaxation occurs via a classical pathway. This is not observed in SCO complexes and instead relaxation occurs via a quantum mechanical, non-adiabatic multiphoton tunnelling process with a probability given by Fermi's golden rule.[9] The effective activation energy for quantum mechanical tunnelling (E^a_{eff}) is always lower than E^a_{class} at finite temperatures. For a typical iron(II)

complex, K_{HL} and E_{eff}^{a} show changes as a function of temperature with respect to the energy difference, $n = \Delta E_{HL}^{0}/\bar{h}\omega$, between vibrational energy levels m and m' in the HS and LS states respectively.[9]

Below ~50 K relaxation via tunnelling is predicted to be temperature independent. Spontaneous transfer of electronic energy from the lowest vibrational HS state energy level to vibrational energy in the LS state is dispersed into the surrounding lattice environment. In this temperature region the "inverse energy gap law" applies; increasing ΔE_{HL}^{0} (larger n), by increasing the ligand field strength through ligand substitution, doping to create internal pressure or applying external hydrostatic pressure, increases k_{HL} and decreases t_{HL}, the lifetime.[52] Higher HS state vibrational energy levels are populated with increasing temperature and k_{HL} is temperature dependent above ~50 K because of increased probability of quantum mechanical tunnelling to the LS state.[9] LIESST relaxation, particularly in concentrated SCO systems, often has a sigmoidal nature due to self-acceleration through elastic interactions rather than the expected exponential profile. Increasing population of the LS state causes internal pressure in the lattice, increasing ΔE_{HL}^{0} and therefore k_{HL} and the tail end of the relaxation process is slowed down by nearest neighbour interactions.[9] Consequently, light-induced thermal (LITH),[53] pressure (LIPH),[54] optical (LIOH),[55] magnetic (LIMH) or spectral (LISH) hysteresis can be observed under constant irradiation by varying parameters which alter the relaxation rate.[56] These phenomena are difficult to examine experimentally without unwanted kinetic influences and bulk absorption effects which distort the hysteresis loop.[56]

LIESST has been extensively studied in iron(II) SCO systems in crystalline form, thin films, solution, diluted in polymer matrices or doped by inert metal ions. Reports of LIESST in iron(III) and cobalt(II) systems are less prevalent and the low temperature metastable HS state lifetimes are expected to be much shorter, in the order of milliseconds or microseconds respectively and time resolved pump-probe techniques are needed to study the process.[9]

1.6.1 LIESST towards applications

SCO complexes which undergo LIESST near room temperature are desired because currently prospective applications are restricted by the low temperature required to stabilize the metastable HS structure. T_{LIESST}, the minimum of the curve in a $d\chi_M T/dT$ versus T plot, is the critical LIESST temperature above which metastable HS→LS relaxation occurs and provides a parameter for screening potential technologically viable compounds. T_{LIESST} is dependent on various experimental conditions and Létard *et al.* have defined the following experimental protocol for magnetic measurements to allow comparison between samples:[57]

1. Slow cooling to 10 K.
2. Irradiation at 10 K with an appropriate wavelength laser until a photostationary equilibrium is reached.
3. Sample warming without irradiation at 0.3 K min^{-1} while acquiring temperature dependent magnetic measurements ($\chi_M T$, duration 60 sec) using a SQUID magnetometer.[57]

Comparison of over eighty iron(II) complexes[57-58] has revealed, consistent with the "inverse energy gap law",[9, 52] that $T_{LIESST} = T_0 - 0.3T_{1/2}$ (where T_0 is the limit when $T_{1/2} = 0$ K). Parallel lines with T_0 = 100, 120, 150 and 180 K have been observed for [Fe-N_6] complexes containing six monodentate, three bidentate, two tridentate and one quadridentate plus two monodentate ligands respectively. The relationship appears to extend beyond just SCO systems with a collection of charge transfer induced spin transition (CTIST) cobalt-iron cyanide Prussian Blue analogues forming an additional T_0 = 200 K line.[59] Cooperativity, anion substitution, hydrate formation and electronic influence of the ligand appear not to alter the relationship between T_{LIESST} and $T_{1/2}$, but distortion of the [Fe-N_6] coordination sphere away from regular octahedral has a large effect.[57-58] Groups of complexes with coordination sphere distortions created by similar denticity ligands are located on the same T_0 line, suggesting the relationship is dependent only on the inner coordination sphere and not surrounding parameters. To date, the highest T_{LIESST} value for a mononuclear iron(II) complex is 135 K and is observed for a macrocyclic Schiff base ligand complex which

undergoes an interesting thermal HS hepta-coordinate to LS hexa-coordinate M-L bond breaking SCO transition.[60] Higher values of up to 180 K have been observed for octanuclear 3D cobalt-iron Prussian blue clusters.[61] As T_{LIESST} is increased overlap of thermal and light induced hysteresis loops can occur and has been investigated for $[Fe_xMn_{1-x}(bpp)_2](BF_4)_2$ complexes where increased Mn(II) doping shifts $T_{1/2}$ to lower temperature.[62] The behaviour observed in the T_{LIESST} $T_{1/2}$ overlap region is attributed to a kinetic effect stabilizing the HS species and has also been studied using mean-field simulation.[63]

1.7 Experimental techniques used for investigating spin crossover

SCO behaviour can be examined using techniques which probe property changes accompanying the spin transition. Magnetic susceptibility (χ) is sensitive to spin state change (S=2, HS→S=0, LS for iron(II) complexes) and the spin transition profile and effective magnetic moment (μ_{eff}) can be determined from temperature dependent magnetic susceptibility measurements [χ(T)] using Equation 2(a) and (b) respectively.[2] Solid state and solution magnetochemical studies can be carried out using a SQUID magnometer or Faraday balance and the Evans' NMR method respectively.[2]

$$\text{(a)} \quad \boldsymbol{\chi(T) = \gamma_{HS}(T) \cdot \chi_{HS} + \left(1 - \gamma_{HS}(T)\right) \cdot \chi_{LS}}$$

$$\text{(b)} \quad \boldsymbol{\mu_{eff} = 2.83\sqrt{\chi(T)}}$$

Equation 2: Temperature dependent magnetic susceptibility measurements [$\boldsymbol{\chi(T)}$] used to calculate (a) $\boldsymbol{\gamma_{HS}(T)}$ by measuring χ for pure HS ($\boldsymbol{\chi_{HS}}$) and LS ($\boldsymbol{\chi_{LS}}$) states and (b) $\boldsymbol{\mu_{eff}}$.[2]

^{57}Fe Mössbauer spectroscopy with variable temperature, pressure or under light irradiation is a very powerful technique to obtain information about spin and electronic states, oxidation number and ferro- or antiferromagnetic behaviour of ferrous compounds.[50] Other spectroscopic techniques commonly used to investigate SCO behaviour include:

- Far- or mid-infrared vibrational spectroscopy to probe stretching frequencies of metal-donor or internal ligand modes. IR sample preparation techniques, for example grinding and pressing into KBr pellets, can dramatically alter the SCO properties.[64]
- Raman spectroscopy to probe active stretching modes and for which mechanical processing of the sample is not necessary.[64b]
- UV-Vis optical spectroscopy and optical microscopy to study the nucleation and evolution of the spin transition by monitoring the colour change (thermo-, piezo- or photochromism).[65]

Changes in thermodynamic properties, for example enthalpy and entropy, can be examined using calorimetry. A discontinuity (large "jump") in heat capacity (C_p) occurs at the spin transition temperature and this has led to the understanding of thermal SCO as an entropy driven reaction in the solid state.[66] Powder and single-crystal X-ray diffraction are very important techniques for investigating structure-property relationships in SCO materials[6] and will be discussed in further detail in the next section.

1.8 Crystallographic studies of spin crossover systems

Variable temperature, pressure and photocrystallographic studies have revealed exciting information about key structure-property relationships[6] and cooperative interactions[26b, 27] in solid state SCO materials.[42] Variable temperature studies monitoring the unit cell evolution[35] and characterizing the thermal HS (HS-1) and LS structures are frequently carried out but reports of the light induced metastable HS structure (HS-2) are less common. It is important to note that although HS-1 and HS-2 often have similar structural characteristics they are not the same structure. The pressure induced structure is reported even less often with fewer than ten high pressure SCO structures published to date.[42] Thermal

and pressure induced SCO behaviour may be similar; for example, a two-step spin transition is observed both thermally and under pressure for $[Fe(bapbpy)(NCS)_2]$[4] although unexpectedly broadening of both hystereses is observed with increasing pressure.[67] $[[Fe(3\text{-}bpp)(NCS)_2]_2(4,4'\text{-}bpy)].2MeOH$, an interesting dinuclear complex, displays an incomplete thermal symmetry breaking spin transition but under pressure the symmetry breaking is unfavourable and a gradual transition to the thermally inaccessible complete LS state is observed.[68] Negative linear compressibility (NLC) in a SCO material via a scissor-like mechanism has also been revealed by high pressure studies, opening up the possibility for high sensitivity pressure sensors and piezoelectrics.[69] Systematic thermal, piezo- and photocrystallographic studies need to be carried out for more SCO systems to produce detailed temperature-pressure-light (P, T, hv) phase diagrams and develop further understanding of structure-property relationships and the complex structural nature of the spin transition.[5]

The design of new intense X-ray sources and sensitive area detectors allows faster, higher quality data collections from smaller crystals with complex structures, including highly disordered or incommensurate systems, to be collected in-house.[70] Synchrotron sources and X-ray free electron lasers (XFELs) have opened up the possibility for time resolved structural studies to probe photoinduced pico- and femtosecond timescale electronic and atomic motions in SCO systems.[71] To fully understand solid state SCO, structural changes resulting from or driving the spin transition at molecular and macroscopic levels need to be studied (

Figure).[5]

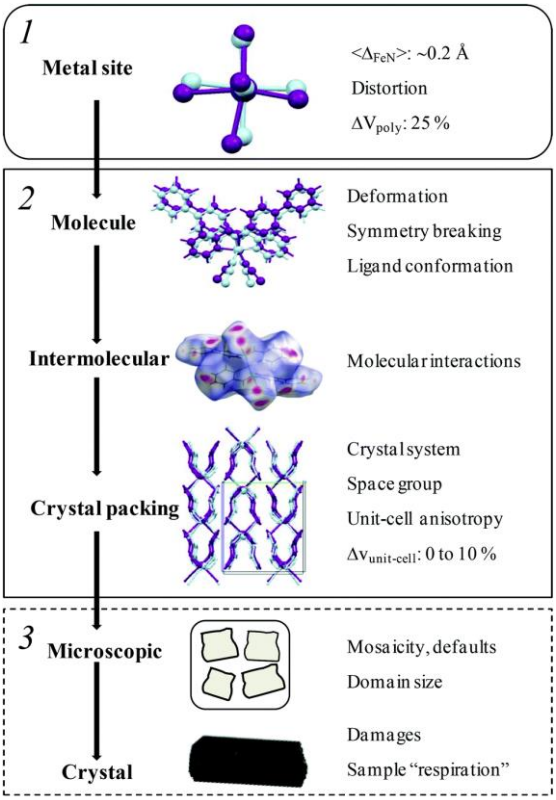

Figure 1.7 - Flow chart showing structural changes observed in SCO materials from molecular to macroscopic scale. Reproduced with permission from the Royal Society of Chemistry.[5]

[4] bapbpy = 6,6'-bis(amino-2-pyridyl)-2,2'-bipyridine

1.8.1 Central metal ion coordination geometry

The central metal ion coordination geometry changes during a HS→LS transition. Shortening of M-L bond lengths by $\Delta r_{HL} = r_{HS} - r_{LS}$ and changes in L-M-L angles are observed, but these features alone cannot be used to determine the nature of SCO behaviour in different systems. In particular, Δr_{HL} values must be compared cautiously because this is an average of M-L bond lengths which may individually differ depending on the nature of the ligand. r_{HS} and r_{LS} may also have been determined at different temperatures in each study. A decrease in volume of the coordination polyhedron (ΔV_{poly}) is also observed and for [Fe-N_6] systems ΔV_{poly} ~ 25%.[5, 35] These fundamental changes to the coordination polyhedron lead to distortion of the coordination symmetry. The HS state is stabilized by a larger distortion angle (weaker ligand field) than the LS state which displays less distortion usually due to an increase in π-backbonding.[72] Distortion from regular octahedral symmetry is often characterized by the following parameters, where Σ and θ provide independent complementary information and d_G and υ also include information about the dimensions:[73]

- Σ (angle distortion parameter) is the sum of the deviations of all 12 *cis* N-Fe-N bond angles (ϕ_i) from 90° [Figure 1.8(a)]. In a regular octahedron Σ = 0 and the change in Σ during a HS→LS transition (ΔΣ) is normally >30 % and can be up to 55 %.[73a]
- θ (trigonal twist angle) is the angle between opposite octahedron faces when viewed along a C_3 axis. This parameter can be defined in two ways; either as Θ, the sum of deviations from 60° of all 24 twist angles (θ_i) obtained by viewing along the four different C_3 axes in the octahedron [Figure 1.8(b)][74] or by one angle explicitly defined for comparison in a set of compounds. For example, Létard *et al.* defined θ_{NCS} to be the angle opposite the NCS ligands in [$FeL_n(NCS)_2$] compounds [Figure 1.8(c)].[73a] Interestingly, Θ can be directly linked to physical properties, including T_{LIESST}[74-75] and also the abruptness (cooperativity) of the transition.[74, 76]
- υ – the percentage volume distortion from regular octahedral symmetry (υ = 0 %) of a polyhedron (V_p) in the circumscribed sphere (V_s) [Figure 1.8(d)].[73b, 77]
- d_G – distance between the centre of gravity of the six coordinated N atoms and the actual metal atom position.[73b]
- ζ (length distortion parameter) is the sum of the differences of all six Fe-N bond lengths from the average bond length. $\zeta = \sum_{i=1}^{6} |(\text{Fe-N}_i) - \langle\text{Fe-N}\rangle|$.[78]

Continuous symmetry measures[79] – a more sophisticated but computationally demanding approach whereby a continuous scale of octahedral distortion can be correlated with various physical properties in SCO systems.[80]

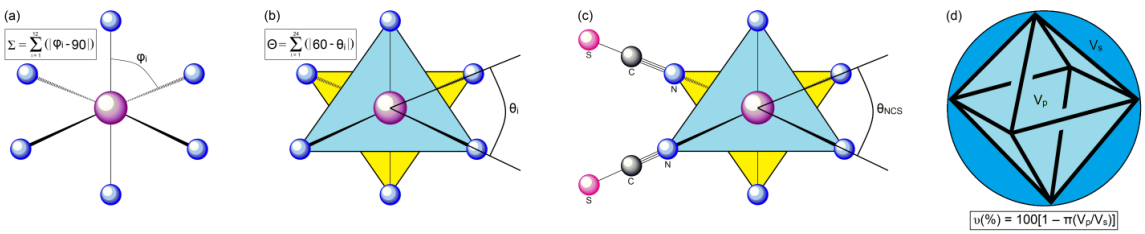

Figure 1.8 - Pictorial illustrations and equations for the calculation of distortion parameters (a) Σ,[73] (b) Θ,[74] (c) θ_{NCS}[73a, 76] and (d) υ.[73b, 77]

1.8.2 Molecular, unit cell and crystal geometry

The reversible contraction and expansion, "breathing", of the coordination polyhedron in SCO systems can propagate through to molecular and unit cell scale but is absorbed to some extent within the crystal

lattice.[5] Molecular geometry is compared using common features within a set of SCO compounds, for example ligand torsion or bite angles, and within the literature certain parameters are used for particular ligand types.[6a] SCO may cause subtle anisotropic elongation/contraction of the unit cell axes which can often be correlated with crystal packing changes. However, if a large metal coordination or ligand conformational change[6a] occurs a structural phase transition associated with an abrupt hysteretic transition is more likely. Crystallinity may not be retained through a phase transition where there is a large structural rearrangement and obtaining both the HS and LS structures can be difficult for these systems. Standard diffraction techniques cannot determine whether the hysteresis originates from the phase or spin transition and this is an unsolved problem in many cases which requires complementary time resolved spectroscopic and diffraction studies.[73a] $\Delta V_{unit\ cell}$, the unit cell volume difference between pure HS and LS states, represents the lattice deformation corresponding only to the SCO phenomenon. $\Delta V_{unit\ cell}$ is normally ~1-5 % for all transition types in iron(II) systems.[5, 73a] Two methods to determine $\Delta V_{unit\ cell}$ are:

1. Compare with an isostructural non-SCO system to estimate and eliminate changes associated with normal thermal contraction from $\Delta V_{unit\ cell}$. For example, $[Fe(PM\text{-}BiA)_2(NCS)_2]$[5] polymorph II has been compared with a non-SCO room temperature isostructural HS Co(II) analogue.[73b]
2. Compare HS and LS unit cell volumes at the same temperature. This can be done if the HS state is thermally trapped by flash freezing; for example, in $[Fe(PM\text{-}BiA)_2(NCS)_2]$ polymorph I almost 100% thermal HS state can be trapped at 30 K for >16 hours without relaxation to the LS state.[81]

Magnetic behaviour, including cooperativity, hysteresis and spin transition abruptness,[5, 73a] is strongly influenced by intermolecular interactions and crystal packing; for example, the large hysteresis, $\Delta T_{1/2}$ = 40 K, in $[Fe(dpp)_2(NCS)_2].py$[6] is attributed to a network of strong π-π stacking interactions[82] and hydrogen bonding plays an important role in the behaviour of $[FeL_n(NCS)_2]$ systems.[73a] Crystallographic studies, including Hirshfeld surface analysis,[83] are important in identifying predominant intermolecular interactions, but direct correlation with magnetic properties is very challenging because a vast array of interactions are usually modified during SCO. The crystal contact index (CCI) has been proposed as a single parameter to quantitatively describe the sum of close contacts [shorter than sum of vdW radii] in a system by assuming all interactions contribute (with different weights depending on the interaction strength) to elastic interactions causing cooperativity.[84] Crystallographic charge density analysis has started to emerge as a suitable but challenging technique for examining intermolecular interactions and comparing electron density distributions in LS and metastable HS states.[85] Identifying structure-property relationships in SCO materials is sometimes possible within groups of similar compounds but general correlations that span a wide variety of SCO systems are more rare.[6a]

Some SCO complexes exist in multiple crystalline forms; for example, $[Fe(bt)_2(NCS)_2]$[7] and $[Fe(abpt)_2(NCS)_2]$[8] have two[86] and four[87] structural polymorphs respectively which display different magnetic properties. Polymorphism provides a unique opportunity whereby molecular conformations and/or configurations in the lattice can be compared and correlated with properties without the influence of chemical alteration.[88] Polymorphs I and II of $[Fe(PM\text{-}BiA)_2(NCS)_2]$ display abrupt hysteretic ($T_{1/2}^{\downarrow}$ = 168 K and $T_{1/2}^{\uparrow}$ = 173 K) and gradual ($T_{1/2}$ = 205 K) thermal spin transitions respectively.[53] Their packing structures are similar, but S···C(H) intermolecular hydrogen bond distances and θ_{NCS} angle sizes are found to correlate with the spin transition abruptness.[76] A comprehensive review of polymorphism in mononuclear and polymeric Fe(II), Fe(III) and Co(II) SCO systems was published in 2012.[88]

[5] PM-BiA = *N*-(2-pyridylmethylene)-4-(aminobiphenyl)
[6] dpp = dipyrido[3,2-*a*:2'3'-*c*]phenazine, py = pyridine
[7] bt = 2,2'-bi-2-thiazoline
[8] abpt = 4-amino-3,5-bis(pyridin-2-yl)-1,2,4-triazole

1.8.3 Microscopic to macroscopic geometry

SCO crystal lattice "breathing" is unlikely to be observed at the macroscopic level because mosaicity and defects probably absorb any lattice contraction and expansion. Macroscopic scale studies of the propagation of SCO switching have been limited to optical, Raman and atomic force microscopy (AFM) techniques.[89] Crystallographic studies have recently been utilized to study the single crystal fatigability of an iron(II) SCO material displaying a gradual thermal transition.[90] Mosaicity values collected after controlled thermal (300 K↔80 K) cycles were compared with a non-SCO isostructural Zn(II) analogue. The single crystals remained intact but for the SCO system within the first 10 cycles major mosaic domain rearrangement occurred and then no further alteration within 40 cycles.[90] The mosaicity value obtained from diffraction experiments varies for different experimental set-ups, data collection strategies, single crystals from the same crystallization batch, sample orientation etc., and therefore can only be taken as a relative value. More mosaicity studies under controlled experimental conditions need to be carried out on the same and different types of SCO systems to draw more conclusions. Powder diffraction may also prove to be a suitable method for investigating structural defects and crystalline domains in SCO materials.

1.8.4 Dynamic structural science

Photocrystallographic techniques[91] to investigate irreversible photoreactions, metastable and transient species are undergoing rapid development and open up a whole new perspective for the study of SCO materials. Closely examining the progress of a photoreaction to create a "molecular movie"[71a] will provide new insight into the structural mechanism and dynamics of the LIESST process.[42]

Photocrystallographic studies of the continuous wave (CW) laser generated metastable HS-2 structure at low temperature have been carried out for several years.[92] Although compound dependent, below 50 K the lifetime of the metastable HS-2 state can rapidly increase from seconds to hours with decreasing temperature. The experimental protocol needs to be careful considered for each system because residual LS ground state species will bias the structure and its precision could be questionable.[93] Laser excitation with different wavelengths can be used to observe LIESST and reverse LIESST processes. In iron multinuclear systems wavelength selective multi-step switching from LS-LS to (HS-2)-LS or (HS-2)-(HS-2) structures and metastable structure interconversion has indicated the possibility for selective photocontrol.[94] Monitoring the evolution of Bragg peak profiles during SCO has shown that cooperativity alters the spatial distribution of HS domains in the crystal lattice. Weakly cooperative systems, for example monoclinic $[Fe(PM\text{-}BIA)_2(NCS)_2]$ polymorph II (BIA II) [Figure 1.9(a)], display a random distribution of HS molecules throughout the crystal lattice leading to a gradual shift in Bragg peak positions [Figure 1.9(c)]. In more cooperative systems with thermal hysteresis, for example orthorhombic $[Fe(PM\text{-}BIA)_2(NCS)_2]$ polymorph I (BIA I), phase nucleation of HS domains occurs within the LS lattice leading to the coexistence of two phases both with coherent diffracted intensity [Figure 1.9(b)].[78] Bragg peak splitting during excitation and relaxation processes is observed due to the different lattice parameters of the two phases.[92b] SCO nucleation domains have also been observed by optical microscopy[65] and Raman spectroscopy.[89]

Time resolved pump-probe diffraction and spectroscopy have been used to reveal interesting information about SCO structural dynamics in solution and the solid state.[51, 95] Photocrystallographic time resolved experiments are complex and detailed preliminary studies are required to select suitable SCO compounds displaying significant photoconversion, appropriate relaxation rates and fatigue resistance to multiple pump-probe cycles. In aqueous solution, for example the short intense hard X-ray pulses at the Linac Coherent Light Source (LCLS) XFEL[96] have been utilized to study the SCO dynamics of $[Fe(bpy)_3]Cl_2$by time resolved femtosecond X-ray absorption near-edge spectroscopy (XANES).[97] Single crystal time resolved diffraction experiments have only been carried out for $[(TPA)Fe^{III}(TCC)]^+$ [Figure 1.10(a)].[98] In this case, gradual thermal spin transitions ($T_{1/2}$ between 200 K and 250 K) are observed for two polymorphs with a SbF_6^- counterion and the isostructural analogues with a PF_6^- counterion.[98a] Pump-probe experiments were

carried out on the ID09B beamline[99] at the ESRF synchrotron using 100 fs, 800 nm laser pump pulses at a 1 KHz repetition rate and ~100 ps X-ray pulses to probe various time delays.[100] Extensive time resolved optical pump-probe spectroscopic studies were carried out to identify suitable experimental conditions; including temperatures in the thermal SCO region where LS population is high but HS→LS relaxation occurs on the millisecond timescale.[101] These studies have revealed a multistep mechanism for SCO photoexcitation and relaxation in the solid state [Figure 1.10(b)-(d)].[95, 100, 102] The HS population achieved and timescale for each mechanistic step varies for different anions and polymorphs of $[(TPA)Fe^{III}(TCC)]^{+}$ and also for different crystal sizes and temperatures:[98a]

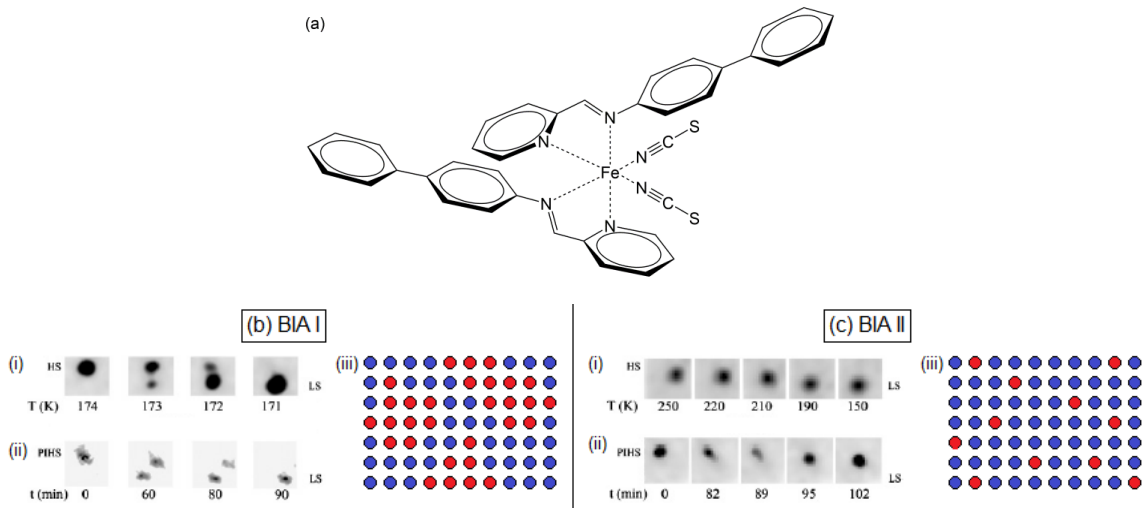

Figure 1.9 - (a) $[Fe(PM\text{-}BIA)_2(NCS)_2]$. Evolution of Bragg peak profiles for (b) BIA I and (c) BIA II; (i) with temperature, (ii) during HS-2 to LS relaxation at (b)(ii) 78 K and (c)(ii) 20 K [reproduced with permission][78]. (iii) Pictorial representation of the formation of HS molecules (red) within a LS lattice (blue).

Step 1 - Photoinduced switching of molecules within the laser penetration depth. Diffraction experiments monitoring <Fe-N> bond elongation observe ~3% conversion to the HS state on the subpicosecond timescale (<300 fs)[101] without change in lattice parameters.

Step 2 - Unit cell volume expansion occurs as a non-linear shock-wave from the photoirradiated face throughout the crystal bulk on the nanosecond timescale (for crystals a few micrometres thick). Elastic interactions anisotropically propagate the LS→HS transition through the lattice allowing internal pressure created through thermal heating and formation of HS molecules to be dissipated.

Step 3 - Thermal heating from the laser pulse is thought not to influence initial photoinduced switching and only become detectable on the microsecond timescale as homogenous heat distribution is reached within the lattice. In these studies, where temperatures close to or within the thermal SCO region are utilized due to favourable relaxation characteristics, the "jump" in HS population due to thermal heating is particularly noticeable and the resulting HS population (~8-10%) is an indistinguishable mixture of HS-1 and HS-2.

Step 4 - Relaxation of the HS state back to thermal equilibrium through homogeneous dissipation of heat into the environment occurs on the millisecond timescale. If incoherent thermal vibrations from thermal heating and diffusion in the crystal are assumed to increase isotropic atomic motion (ΔB), a corresponding decrease in Bragg peak intensities will be observed. Wilson graphs [$\ln(I_1/I_0)$ versus q^2 (scattering vector)] can be used to examine ΔB by comparing Bragg peak intensities (I) between data collections before (I_0 at a known reference temperature, T_0), and after irradiation (I_1 at an unknown higher temperature, T_1) at various time delays [Figure 1.10(d)].[102a, 102b]

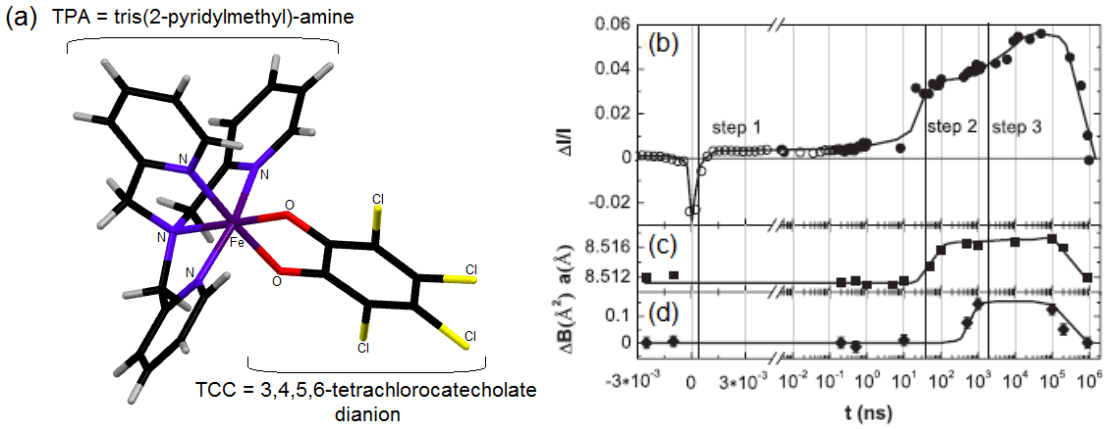

Figure 1.10 - (a) $[(TPA)Fe(TCC)]PF_6$ monoclinic polymorph at 80 K[98b] (reproduced from CCDC 719405, IUCr OG5037, ref code TAMTEH02 using Mercury 3.3). Steps 1-3 of the proposed SCO mechanism for this polymorph plotted as time versus: (b) differential transmitted light intensity (ΔI/I) from a time resolved optical study, (c) change in lattice parameter, *a*, and (d) ΔB, the difference between the Debeye-Waller factor at t < 0 and t > 0 [reproduced with permission][102a]

1.8.5 Crystallographic studies of spin crossover polymers and nanomaterials

Development of new crystallographic techniques and equipment has made it possible to obtain previously unknown structural information from poorly crystalline powders and particles down to nanometre sizes.[5] Direct coupling of SCO metal centres via rigid bridging linkers can lead to strong communication, and abrupt room temperature hysteretic polymeric SCO systems have been obtained.[29, 103] Utilizing the interesting magnetic and optical SCO properties of polymeric $[Fe(Rtrz)_3]A_2{\cdot}nH_2O$[9] and related systems in display and memory devices is envisioned,[29, 103] but poor crystallinity, small particle and coherent domain sizes mean that obtaining structural information using standard diffraction methods is extremely challenging. Recently, high resolution powder X-ray diffraction (PXRD) studies elucidated the HS-1 and LS structures of polymeric $[Fe(Htrz)_2(trz)](BF_4)$[10].[104] The structure was validated using the pair distribution function (PDF) method[105] and found to be unaffected by reduction of the particle and coherent domain size from 50 nm to 10 nm.[104] The room temperature thermal hysteresis loop in nanoparticles of the $[Fe(NH_2trz)_3]Br_2.3H_2O$[11] coordination polymer is undetectable below a particle size of ~50-30 nm. The PDF method revealed that in this system the number of coherent domains decreases with particle size and thermal bistability is only observed if more than five coherent domains are present.[106] Correlating the size and number of coherent domains with SCO properties is vitally important for the miniaturization of SCO materials towards applications in nanophotonic, spintronic and nanoelectronic devices.[11] High resolution powder diffraction and the PDF method are therefore likely to play important roles in the future of SCO structural studies.

1.9 Ligand-driven light-induced spin change (LD-LISC)

To design systems which have room temperature bistability and are extendable to single molecule switching devices new strategies employing external switching moieties which induce a spin state change are being investigated. Two methods are “ligand-driven light-induced spin change”, LD-LISC, and “light-driven coordination-induced spin-state switching”, LD-CISSS are being used by several research groups.[66]

[9] Rtrz = 4-*R*-1,2,4-triazole, A^- = anion, n = number of non-coordinated water molecules
[10] Htrz = 1*H*-1,2,4-triazole, trz^- = deprotonated triazolato ligand
[11] NH_2trz = 4-amino-1,2,4-triazole

The advantage of these two methods is that they do not rely on solid state cooperativity to induce a spin transition therefore are extendable to single molecule devices.

LD-LISC utilizes photoexcitable ligands which undergo a reversible structural change to modulate the ligand field strength upon light irradiation and induce a spin transition in a spin crossover complex. Suitable ligands should ideally be thermally stable in both conformations, display good fatigue resistance to switching and significant interconversion (ideally 100%) in the two directions either at distinct wavelengths or by thermal conversion in one direction with a significant lifetime. The complexes containing the ligands need to display different magnetic behaviour with respect to temperature for switching to be possible, ideally in one configuration to display a complete thermal HS to LS transition in the room temperature region because small changes in the ligand field strength are therefore known to alter the properties. Complexes where one configuration is HS and the other LS should also be suitable but photoisomerization will need to induced a larger change in ligand field strength for switching to be observed. In iron(II) complexes photoexcitable ligands which undergo photoinduced cis-trans isomerization are found to alter the ligand field in the correct order of magnitude for switching to occur. Work is this area has included complexes incorporating styryl, azo, chromene and diarylethene moieties being reported. The first complex identified to undergo LD-LISC was $[Fe(stpy)_4(NCBPh_3)_2]$ embedded in a cellulose acetate film at 140 K[107] and a room temperature system, $[Fe(\textit{trans}\text{-msbpy})_2(NCS)_2]$, where msbpy = 4-methyl-4'-styryl-2,2'-bipyridine in acetonitrile solution, was discovered in 1999.[108] Since then many other systems which undergo LD-LISC in solution and polymer films[109] have been identified and started to be investigated using computational methods.[110] Solid state studies of the actual switching process have not been successful with only isolated ligand configuration being reported. Cis-trans isomerization involves a large geometrical change and therefore is generally restricted in the solid state and can lead to either no or very low photoconversion or destruction of the crystal lattice. Photocrystallographic studies at RT on powder and single crystal samples of $[Fe(\textit{cis}\text{-stpy})_4(NCSe)_2]$ indicated a gradual single-crystal to amorphous solid phase transformation upon 534 nm laser irradiation in the MLCT band.[111] For systems for which the thermal spin transition is below room temperature, the application of external pressure to raise $T_{1/2}$ closer to RT has been suggested but this method has not yet been successful for observing LD-LISC.[112] Modification of 2,6-di(pyrazol-1-yl)pyridine, a ligand well known to produce spin crossover complexes,[21a-c] to incorporate differently substituted 4-styrylpyridine has used to produce room temperature LD-LISC systems in acetonitrile, in KBr discs and in the crystalline state upon excitation in the MLCT band.[113] Room temperature azobenzene containing systems in acetone have also been reported and have the advantage of reversible *trans-cis* switching upon irradiation with 365 nm and 436 nm light which correspond to irradiation in the π-π*(azo) and n-π*(azo) bands respectively.[114] This is an advantage over stilbenes which undergo unwanted side reactions, including oxidisation and electrocyclic ring closure, in addition to *cis-trans* photoisomerization. Iron(III) complexes are less susceptible to changes in π-backbonding than analogous iron(II) systems therefore small changes in this effect cause a larger conversion photoswitching LD-LISC yield.[115] The unique photoswitching behaviour of diarylethenes will be discussed in Chapter 6 and the exceptional fatigue resistance, thermal stability, quantum yield, fast photoswitching response (~1 ps) and no overlapping absorption bands in both states would be directly suitable for devices. These properties give these systems an advantage over stilbenes and azo compounds for producing photoactive ligands for the LD-LISC effect which have potential for technological applications. The first reports coupling diarylethene moieties to Fe(II) involved complexation through terminal pyridine rings.[116] Photocyclization of at least one diarylethene ligand was observed in solid state and solution for both metal complexes reported but did not result in the required change in magnetic properties upon photoswitching. One metal complex was HS at all temperatures[116b] and in the other system an interesting metal-to-ligand electron transfer equilibrium between Fe(II)-L and Fe(III)-L^- is proposed and its potential as a molecular component in a memory device or light sensor discussed.[116a] Following these results two groups almost simultaneously reported LD-LISC at room temperature in solution by the direct complexation of a diarylethene-phenanthroline derivative to iron(II).[117]

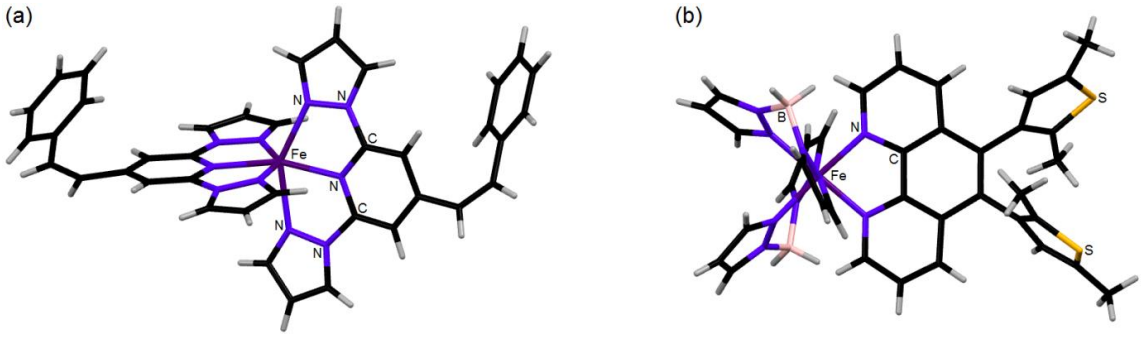

Figure 1.11 - Crystal structures of (a) [Fe(*E*-2,6-di(1H-pyrazol-1-yl)-4-styrylpyridine$)_2$] (BF_4 anions and solvent molecules are excluded for clarity) and (b) [Fe($H_2B(pz)_2)_2$phen*] (pz = 1-pyrazolyl, phen* = diarylethene fused phen ligand).

Nihei *et al.*[117b] crystallized [Fe$(bpz)_2$(btphen)] from acetonitrile with the thiophene in the photoinactive parallel conformation and did not observe photocyclization in the solid state for a bulk [Fe$(bpz)_2$(btphen)].H_2O but did see a thermal HS to LS spin transition, LIESST and reverse-LIESST at low temperature. In butylronitrile solution they report LD-LISC to occur with a 20% spin conversion at 173 K but not at room temperature.[117b] The same complex recrystallized from toluene/n-hexane produces a disordered structure with the thiophene rings coexisting in both parallel and antiparallel conformations in a ratio of 29.9%:70.1% with the ratio staying the same at all temperatures. Room temperature photocyclization in the solid state and in acetonitrile are reported. In butylronitrile the molar fraction of HS species versus temperature are estimated from absorption intensity changes in variable temperature UV-Vis spectra of the complex in the open and closed forms to be the same hence why experiments were carried out in the thermal HS↔LS hysteresis region where a 13 K difference in $T_{1/2}$ is observed.[117b] In acetonitrile however photocyclization at room temperature is reported to generate HS→LS conversion of >40% suggesting the open and closed forms in this solvent must have different magnetic properties at this temperature. This is reported to be the first true observation of reversible room temperature LD-LISC in a diarylethene iron(II) complex and is stated as the highest spin state photoswitching efficiency in solution reported at room temperature to date.[117a] Using photoexcitable ligands as linkers in 3D porous spin crossover systems, in which photoreversible absorption/desorption of gas molecules has already been observed, could also be an interesting prospect for the future.

The spin state of some metal ions, including Ni(II), Mn(III), Co(II), Co(III), Fe(II) and Fe(III), depends on their coordination number and if this can be switched by an external stimuli a phenomenon termed "light-driven coordination-induced spin-state switching", LD-CISSS, is observed. Unlike LD-LISC this effect is based on a discrete quantity, coordination number, rather than a gradual potentially incomplete spin switching based on ligand field strength modulation and environment changes, for example temperature jumps are less likely to change the systems properties. Square planar nickel(II) (coordination number n=4) is diamagnetic (LS, S = 0) with d_{z^2} doubly occupied, square-pyramidal (n=5) can be diamagnetic or paramagnetic depending on the ligands and octahedral (n=6) geometries are paramagnetic (HS, S = 1) with d_{z^2} and $d_{x^2-y^2}$ singularly occupied. Therefore changing the coordination number from n=4 to n=5 (or 6) in a nickel(II) complexes causes a spin transition S=0 to S=1. Ni(II) porphyrins are particular suitable for these systems because they form stable square planar complexes which display only limited distortion when axially coordinated.[118] Two options for producing LD-CISSS systems have been reported: Firstly, using photodissociable ligands (PDLs) where one conformation can complex to the metal centre but the other is sterically hindered preventing binding to the complex.[119] 4-methyl-3-phenylazo-3-tertbutyl-pyridine has been identified and tested and found to show fatigue resistant, reversible 40.1% LS↔HS photoswitching efficiency in a nickel(II) porphyrin upon *cis*(non-binding) to *trans*(binding) photoisomerization of the azo moiety in toluene by irradiating with 365 nm and 440 nm light respectively.[119a] Secondly, designing systems where the photoexcitable ligand is tethered to the

extremities of the porphyrin but has an "arm" located at the correct distance such that binding to the metal ion is possible under specified criteria. The design of these "record player" type systems is difficult but can produce systems that display high fatigue resistance (>10000 cycles) and excellent switching efficiency. All LD-CISSS studies to date have been carried out in solution, the mechanisms involved and large geometrical changes needed are unlikely to allow this method to be transferred to the solid state but it does show great potential for application in magnetic resonance imaging contrast agents because of the paramagnetic ions used.[120]

1.10 Conclusions from literature review

Spin crossover has been identified in many d^4-d^7 complexes, but is particularly common and has been well studied in $Fe(II)N_6$ complexes. A variety of stimuli can potentially induce spin crossover behaviour in a complex including changes in temperature or pressure or through light irradiation. Spin crossover behaviour is both complex and interesting and its' occurrence is not currently fully understood but is sensitive to a number of factors including, metal centre, ligand, solvent, packing and interactions. The change in spin state of a complex results in changes in a number of structural parameters which enables spin crossover to be studied using single crystal X-ray diffraction. A variety of potential applications have been identified for spin crossover complexes including data storage, sensors or molecular switches, however realising these applications will require compounds with controllable, fatigue resistant spin crossover occurring around room temperature.

1.11 References

1. Cambi, L.; Szegö, L., *Berichte der deutschen chemischen Gesellschaft, Abteilung B* **1931,** *64* (10), 2591-2598.
2. Gütlich, P.; Gaspar, A. B.; Garcia, Y., *Beilstein J. Org. Chem.* **2013,** *9*, 342–391.
3. (a) Gütlich, P.; Goodwin, H. A.; (Eds.), *Spin Crossover in Transition Metal Compounds I, II and III*. Springer-Verlag: Berlin, Heidelberg, New York, 2004; (b) Halcrow, M. A.; (Ed), *Spin-Crossover Materials: Properties and Applications*. 1 ed.; John Wiley & Sons, Ltd.: Chichester, UK, 2013; p 546.
4. (a) Hauser, A., Ligand Field Theoretical Considerations. *Spin Crossover in Transition Metal Compounds I*, Wales), P. G. J.-G.-U. o. M. a. H. A. G. U. o. N. S., Ed. Springer-Verlag: Berlin, Heidelberg, New York, 2004; Vol. Topics in Current Chemistry, 233, pp 49-58; (b) Griffith, J. S.; Orgel, L. E., *Quarterly Reviews, Chemical Society* **1957,** *11* (4), 381-393.
5. Guionneau, P., *Dalton Trans.* **2014,** *43* (2), 382-393.
6. (a) Halcrow, M. A., *Chem. Soc. Rev.* **2011,** *40* (7), 4119-4142; (b) Halcrow, M. A., *Spin-Crossover Materials: Properties and Applications*, 1 ed.; Halcrow, M. A., Ed. John Wiley & Sons, Ltd.: Chichester, UK, 2013; pp 147-169.
7. (a) Ksenofontov, V.; Gaspar, A. B.; Gütlich, P., *Spin Crossover in Transition Metal Compounds III*, Wales), P. G. J.-G.-U. o. M. a. H. A. G. U. o. N. S., Ed. Springer-Verlag: Berlin, Heidelberg, New York, 2004; Vol. Topics in Current Chemistry, 235, pp 23-64; (b) Gütlich, P.; Ksenofontov, V.; Gaspar, A. B., *Coord. Chem. Rev.* **2005,** *249* (17–18), 1811-1829.
8. Bousseksou, A.; Varret, F.; Goiran, M.; Boukheddaden, K.; Tuchagues, J.-P., *Spin Crossover in Transition Metal Compounds III*, Wales), P. G. J.-G.-U. o. M. a. H. A. G. U. o. N. S., Ed. Springer-Verlag: Berlin, Heidelberg, New York, 2004; Vol. Topics in Current Chemistry, 235, pp 65-84.
9. Hauser, A., *Spin Crossover in Transition Metal Compounds II*, Wales), P. G. J.-G.-U. o. M. a. H. A. G. U. o. N. S., Ed. Springer-Verlag: Berlin, Heidelberg, New York, 2004; Vol. Topics in Current Chemistry, 234, pp 155-198.
10. Gaspar, A. B.; Seredyuk, M.; Gütlich, P., *Coord. Chem. Rev.* **2009,** *253* (19–20), 2399-2413.
11. Shepherd, H. J.; Molnár, G.; Nicolazzi, W.; Salmon, L.; Bousseksou, A., *Eur. J. Inorg. Chem.* **2013,** *2013* (5-6), 653-661.

12. (a) Gütlich, P.; Garcia, Y.; Goodwin, H. A., *Chem. Soc. Rev.* **2000,** *29* (6), 419-427; (b) Gütlich, P.; Hauser, A.; Spiering, H., *Angew. Chem., Int. Ed. Engl.* **1994,** *33* (20), 2024-2054.
13. Koningsbruggen, P. J. v.; Maeda, Y.; Oshio, H., *Spin Crossover in Transition Metal Compounds I*, Wales), P. G. J.-G.-U. o. M. a. H. A. G. U. o. N. S., Ed. Springer-Verlag: Berlin, Heidelberg, New York, 2004; Vol. Topics in Current Chemistry, 233, pp 259–324.
14. (a) Goodwin, H. A., *Spin Crossover in Transition Metal Compounds II*, Wales), P. G. J.-G.-U. o. M. a. H. A. G. U. o. N. S., Ed. Springer-Verlag: Berlin, Heidelberg, New York, 2004; Vol. Topics in Current Chemistry, 234, pp 23-47; (b) Miller, R. G.; Narayanaswamy, S.; Tallon, J. L.; Brooker, S., *New J. Chem.* **2014,** **Advance article**.
15. Garcia, Y.; Gütlich, P., *Spin Crossover in Transition Metal Compounds II*, Wales), P. G. J.-G.-U. o. M. a. H. A. G. U. o. N. S., Ed. Springer-Verlag: Berlin, Heidelberg, New York, 2004; Vol. Topics in Current Chemistry, 234, pp 49-62.
16. Bousseksou, A.; Molnar, G.; Salmon, L.; Nicolazzi, W., *Chem. Soc. Rev.* **2011,** *40* (6), 3313-3335.
17. (a) Orgel, L. E., *The Journal of Chemical Physics* **1955,** *23* (10), 1819-1823; (b) Orgel, L. E., *The Journal of Chemical Physics* **1955,** *23* (6), 1004-1014.
18. Sugano, S.; Tanabe, Y.; Kamimura, H., *Multiplets of Transition-Metal Ions in Crystals*. Academic Press: The University of Michigan, 1970; Vol. Volume 33 of Pure and Applied Physics.
19. Schläfer, H. L.; Gliemann, G., *Einführung in die Ligandenfeldtheorie*. Akademische Verlagsgesellschaft: Wiesbaden, 1980; p 535.
20. (a) Šalitroš, I.; Madhu, N. T.; Boča, R.; Pavlik, J.; Ruben, M., *Monatsh Chem* **2009,** *140* (7), 695-733; (b) Mikami, M.; Konno, M.; Saito, Y., *Acta Crystallogr., Sect. B: Struct. Crystallogr. Cryst. Chem.* **1980,** *36* (2), 275-287.
21. (a) Halcrow, M. A., *Coord. Chem. Rev.* **2009,** *253* (21-22), 2493–2514; (b) Carbonera, C.; Sánchez Costa, J.; Money, V. A.; Elhaïk, J.; Howard, J. A. K.; Halcrow, M. A.; Létard, J.-F., *Dalton Trans.* **2006,** (25), 3058-3066; (c) Halcrow, M. A., *Coord. Chem. Rev.* **2005,** *249* (24), 2880-2908; (d) Goodwin, H. A., *Spin Crossover in Transition Metal Compounds I*, Wales), P. G. J.-G.-U. o. M. a. H. A. G. U. o. N. S., Ed. Springer-Verlag: Berlin, Heidelberg, New York, 2004; Vol. Topics in Current Chemistry, 233, pp 59–90.
22. (a) Lavrenova, L. G.; Shakirova, O. G., *Eur. J. Inorg. Chem.* **2013,** *2013* (5-6), 670-682; (b) Long, G. J.; Grandjean, F.; Reger, D. L., *Spin Crossover in Transition Metal Compounds I*, Wales), P. G. J.-G.-U. o. M. a. H. A. G. U. o. N. S., Ed. Springer-Verlag: Berlin, Heidelberg, New York, 2004; Vol. Topics in Current Chemistry, 233, pp 91–122.
23. Koningsbruggen, P. J. v., *Spin Crossover in Transition Metal Compounds I*, Wales), P. G. J.-G.-U. o. M. a. H. A. G. U. o. N. S., Ed. Springer-Verlag: Berlin, Heidelberg, New York, 2004; Vol. Topics in Current Chemistry, 233, pp 123–149.
24. Weber, B., *Coord. Chem. Rev.* **2009,** *253* (19–20), 2432-2449.
25. Shores, M. P.; Klug, C. M.; Fiedler, S. R., *Spin-Crossover Materials: Properties and Applications*, 1 ed.; Halcrow, M. A., Ed. John Wiley & Sons, Ltd.: Chichester, UK, 2013; pp 281-301.
26. (a) Létard, J.-F.; Guionneau, P.; Goux-Capes, L., *Spin Crossover in Transition Metal Compounds III*, Wales), P. G. J.-G.-U. o. M. a. H. A. G. U. o. N. S., Ed. Springer-Verlag: Berlin, Heidelberg, New York, 2004; Vol. Topics in Current Chemistry, 235, pp 221–249; (b) Murray, K. S.; Kepert, C. J., *Spin Crossover in Transition Metal Compounds I*, Wales), P. G. J.-G.-U. o. M. a. H. A. G. U. o. N. S., Ed. Springer-Verlag: Berlin, Heidelberg, New York, 2004; Vol. Topics in Current Chemistry, 233, pp 195–228.
27. Real, J. A.; Gaspar, A. B.; Niel, V.; Muñoz, M. C., *Coord. Chem. Rev.* **2003,** *236* (1–2), 121-141.
28. Gütlich, P.; Goodwin, H. A., *Spin Crossover in Transition Metal Compounds I*, Wales), E. b. P. G. J.-G.-U. o. M. a. H. A. G. U. o. N. S., Ed. Springer-Verlag: Berlin, Heidelberg, New York, 2004; Vol. Topics in Current Chemistry, 233, pp 1-47.
29. Kahn, O.; Martinez, C. J., *Science* **1998,** *279* (5347), 44-48.
30. (a) Goodwin, H. A.; Sylva, R. N., *Aust. J. Chem.* **1968,** *21* (1), 83-90; (b) Goodwin, H. A.; Kucharski, E. S.; White, A. H., *Aust. J. Chem.* **1983,** *36* (6), 1115-1124

31. Holland, J. M.; McAllister, J. A.; Kilner, C. A.; Thornton-Pett, M.; Bridgeman, A. J.; Halcrow, M. A., *Journal of the Chemical Society, Dalton Transactions* **2002,** *0* (4), 548-554.
32. (a) Chernyshov, D.; Hostettler, M.; Törnroos, K. W.; Bürgi, H.-B., *Angewandte Chemie International Edition* **2003,** *42* (32), 3825-3830; (b) Hostettler, M.; Törnroos, K. W.; Chernyshov, D.; Vangdal, B.; Bürgi, H.-B., *Angewandte Chemie International Edition* **2004,** *43* (35), 4589-4594; (c) Törnroos, K. W.; Hostettler, M.; Chernyshov, D.; Vangdal, B.; Bürgi, H.-B., *Chemistry - a European Journal* **2006,** *12* (24), 6207-6215; (d) Chernyshov, D.; Vangdal, B.; Törnroos, K. W.; Bürgi, H.-B., *New J. Chem.* **2009,** *33* (6), 1277-1282; (e) Chernyshov, D.; Klinduhov, N.; Törnroos, K. W.; Hostettler, M.; Vangdal, B.; Bürgi, H.-B., *Physical Review B* **2007,** *76* (1), 014406-1 to 014406-7.
33. Lemercier, G.; Bréfuel, N.; Shova, S.; Wolny, J. A.; Dahan, F.; Verelst, M.; Paulsen, H.; Trautwein, A. X.; Tuchagues, J.-P., *Chemistry - a European Journal* **2006,** *12* (28), 7421-7432.
34. Yamada, M.; Hagiwara, H.; Torigoe, H.; Matsumoto, N.; Kojima, M.; Dahan, F.; Tuchagues, J.-P.; Re, N.; Iijima, S., *Chemistry - a European Journal* **2006,** *12* (17), 4536-4549.
35. Shepherd, H. J.; Rosa, P.; Fallis, I. A.; Guionneau, P.; Howard, J. A. K.; Goeta, A. E., *J. Phys. Chem. Solids* **2012,** *73* (2), 193-197.
36. (a) Baker, W. A.; Bobonich, H. M., *Inorg. Chem.* **1964,** *3* (8), 1184-1188; (b) Gallois, B.; Real, J. A.; Hauw, C.; Zarembowitch, J., *Inorg. Chem.* **1990,** *29* (6), 1152-1158; (c) Real, J. A.; Gallois, B.; Granier, T.; Suez-Panama, F.; Zarembowitch, J., *Inorg. Chem.* **1992,** *31* (24), 4972-4979.
37. König, E.; Madeja, K.; Watson, K. J., *J. Am. Chem. Soc.* **1968,** *90* (5), 1146-1153.
38. Ganguli, P.; Gutlich, P.; Muller, E. W.; Irler, W., *Journal of the Chemical Society, Dalton Transactions* **1981,** (2), 441-446.
39. Müller, E. W.; Spiering, H.; Gütlich, P., *Chem. Phys. Lett.* **1982,** *93* (6), 567-571.
40. (a) Paulsen, H.; Schünemann, V.; Wolny, J. A., *Eur. J. Inorg. Chem.* **2013,** *2013* (5-6), 628-641; (b) Pavlik, J.; Boča, R., *Eur. J. Inorg. Chem.* **2013,** *2013* (5-6), 697-709.
41. Bousseksou, A.; Molnár, G.; Matouzenko, G., *Eur. J. Inorg. Chem.* **2004,** *2004* (22), 4353-4369.
42. Guionneau, P.; Collet, E., *Spin-Crossover Materials: Properties and Applications*, 1 ed.; Halcrow, M. A., Ed. John Wiley & Sons, Ltd.: Chichester, UK, 2013; pp 507-526.
43. Ewald, A. H.; Martin, R. L.; Sinn, E.; White, A. H., *Inorg. Chem.* **1969,** *8* (9), 1837-1846.
44. Perutz, M. F.; Kilmartin, J. V.; Nagai, K.; Szabo, A.; Simon, S. R., *Biochemistry* **1976,** *15* (2), 378-387.
45. (a) Ohnishi, S., *Physics of the Earth and Planetary Interiors* **1978,** *17* (2), 130-139; (b) Rueff, J.-P., *Spin-Crossover Materials: Properties and Applications*, 1 ed.; Halcrow, M. A., Ed. John Wiley & Sons, Ltd.: Chichester, UK, 2013; pp 527-541.
46. Usha, S.; Srinivasan, R.; Rao, C. N. R., *Chemical Physics* **1985,** *100* (3), 447-455.
47. (a) McGarvey, J. J.; Lawthers, I., *J. Chem. Soc., Chem. Commun.* **1982,** (16), 906-907; (b) Lawthers, I.; McGarvey, J. J., *J. Am. Chem. Soc.* **1984,** *106* (15), 4280-4282.
48. Decurtins, S.; Gütlich, P.; Köhler, C. P.; Spiering, H.; Hauser, A., *Chem. Phys. Lett.* **1984,** *105* (1), 1-4.
49. Franke, P. L.; Haasnoot, J. G.; Zuur, A. P., *Inorg. Chim. Acta* **1982,** *59*, 5-9.
50. Gütlich, P., *Z. Anorg. Allg. Chem.* **2012,** *638* (1), 15-43.
51. Chergui, M., *Spin-Crossover Materials: Properties and Applications*, 1 ed.; Halcrow, M. A., Ed. John Wiley & Sons, Ltd.: Chichester, UK, 2013; pp 405-424.
52. Hauser, A., *Coord. Chem. Rev.* **1991,** *111*, 275-290.
53. Létard, J.-F.; Guionneau, P.; Rabardel, L.; Howard, J. A. K.; Goeta, A. E.; Chasseau, D.; Kahn, O., *Inorg. Chem.* **1998,** *37* (17), 4432-4441.
54. Boukheddaden, K.; Shteto, I.; Hôo, B.; Varret, F., *Physical Review B* **2000,** *62* (22), 14806-14817.
55. Desaix, A.; Roubeau, O.; Jeftic, J.; Haasnoot, J. G.; Boukheddaden, K.; Codjovi, E.; Linarès, J.; Noguès, M.; Varret, F., *Eur. Phys. J. B* **1998,** *6* (2), 183-193.

56. Varret, F.; Boukheddaden, K.; Codjovi, E.; Enachescu, C.; Linarès, J., *Spin Crossover in Transition Metal Compounds II*, Wales), P. G. J.-G.-U. o. M. a. H. A. G. U. o. N. S., Ed. Springer-Verlag: Berlin, Heidelberg, New York, 2004; Vol. Topics in Current Chemistry, 234, pp 199-229.
57. (a) Létard, J.-F.; Capes, L.; Chastanet, G.; Moliner, N.; Létard, S.; Real, J.-A.; Kahn, O., *Chem. Phys. Lett.* **1999,** *313* (1–2), 115-120; (b) Létard, J.-F., *J. Mater. Chem.* **2006,** *16* (26), 2550-2559.
58. (a) Marcén, S.; Lecren, L.; Capes, L.; Goodwin, H. A.; Létard, J. F., *Chem. Phys. Lett.* **2002,** *358* (1–2), 87-95; (b) Létard, J.-F.; Chastanet, G.; Guionneau, P.; Desplanches, C., *Spin-Crossover Materials: Properties and Applications*, 1 ed.; Halcrow, M. A., Ed. John Wiley & Sons, Ltd.: Chichester, UK, 2013; pp 475-506.
59. Sato, O.; Iyoda, T.; Fujishima, A.; Hashimoto, K., *Science* **1996,** *272* (5262), 704-705.
60. (a) Guionneau, P.; Le Gac, F.; Kaiba, A.; Costa, J. S.; Chasseau, D.; Létard, J.-F., *Chem. Commun.* **2007,** (36), 3723-3725; (b) Hayami, S.; Gu, Z.-z.; Einaga, Y.; Kobayasi, Y.; Ishikawa, Y.; Yamada, Y.; Fujishima, A.; Sato, O., *Inorg. Chem.* **2001,** *40* (13), 3240-3242.
61. Li, D.; Clérac, R.; Roubeau, O.; Harté, E.; Mathonière, C.; Le Bris, R.; Holmes, S. M., *J. Am. Chem. Soc.* **2007,** *130* (1), 252-258.
62. Paradis, N.; Chastanet, G.; Varret, F.; Létard, J.-F., *Eur. J. Inorg. Chem.* **2013,** *2013* (5-6), 968-974.
63. Varret, F.; Boukheddaden, K.; Chastanet, G.; Paradis, N.; Létard, J.-F., *Eur. J. Inorg. Chem.* **2013,** *2013* (5-6), 763-769.
64. (a) Tuchagues, J.-P.; Bousseksou, A.; Molnár, G.; McGarvey, J. J.; Varret, F., *Spin Crossover in Transition Metal Compounds III*, Wales), P. G. J.-G.-U. o. M. a. H. A. G. U. o. N. S., Ed. Springer-Verlag: Berlin, Heidelberg, New York, 2004; Vol. Topics in Current Chemistry, 235, pp 85-103; (b) Wolny, J. A.; Diller, R.; Schünemann, V., *Eur. J. Inorg. Chem.* **2012,** *2012* (16), 2635-2648.
65. Varret, F.; Chong, C.; Slimani, A.; Garrot, D.; Garcia, Y.; Naik, A. D., *Spin-Crossover Materials: Properties and Applications*, 1 ed.; Halcrow, M. A., Ed. John Wiley & Sons, Ltd: Chichester, UK, 2013; pp 425-441.
66. Sorai, M., *Spin Crossover in Transition Metal Compounds III*, Wales), P. G. J.-G.-U. o. M. a. H. A. G. U. o. N. S., Ed. Springer-Verlag: Berlin, Heidelberg, New York, 2004; Vol. Topics in Current Chemistry, 235, pp 153-170.
67. Shepherd, H. J.; Bonnet, S.; Guionneau, P.; Bedoui, S.; Garbarino, G.; Nicolazzi, W.; Bousseksou, A.; Molnár, G., *Phys. Rev. B: Condens. Matter Mater. Phys.* **2011,** *84* (14), 144107-1 to 144107-9.
68. Shepherd, H. J.; Rosa, P.; Vendier, L.; Casati, N.; Létard, J.-F.; Bousseksou, A.; Guionneau, P.; Molnár, G., *Phys. Chem. Chem. Phys.* **2012,** *14* (15), 5265-5271.
69. Shepherd, H. J.; Palamarciuc, T.; Rosa, P.; Guionneau, P.; Molnár, G.; Létard, J.-F.; Bousseksou, A., *Angewandte Chemie International Edition* **2012,** *51* (16), 3910-3914.
70. Howard, J. A. K.; Probert, M. R., *Science* **2014,** *343* (6175), 1098-1102.
71. (a) Miller, R. J. D., *Science* **2014,** *343* (6175), 1108-1116; (b) Elsaesser, T.; Woerner, M., *The Journal of Chemical Physics* **2014,** *140* (2), 020901-1 to 020901-11.
72. McCusker, J. K.; Rheingold, A. L.; Hendrickson, D. N., *Inorg. Chem.* **1996,** *35* (7), 2100-2112.
73. (a) Guionneau, P.; Marchivie, M.; Bravic, G.; Létard, J.-F.; Chasseau, D., *Spin Crossover in Transition Metal Compounds II*, Wales), P. G. J.-G.-U. o. M. a. H. A. G. U. o. N. S., Ed. Springer-Verlag: Berlin, Heidelberg, New York, 2004; Vol. Topics in Current Chemistry, 234, pp 97-128; (b) Guionneau, P.; Marchivie, M.; Bravic, G.; Létard, J.-F.; Chasseau, D., *J. Mater. Chem.* **2002,** *12* (8), 2546-2551.
74. Marchivie, M.; Guionneau, P.; Létard, J.-F.; Chasseau, D., *Acta Crystallographica Section B* **2005,** *61* (1), 25-28.
75. Boilleau, C.; Suaud, N.; Guihéry, N., *The Journal of Chemical Physics* **2012,** *137* (22), 224304-1 to 224304-9.
76. Marchivie, M.; Guionneau, P.; Létard, J.-F.; Chasseau, D., *Acta Crystallographica Section B* **2003,** *59* (4), 479-486.
77. Makovicky, E.; Balić-Žunić, T., *Acta Crystallographica Section B* **1998,** *54* (6), 766-773.

78. Buron-Le Cointe, M.; Hébert, J.; Baldé, C.; Moisan, N.; Toupet, L.; Guionneau, P.; Létard, J. F.; Freysz, E.; Cailleau, H.; Collet, E., *Physical Review B* **2012,** *85* (6), 064114-1 to 064114-9.
79. (a) Zabrodsky, H.; Peleg, S.; Avnir, D., *J. Am. Chem. Soc.* **1992,** *114* (20), 7843-7851; (b) Zabrodsky, H.; Peleg, S.; Avnir, D., *J. Am. Chem. Soc.* **1993,** *115* (18), 8278-8289; (c) Pinsky, M.; Zait, A.; Bonjack, M.; Avnir, D., *J. Comput. Chem.* **2013,** *34* (1), 2-9.
80. Alvarez, S., *J. Am. Chem. Soc.* **2003,** *125* (22), 6795-6802.
81. Marchivie, M.; Guionneau, P.; Létard, J. F.; Chasseau, D.; Howard, J. A. K., *J. Phys. Chem. Solids* **2004,** *65* (1), 17-23.
82. Jin Zhong, Z.; Tao, J.-Q.; Yu, Z.; Dun, C.-Y.; Liu, Y.-J.; You, X.-Z., *Journal of the Chemical Society, Dalton Transactions* **1998,** (3), 327-328.
83. Spackman, M. A.; Jayatilaka, D., *CrystEngComm* **2009,** *11* (1), 19-32.
84. Pfaffeneder, T. M.; Thallmair, S.; Bauer, W.; Weber, B., *New J. Chem.* **2011,** *35* (3), 691-700.
85. Legrand, V.; Pillet, S.; Souhassou, M.; Lugan, N.; Lecomte, C., *J. Am. Chem. Soc.* **2006,** *128* (42), 13921-13931.
86. (a) Ozarowski, A.; McGarvey, B. R.; Sarkar, A. B.; Drake, J. E., *Inorg. Chem.* **1988,** *27* (4), 628-635; (b) Galet, A.; Gaspar, A. B.; Muñoz, M. C.; Levchenko, G.; Real, J. A., *Inorg. Chem.* **2006,** *45* (24), 9670-9679.
87. (a) Gaspar, A. B.; Carmen Muñoz, M.; Moliner, N.; Ksenofontov, V.; Levchenko, G.; Gütlich, P.; Antonio Real, J., *Monatsh. Chem.* **2003,** *134* (2), 285-294; (b) Moliner, N.; Muñoz, M. C.; Létard, S.; Létard, J.-F.; Solans, X.; Burriel, R.; Castro, M.; Kahn, O.; Real, J. A., *Inorg. Chim. Acta* **1999,** *291* (1–2), 279-288; (c) Sheu, C.-F.; Shih, C.-H.; Sugimoto, K.; Cheng, B.-M.; Takata, M.; Wang, Y., *Chem. Commun.* **2012,** *48* (46), 5715-5717; (d) Shih, C.-H.; Sheu, C.-F.; Kato, K.; Sugimoto, K.; Kim, J.; Wang, Y.; Takata, M., *Dalton Trans.* **2010,** *39* (41), 9794-9800; (e) Sheu, C.-F.; Chen, S.-M.; Wang, S.-C.; Lee, G.-H.; Liu, Y.-H.; Wang, Y., *Chem. Commun.* **2009,** (48), 7512-7514.
88. Tao, J.; Wei, R.-J.; Huang, R.-B.; Zheng, L.-S., *Chem. Soc. Rev.* **2012,** *41* (2), 703-737.
89. Bedoui, S.; Molnár, G.; Bonnet, S.; Quintero, C.; Shepherd, H. J.; Nicolazzi, W.; Salmon, L.; Bousseksou, A., *Chem. Phys. Lett.* **2010,** *499* (1-3), 94-99.
90. Guionneau, P.; Lakhloufi, S.; Lemée-Cailleau, M.-H.; Chastanet, G.; Rosa, P.; Mauriac, C.; Létard, J.-F., *Chem. Phys. Lett.* **2012,** *542*, 52-55.
91. Cole, J. M., *Acta Crystallogr., Sect. A: Found. Crystallogr.* **2008,** *A64* (1), 259–271.
92. (a) Money, V. A.; Radosavljevic Evans, I.; Halcrow, M. A.; Goeta, A. E.; Howard, J. A. K., *Chem. Commun.* **2003,** (1), 158-159; (b) Huby, N.; Guérin, L.; Collet, E.; Toupet, L.; Ameline, J.-C.; Cailleau, H.; Roisnel, T.; Tayagaki, T.; Tanaka, K., *Physical Review B* **2004,** *69* (2), 020101-1 to 020101-4; (c) Thompson, A. L.; Money, V. A.; Goeta, A. E.; Howard, J. A. K., *Comptes Rendus Chimie* **2005,** *8* (9–10), 1365-1373.
93. Legrand, V.; Pillet, S.; Weber, H.-P.; Souhassou, M.; Létard, J.-F.; Guionneau, P.; Lecomte, C., *J. Appl. Crystallogr.* **2007,** *40* (6), 1076-1088.
94. Trzop, E.; Buron-Le Cointe, M.; Cailleau, H.; Toupet, L.; Molnar, G.; Bousseksou, A.; Gaspar, A. B.; Real, J. A.; Collet, E., *J. Appl. Crystallogr.* **2007,** *40* (1), 158-164.
95. Lorenc, M.; Hébert, J.; Moisan, N.; Trzop, E.; Servol, M.; Buron-Le Cointe, M.; Cailleau, H.; Boillot, M. L.; Pontecorvo, E.; Wulff, M.; Koshihara, S.; Collet, E., *Phys. Rev. Lett.* **2009,** *103* (2), 028301-1 to 028301-4.
96. Emma, P.; Akre, R.; Arthur, J.; Bionta, R.; Bostedt, C.; Bozek, J.; Brachmann, A.; Bucksbaum, P.; Coffee, R.; Decker, F.-J.; Ding, Y.; Dowell, D.; Edstrom, S.; Fisher, A.; Frisch, J.; Gilevich, S.; Hastings, J.; Hays, G.; Hering, P.; Huang, Z.; Iverson, R.; Loos, H.; Messerschmidt, M.; Miahnahri, A.; Moeller, S.; Nuhn, H. D.; Pile, G.; Ratner, D.; Rzepiela, J.; Schultz, D.; Smith, T.; Stefan, P.; Tompkins, H.; Turner, J.; Welch, J.; White, W.; Wu, J.; Yocky, G.; Galayda, J., *Nat. Photonics* **2010,** *4* (9), 641-647.
97. Lemke, H. T.; Bressler, C.; Chen, L. X.; Fritz, D. M.; Gaffney, K. J.; Galler, A.; Gawelda, W.; Haldrup, K.; Hartsock, R. W.; Ihee, H.; Kim, J.; Kim, K. H.; Lee, J. H.; Nielsen, M. M.; Stickrath, A. B.; Zhang, W.; Zhu, D.; Cammarata, M., *The Journal of Physical Chemistry A* **2013,** *117* (4), 735-740.

98. (a) Kaszub, W.; Buron-Le Cointe, M.; Lorenc, M.; Boillot, M.-L.; Servol, M.; Tissot, A.; Guérin, L.; Cailleau, H.; Collet, E., *Eur. J. Inorg. Chem.* **2013,** *2013* (5-6), 992-1000; (b) Collet, E.; Boillot, M.-L.; Hebert, J.; Moisan, N.; Servol, M.; Lorenc, M.; Toupet, L.; Buron-Le Cointe, M.; Tissot, A.; Sainton, J., *Acta Crystallographica Section B* **2009,** *65* (4), 474-480.
99. Cammarata, M.; Eybert, L.; Ewald, F.; Reichenbach, W.; Wulff, M.; Anfinrud, P.; Schotte, F.; Plech, A.; Kong, Q.; Lorenc, M.; Lindenau, B.; Räbiger, J.; Polachowski, S., *Rev. Sci. Instrum.* **2009,** *80* (1), 015101-1 to 015101-10.
100. Collet, E.; Lorenc, M.; Cammarata, M.; Guérin, L.; Servol, M.; Tissot, A.; Boillot, M. L.; Cailleau, H.; Buron-Le Cointe, M., *Chemistry – A European Journal* **2012,** *18* (7), 2051-2055
101. Kaszuba, W.; Collet, E.; Cailleau, H.; Servol, M.; Boillot, M.-L.; Tissot, A.; Lorenc, M., *Acta Phys. Pol., A* **2012,** *121* (2), 324-327.
102. (a) Lorenc, M.; Balde, C.; Kaszub, W.; Tissot, A.; Moisan, N.; Servol, M.; Buron-Le Cointe, M.; Cailleau, H.; Chasle, P.; Czarnecki, P.; Boillot, M. L.; Collet, E., *Physical Review B* **2012,** *85* (5), 054302-1 to 054302-8; (b) Cailleau, H.; Lorenc, M.; Guérin, L.; Servol, M.; Collet, E.; Buron-Le Cointe, M., *Acta Crystallographica Section A; Foundations of Crystallography* **2010,** *66* (2), 189-197; (c) Collet, E.; Moisan, N.; Balde, C.; Bertoni, R.; Trzop, E.; Laulhe, C.; Lorenc, M.; Servol, M.; Cailleau, H.; Tissot, A.; Boillot, M.-L.; Graber, T.; Henning, R.; Coppens, P.; Cointe, M. B.-L., *Phys. Chem. Chem. Phys.* **2012,** *14* (18), 6192-6199.
103. Aromí, G.; Barrios, L. A.; Roubeau, O.; Gamez, P., *Coord. Chem. Rev.* **2011,** *255* (5–6), 485-546.
104. Grosjean, A.; Négrier, P.; Bordet, P.; Etrillard, C.; Mondieig, D.; Pechev, S.; Lebraud, E.; Létard, J.-F.; Guionneau, P., *Eur. J. Inorg. Chem.* **2013,** *2013* (5-6), 796-802.
105. Billinge, S. J. L.; Kanatzidis, M. G., *Chem. Commun.* **2004,** (7), 749-760.
106. Forestier, T.; Kaiba, A.; Pechev, S.; Denux, D.; Guionneau, P.; Etrillard, C.; Daro, N.; Freysz, E.; Létard, J.-F., *Chemistry - a European Journal* **2009,** *15* (25), 6122-6130.
107. Boillot, M.-L.; Roux, C.; Audière, J.-P.; Dausse, A.; Zarembowitch, J., *Inorg. Chem.* **1996,** *35* (13), 3975-3980.
108. Boillot, M.-L.; Chantraine, S.; Zarembowitch, J.; Lallemand, J.-Y.; Prunet, J., *New J. Chem.* **1999,** *23* (2), 179-184.
109. (a) Kolb, J. S.; Thomson, M. D.; Novosel, M.; Sénéchal-David, K.; Rivière, É.; Boillot, M.-L.; Roskos, H. G., *Comptes Rendus Chimie* **2007,** *10* (1–2), 125-136; (b) Boillot, M. L.; Pillet, S.; Tissot, A.; Rivière, E.; Claiser, N.; Lecomte, C., *Inorg. Chem.* **2009,** *48* (11), 4729-4736.
110. Cirera, J.; Paesani, F., *Inorg. Chem.* **2012,** *51* (15), 8194-8201.
111. Tissot, A.; Boillot, M.-L.; Pillet, S. b.; Codjovi, E.; Boukheddaden, K.; Lawson Daku, L. v. M., *The Journal of Physical Chemistry C* **2010,** *114* (49), 21715-21722.
112. Sugahara, A.; Moriya, K.; Enomoto, M.; Okazawa, A.; Kojima, N., *Polyhedron* **2011,** *30* (18), 3127-3130.
113. (a) Takahashi, K.; Hasegawa, Y.; Sakamoto, R.; Nishikawa, M.; Kume, S.; Nishibori, E.; Nishihara, H., *Inorg. Chem.* **2012,** *51* (9), 5188-5198; (b) Hasegawa, Y.; Takahashi, K.; Kume, S.; Nishihara, H., *Chem. Commun.* **2011,** *47* (24), 6846-6848.
114. Hasegawa, Y.; Kume, S.; Nishihara, H., *Dalton Trans.* **2009,** (2), 280-284.
115. Bannwarth, A.; Schmidt, S. O.; Peters, G.; Sönnichsen, F. D.; Thimm, W.; Herges, R.; Tuczek, F., *Eur. J. Inorg. Chem.* **2012,** *2012* (16), 2776-2783.
116. (a) Garcia, Y.; Ksenofontov, V.; Lapouyade, R.; Naik, A. D.; Robert, F.; Gütlich, P., *Opt. Mater.* **2011,** *33* (6), 942-948; (b) Sénéchal-David, K.; Zaman, N.; Walko, M.; Halza, E.; Rivière, E.; Guillot, R.; Feringa, B. L.; Boillot, M. L., *Dalton Trans.* **2008,** (14), 1932-1936.
117. (a) Milek, M.; Heinemann, F. W.; Khusniyarov, M. M., *Inorg. Chem.* **2013,** *52* (19), 11585-11592; (b) Nihei, M.; Suzuki, Y.; Kimura, N.; Kera, Y.; Oshio, H., *Chemistry – A European Journal* **2013,** *19* (22), 6946-6949
118. Thies, S.; Bornholdt, C.; Köhler, F.; Sönnichsen, F. D.; Näther, C.; Tuczek, F.; Herges, R., *Chemistry – A European Journal* **2010,** *16* (33), 10074-10083

119. (a) Thies, S.; Sell, H.; Bornholdt, C.; Schütt, C.; Köhler, F.; Tuczek, F.; Herges, R., *Chemistry – A European Journal* **2012,** *18* (51), 16358-16368; (b) Thies, S.; Sell, H.; Schütt, C.; Bornholdt, C.; Näther, C.; Tuczek, F.; Herges, R., *J. Am. Chem. Soc.* **2011,** *133* (40), 16243-16250.
120. Venkataramani, S.; Jana, U.; Dommaschk, M.; Sönnichsen, F. D.; Tuczek, F.; Herges, R., *Science* **2011,** *331* (6016), 445-448.

Chapter 2

Structural and spectroscopic characterisation of the spin crossover in $[Fe(abpt)_2(NCS)_2]$ polymorph A

Helen E. Mason, Wei Li, Michael A. Carpenter, Michelle L. Hamilton, Judith A. K. Howard and Hazel A. Sparkes

Published *New Journal of Chemistry*, 2016, **40(3)**, 2466-2478, doi 10.1039/C5NJ02359A. Reproduced with permission for the Royal Society of Chemistry.

2.1 Abstract

A crystallographic and solid state spectroscopic study of the spin crossover behaviour of $[Fe(abpt)_2(NCS)_2]$ (abpt = 4-amino-3,5-bis(pyridin-2-yl)-1,2,4-triazole) polymorph **A** is reported. Structural features including crystallographic cell parameters, bond lengths and distortion parameters are monitored between 375 K and 30 K and crystal structures are reported at seven temperatures across the spin transition. In addition, the light induced excited spin state trapping (LIESST) metastable high spin structure, HS*, is reported at 30 K by continuous irradiation with a 670 nm, 5 mW CW laser during the data collection. Relaxation of the HS* state at 30 K with the laser switched off is found to occur within ~4000 s in accordance with the literature. High pressure single crystal datasets are also reported to examine the effect of pressure on the spin transition. Single crystal variable temperature UV-Vis spectroscopy and resonant ultrasound spectroscopy support the crystallographic evidence relating to the spin crossover transition presented herein. Strain analysis of the lattice parameters yields the temperature dependence of the spin order parameter, indicating strong spin-lattice coupling to give a volume strain of up to ~4% and a shear strain of up to ~1.5%. These, in turn, are responsible for changes in elastic constants by up to ~35%.

2.2 Introduction

Spin crossover is a reversible spin state transition of a metal centre which can occur upon change in temperature, pressure,[1] magnetic field or through light irradiation.[2] Spin crossover is a relatively common phenomenon for octahedral $3d^4$-$3d^7$ metal centres and has been extensively studied in a large range of systems.[3] A significant proportion of the spin crossover compounds that have been studied are octahedral Fe(II) complexes with nitrogen donor ligands,[3] although spin crossover is also commonly observed in six-coordinate Fe(III)[4] or Co(II) complexes.[5, 6] A number of potential applications have been suggested for spin crossover complexes, e.g. molecular switches, data storage[7, 8] and liquid crystals. Spin crossover is a very complex process which can occur in both solution and the solid state and involves the switching of magnetic, optical and structural properties. In solution there is no cooperativity as molecules are far apart and transitions tend to be gradual. However, in the solid state the potential for cooperativity results in a wide range of different behaviours, from abrupt transitions with hysteresis (strong cooperativity) to gradual transitions with no hysteresis (weak or no cooperativity), and can include single or multistep spin transition[9] processes. Factors such as inclusion of solvent in the lattice, intermolecular interactions and counterion type are all known to influence the spin transition behaviour. Given the complex nature of the process it is particularly interesting to study compounds with more than one polymorph and which show different spin crossover behaviour.[10] Comparing the structures and spin crossover processes in such species can provide significant insight into the phenomenon.

Four polymorphs of $[Fe(abpt)_2(NCS)_2]$ (abpt = 4-amino-3,5-bis(pyridin-2-yl)-1,2,4-triazole) (**A**-**D**) have been reported previously. Three of these, **A**,[11] **C**[12, 13] and **D**,[12, 14] have been shown to undergo temperature induced spin crossover of at least one of the Fe(II) centres in the asymmetric unit from high spin (HS) to low spin (LS) upon cooling. On the other hand, polymorph **B** does not undergo a thermal spin transition at ambient pressure, but has been shown to undergo thermal spin crossover at pressures >4.4 kbar.[15] The room temperature crystal structures of the three polymorphs which undergo temperature induced spin crossover have been established and while **A** has one independent Fe(II) centre in the asymmetric unit, **C** and **D** both contain two independent Fe(II) centres. The first magnetic susceptibility measurements on a single crystal sample of polymorph **A** indicated an incomplete spin transition from HS to LS with ~23% of the molecules remaining HS in the 'LS' structure.[11] A more recent publication using a different sample preparation method has shown that this polymorph can undergo a virtually complete spin transition upon cooling.[12] In polymorphs **C** and **D** only one Fe centre undergoes a spin transition and the other remains HS upon cooling.[12] All three polymorphs displaying thermal spin crossover behaviour also show light induced excited spin state trapping (LIESST) at low temperature. For **C**, $T_{1/2}$ = 86 K and upon low temperature photoexcitation it forms a commensurate modulated LIESST state with four crystallographically independent Fe centres.[13] For **D** $T_{1/2}$ = 162 K and, in addition to displaying LIESST, the compound also displays photoinduced linkage isomerism with the NCS ligand changing from N to S bound.[14] For **A**, which has a thermal spin crossover that occurs without hysteresis, $T_{1/2}$ was initially reported as 180 K,[11] but has been remeasured as $T_{1/2}$ = 188 K[12] for single crystals prepared using a different method. T_{LIESST} = 40 K and up to approximately 30 K a significant fraction of the HS* state can be maintained for >1000 s; as the temperature is increased above 30 K this fraction decreases rapidly. Although the thermally induced spin crossover shows no hysteresis, a light induced thermal hysteresis (LITH)[16] associated with the HS* state has been identified from the photomagnetic data.[11] LS and HS* state structures for **A** have not been characterised previously and these are reported herein alongside a detailed crystallographic study of structural changes occurring during the spin transition and examination of the HS* relaxation behaviour of this polymorph. The results are supported by single crystal variable temperature UV-Vis spectroscopy and resonant ultrasound spectroscopy (RUS). An analysis of changes in the lattice parameters reveals strong coupling of both volume and shear strains with the spin state order parameter which, in turn, gives rise to large anomalies in elastic properties.

2.3 Experimental

2.3.1 Synthesis

Synthesis of $[Fe(abpt)_2(NCS)_2]$ was carried out using a slow diffusion method which has been previously reported to produce crystals of polymorph **A** which undergo a virtually complete HS to LS transition upon cooling.[12] Precursor materials were used without further purification, solvents degassed and all manipulations carried out under a nitrogen atmosphere. $FeSO_4.7H_2O$ (1 mmol, 0.278 g) and KNCS (2 mmol, 0.194 g) were stirred in MeOH (10 ml) for 15 min. Pale yellow insoluble K_2SO_4 precipitate was removed by filtration and deionised H_2O (10 ml) added to the remaining clear solution. abpt ligand (2 mmol, 0.477 g) was dissolved in MeOH (20 ml) and transferred to a narrow (<5 cm) Schlenk tube. The $Fe^{2+}/2(NCS)^-$ solution was carefully injected underneath the abpt solution to form a lower layer. A coloured band containing the target complex immediately formed at the interface between the two layers. Within 1-4 weeks single crystals of **A**, **B** and **D** suitable for X-ray diffraction studies were formed and separated under the microscope.[12] Crystals of **A** were also formed using a methanol-chloroform solution which favours the formation of this polymorph,[15] however the quality of the crystals formed was lower than that obtained from methanol-water.

2.3.2 X-ray Crystallography

2.3.2.1 Variable temperature and LIESST measurements

X-ray diffraction data were collected on a Bruker Smart 1K CCD diffractometer using graphite monochromated Mo-*Kα* (λ = 0.71073 Å) radiation. Datasets below 105 K were collected using an Oxford Cryosystems HeliX,[17] while those above 105 K were collected using an Oxford Instruments open flow N_2 Cryostream for cooling. Data collection was carried out using the SMART software,[18] integration was performed using SAINT[19] and multi-scan absorption corrections were applied to all datasets using SADABS.[20] The structures were solved by direct methods in SHELXS[21] and refined by full matrix least squares on F^2 in SHELXL[21] using Olex2.[22] All non-hydrogen atoms were refined anisotropically and all hydrogen atoms were located geometrically and refined using a riding model with the exception of the hydrogen atoms on N6 which were located in the difference map. The LIESST structure at 30 K was obtained by irradiating the crystal *in-situ* using a 670 nm, 5 mW CW laser. The crystal was irradiated for 60 minutes prior to and also continued throughout the data collection to try to establish and maintain a photostationary state, i.e. the metastable LIESST HS* structure. The same crystal was used for all data collections below 300 K, including the full datasets at 270, 210, 180, 165, 150, 120, 30 K and 30 K under laser irradiation. A second crystal was used to collect the data between 300 K and 375 K illustrated in the variable temperature plots. Temperature calibration of the Cryostream and HeliX was carried out using phase transition materials benzil (83 K)[23] and $NH_4H_2PO_4$ (148 K).[24] Offsets of -3 K and +3 K were observed for the Cryostream and HeliX respectively; i.e. a temperature set at 105 K corresponds to a temperature of 102 K or 108 K at the crystal surface for Cryostream or HeliX measurements respectively.[25] This offset is taken into account in the variable temperature plots where the transition profile is discussed. Full structure determinations were carried out at twenty-four temperatures; seven of these structures (30, 120, 150, 165, 180, 210 and 270 K) are published herein.

2.3.2.2 LIESST HS* relaxation

LIESST HS* structure relaxation measurements were carried out by continuous collection of omega scans (scan width 0.4°) consisting of 50 frames at alternating phi positions of 0 and 90° immediately after switching off the laser. The program SMARTreduce,[26] a script to harvest reflections, perform cell indexation and least squares refinement automatically in SMART,[18] was used to iteratively determine a unit cell from each consecutive set of two runs. This allowed the evolution of the unit cell dimensions as a function of time to be monitored.

2.3.2.3 High pressure

A single crystal was mounted in a modified Merrill-Bassett type diamond anvil cell (DAC) custom built at Durham University using tungsten carbide backing plates with an opening angle of 85° and type IA Boehler-Almax diamond anvils with 0.8 mm culets. Stainless steel gaskets were pre-indented and drilled to give a gasket chamber of ~0.3 mm diameter and 0.15 mm depth and paraffin oil was used as the pressure transmitting medium. A small ruby chip was used to measure the pressure in the DAC using the Ruby R_1 fluorescence method.[27] Fluorescence measurements were carried out before and after data collection to ensure there was no change in pressure during the experiment. The pressure can alter if insufficient time has been given for the pressure in the DAC to equilibrate prior to data collection. The laser used for fluorescence measurements can induce a spin transition, therefore exposure was minimised as much as possible, although because the pressure measurement is almost always taken above T_{LIESST} any structural change is short lived. Room temperature (296 K) single crystal X-ray diffraction data were collected at ambient pressure, 1.4(2) kbar and 5.1(2) kbar. Data collection was carried out using XIPHOS II,[28] part of the XIPHOS diffraction facility.[29] This diffractometer, custom built for high pressure studies, is equipped with an Incoatec Ag-*Kα* (λ = 0.56086 Å) I*μ*S source.[30] Data collection was carried out using the Bruker

APEX2 software suite,[31] integration was performed using SAINT[32] and multi-scan absorption corrections were applied to all datasets using SADABS.[20] ECLIPSE[33] was used to generate dynamic mask files to exclude areas of the diffraction pattern which contain no data due to the body of the DAC from the integration. The structures were solved by direct methods in SHELXS[21] and refined by full matrix least squares on F^2 in SHELXL[21] using Olex2.[22] All of the non-hydrogen atoms were refined anisotropically and all hydrogen atoms were located geometrically and refined using a riding model with the exception of the hydrogen atoms on N6 which were located in the difference map.

2.3.3 Variable temperature UV-Vis transmission spectroscopy

The single crystal UV-Vis setup used (Figure 2.1) is based on a cassegrain system (Bruker) which utilises fibre optic cables to transmit radiation from a broadband light source (Hamamatsu UV-VIS fibre light source, L10290) to the sampling optics and from the optics into a UV-Vis spectrometer [Andor Shamrock SR-303i imaging spectrograph using 150 lines/mm grating groove density, (specifications quote a resolution of 0.88 nm at a 500 nm centre wavelength) coupled with a Newton EMCCD camera]. The sample temperature was controlled using a non-liquid N_2 Cryostream (Oxford Cryosystems, Cobra).

A single crystal fragment of <100×100×25 µm was mounted using perfluoropolyether oil on a UV-Vis 100 µm aperture MicroLoop (MiTeGen, LLC) which was fixed on an XRD goniometer head. The crystals were visualised using a high-magnification zoom lens system mounted on a CMOS camera (Thorlabs) and positioned at the focus of the cassegrain system in the orientation giving the cleanest spectroscopic signal.

The area sampled by the UV-Vis radiation is controlled by the focus size of the cassegrain optics which is determined by the core size of the input fibre optic cable; for the crystals presented here the spot size was ~50 µm in diameter. Spectra were collected using Andor's Solis software with a 20 ms exposure. Background (no light source) and reference (light source on a MicroLoop without sample) spectra were collected and data were presented by the Solis software in absorbance mode. OriginPro software[34] was used for further data processing. Raw data were smoothed using a Savitzky-Golay filter (window size 13 points, polynomial order 2). The % transmittance, but not the spectral shape, is dependent on the orientation of the crystal within the light beam, and therefore raw spectra were normalised.

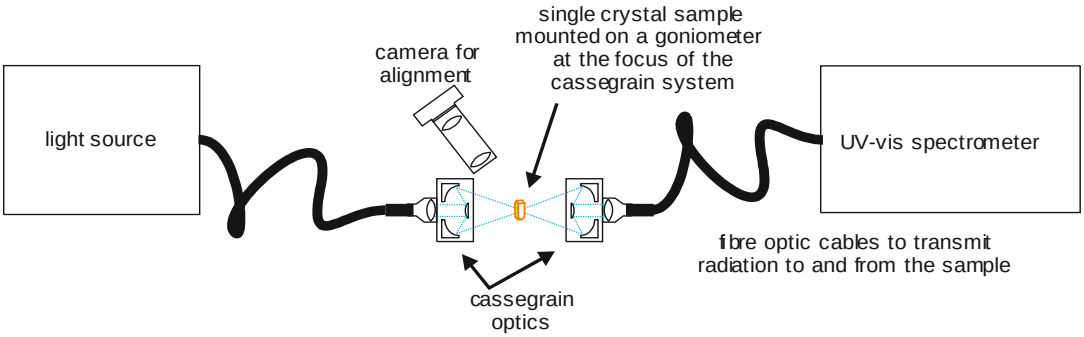

Figure 2.1 - Schematic of the cassegrain system used to collect UV-Vis spectra from single crystals.

2.3.4 Resonant Ultrasound Spectroscopy

The principle of the resonant ultrasound spectroscopy (RUS) technique is quite straightforward.[35] A sample with dimensions of ~1 mm is held lightly between two piezoelectric transducers. The first transducer is driven by a frequency synthesizer at constant amplitude across a range of ultrasonic frequencies (0.1 - 2 MHz) which in turn causes the sample to resonate at particular frequencies. The second transducer acts as a signal detector which records the response of the sample in terms of its displacement when it is vibrated across the frequency range. Vibrational frequencies detected represent the frequency of normal modes of the sample. The square of a given peak frequency is directly proportional to the elastic constants associated with that normal mode.[35] Low temperature measurements presented here were obtained using a single crystal of $[Fe(abpt)_2(NCS)_2]$ polymorph **A** with irregular shape (~0.4 mm in diameter, 0.0003 g) in a helium flow cryostat which has been described by McKnight *et al*.[36] Data were collected with the sample chamber filled with a few mbar of helium to allow heat exchange between sample and cryostat. All spectra were transferred to the software package Igor Pro (WaveMetrics) for analysis. Peak positions and widths at half height were determined for a selection of peaks by fitting with an asymmetric Lorentzian function. The mechanical quality factor, Q, was calculated using the relationship $Q = f/\Delta f$, where f is the peak frequency and Δf is the width of the peak at half its maximum height. The inverse of the quality factor, Q^{-1}, is a measure of acoustic dissipation (energy loss) in the sample.

2.4 Results

2.4.1 Thermal spin crossover

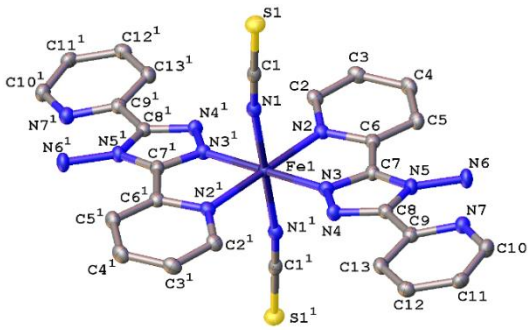

Figure 2.2 - Ellipsoid plot of $[Fe(abpt)_2(NCS)_2]$ polymorph **A** at 120 K with the ellipsoids depicted at 50% probability level. The asymmetric unit (asu) consists of half a molecule and '¹' represents the other half of the molecule which is symmetry generated by the operator 1-*x*, 1-*y*, 1-*z*. Hydrogen atoms have been omitted for clarity.

The magnetic data for polymorph **A** indicates that it undergoes thermal spin crossover without hysteresis between ~202 K and 100 K[11] (remeasured ~250 K and 160 K),[12] with $T_{1/2}$ = 180 K[11] (remeasured $T_{1/2}$ = 188 K)[12] and a residual HS fraction, γ_{HS}, of 23%[11] (remeasured γ_{HS} ~ 0%) at low temperature. The sample preparation method differs in the two reports[11, 12] which could explain the slight difference in the observed transition profile and completeness. The transition has been reported as gradual with moderate cooperativity between molecules[11] playing a role in the propagation of the spin transition.[37] Full crystallographic structure determinations upon cooling through the transition are reported from the same crystal at seven temperatures: 270, 210, 180, 165, 150, 120 and 30 K (Table 2.1 and Appendix 2, Table S2.1). The structure of **A** at 293 K[11] has been previously reported and is consistent with the HS structure discussed here. All of the

structures were solved in the monoclinic space group $P2_1/n$ with half a molecule in the asymmetric unit (Z' = 0.5) (Figure 2.2). Each Fe(II) centre has 6 coordinated nitrogen atoms: one from each NCS group and two from each abpt ligand (one pyridyl nitrogen and one triazole nitrogen). An intramolecular hydrogen bond exists between N6-H6···N7, for which D-H = 0.88(2) Å, H···A = 2.16(2) Å, D···A = 2.853(2) Å, <DHA = 135(2)° at 30 K and D-H = 0.93(2) Å, H···A = 2.12(2) Å, D···A = 2.847(3) Å, <DHA = 135(2)° at 270 K. In addition, a weak C2-H2···N4#1 (#1 = -*x*+1, -*y*+1, -*z*+1) interaction was also identified (Appendix 2, Table S2.2). The structures all contain π-π interactions between pairs of counterpart abpt pyridyl groups on adjacent molecules [centroid (N2, C2-C6) to centroid (N7#2, C9#2-C13#2, #2 = 1-*x*, 2-*y*, 1-*z*) distance of ~3.6 Å with an offset of ~1.3 - 1.4 Å at all temperatures] creating a 1-dimensional chain through the structure which can be viewed along the (110) direction. Indeed the spin transition has been linked to the presence of these π-π interactions.[12] Molecules along the *c*-axis direction are rotated by ~40° from each other, molecules along the *a*-axis direction are in the same orientation as each other (Figure 2.3). The differences between the HS, LS and HS* structures are discussed in more detail below.

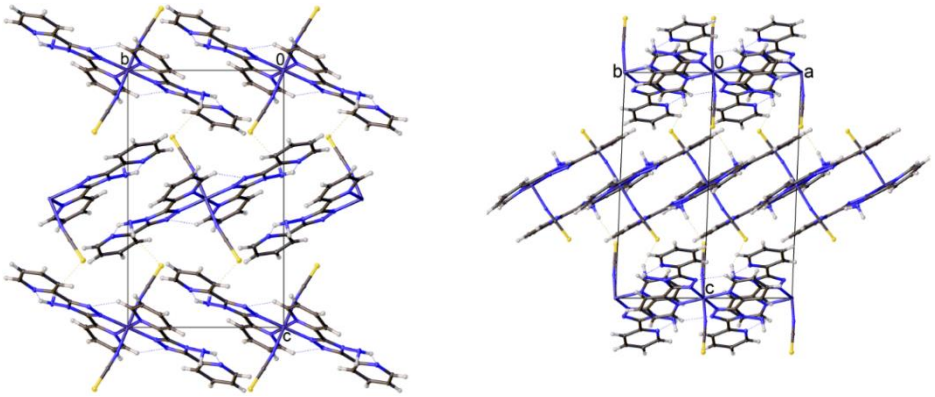

Figure 2.3 - Diagrams showing the packing of $[Fe(abpt)_2(NCS)_2]$ polymorph **A** at 30 K viewed along the (left) (100) and (right) (110) directions.

Table 2.1 - Crystal data and refinement results for $[Fe(abpt)_2(NCS)_2]$ polymorph **A** at 270 K, 30 K and 30 K after irradiation.

Spin state (temperature)	HS (270 K)	LS (30 K)	HS*, LIESST (30 K)
Empirical formula	$C_{26}H_{20}FeN_{14}S_2$	$C_{26}H_{20}FeN_{14}S_2$	$C_{26}H_{20}FeN_{14}S_2$
Formula weight	648.53	648.53	648.53
λ (Å)	0.71073	0.71073	0.71073
Crystal system	Monoclinic	Monoclinic	Monoclinic
Space group	$P2_1/n$	$P2_1/n$	$P2_1/n$
a (Å)	8.5367(4)	8.3411(4)	8.4505(4)
b (Å)	10.2206(5)	9.9442(5)	10.1273(5)
c (Å)	16.4268(8)	16.1668(8)	16.3033(8)
β (°)	93.899(1)	93.112(1)	93.491(1)
V (Å^3)	1429.92(12)	1338.99(11)	1392.66(12)
Z	2	2	2
Temperature (K)	270(2)	30(2)	30(2)
D_c (Mg/m^3)	1.506	1.609	1.547
μ (mm^{-1})	0.719	0.768	0.738
F(000)	664	664	664
Crystal size (mm^3)	0.36 x 0.30 x 0.26	0.36 x 0.30 x 0.26	0.36 x 0.30 x 0.26
θ range for data collection (°)	2.35 - 28.28	2.41 - 28.28	2.37 - 28.29
Ranges of h, k, l	$-11 \le h \le 11$, $-13 \le k \le 10$, $-21 \le l \le 16$	$-10 \le h \le 11$, $-13 \le k \le 9$, $-21 \le l \le 15$	$-10 \le h \le 11$, $-13 \le k \le 10$, $-21 \le l \le 16$
Refl. collected	9716	9018	9399
R_{int}	0.0301	0.0370	0.0293
Data/parameters	3554/202	3318/202	3453/202
Absorption coef. min/max	0.697/1.000	0.787/1.000	0.471/0.743
GooF (F^2)	1.034	1.040	1.049
Final R_1 [$I > 2\sigma(I)$]	0.0362	0.0341	0.0311
wR_2 [$I > 2\sigma(I)$]	0.0845	0.0797	0.0727
Largest diff. peak/hole (e Å^{-3})	0.41/-0.37	0.73/-0.52	0.37/-0.33

2.4.2 Variable temperature data collections at 30, 120, 150, 165, 180, 210 and 270 K and unit cell parameter changes

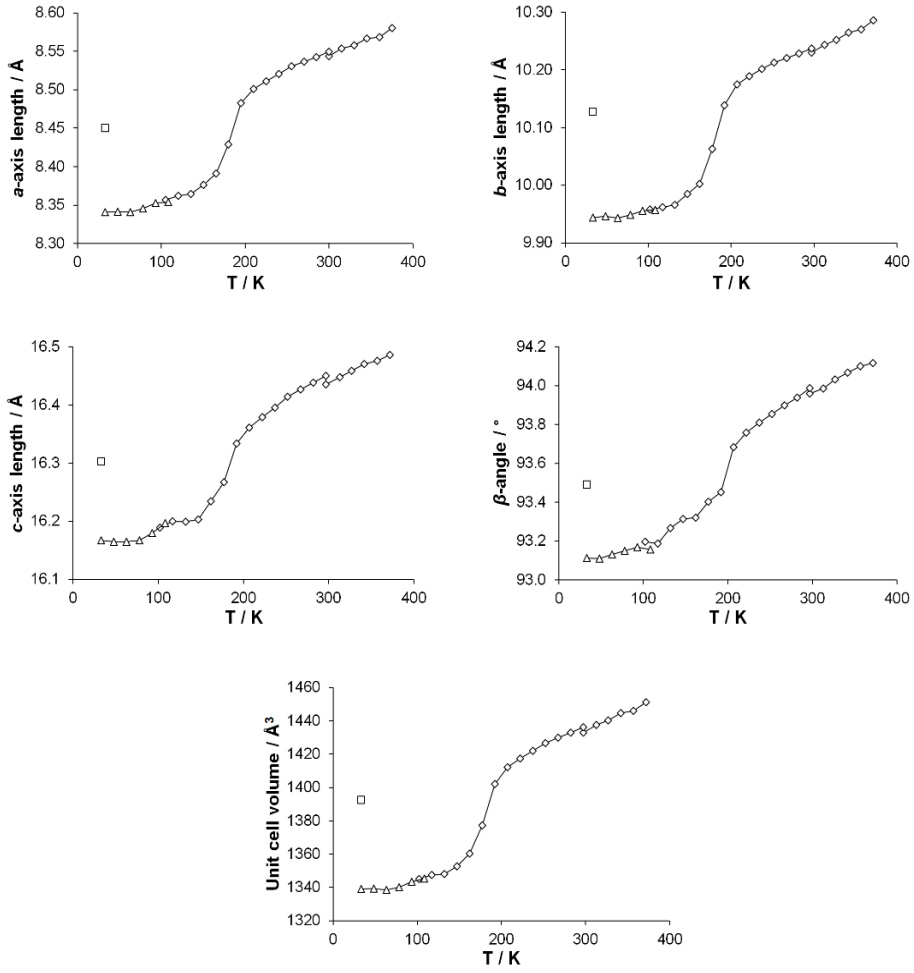

Figure 2.4 - Changes in cell parameters for $[Fe(abpt)_2(NCS)_2]$ polymorph **A** with temperature are shown as points connected by a line: ◊ and Δ denote data collected using the Cryostream or HeliX respectively and □ show corresponding LIESST, HS* cell parameters. The temperature scale has been adjusted to show temperature at the crystal surface for both Cryostream and HeliX measurements, see Experimental section, Variable temperature and LIESST measurements, for details. Error bars are included but obscured by the data markers.

Cell parameters were monitored over the temperature range 30 - 375 K on two different crystals (crystal 1, 300 - 30 K; crystal 2, 375 - 300 K). As can be seen from Figure 2.4, all the cell axes lengths and the *β* angle decrease as the temperature decreases. Although only small changes are seen in the axes lengths and *β* angle, overall they follow the same pattern as that observed in the magnetic data and the occurrence of the spin transition can clearly be seen.

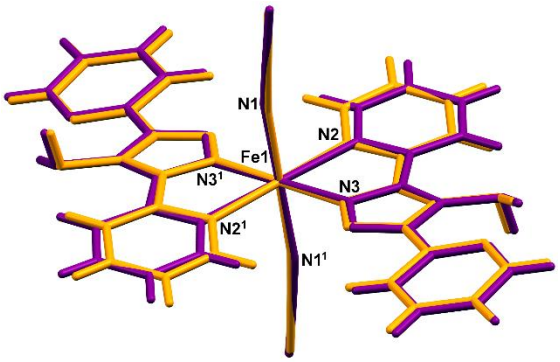

Figure 2.5 - Overlay of (purple) HS, 270 K and (orange) LS, 30 K structures of $[Fe(abpt)_2(NCS)_2]$ polymorph **A**. The asu consists of half a molecule and '[1]' represents the other half of the molecule which is symmetry generated by the operator 1-*x*, 1-*y*, 1-*z*.

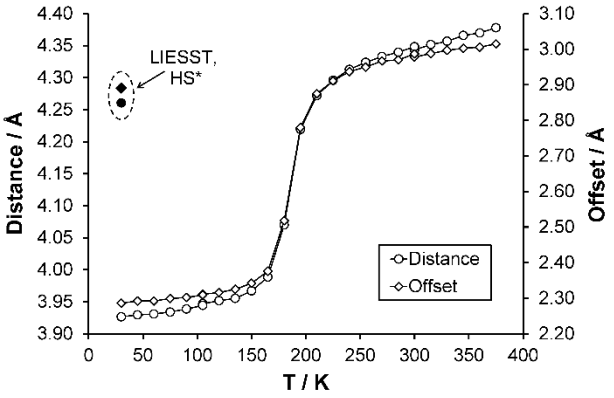

Figure 2.6 - Change in centroid (N2, C2-C6) to centroid (N2#3, C2#3-C6#3, where #3 = 2-*x*, 1-*y*, 1-*z*) (○) distance and (◊) offset with temperature. ● and ♦ denote distance and offset observed respectively for the HS* structure at 30 K. Error bars are included but obscured by the data markers.

The unirradiated structures at the two extremes of the measured temperature range, i.e. 30 K and 270 K, were examined and although very similar there are some clear differences between the structures (Figure 2.5). The Fe-N bond lengths range from 2.131(2) to 2.215(3) Å at 270 K and 1.952(2) to 2.010(2) Å at 30 K. This ~0.2 Å decrease in the Fe-N distances with decreasing temperature is consistent with the structure having undergone the expected spin crossover from HS (270 K) to LS (30 K) (Table 2.2). In addition to a decrease in the Fe-N bond lengths upon cooling, the N2-Fe1-N3 bond angle increases from 74.76(26)° to 79.98(6)° with a concomitant decrease in the N1-Fe-N3#1 (#1 = -*x*+1, -*y*+1, -*z*+1) bond angle from 105.24(6)° to 100.02(6)°. This results in a shortening of the D···A distance associated with the weak C2-H2···N4#1 (#1 = -*x*+1, -*y*+1, -*z*+1) interaction giving a trend consistent with that associated with the magnetic data (Appendix 2, Table S2.2, Appendix 2 Figure S2.2).

After the HS to LS transition upon cooling the interpenetration of adjacent pairs of molecules along approximately the *ab* direction increases, this results in a decrease of the centroid (N2, C2-C6) to centroid (N2#3, C2#3-C6#3, where #3 = 2-*x*, 1-*y*, 1-*z*) distance from ~4.3 Å with an offset of 3.0 Å (270 K) to ~3.9 Å with an offset of 2.3 Å (30 K) (Figure 2.6). Structures obtained upon flash freezing

below the spin transition temperature are identical to those obtained with gradual cooling through the spin transition. No reduction in crystallinity was observed after the spin transition, probably due to the fact that the HS, LS and HS* crystal structures are isostructural and only very small changes occur as a result of the spin transition.

Full structure determinations are reported at 30, 120, 150, 165, 180, 210 and 270 K. Examining the three independent bond lengths around the Fe centre (Table 2.2, Figure 2.7) shows a marked decrease in all the Fe-N bond lengths going through the temperature range of the spin transition (datasets at 210 - 150 K). In the case of the unirradiated structure at 30 K and the 120 K structure; the Fe-N bond lengths, the distortion parameter Σ (~49°) and Fe octahedron volume V_p (~10 Å^3) are essentially identical and V_p is consistent with values previously associated with the presence of a LS state in an FeN_6 complex. At the other end of the temperature range the 270 K structure along with the ~0.2 Å increase in the Fe-N bond lengths shows a significant increase in the value of Σ (~70°) and V_p (~13 Å^3), supporting the formation of the HS state. For the structures obtained during the spin transition (165 K and 180 K) it can be seen that Σ and V_p also decrease markedly as the temperature decreases and suggest that the Fe centre is in between the HS and LS states as expected.

Table 2.2 - Fe-N bond lengths for all structures, including the three 296 K structures collected in the DAC, along with the distortion parameter Σ and the volume of the Fe octahedron V_p.

	Fe1-N1 (Å)	Fe1-N2 (Å)	Fe1-N3 (Å)	Σ[a] (°)	V_p[b] (Å^3)
30(2) K LIESST	2.1384(13)	2.2096(13)	2.1312(13)	69.2(3)	12.957(5)
30(2) K	1.952(2)	2.010(2)	1.958(2)	49.2(4)	10.080(5)
120(2) K	1.953(2)	2.007(2)	1.955(2)	49.0(4)	10.053(5)
150(2) K	1.955(1)	2.013(1)	1.958(1)	49.8(4)	10.104(4)
165(2) K	1.964(2)	2.023(1)	1.970(1)	50.8(4)	10.255(5)
180(2) K	2.012(2)	2.074(2)	2.015(3)	56.1(4)	10.964(5)
210(2) K	2.112(2)	2.185(1)	2.112(1)	67.5(4)	12.564(5)
270(2) K	2.131(2)	2.215(2)	2.134(2)	69.9(4)	12.947(6)
ambient	2.127(5)	2.217(6)	2.129(8)	65.2(14)	12.96(2)
1.4(2) kbar	2.128(3)	2.202(4)	2.111(6)	68.8(10)	12.74(2)
5.1(2) kbar	2.006(3)	2.063(4)	1.991(6)	54.9(16)	10.76(2)

[a] Σ, the distortion parameter, is the sum of the absolute value of the deviation of all 12 *cis* N-Fe-N angles from 90°. [b] V_p is the volume of the Fe octahedron calculated in Olex2.[22]

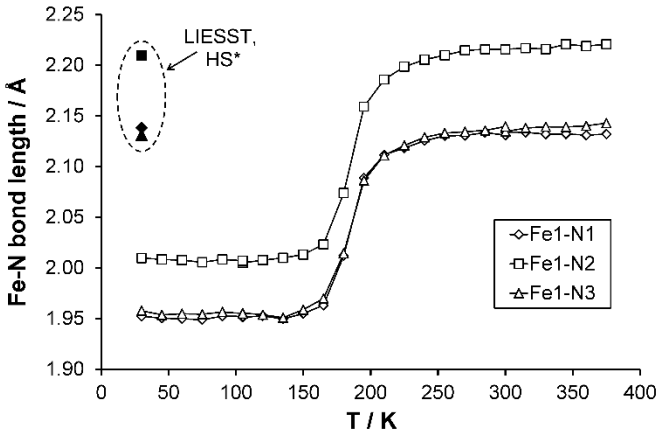

Figure 2.7 - Fe-N bond length changes as a function of temperature, LIESST values are contained within the dashed oval. Error bars are included but obscured by the data markers.

2.4.3 LIESST metastable HS* structure at 30 K

The reported value of T_{LIESST} for **A** is ~40 K.[11] Given that previously reported magnetic data had established that at 30 K around 50% of the HS* state in a precipitated sample reverts back to the LS state after <1000 s and almost 100% relaxes within 4000 s,[11] the laser was left on to continue irradiation throughout the data collection. Whether any residual ground state (LS) species remain even during continuous irradiation is not known for the crystals used in this study and the possibility of any resulting bias in the HS* structural parameters was not investigated.[38] After irradiation there is a 4% increase in the unit cell volume at 30 K which would be anticipated with the formation of a metastable HS* state through LIESST. The HS* structure retains the monoclinic space group $P2_1/n$ previously measured for the HS and LS ground state structures. As expected with the formation of the HS* state there is an increase of ~0.2 Å in all of the Fe-N bond lengths upon irradiation at 30 K, ranging from 1.952(2) to 2.010(2) Å in the LS state structure to 2.1312(13) to 2.2096(13) Å in the HS* state structure. The range of Fe-N bond lengths seen in the HS* structure at 30 K align very closely with those observed in the HS structure at 270 K [2.131(2) to 2.215(2) Å]. In addition, upon the spin transition from LS to HS* at 30 K there is an increase in Σ from 49.2(4)° to 69.2(3)° and likewise an increase in V_p from ~10 Å^3 to ~13 Å^3, these values are in line with those observed in the HS state at 270 K [Σ = 69.9(4)° and V_p = 12.947(6) Å^3]. Indeed the key structural features of the HS* structure at 30 K are very similar to those of the 270 K HS structure discussed previously and hence they are not examined in any further detail here.

2.4.4 LIESST metastable HS* structure relaxation at 30 K

The relaxation of the HS* state to the LS ground state was monitored crystallographically by irradiating a crystal at 30 K to induce the HS* state, switching the laser off and monitoring the evolution of unit cell parameters with time. This confirmed that at 30 K within ~4000 s the metastable HS* state had reverted to the LS ground state structure (Figure 2.8).[11]

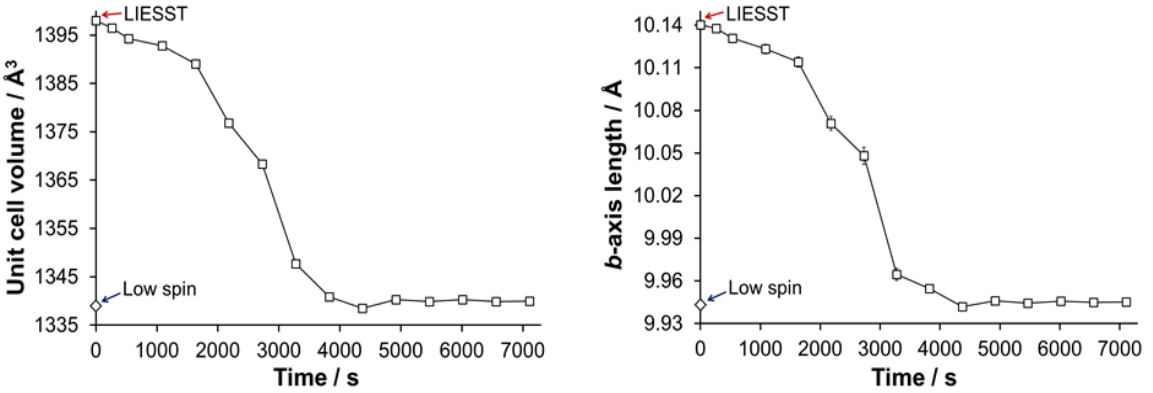

Figure 2.8 - Illustration of the change in (left) unit cell volume and (right) *b*-axis length as a function of time at 30 K as a result of relaxation of the LIESST HS* state. Note: each data point is plotted at the time mid-point of its two consecutive omega runs, therefore an error between +/-(535 to 538) s is associated with all data points except the 1st data point after turning the laser off (at 262 s) where the error is +/-262 s. Plots showing *a*-axis, *c*-axis and *β*-angle relaxation are included in Appendix 2, Figure S2.1.

2.4.5 High pressure structure

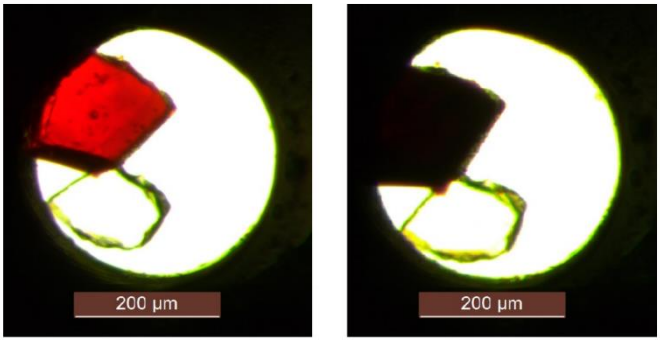

Figure 2.9 - Photograph of a single crystal of **A** loaded in the DAC showing the colour change associated with the pressure induced spin transition: (left) ambient pressure, (right) 5.1(2) kbar.

Examining the change in Fe-N bond lengths between ambient and high pressure 5.1(2) kbar structures (Table 2.2) indicates that **A** undergoes a pressure induced spin transition. While a pressure induced spin transition can produce the same LS structure as that obtained from a thermal spin transition,[39] this is not always the case.[40] Indeed some compounds display a pressure induced spin transition where either no spin transition[15] or only a partial spin transition[41] is observed thermally. In the case of **A**, the application of pressure results in a decrease in the length of all of the cell axes and a reduction in the *β*-angle, this gives an ~8% decrease in the cell volume between ambient pressure and 5.1(2) kbar (Table 2.3). The structure maintained the monoclinic $P2_1/n$ crystal system and space group across the range of pressures measured, as was also observed in the variable temperature studies at ambient pressure. It is worth noting that the cell parameters for the pressure LS structures are compressed compared to the thermal LS cell parameters. The structural features associated with the pressure induced LS structure are similar to the thermal LS structure, although the bond lengths, distortion parameter Σ and V_p at 5.1(2) kbar are very slightly larger than those seen at 120 K. This indicates that the spin transition may

not be fully complete at this pressure; however a partial spin transition has clearly occurred. It is highly likely that at slightly higher pressure the spin transition from HS to LS would be complete. Both the thermal and pressure induced spin transitions result in a darkening of the crystal colour which can clearly be seen between ambient pressure and 5.1(2) kbar (Figure 2.9).

Table 2.3 - Crystal data and refinement results for $[Fe(abpt)_2(NCS)_2]$ polymorph **A** at 296 K in the DAC at ambient pressure, 1.4(2) kbar and 5.1(2) kbar.

	ambient	1.4(2) kbar	5.1(2) kbar
Empirical formula	$C_{26}H_{20}FeN_{14}S_2$	$C_{26}H_{20}FeN_{14}S_2$	$C_{26}H_{20}FeN_{14}S_2$
Formula weight	648.53	648.53	648.53
λ (Å)	0.56086	0.56086	0.56086
Crystal system	Monoclinic	Monoclinic	Monoclinic
Space group	$P\,2_1/n$	$P\,2_1/n$	$P\,2_1/n$
a (Å)	8.552 (3)	8.484(2)	8.3440(15)
b (Å)	10.236(6)	10.159(5)	9.955(3)
c (Å)	16.444(6)	16.253(5)	15.960(3)
β (°)	93.978(11)	93.894(12)	93.414(7)
V (Å^3)	1435.9(10)	1397.7(9)	1323.4(5)
Z	2	2	2
Temperature (K)	296	296	296
D_c (Mg/m^3)	1.500	1.541	1.627
μ (mm^{-1})	0.377	0.387	0.409
F(000)	664	664	664
Crystal size (mm^3)	0.17 x 0.15 x 0.10	0.17 x 0.15 x 0.10	0.17 x 0.15 x 0.10
ϑ range for data collection (°)	3.92 - 41.00	3.96 - 39.47	4.03 - 39.48
Ranges of h, k, l	$-10 \le h \le 10$, $-8 \le k \le 7$, $-20 \le l \le 20$	$-9 \le h \le 9$, $-6 \le k \le 6$, $-19 \le l \le 19$	$-9 \le h \le 9$, $-6 \le k \le 6$, $-19 \le l \le 19$
Refl. collected	9085	5050	4597
R_{int}	0.0343	0.0317	0.0273
Data / parameters	1158/202	921/204	794/202
Absorption coef. min/max	0.939/0.963	0.937/0.962	0.812/0.928
GooF (F^2)	1.130	1.055	1.052
Final R_1 [$I > 2\sigma(I)$]	0.0430	0.0277	0.0229
wR_2 [$I > 2\sigma(I)$]	0.0987	0.0561	0.0492
Largest diff. peak/hole (e Å^{-3})	0.19/-0.22	0.13/-0.12	0.12/-0.10

2.4.6 Variable temperature UV-Vis transmission spectroscopy

Single crystals of $[Fe(abpt)_2(NCS)_2]$ polymorph **A** are red and dark red in the HS and LS states respectively. Normalised single crystal UV-Vis absorption spectra obtained for **A** in the HS state at 298 K and LS state at 83 K (the lowest temperature achievable with the Cryostream) are shown in Figure 2.10. The intense colour in both spin states and the residual HS fraction, γ_{HS}, remaining at low temperature make assignment of absorption bands to particular transitions challenging and beyond the scope of this study. The ligand field (*d*-*d*) transition bands could be partially obscured by low lying intense charge-transfer (CT) bands in the UV-Vis spectral region. At 298 K, the complex is expected to be purely HS.[11] Whether the one featureless band centred at ~505 nm, similar to the broad band at ~500 nm observed for polymorph **D** at 300 K,[13] can be attributed to the spin allowed, parity forbidden $^5T_2 \rightarrow {}^5E$ transition[2] is not yet known and computational studies would need to be carried out to draw further conclusions. The spectra at 83 K may incorporate a contribution from a small residual HS fraction. Two main overlapping bands are visible: one with two peaks at ~535 nm and ~496 nm and a shoulder at ~605 nm and a second band below ~450 nm. The completeness of the spin transition for this particular crystal is unknown; previously reported magnetic data suggest a residual γ_{HS} at low temperature of between 0% and 23% for a single crystal sample depending on the crystallization method used[11, 12] but 4.4% for a precipitated microcrystalline sample.[42] The crystal was repositioned in the beam between collection of HS and LS spectra due to contraction of the crystal mount during cooling; therefore, calculation of the % conversion is not possible. A similar spectrum is observed at 83 K either upon slow cooling (150 K/hr) or flash cooling (Figure 2.10), indicating that thermal trapping of the HS state (TIESST)[43] is not observed at 83 K.

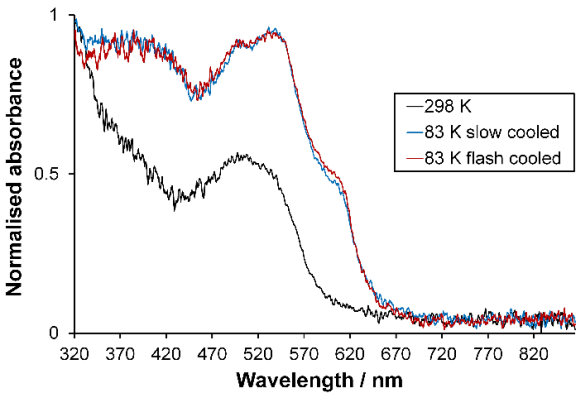

Figure 2.10 - Normalised single crystal UV-Vis absorption spectra collected at 298 K (HS) and 83 K (LS) for $[Fe(abpt)_2(NCS)_2]$ polymorph **A**. The consistency in the spectrum at 83 K independent of cooling strategy is also shown.

2.4.7 Resonant Ultrasound Spectroscopy

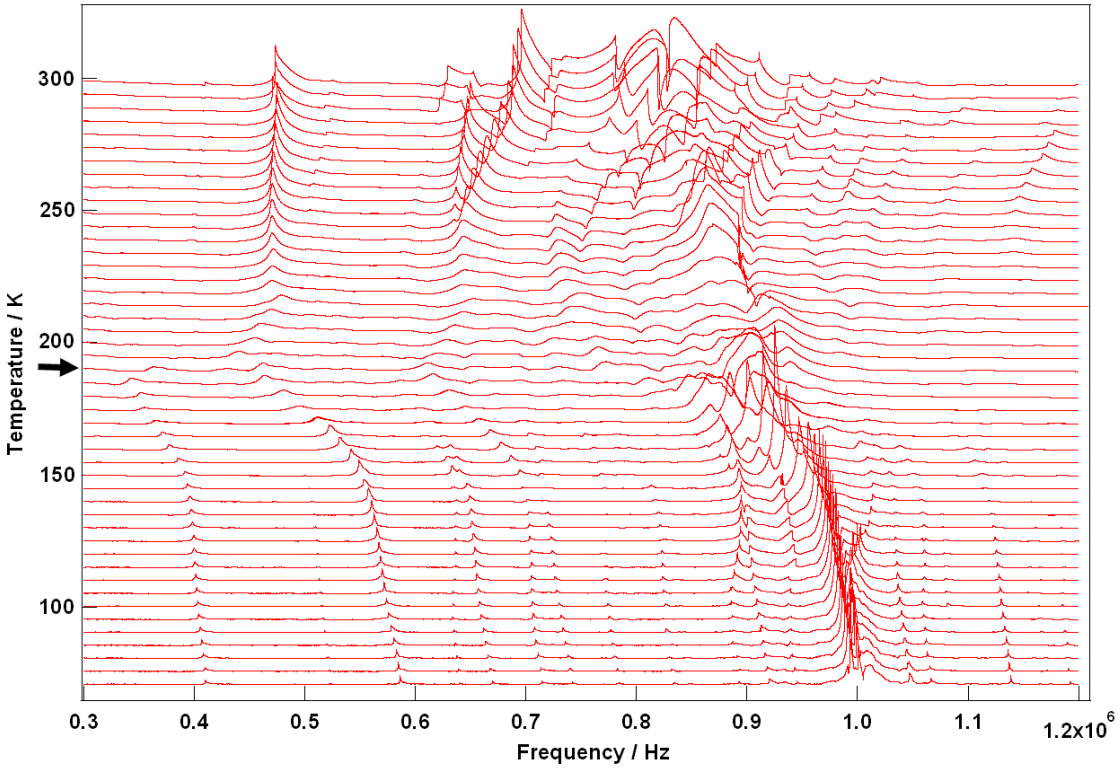

Figure 2.11 - Stack of RUS spectra as a function of frequency for $[Fe(abpt)_2(NCS)_2]$ polymorph **A** from 70 - 300 K, the arrow at around ~190 K indicates the spin crossover transition, $T_{1/2}$ = 188 K.[12]

Selected RUS spectra from the single crystal collected during a heating sequence from 70 - 300 K are illustrated in Figure 2.11. The *y*-axis is real amplitude from the voltmeter but the spectra have been offset in proportion to the temperature at which they were collected and the axis labelled as temperature. Peaks in the spectra which are dependent on temperature reflect the vibrational frequencies of the normal modes of the sample; the square of the frequency of each mode, f^2, is proportional to the elastic constants associated with that mode. The inverse of the mechanical quality factor, Q^{-1}, is a measure of acoustic dissipation (energy loss) in the sample.[35] The raw spectra clearly show a change in trend of peak frequencies near ~190 K, changes in line widths between ~160 and ~220 K, and relatively sharp peaks reappear in the low temperature region (Figure 2.11). Data for f^2 and Q^{-1} obtained from fitting selected peaks in the high temperature region are shown in Figure 2.12 and Figure 2.13. All the resonance peaks have the same form of elastic softening (reducing values of f^2) as $T_{1/2}$ is approached from both above and below, with a minimum at ~190 K corresponding to the known spin crossover transition point $T_{1/2}$ = 188 K[12] for polymorph **A** (Figure 2.12). This is a relaxational effect due to coupling of the spin state variation with strain, as seen also in the variation of lattice parameters with temperature. An applied stress in the mechanical resonance induces a strain which, in turn, results in a change in the spin state, giving rise to additional softening in the temperature interval of the spin crossover. Although one of the effects of changing spin configurations is a change in unit cell volume, the monoclinic symmetry means that there are also shear strains involved and the observed elastic softening is mainly through combinations of shear elastic constants. There is a significant increase in acoustic loss (increasing Q^{-1}) in the vicinity of 200 K which appears to be frequency independent (Figure

2.13). This is due to the strain/spin state relaxations occurring on the time scale of the applied stress, i.e. ~10^{-6} s.

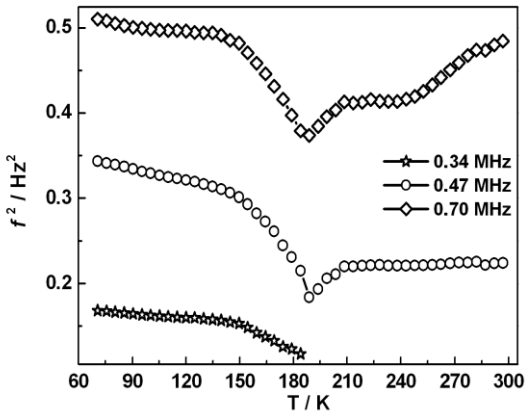

Figure 2.12 - Temperature dependency of *resonance frequencies* from fitting of selected peaks. f^2 scales with combinations of shear elastic constants. The softening is due predominantly to coupling of spin state changes with changes in shear strain of the crystal.

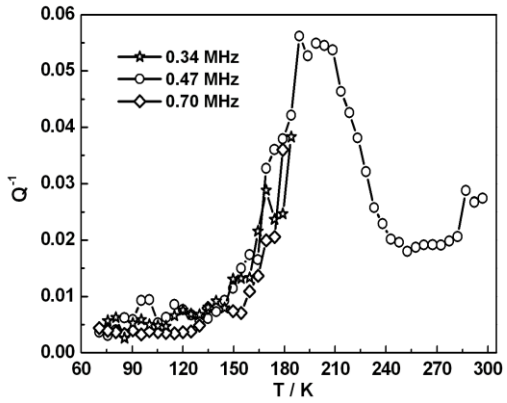

Figure 2.13 - Temperature dependency of Q^{-1} from fitting of selected resonance peaks. The increasing acoustic loss is due to dynamic coupling of strains with spin state relaxations on a time scale commensurate with the resonance frequencies.

2.4.8 A simple model for the strain relaxation behaviour

The strain coupling recognised both from the changes in lattice parameters and from the elastic anomalies is similar to that found in Co oxide phases for which a formal treatment has previously been set out.[44, 45] The spin state transition is first described in terms of an order parameter, q_s, which takes on values between 0 and 1 to represent the proportion of atoms with low spin state. Variations in lattice parameters are represented in terms of coupling between q_s and strains, e_i, which in turn give rise to softening of the elastic constants, C_{ik}. Relationships between the order parameter, strains and elastic constants derive from the change in free energy, G, due to the transition which, for a monoclinic crystal, may be expressed as

$$G = G(q_s) + (\lambda_1 e_1 + \lambda_2 e_2 + \lambda_3 e_3 + \lambda_5 e_5) q_s + \lambda_4 q_s (e_4^2 + e_6^2) + \frac{1}{2} \sum_{i,k} C_{ik}^o e_i e_k . \quad (1)$$

$G(q_s)$ describes the free energy change due to changes in spin state, excluding the contribution of lattice relaxation, and will be some form of partition function. The coupling coefficients, λ_i, describe the strength of coupling between the order parameter and strain, and the last term is the Hooke's law elastic energy. C_{ik}^o represents the elastic constants of the crystal in its high spin state. The equilibrium condition, $\partial G/\partial e = 0$, then gives

$$e_1 \mu e_2 \mu e_3 \mu e_5 \mu q_s, \quad (2)$$

with proportionality constants depending on combinations of λ_i and C_{ik}^o, and

$$e_4 = e_6 = 0. \quad (3)$$

As shown in the supplementary material, values of the strains are defined with respect to the lattice parameters, a_o, b_o,..... of the high spin state, giving $e_1 = \Delta a/a_o$, $e_2 = \Delta b/b_o$ …… Calculated strains obtained from the lattice parameter data are given in full in Appendix 2, Figure S2.3. From the observation that e_1, e_2 and e_3 are approximately equal, it is evident that the negative unit cell volume strain of up to ~4% accompanying the HS* (30 K) – LS (30 K) transition is nearly isotropic. There is however a significant shear strain, e_5, with magnitude of up to ~1.5%. All the strains show the same pattern of variation with temperature, consistent with Equation 2 and a spin transition model which includes the effects of lattice vibrations (e.g. Fig. 6 of Zimmerman and Konig).[46] Figure 2.14a shows the shear strain e_5 and the volume strain $V_s = \Delta V/V_o$ and the latter has been scaled to give the variation of q_s in Figure 2.14b. The variation of q_s is well represented by a sigmoidal function

$$q_s = 1 - \frac{1}{1 + \exp\left(\frac{T_{1/2} - T}{A}\right)}. \quad (4)$$

The fit parameters are $T_{1/2} = 182 \pm 1$ K and $A = 10.1 \pm 0.6$ K, and the transition occurs predominantly between limits of ~130 and ~250 K. Although the fit appears to produce a tightly constrained value of $T_{1/2}$, it is actually highly dependent on a single data point at 192 K and a similar treatment of e_5 gave $T_{1/2} = 199 \pm 2$ K. The Fe-N bond lengths, Fe octahedron volume (V_p) and distortion parameter (Σ) are thought to be representative of the sample's spin state. Fitting a sigmoidal function to each of these parameters gives $T_{1/2}$ values between 183 K and 185 K, see Appendix 2, Figure S2.4. The data are permissive of $T_{1/2} = 188$ K,[12] reported previously.

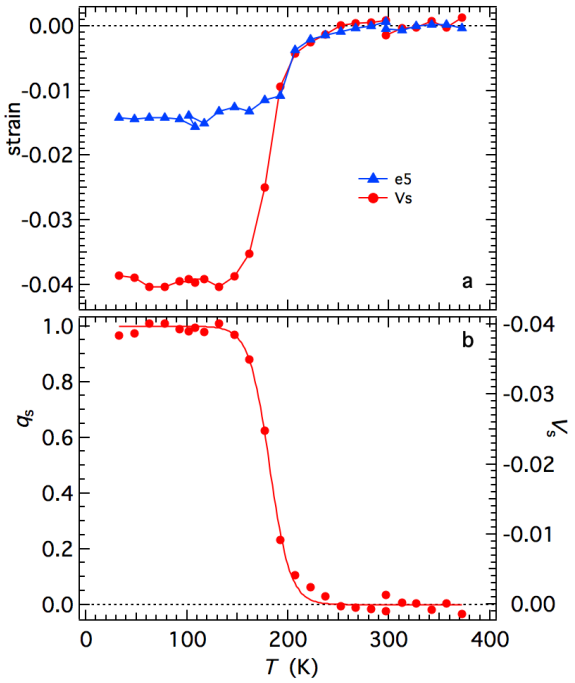

Figure 2.14 - (a) Spontaneous volume and shear strains determined from the lattice parameters, as set out in the ESI. (b) Variation of the volume strain rescaled to values of between 0 and 1 as a representation of the order parameter. The curve is a fit of Equation 4 with $T_{1/2}$ = 182 ± 1 K and A = 10.1 ± 0.6 K.

The variation of elastic constants associated with changes in spin state can in principle be determined from Equation 1, by applying (after Slonczewski and Thomas,[47] Zhang et al).[44]

$$C_{ik} = C_{ik}^{o} - \frac{\partial^2 G}{\partial e_i \partial q_s}\left(\frac{\partial^2 G}{\partial q_s^2}\right)^{-1}\cdot\frac{\partial^2 G}{\partial e_k \partial q_s}. \qquad (5)$$

Strain coupling terms which are of the form $\lambda q_s e$ will contribute to softening of the form

$$C = C^{o} - \Lambda^2\left(\frac{\partial^2 G}{\partial q_s^2}\right)^{-1}, \qquad (6)$$

while terms of the form $\lambda q_s e^2$ will give elastic constant variations of the form

$$C = \frac{\partial^2 G}{\partial e^2} = C^{o} + 2\Lambda q_s. \qquad (7)$$

The difference, Δf^2, between a simple linear baseline and the observed variations of f^2 from one of the resonances corresponds to $C - C^{o}$ and reaches a maximum softening of ~35%. This is expected to be for shear elastic constants and made up of contributions of the form given by both Equations 6 and 7 (including C_{44}, C_{55}, C_{66}). A breakdown into these two contributions is shown in Figure 2.15. The change due to the part proportional to q_s with $T_{1/2}$ taken as the temperature (188 K) where the softening is largest, was subtracted from Δf^2 to give the remainder as the contribution proportional to the susceptibility. Softening of the latter is asymmetric about 188 K and this asymmetry is mirrored also in the acoustic loss, Q^{-1}. The maximum loss and the maximum

value of $(\partial^2 G/\partial q_s^2)^{-1}$ approximately coincide, corresponding to the point at which a given applied stress induces the largest number of changes from one spin state to the other. The bulk modulus would be expected to follow Equation 6 and should show a large softening, with the same form as the susceptibility component.

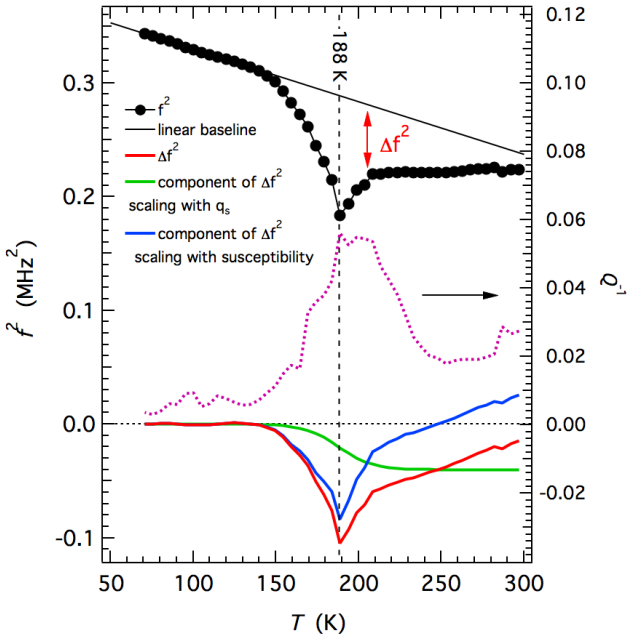

Figure 2.15 - Analysis of elastic softening through the thermal HS to LS spin transition. An estimate of the amount of softening, Δf^2, for one of the resonance modes is given by the difference between a linear baseline and the observed values. This is then shown as being made up of two contributions, one which scales with q_s (green curve) and the remainder which is assumed to scale with $(\partial^2 G/\partial q_s^2)^{-1}$. This is only a semi-quantitative and non-unique solution but it fits with the pattern predicted on the basis of the model represented by Equations 1, 6 and 7.

2.5 Comparison of the four [Fe(abpt)$_2$(NCS)$_2$] polymorphs

As discussed earlier three of the known polymorphs undergo thermal spin crossover at ambient pressure, namely **A**, **C** and **D**. Sheu *et al.*,[12] reported that the value of the distortion parameter (∑) and the volume of the Fe octahedron (V_p) for the HS and LS structures for all of these polymorphs are consistent with the expected values for an octahedral FeN_6 geometry. These polymorphs all contain π-π interactions between uncoordinated and coordinated pyridyl rings of the abpt ligands on adjacent molecules. The shortest π-π separation (at room temperature) is different for each polymorph. For **A**, the centroid to centroid distance is ~3.6 Å with an offset of ~1.3 - 1.4 Å. For **D**, only the abpt ligands on one of the two independent Fe centres are involved in π-π interactions with a centroid to centroid distance of 3.8 Å and an offset of 2.0 Å. In the commensurate modulated structure of **C** at 130 K two of the four unique Fe centres have parallel or near parallel alignment for pairs of uncoordinated and coordinated pyridyl rings on adjacent abpt ligands with centroid to centroid distances of ~3.8 - 4.1 Å and offsets of ~1.7 - 2.0 Å. The presence of intermolecular interactions has often been linked to the occurrence of a spin transition and interestingly in polymorphs **A** and **D** the spin transition only occurs for Fe centres where the abpt ligands are involved in π-π interactions. In **C** the situation is complicated by the commensurate modulated structure prior to the spin transition, but at 130 K there is evidence of π-π interactions and at 25 K it is the Fe(II) centre with parallel alignment of pairs of rings on adjacent abpt ligands

that is LS. In the case of **B**, which undergoes a thermal spin transition at high pressure, π-π interactions are also present between the uncoordinated and coordinated pyridyl rings on adjacent molecules (centroid to centroid distances of 3.7 Å and an offset of 1.1 Å at room temperature). Similar to the Fe centres in **C** and **D** which do not undergo spin crossover at ambient pressure, in **B** the abpt pyridyl group not coordinated to the Fe centre is twisted out of the plane of the rest of the abpt ligand.[12]

All three of the polymorphs that undergo a thermal spin transition at ambient pressure display LIESST. In the case of **C** the LIESST causes the formation of a commensurate modulated phase in which the *c*-axis is tripled,[12, 13] while for **D** upon irradiation at 20 K two photoinduced metastable HS states can be formed, one the standard LIESST structure and the second with linkage isomerism of the NCS group.[14] In the case of **A**, reported here, the LIESST structure formed was not found to be associated with any modulation or linkage isomerism and at 30 K was consistent with the HS structure above the thermal spin transition.

2.6 Conclusions

In summary, the spin crossover behaviour of $[Fe(abpt)_2(NCS)_2]$ polymorph **A** has been structurally characterised. The integrity of the single crystal was maintained throughout the transition enabling structural information to be obtained. This showed that the Fe-N bond lengths change gradually and the molecules distort slightly over the temperature range of the spin transition. π-π interactions exist between adjacent abpt ligands in the crystal allowing potential communication between Fe(II) centres,[12] this could explain the moderately cooperative nature of the spin transition in **A**. In addition to characterising the HS and LS structures of **A**, a LIESST HS* structure was obtained at 30 K which showed a 4% increase in unit cell volume occurred upon irradiation at that temperature. The structural parameters associated with the HS* structure were found to be consistent with those in the 270 K HS structure. It was necessary to irradiate the sample continuously throughout the data collection as the LIESST state relaxes back to the LS ground state within ~4000 s, i.e. during the timeframe of the experiment. It has also been demonstrated that **A** undergoes a pressure induced spin transition resulting in a similar LS structure to that obtained at low temperature. The results of variable temperature UV-Vis spectroscopy and RUS experiments, which show obvious anomalies of both elastic moduli and acoustic dissipation at about 190 K, further confirm the thermal spin crossover transition and demonstrate strong spin-lattice coupling.

2.7 References

1. P. Gütlich, V. Ksenofontov and A. B. Gaspar, *Coord. Chem. Rev.*, 2005, **249**, 1811-1829.
2. A. Hauser, *Light-Induced Spin Crossover and the High-Spin→Low-Spin Relaxation. Spin Crossover in Transition Metal Compounds II, Top. Curr. Chem., 234, 155-198*, Springer-Verlag: Berlin, Heidelberg, New York, 2004.
3. P. Gütlich, A. B. Gaspar and Y. Garcia, *Beilstein Journal of Organic Chemistry*, 2013, **9**, 342–391.
4. M. Nihei, T. Shiga, Y. Maeda and H. Oshio, *Coord. Chem. Rev.*, 2007, **251**, 2606-2621.
5. A. B. Gaspar, M. C. Muñoz, V. Niel and J. A. Real, *Inorganic Chemistry*, 2001, **40**, 9-10.
6. P. Nielsen, H. Toftlund, A. D. Bond, J. F. Boas, J. R. Pilbrow, G. R. Hanson, C. Noble, M. J. Riley, S. M. Neville, B. Moubaraki and K. S. Murray, *Inorganic Chemistry*, 2009, **48**, 7033-7047.
7. P. Gütlich and H. A. Goodwin, eds., *Spin Crossover in Transition Metal Compounds I, II and III*, Springer-Verlag: Berlin, Heidelberg, New York, 2004.
8. M. A. Halcrow, ed., *Spin-Crossover Materials: Properties and Applications*, John Wiley & Sons, Ltd.: Chichester, UK, 2013.

9. M. Griffin, S. Shakespeare, H. J. Shepherd, C. J. Harding, J.-F. Létard, C. Desplanches, A. E. Goeta, J. A. K. Howard, A. K. Powell, V. Mereacre, Y. Garcia, A. D. Naik, H. Müller-Bunz and G. G. Morgan, *Angewandte Chemie International Edition*, 2011, **50**, 896-900.
10. J. Tao, R.-J. Wei, R.-B. Huang and L.-S. Zheng, *Chem. Soc. Rev.*, 2012, **41**, 703-737.
11. N. Moliner, M. C. Muñoz, S. Létard, J. F. Létard, X. Solans, R. Burriel, M. Castro, O. Kahn and J. A. Real, *Inorg. Chim. Acta*, 1999, **291**, 279-288.
12. C.-F. Sheu, S.-M. Chen, S.-C. Wang, G.-H. Lee, Y.-H. Liu and Y. Wang, *Chem. Commun.*, 2009, 7512-7514.
13. C.-H. Shih, C.-F. Sheu, K. Kato, K. Sugimoto, J. Kim, Y. Wang and M. Takata, *Dalton Trans.*, 2010, **39**, 9794-9800.
14. C.-F. Sheu, C.-H. Shih, K. Sugimoto, B.-M. Cheng, M. Takata and Y. Wang, *Chem. Commun.*, 2012, **48**, 5715-5717.
15. A. B. Gaspar, M. C. Muñoz, N. Moliner, V. Ksenofontov, G. Levchenko, P. Gütlich and J. A. Real, *Monatsh. Chem.*, 2003, **134**, 285-294.
16. J.-F. Létard, P. Guionneau, L. Rabardel, J. A. K. Howard, A. E. Goeta, D. Chasseau and O. Kahn, *Inorg. Chem.*, 1998, **37**, 4432-4441.
17. A. E. Goeta, L. K. Thompson, C. L. Sheppard, S. S. Tandon, C. W. Lehmann, J. Cosier, C. Webster and J. A. K. Howard, *Acta Crystallographica, Section C: Crystal Structure Communications*, 1999, **C55**, 1243-1246.
18. Bruker, *SMART-NT, Data Collection Software, Version 5.63, Bruker Analytical X-ray Instruments Inc., Madison, WI, USA*, 2000.
19. Bruker, *SAINT-NT, Data Reduction Software Ver. 6.14, Bruker Analytical X-ray Instruments Inc., Madison, WI, USA*, 2000.
20. Bruker, *SADABS, Bruker AXS area detector scaling and absorption correction, Bruker Analytical X-ray Instruments Inc., Madison, Wisconsin, USA*, 2001.
21. G. M. Sheldrick, *Acta Crystallogr., Sect. A: Found. Crystallogr.*, 2008, **64**, 112-122.
22. O. V. Dolomanov, L. J. Bourhis, R. J. Gildea, J. A. K. Howard and H. Puschmann, *J. Appl. Crystallogr.*, 2009, **42**, 339-341.
23. M. More, G. Odou and J. Lefebvre, *Acta Crystallogr., Sect. B: Struct. Sci.*, 1987, **B43**, 398-405.
24. T. Fukami, S. Akahoshi, K. Hukuda and T. Yagi, *J. Phys. Soc. Jpn.*, 1987, **56**, 2223-2224.
25. P. N. Martinho, B. Gildea, M. M. Harris, T. Lemma, A. D. Naik, H. Müller-Bunz, T. E. Keyes, Y. Garcia and G. G. Morgan, *Angew. Chem., Int Ed.*, 2012, **51**, 12597-12601.
26. M. R. Probert, *SMARTreduce, Durham University, UK*, 2009.
27. G. J. Piermarini, S. Block, J. D. Barnett and R. A. Forman, *Journal of Applied Physics*, 1975, **46**, 2774-2780.
28. M. R. Probert, J. A. Coome, A. E. Goeta and J. A. K. Howard, *Acta Crystallogr., Sect. A: Found. Crystallogr.*, 2011, **A67, Supplement**, C528.
29. M. R. Probert, C. M. Robertson, J. A. Coome, J. A. K. Howard, B. C. Michell and A. E. Goeta, *J. Appl. Crystallogr.*, 2010, **43**, 1415-1418.
30. T. Schulz, K. Meindl, D. Leusser, D. Stern, J. Graf, C. Michaelsen, M. Ruf, G. M. Sheldrick and D. Stalke, *J. Appl. Crystallogr.*, 2009, **42**, 885-891.
31. Bruker, *APEX2, Data Collection Software, Version 1.08, Bruker Analytical X-ray Instruments Inc., Madison, WI, USA*, 2004.
32. Bruker, *SAINT+ Integration Engine, Data Reduction Software, Bruker Analytical X-ray Instruments Inc., Madison, WI, USA*, 2007.
33. S. Parsons, *ECLIPSE, University of Edinburgh, Edinburgh, UK*, 2009.
34. OriginLab, *OriginLab, OriginPro 8, Northampton, MA, USA.*
35. A. Migliori and J. L. Sarrao, *Resonant Ultrasound Spectroscopy: Applications to Physics, Material Measurements and Nondestructive Evaluation*, Wiley, New York, 1997.

36. R. E. A. McKnight, M. A. Carpenter, T. W. Darling, A. Buckley and P. A. Taylor, *American Mineralogist*, 2007, **92**, 1665–1672.
37. P. Gütlich, Y. Garcia and H. A. Goodwin, *Chem. Soc. Rev.*, 2000, **29**, 419-427.
38. V. Legrand, S. Pillet, H.-P. Weber, M. Souhassou, J.-F. Létard, P. Guionneau and C. Lecomte, *J. Appl. Crystallogr.*, 2007, **40**, 1076-1088.
39. H. J. Shepherd, S. Bonnet, P. Guionneau, S. Bedoui, G. Garbarino, W. Nicolazzi, A. Bousseksou and G. Molnár, *Phys. Rev. B: Condens. Matter Mater. Phys.*, 2011, **84**, 145401.
40. V. Legrand, S. Pechev, J.-F. Létard and P. Guionneau, *Phys. Chem. Chem. Phys.*, 2013, **15**, 13872-13880.
41. H. J. Shepherd, P. Rosa, L. Vendier, N. Casati, J.-F. Létard, A. Bousseksou, P. Guionneau and G. Molnár, *Phys. Chem. Chem. Phys.*, 2012, **14**, 5265-5271.
42. N. Moliner, M. C. Muñoz, P. J. van Koningsbruggen and J. A. Real, *Inorg. Chim. Acta*, 1998, **274**, 1-6.
43. M. Marchivie, P. Guionneau, J. F. Létard, D. Chasseau and J. A. K. Howard, *J. Phys. Chem. Solids*, 2004, **65**, 17-23.
44. Z. Zhang, J. Koppensteiner, W. Schranz and M. A. Carpenter, *Am. Mineral.*, 2012, **97**, 399-406.
45. Z. Zhang, J. Koppensteiner, W. Schranz, D. Prabhakaran and M. A. Carpenter, *J. Phys.: Condens. Mat.*, 2011, **23**, 145401.
46. R. Zimmermann and E. König, *J. Phys. Chem. Solids*, 1977, **38**, 779-788.
47. J. C. Slonczewski and H. Thomas, *Phys. Rev. B: Condens. Matter Mater. Phys.*, 1970, **1**, 3599-3608.

Chapter 3

Structural Studies into the Spin Crossover Behaviour of $Fe(abpt)_2(NCS)_2$ Polymorphs B and D

Helen E. Mason, Jake R. C. Musselle-Sexton, Judith A. K. Howard, Michael R. Probert and Hazel A. Sparkes

Published *New Journal of Chemistry*, 2021, **45(31)**, 14014-14023, doi 10.1039/D1NJ02607K. Reproduced with permission for the Royal Society of Chemistry.

3.1 Abstract

The spin-crossover behaviour of $[Fe(abpt)_2(NCS)_2]$ (abpt = 4-amino-3,5-bis(pyridin-2-yl)-1,2,4-triazole) polymorphs **B** and **D** have been studied using single crystal X-ray diffraction to monitor changes in structural features. High pressure single crystal measurements on polymorph **B** showed that it underwent a monoclinic $P2_1/n$ (Z' = 0.5) to triclinic P-1 (Z' = 2 x 0.5) phase transition between 11.5-13.5 kbar. At which point, it also starts to undergo a thermally inaccessible spin crossover. In polymorph **D** which also crystallises in the monoclinic space group $P2_1/n$ (Z' = 2 x 0.5) one of the unique Fe centres undergoes a thermal spin transition. It also displays light-induced excited spin-state trapping (LIESST), and a structure has been obtained at 30 K through continuous irradiation with a 670 nm 5 mW CW laser. In addition high pressure single crystal measurements on polymorph **D** showed a stepped pressure induced spin transition. At ~9.6 kbar one of the unique Fe centres had undergone a spin transition and by ~15 kbar both of the unique Fe centres are shown to be essentially low spin, a situation that is thermally inaccessible. Crystallographic data were collected for both polymorphs using variable temperature or high pressure single crystal X-ray diffraction to allow changes in cell parameters, bond lengths and distortion parameters to be monitored for the spin crossover or phase transitions.

3.2 Introduction

In the 1930s, the first observation of spin crossover was reported.[1] Spin crossover compounds display a reversible high spin (HS) to low spin (LS) transition at a metal centre, which can be induced by external stimuli such as temperature, pressure[2] or light irradiation[3, 4] and can occur in both solution and the solid state. The phenomenon is relatively common for $3d^4$-$3d^7$ metal centres.[5] While many of the spin crossover complexes that have been studied are octahedral Fe(II) complexes with nitrogen[5-10] ligands, other examples include Fe(III)[4, 11-14], Co(II)[15-17] and Ni(II)[18]. The change in electronic structure, as a result of the spin crossover, can result in changes in properties including molecular structure, colour and magnetism.[19] These property changes give rise to a number of potential applications including molecular switches, data storage or sensors.[20-24] There are significant challenges in developing materials for commercial applications as spin crossover is a very complex process. The manner in which the transition occurs e.g. gradual or abrupt, stepped, with or without hysteresis can also affect potential uses. Spin crossover in solution tends to result in a gradual transition as there is no cooperativity between molecules. In the solid state, where cooperativity is possible, a much wider range of transitions are seen. Where strong cooperativity exists between molecules the transitions can be abrupt and show hysteresis or without cooperativity transitions tend to be more gradual and without hysteresis. They can also be full transitions, partial or multi-stepped transitions.[25] A large number of factors influence the spin crossover behaviour of a compound e.g. inclusion of solvent in the lattice,[8] polymorphism or intermolecular interactions.[19] It is therefore important to gain as much insight into the phenomena to allow accurate design and control of potential devices. A number of X-ray diffraction studies have been carried out into the spin crossover behaviour of various compounds to help gain insights into the structure property relationships affecting spin crossover complexes.

These have included variable temperature measurements to follow thermally induced structural changes, *in-situ* light irradiation to obtain and characterise Light Induced Excited Spin State Trapping (LIESST) states and high-pressure studies looking at changes upon the application of pressure.[3, 6, 26-30] Alongside magnetic measurements and X-ray diffraction, other techniques[31, 32] including Mossbauer spectroscopy[33] and differential scanning calorimetry[34] can also be used to give useful insights into the behaviour of spin crossover complexes.

In addition to spin crossover complexes with single metal centres, dimeric[10] and polymeric species have also been developed that show spin crossover behaviour. Having more than one metal centre linked can allow for increased cooperativity between the metal centres potentially raising T_c and resulting in hysteresis. Most potential applications require a T_c around room temperature and for applications such as data storage there also needs to be hysteresis. There is therefore much interest in preparing spin-crossover complexes with more than one metal centre. Recently a series of three novel 3D coordination polymers containing Fe(II) metal centres with AgCN linkers have been prepared and found to display spin crossover behaviour.[34] These showed thermal spin crossover with T_c ranging from 240-250K with no hysteresis. The lack of hysteresis was attributed to the relatively long linker distances between the Fe centres having reduced the cooperativity. However, coordination polymers have also been shown to display hysteresis with a particularly exciting set of 1D coordination polymers containing Fe(II), a tetradentate $N_2O_2^{2-}$ and N-(pyrid-4-yl)isocnicotinamide, showing wide, repeatable hysteresis loops, ranging from 46-88 K, around room temperature.[35]

Spin crossover is a complex process so $[Fe(abpt)_2(NCS)_2]$ (abpt = 4-amino-3,5-bis(pyridin-2-yl)-1,2,4-triazole), which has four reported polymorphs (**A**-**D**) all showing slightly different spin crossover behaviour, is a particularly interesting compound to study to try and obtain insights into the phenomenon.[36] Three of the polymorphs **A**,[37-39] **C**[39, 40] and **D**[39, 41] undergo at least a partial thermal spin transition at ambient pressure while the fourth polymorph **B** only undergoes a thermal spin transition at pressures > 4.4 kbar.[42] Polymorph **A** has one independent Fe(II) centre (Z' = 0.5) in the asymmetric unit which undergoes a thermal spin transition without hysteresis, $T_{1/2}$ was initially reported as 180 K,[37] but has been remeasured as $T_{1/2}$ = 188 K.[39] **A** also displays LIESST (light induced excited spin state trapping) T_{LIESST} = 40 K, for which a significant proportion of the HS* state can be maintained for > 1000 s up to 30 K. Although the thermally induced spin crossover shows no hysteresis, a light induced thermal hysteresis (LITH) associated with the HS* state has been identified from the photomagnetic data.[37] Crystal structures of the high spin (HS), low spin (LS) and LIESST HS* (30 K) have all been determined and changes in crystallographic parameters across the temperature range 375 K to 30 K reported.[38] It has also been shown crystallographically that **A** undergoes a pressure induced spin crossover, as demonstrated by a structure at 5.1(2) kbar. The exact point of the pressure induced spin transition has not been determined as it is challenging to accurately control the pressure increase in the diamond anvil cells used for high pressure crystallography.[38] For **C** which has two independent Fe(II) centres in the asymmetric unit (Z' = 2 x 0.5) , only one of the unique Fe centres undergoes a thermal spin transition $T_{1/2}$ = 86 K upon cooling.[40] The thermal behaviour of **C** is actually more complicated than a simple thermal spin transition as the method of cooling affects the results obtained: on gradual cooling between 170 and 86 K a tripling of the *c* axis is associated with the formation of a commensurate modulated structure containing four independent Fe(II) centres in the asymmetric unit (Z' = 2 x 1 + 2 x 0.5). Further cooling below $T_{1/2}$ results in the *c* axis being similar in magnitude to its value above 170 K. Flash cooling of **C** to 25 K results in the formation of a TIESST (thermal induced excited spin state trapping) state which has a tripling of the *c* axis and forms a commensurate modulated structure as observed between 170 and 86 K. **C** also displays LIESST again forming the same commensurate modulated structure just discussed. Polymorph **D** also contain two unique Fe(II) centres in the asymmetric unit (Z' = 2 x 0.5), one of which undergoes a

gradual partial thermal spin transition, $T_{1/2}$ = 162 K.[39] Above and below the transition the Fe centres are HS/HS and HS/LS respectively and the structures of these have previously been reported.[41] As with the other two polymorphs that display a thermal spin transition at ambient pressure, the LS Fe centre in **D** has also been shown to display LIESST using a 532 nm laser at 20 K.[41] The nature of the LIESST HS* structure obtained depends on the laser power used, with a 5mW cm^{-2} powered laser the Fe-N bond lengths increase by ~0.2 Å as commonly observed, however a higher powered 40mW cm^{-2} laser more unusually also results in linkage isomerism of the NCS ligands at the Fe centre that undergoes the spin transition. The refined occupancies suggest that 80% of the NCS ligands on this iron centre displayed linkage isomerism, which agreed with that estimated from photomagnetic measurements.[41] Such difference in the behaviour under different types of irradiation have the potential to be useful for tuning responses in applications.

It is also worth noting that $[Fe(abpt)_2(NCSe)_2]$ has been found to have two polymorphs **A**[37, 43] and **B**[42] which are isostructural with the respective $[Fe(abpt)_2(NCS)_2]$ polymorphs. The known spin crossover behaviour is also very similar for the NCS and NCSe polymorphs. In the case of the NCSe polymorph **A** it is known to display a thermally induced spin crossover $T_{1/2}$ = 224 K, with a slightly higher than for the NCS polymorph, as well as LIESST. While in both cases for **B** no thermal spin crossover was observed. High pressure studies have not been carried out for the NCSe polymorphs, so no comparison of the pressure behaviour is possible.

The pressure behaviour of $[Fe(abpt)_2(NCS)_2]$ **B** and **D** at room temperature has not been previously reported and are studied using high pressure single crystal crystallography herein. In addition, the thermal behaviour of **D** is followed crystallographically from 375 to 30 K, examining changes in the cell parameters, Fe-N bond lengths, distortion parameter (Σ) and the octahedron volume (Vp). These results are compared to those obtained in the high pressure experiments.

3.3 Experimental

3.3.1 Synthesis

Synthesis of $[Fe(abpt)_2(NCS)_2]$ was carried out using a slow diffusion method which was previously reported to produce crystals of the various polymorphs.[39] Precursor materials were used without further purification, solvents degassed and all manipulations carried out under a nitrogen atmosphere. $FeSO_4.7H_2O$ (1 mmol, 0.278 g) and KNCS (2 mmol, 0.194 g) were stirred in MeOH (10 ml) for 15 min. Pale yellow insoluble K_2SO_4 precipitate was removed by filtration and deionised H_2O (10 ml) added to the remaining clear solution. abpt ligand (2 mmol, 0.477 g) was dissolved in MeOH (20 ml) and transferred to a narrow (<5 cm) Schlenk tube. The $Fe^{2+}/2(NCS)^-$ solution was carefully injected underneath the abpt solution to form a lower layer. A coloured band containing the target complex immediately formed at the interface between the two layers. Within 1-4 weeks single crystals of **B** and **D** suitable for X-ray diffraction studies were formed and separated under the microscope.[39]

3.3.2 X-ray Crystallography

3.3.2.1 Variable temperature and LIESST measurements

X-ray diffraction data were collected on a Bruker Smart 1K CCD diffractometer or an Oxford Diffraction Gemini diffractometer using Mo-*Kα* (λ = 0.71073 Å) radiation. Datasets below 105 K were collected using an Oxford Cryosystems HeliX,[44] while those above 105 K were collected using an Oxford Instruments open flow N_2 Cryostream for cooling. Data collection was carried out using the SMART software,[45] integration was performed using SAINT[46, 47] and multi-scan absorption

corrections were applied to all datasets using SADABS.[48] The structures were solved by direct methods in SHELXS[49] or charge flipping in Superflip[50, 51] and refined by full matrix least squares on F^2 in SHELXL[49] using the Olex2[52] interface. All non-hydrogen atoms were refined anisotropically and all hydrogen atoms were located geometrically and refined using a riding model with the exception of the hydrogen atoms on N6 which were located in the Fourier difference map. The LIESST structure of D at 30 K was obtained by irradiating the crystal *in-situ* using a 670 nm 5 mW CW laser. The crystal was irradiated for 60 minutes prior to and also continued throughout the data collection. Full structure determinations for **B** were made at 300 and 100 K and for **D** at twelve temperatures between 300 and 30 K. The crystal structure and refinement details are given in Tables S3.1 and S3.2. The data have been deposited with the Cambridge Crystallographic Data Centre for entry into the Cambridge Structural Database, CCDC numbers 2086314-2086340.

3.3.2.2 High pressure

For both **B** and **D** the following procedure was used for the high pressure single crystal measurements. A single crystal of each polymorph was mounted along with a small ruby chip in a modified Merrill-Bassett type diamond anvil cell (DAC) custom built at Durham University using tungsten carbide backing plates, with an opening angle of 85° and type IA Boehler-Almax diamond anvils with 0.8 mm cutlets. Stainless steel gaskets were pre-indented and drilled to give a gasket chamber of ~0.3 mm diameter and 0.15 mm depth, with paraffin oil as the pressure transmitting medium. The Ruby R_1 fluorescence method was used to determine the pressure in the DAC,[53] to ensure that the cell pressure had equilibrated prior to data collection fluorescence measurements were taken before and after each data collection to ensure the pressure had not changed. Exposure of the cell to the laser used for the fluorescence measurements was kept to a minimum as the laser can induce a metastable LIESST spin transition, however since the pressure measurements are almost always taken above T_{LIESST} any structural change would not be long lived so should not affect the results. The pressure in the DAC is increased by tightening screws on the cell, hence it is not possible to accurately control the extent of the pressure increase each time. In the case of **B** pressure measurements were made at ambient pressure, 9.0(2), 11.5(2), 13.5(2), 16.0(2) and 23.4(2) kbar while for **D** pressure measurements were made at ambient pressure, 1.8(2), 7.5(2), 9.6(2), 12.0(2) and 15(2) kbar. All measurements were made at room temperature. All data collections were carried out using XIPHOS II,[54] part of the XIPHOS diffraction facility.[55] This diffractometer, custom built for high pressure studies, is equipped with an Incoatec Ag-Kα (λ = 0.56086 Å) IμS source.[56] The data collections were carried out using the Bruker APEX2 software suite,[57] integration was performed using SAINT[46] and multi-scan absorption corrections were applied to all datasets using SADABS.[48] Masking for the diamond anvil cell occluded regions of the data collections was performed within the integration software. The structures were solved using the dual space methods employed within SHELXT and refined by full matrix least squares on F^2 in SHELXL[49] using the Olex2[52] graphical interface. All of the non-hydrogen atoms were refined anisotropically and all hydrogen atoms were located geometrically and refined using a riding model with the exception of the hydrogen atoms on N6 which were located in the difference map. Crystal structure and refinement details are given in Tables 3.1 and 3.2, Appendix 3, Tables S3.1 and S3.3.

Table 3.1 – Selected crystal data and refinement results for $[Fe(abpt)_2(NCS)_2]$ polymorph **B** at 300(2) K, 100(2) K, ambient, 13.5(2) kbar and 23.4(2) kbar.

Spin state	HS 300(2) K	HS 100(2) K	HS ambient, 296 K
Crystal system	monoclinic	monoclinic	monoclinic
Space group	$P2_1/n$	$P2_1/n$	$P2_1/n$
a/Å	11.5730(6)	11.47261(8)	11.5739(6)
b/Å	9.6589(5)	9.58685(8)	9.6588(8)
c/Å	12.8541(7)	12.72647(10)	12.8455(9)
α/°	90	90	90
β/°	101.2740(10)	100.5225(7)	101.244(4)
γ/°	90	90	90
Volume/Å^3	1409.14(13)	1376.197(18)	1408.44(17)
Z	2	2	2
λ / Å	MoKα (λ = 0.71073)	MoKα (λ = 0.71073)	AgKα (λ = 0.56086)
2θ range for data collection/°	4.334 - 52.744	5.286 - 52.726	3.422 - 47.228
Reflections collected	8218	44396	20877
R_{int} / R_{sigma}	0.0205 / 0.0222	0.0342 / 0.0113	0.0557 / 0.0446
Data / restraints / parameters	2875/0/202	2806/0/202	2101/0/202
Goodness-of-fit on F^2	1.029	1.073	1.081
Final R indexes [I>=2σ (I)]	R_1 = 0.0283, wR_2 = 0.0717	R_1 = 0.0221, wR_2 = 0.0552	R_1 = 0.0387, wR_2 = 0.0924
Final R indexes [all data]	R_1 = 0.0352, wR_2 = 0.0754	R_1 = 0.0229, wR_2 = 0.0556	R_1 = 0.0800, wR_2 = 0.1159
Largest diff. peak/hole / e Å^{-3}	0.19/-0.20	0.26/-0.25	0.25/-0.25

Table 3.1 continued – Selected crystal data and refinement results for $[Fe(abpt)_2(NCS)_2]$ polymorph **B** at 300(2) K, 100(2) K, ambient, 13.5(2) kbar and 23.4(2) kbar.

Spin state	HS 13.5(2) kbar, 296 K	LS 23.4(2) kbar, 296 K
Crystal system	triclinic	triclinic
Space group	*P*-1	*P*-1
a/Å	9.2535(13)	8.985(4)
b/Å	11.3483(8)	11.328(3)
c/Å	12.2374(15)	12.013(5)
α/°	101.283(7)	101.89(2)
β/°	90.790(8)	92.74(3)
γ/°	90.653(9)	91.31(3)
Volume/Å^3	1260.0(3)	1194.4(8)
Z	2	2
λ / Å	AgKα (λ = 0.56086)	AgKα (λ = 0.56086)
2θ range for data collection/°	2.888 - 45.82	2.9 - 47.216
Reflections collected	17608	6813
R_{int} / R_{sigma}	0.0564 / 0.0445	0.0679 / 0.0866
Data / restraints / parameters	1985/346/375	1305/346/363
Goodness-of-fit on F^2	1.060	1.075
Final R indexes [I>=2σ (I)]	R_1 = 0.0399, wR_2 = 0.0994	R_1 = 0.0514, wR_2 = 0.1196
Final R indexes [all data]	R_1 = 0.0699, wR_2 = 0.1127	R_1 = 0.0980, wR_2 = 0.1373
Largest diff. peak/hole / e Å^{-3}	0.20/-0.21	0.23/-0.27

Table 3.2 - Crystal data and refinement results for $[Fe(abpt)_2(NCS)_2]$ polymorph **D** at 270 K, 30 K and 30 K after irradiation, along with ambient, 9.6(2) kbar and 15.0(2) kbar.

Spin state (Fe1/Fe2)	HS HS 300 K	HS/LS 30 K	HS/HS* LIESST 30 K
Crystal system	monoclinic	monoclinic	monoclinic
Space group	$P2_1/c$	$P2_1/c$	$P2_1/c$
a/Å	10.8097(3)	10.8082(4)	10.7016(4)
b/Å	15.9326(4)	15.6979(5)	15.9017(6)
c/Å	17.4617(5)	16.9850(6)	17.1557(6)
β/°	106.8470(10)	107.6180(10)	106.0400(10)
Volume/Å^3	2878.30(14)	2746.61(17)	2805.79(18)
Z	4	4	4
λ / Å	MoKα (λ = 0.71073)	MoKα (λ = 0.71073)	MoKα (λ = 0.71073)
2θ range for data collection/°	3.532 - 52.744	3.614 - 52.734	3.558 - 52.742
Reflections collected	23130	31139	22558
R_{int} / R_{sigma}	0.0340 / 0.0298	0.0363 / 0.0245	0.0357 / 0.0312
Data/restraints/parameters	5880/1/407	5621/0/403	5744/0/403
Goodness-of-fit on F^2	1.018	1.039	1.029
Final R indexes [I>=2σ (I)]	R_1 = 0.0340, wR_2 = 0.0792	R_1 = 0.0279, wR_2 = 0.0646	R_1 = 0.0293, wR_2 = 0.0682
Final R indexes [all data]	R_1 = 0.0505, wR_2 = 0.0864	R_1 = 0.0336, wR_2 = 0.0673	R_1 = 0.0379, wR_2 = 0.0719
Largest diff. peak/hole / e Å^{-3}	0.20/-0.28	0.34/-0.45	0.36/-0.38

Table 3.2 continued - Crystal data and refinement results for $[Fe(abpt)_2(NCS)_2]$ polymorph **D** at 270 K, 30 K and 30 K after irradiation, along with ambient, 9.6(2) kbar and 15.0(2) kbar.

Spin state (Fe1/Fe2)	HS/HS ambient, 296 K	Mainly HS/LS 9.6(2) kbar, 296 K	LS/LS 15.0(2) kbar, 296 K
Crystal system	monoclinic	monoclinic	monoclinic
Space group	$P2_1/c$	$P2_1/c$	$P2_1/c$
a/Å	10.7819(15)	10.6923(8)	10.4607(17)
b/Å	15.870(4)	15.3683(18)	15.203(4)
c/Å	17.415(3)	16.4865(12)	16.348(3)
β/°	106.875(10)	107.682(4)	105.886(11)
Volume/Å^3	2851.7(9)	2581.1(4)	2500.7(9)
Z	4	4	4
λ / Å	AgKα (λ = 0.56086)	AgKα (λ = 0.56086)	AgKα (λ = 0.56086)
2θ range for data collection/°	2.796 - 39.206	2.926 - 39.064	2.94 - 39.182
Reflections collected	15847	22491	13610
R_{int} / R_{sigma}	0.0858 / 0.0948	0.0599 / 0.0403	0.0727 / 0.0687
Data/restraints/parameters	2524/346/403	2669/346/403	2354/346/393
Goodness-of-fit on F^2	1.047	1.084	1.085
Final R indexes [I>=2σ (I)]	R_1 = 0.0821, wR_2 = 0.1916	R_1 = 0.0498, wR_2 = 0.1220	R_1 = 0.0735, wR_2 = 0.1762
Final R indexes [all data]	R_1 = 0.1318, wR_2 = 0.2231	R_1 = 0.0705, wR_2 = 0.1343	R_1 = 0.1088, wR_2 = 0.1986
Largest diff. peak/hole / e Å^{-3}	0.48/-0.42	0.31/-0.34	0.46/-0.52

3.4 Results

3.4.1 Polymorph B and D structural features

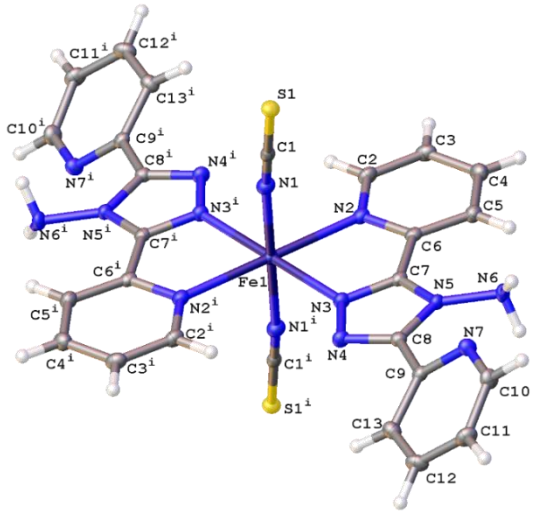

Figure 3.1 - Structure of **B** with the atomic numbering scheme depicted at 100(2) K. Thermal ellipsoids depicted at the 50% probability level. Symmetry code ^{i} = 1-*x*, 1-*y*, 1-*z*.

The structures obtained here at 300 K are consistent with the previously published structures for the polymorphs. Polymorph, **B**, crystallises in the monoclinic space group $P2_1/n$ with half a molecule in the asymmetric unit ($Z' = 0.5$) due to the central Fe sitting on an inversion centre, Figure 3.1. While Polymorph **D** crystallises in the monoclinic space group $P2_1/c$ and has 2 x 0.5 molecules in the asymmetric unit so there are two unique Fe centres, see Figure 3.2. However, the main structural features of the two polymorphs are very similar. The Fe(II) centres are in approximately octahedral Fe-N_6 coordination geometry, with the six coordinated nitrogen atoms: one from each NCS group and two from each abpt ligand (one pyridyl nitrogen and one triazole nitrogen). The structures contain intramolecular N-H···N hydrogen bonding interactions existing between the NH_2 group attached to the triazole and the N of the free pyridyl, and intramolecular C-H···N interactions between a pyridyl C-H and the N of the NH_2 group attached to the triazole and a pyridyl C-H and the uncoordinated N on the triazole (Table 3.3). In addition, there are weak π-π interactions existing between pairs of counterpart abpt pyridyl groups on adjacent molecules. For Polymorph **B** centroid (N2, C2-C6) to centroid (N7#1, C9#1-C13#1, #1 = ½+*x*, $^{3}/_{2}$-*y*, ½+*z*) distance ~3.7 Å with an offset of ~1.3 Å at 300(2) K, while for Polymorph **D** only Fe2 is involved in weak π-π interactions with the centroid (N9, C15-C19) to centroid (N14#2, C22#2-C26#2, #2 = -*x*, ½+*y*, ½-*z*) distance ~3.8 Å, offset distance ~2.0 Å at 300(2) K. At 300(2) K the Fe-N bond lengths, distortion parameter and octahedron volume are consistent with those associated with a HS Fe centre for both polymorphs.

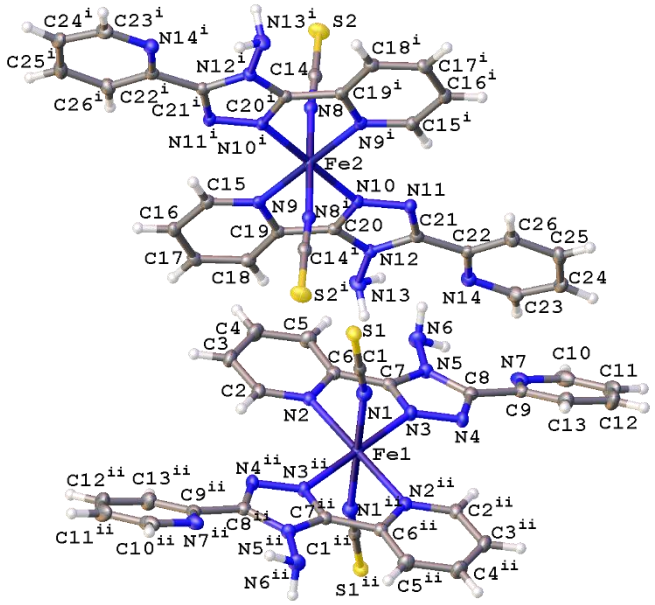

Figure 3.2 - Structure of **D** with the atomic numbering scheme depicted at 100(2) K. Thermal ellipsoids depicted at the 50% probability level. Symmetry codes [i] = -*x*, 1-*y*, 1-*z*, [ii] = -*x*, 1-*y*, -*z*.

Table 3.3 – Hydrogen bonding $[Fe(abpt)_2(NCS)_2]$ polymorph **B** and **D** at 300(2) K.

	D-H / Å	H···A / Å	D···A / Å	D-H···A / °
Polymorph **B**				
N6-H6B···N7	0.86(2)	2.45(2)	2.912(2)	114.6(17)
C2-H2···N4^{i}	0.93	2.83	3.629(2)	144.7
C5-H5···N6	0.93	2.46	3.070(2)	123.7
Polymorph **D**				
N6-H6B···N7	0.88(3)	2.12(2)	2.862(3)	141(2)
N13-H13B···N14	0.80(2)	2.38(2)	2.864(3)	120(2)
C2-H2···N4^{ii}	0.93	2.81	3.605(3)	144.1
C5-H5···N6	0.93	2.48	3.090(3)	122.9
C15-H15···N11^{iii}	0.93	2.77	3.582(3)	145.9
C18-H18···N13	0.93	2.43	3.042(3)	123.4

[i]1-*x*,1-*y*,1-*z*, [ii] *x*,1-*y*,-*z*; [iii] -*x*,1-*y*,1-*z*

3.4.2 Polymorph B thermal behaviour

In line with the magnetic data for Polymorph **B** no thermal spin transition was observed upon cooling from 300(2) to 100(2) K, at ambient pressure, and the structures obtained at these temperatures were essentially identical to the published structure reported at 293(2) K.[42] It is however known that **B** does undergo a thermal spin transition above 4.4 kbar.[42]

3.4.3 Polymorph B pressure induced spin crossover

The study carried out here monitored the structure of polymorph **B** upon the application of pressure at room temperature, with structures reported between ambient pressure and 23.4(2) kbar. The unit cell parameters are provided in Table 3.1, Appendix 3, Table S3.1 and Figure S3.1.

Up to a pressure of 11.5(2) kbar reductions in the length of all of the cell axes are observed which results in an ~8.8% decrease in the cell volume. However, the key structural features for **B** up to this pressure are essentially consistent with those already described at 300(2) K and the parameters associated with the Fe centre indicate that it is HS, Table 3.4 and Appendix 3, Table S3.1.

Somewhere between 11.5(2) and 13.5(2) kbar the crystal undergoes a phase transition from monoclinic to triclinic (*P*-1). The cell axes at 13.5(2) kbar are similar in magnitude to those obtained at ambient pressure (with *a* and *b* switched in line with cell conventions) however the initial monoclinic *α* and *γ* cell angles (*β* and γ respectively in the triclinic cell) have distorted significantly away from 90° hence the triclinic cell. The phase transition results in an increase in the number of molecules in the asymmetric unit from *Z'* = 0.5 (ambient pressure) to *Z'* = 2 x 0.5 (13.5(2) kbar). The phase transition occurs within a single crystal so despite the reduction in symmetry it is not surprising that the overall structure is still very similar to the 300(2) K structure discussed previously. However, with the phase change is the start of a spin crossover with a reduction in the Fe-N bond lengths for the system with one of the Fe centres undergoing a significantly larger change than the other at this stage, 0.02-0.04 Å (Fe1) and 0.07-0.08 Å (Fe1'). Alongside the change in the Fe-N bond length there is also a reduction in the distortion parameter (Σ) and octahedron volume (V_p) which is commonly observed for spin crossover compounds. As expected larger reductions are observed for Fe1' than Fe1, due to the spin crossover having progressed further, see Figure 3.3, Table 3.4 and Appendix 3, Table S3.1.

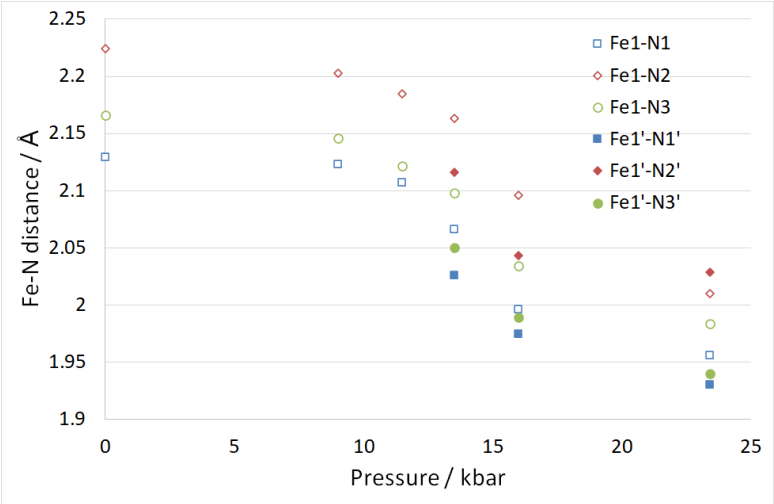

Figure 3.3 - Change in Fe-N bond length for **B** as a function of pressure. At 13.5 kbar and above there were two unique Fe centres, the second of which has been given the solid filled markers.

Table 3.4 - Fe-N bond lengths for **B**, along with the distortion parameter Σ and the volume of the Fe octahedron V_p. Below 13.5(2) kbar there is only one unique Fe centre.

	300K	100K	ambient	9.0(2) kbar
Fe1-N1 (Å)	2.1310(16)	2.1309(11)	2.129(3)	2.123(3)
Fe1-N2 (Å)	2.2235(15)	2.2173(11)	2.224(3)	2.203(3)
Fe1-N3 (Å)	2.1631(13)	2.1610(10)	2.166(2)	2.146(2)
Fe1 Σ[a] (º)	76.5(4)	77.5(3)	77.7(8)	84.3(8)
Fe1 V_p[b] (Å^3)	13.168(6)	13.137(4)	13.168(11)	12.896(9)

[a] Σ, the distortion parameter is the sum of the absolute value of the deviation of all 12 cis N-Fe-N angles from 90°. [b] V_p is the volume of the Fe octahedron calculated in Olex2.[52]

Table 3.4 continued - Fe-N bond lengths for **B**, along with the distortion parameter Σ and the volume of the Fe octahedron V_p. Below 13.5(2) kbar there is only one unique Fe centre.

	11.5(2) kbar	13.5(2) kbar	16.0(2) kbar	23.4(2) kbar
Fe1-N1 (Å)	2.107(3)	2.066(4)	1.996(4)	1.956(11)
Fe1-N2 (Å)	2.185(3)	2.163(12)	2.096(11)	2.01(2)
Fe1-N3 (Å)	2.122(2)	2.098(5)	2.034(4)	1.984(7)
Fe1'-N1' (Å)	-	2.026(12)	1.975(10)	1.93(2)
Fe1'-N2' (Å)	-	2.116(5)	2.043(5)	2.029(11)
Fe1'-N3' (Å)	-	2.050(5)	1.989(5)	1.940(11)
Fe1 Σ[a] (º)	82.2(7)	82(2)	71(2)	60(4)
Fe1 V_p[b] (Å^3)	12.601(9)	12.10(3)	11.09(2)	10.25(4)
Fe1' Σ[a] (º)	-	70(2)	66(2)	55(4)
Fe1' V_p[b] (Å^3)	-	11.43(2)	10.49(2)	9.96(5)

[a] Σ, the distortion parameter is the sum of the absolute value of the deviation of all 12 cis N-Fe-N angles from 90°. [b] V_p is the volume of the Fe octahedron calculated in Olex2.[52]

Increasing the pressure in the DAC further to 23.4(2) kbar resulted in further reductions in the length of the cell axes and increases in all of the cell angles which results in the cell volume being

~15% smaller than at ambient pressure. The structure is still very similar to that observed at ambient pressure but it was noted that there were differences in the two unique molecules. The angle calculated between planes through the two 6 membered rings on the same ligand changed from 35.1(1)° at ambient pressure to 38.3(5)° (Fe1) and 32.0(6)° (Fe1'). Nonetheless both of the unique Fe centres appear to have undergone a spin transition from HS towards LS, with the Fe-N bond lengths now ranging from 0.14-0.18 Å shorter than at ambient pressure. Usually a reduction of ~0.2 Å is observed for a complete transition so it is possible that the transition is not quite complete. The distortion parameter and octahedron volume have also decreased significantly towards those expected for a LS Fe centre. This indicates that **B** has undergone a thermally inaccessible spin transition (Table 3.4). Given the isostructural nature with the $[Fe(abpt)_2(NCSe)_2]$ polymorph **B**,[42] it would be interesting to establish whether $[Fe(abpt)_2(NCSe)_2]$ polymorph **B** also undergoes a pressure induced spin crossover.

3.4.4 Polymorph D thermal spin crossover and LIESST

Upon cooling one of the unique Fe centres, Fe2, undergoes a spin transition, $T_{1/2}$ = 162 K,[39] and the HS/HS (room temperature) and HS/LS (90 K and 20 K) structures have previously been reported.[41] The LIESST HS* structure for polymorph **D** has also been previously reported using both a 532 nm, 5 mW laser and a 532 nm, 40 mW laser at 20 K.[41]

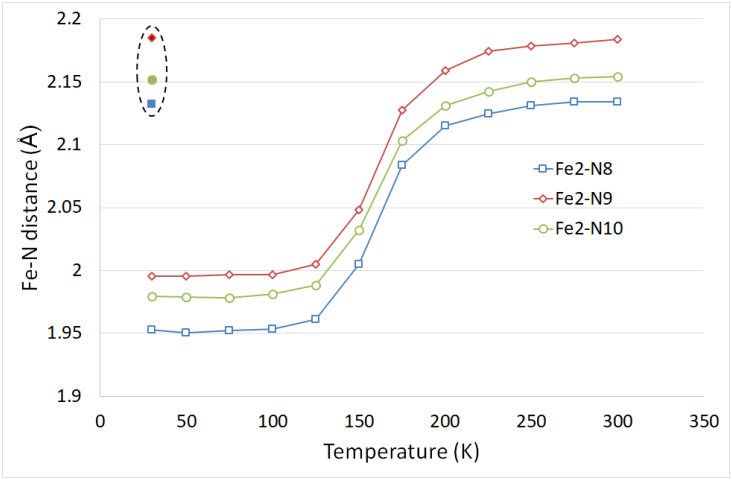

Figure 3.4 - Fe2-N bond length changes in **D** as a function of temperature, LIESST values are contained within the dashed oval. Error bars are not included as they are essentially obscured by the data markers.

In the study reported herein, the structural parameter changes upon cooling are monitored upon cooling from 300 to 30 K. Whilst the *a* axis length does not change significantly as a result of the spin crossover, upon cooling there are small decreases in the *b* and *c* axes lengths and a small increase in the *β* angle, which results in an ~4.5% decrease in the cell volume across the temperature range, see Table 3.2, Appendix 3, Table S3.2 and Figure S3.2. Typically, the Fe centre (Fe2) which undergoes the spin crossover showed a decrease of ~0.18 Å in the Fe2-N bond lengths and a reduction in the distortion parameter (Σ) of ~15° and in the octahedron volume (V_p) of ~2.8 $Å^3$ (Figure 3.4 and Table 3.5). These values are in line with those seen for Polymorph **A**[38] or other Fe-N spin crossover compounds.[19] No significant changes were observed in the parameters associated with Fe1 which does not undergo a spin transition upon cooling.

Table 3.5 - Fe-N bond lengths for **D**, along with the distortion parameter Σ and the volume of the Fe octahedron V_p.

	300(2) K	275(2) K	250(2) K	225(2) K	200(2) K
Fe1-N1 (Å)	2.1146(18)	2.1179(19)	2.1153(18)	2.1167(17)	2.1170(17)
Fe1-N2 (Å)	2.2243(16)	2.2209(17)	2.2224(16)	2.2207(15)	2.2199(16)
Fe1-N3 (Å)	2.1530(16)	2.1508(16)	2.1505(16)	2.1490(15)	2.1490(15)
Fe2-N8 (Å)	2.134(2)	2.134(2)	2.1313(19)	2.1247(18)	2.1151(20)
Fe2-N9 (Å)	2.1838(16)	2.1812(16)	2.1786(16)	2.1743(15)	2.1589(16)
Fe2-N10 (Å)	2.1546(15)	2.1531(16)	2.1503(15)	2.1424(15)	2.1315(16)
Σ[a] Fe1 (°)	73.1(5)	73(5)	72.7(5)	72.4(4)	72.1(5)
V_p[b] Fe1 (Å^3)	13.024(6)	13.012(7)	13.006(6)	13.001(6)	12.998(6)
Σ[a] Fe2 (°)	64.8(5)	64.3(4)	64.2(5)	63.5(4)	63.2(4)
V_p[b] Fe2 (Å^3)	12.965(6)	12.942(7)	12.901(6)	12.799(6)	12.599(6)

[a] Σ, the distortion parameter is the sum of the absolute value of the deviation of all 12 cis N-Fe-N angles from 90°. [b] V_p is the volume of the Fe octahedron calculated in Olex2.[52]

Table 3.5 continued - Fe-N bond lengths for **D**, along with the distortion parameter Σ and the volume of the Fe octahedron V_p.

	175(2) K	150(2) K	125(2) K	100(2) K	75(2) K
Fe1-N1 (Å)	2.1172(16)	2.1145(14)	2.1141(16)	2.1140(16)	2.1152(15)
Fe1-N2 (Å)	2.2179(15)	2.2184(13)	2.2153(15)	2.2148(13)	2.2132(15)
Fe1-N3 (Å)	2.1500(15)	2.1529(13)	2.1500(15)	2.1497(13)	2.1487(14)
Fe2-N8 (Å)	2.0836(18)	2.0052(15)	1.9613(16)	1.9536(13)	1.9521(15)
Fe2-N9 (Å)	2.1278(16)	2.0484(14)	2.0053(15)	1.9969(13)	1.9970(14)
Fe2-N10 (Å)	2.1036(15)	2.0322(14)	1.9884(15)	1.9812(13)	1.9784(15)
Σ[a] Fe1 (°)	72.1(5)	71(4)	70.1(4)	70.4(3)	70.2(4)
V_p[b] Fe1 (Å^3)	12.998(6)	12.996(5)	12.957(6)	12.951(5)	12.950(6)
Σ[a] Fe2 (°)	60.8(4)	54(4)	49.5(3)	49.5(3)	49.6(4)
V_p[b] Fe2 (Å^3)	12.109(6)	10.917(5)	10.267(5)	10.152(4)	10.128(5)

[a] Σ, the distortion parameter is the sum of the absolute value of the deviation of all 12 cis N-Fe-N angles from 90°. [b] V_p is the volume of the Fe octahedron calculated in Olex2.[52]

Table 3.5 continued - Fe-N bond lengths for **D**, along with the distortion parameter Σ and the volume of the Fe octahedron V_p.

	50(2) K	30(2) K	30(2) K LIESST	ambient	1.8(2) kbar
Fe1-N1 (Å)	2.1165(15)	2.1166(14)	2.1232(14)	2.118(5)	2.116(4)
Fe1-N2 (Å)	2.2126(15)	2.2115(14)	2.2203(14)	2.212(4)	2.210(4)
Fe1-N3 (Å)	2.1475(15)	2.1503(14)	2.1434(14)	2.150(4)	2.149(3)
Fe2-N8 (Å)	1.9504(15)	1.9527(14)	2.1320(15)	2.129(5)	2.127(4)
Fe2-N9 (Å)	1.9958(15)	1.9958(13)	2.1848(14)	2.180(5)	2.176(5)
Fe2-N10 (Å)	1.9792(14)	1.9798(13)	2.1519(14)	2.161(4)	2.147(4)
Σ[a] Fe1 (°)	70.1(4)	70.4(3)	74.1(4)	72(1)	71(1)
V_p[b] Fe1 (Å^3)	12.948(6)	12.958(5)	13.016(5)	12.954(15)	12.953(15)
Σ[a] Fe2 (°)	50.0(4)	49.7(4)	66.1(4)	65(1)	63(1)
V_p[b] Fe2 (Å^3)	10.118(5)	10.134(4)	12.954(6)	12.952(18)	12.881(15)

Table 3.5 continued - Fe-N bond lengths for **D**, along with the distortion parameter Σ and the volume of the Fe octahedron V_p.

	7.5(2) kbar	9.6(2) kbar	12(2) kbar	15(2) kbar	ambient pressure released
Fe1-N1 (Å)	2.100(5)	2.069(5)	2.045(5)	1.984(9)	2.106(10)
Fe1-N2 (Å)	2.179(5)	2.144(6)	2.117(5)	2.012(10)	2.203(11)
Fe1-N3 (Å)	2.135(4)	2.110(5)	2.084(4)	1.988(8)	2.147(8)
Fe2-N8 (Å)	1.985(4)	1.956(5)	1.949(4)	1.947(8)	2.144(11)
Fe2-N9 (Å)	2.026(6)	1.993(6)	1.984(5)	1.969(10)	2.188(13)
Fe2-N10 (Å)	2.007(5)	1.983(5)	1.976(5)	1.983(10)	2.165(10)
Σ[a] Fe1 (°)	70(1)	68(2)	67(1)	56(3)	73(3)
V_p[b] Fe1 (Å^3)	12.61(2)	12.127(6)	11.707(19)	10.40(3)	12.82(4)
Σ[a] Fe2 (°)	52(2)	49(2)	50(1)	52(3)	61(3)
V_p[b] Fe2 (Å^3)	10.594(17)	10.174(17)	10.056(16)	10.00(3)	13.16(4)

[a] Σ, the distortion parameter is the sum of the absolute value of the deviation of all 12 cis N-Fe-N angles from 90°. [b] V_p is the volume of the Fe octahedron calculated in Olex2.[52]

The LIESST HS* structure was also obtained during our study using a 670 nm, 5 mW laser at 30(2) K, with no evidence of linkage isomerism. This was as expected since a previous study[41] reporting the LIESST structure for **D** found no linkage isomerism when a low powered laser was used, as is the case here, but did find linkage isomerism when using a high powered laser. Changes were observed in the cell parameters of the 30(2) K LIESST HS* structure relative to the 30(2) K ground state the *a* axis decreases slightly along with the *β* angle, while the *b* and *c* axes increase slightly resulting in a 2% increase in the cell volume. As expected, the Fe2-N distances, distortion parameter and octahedron volume parameters also increase and are consistent with those associated with a HS Fe centre.

3.4.5 Polymorph D pressure induced spin crossover

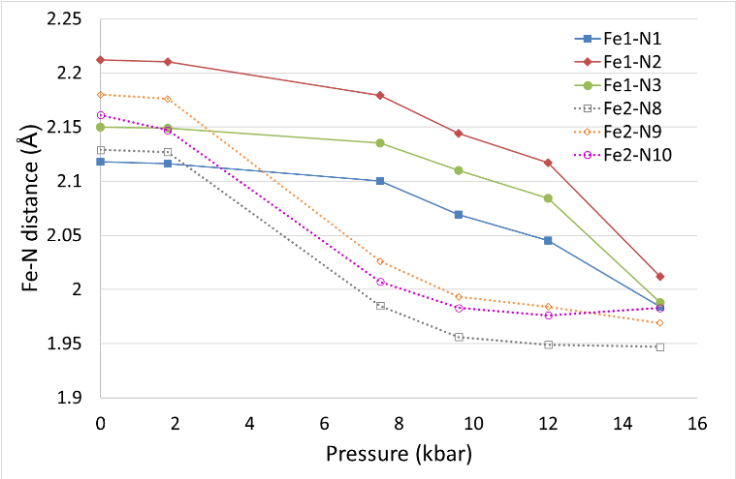

Figure 3.5 - Fe-N bond length changes in **D** as a function of pressure. Error bars are not included as they are essentially obscured by the data markers.

The effect of pressure on the spin transition behaviour of polymorph **D** was examined by collecting datasets using a DAC at six different pressures between ambient and 15.0(2) kbar. For all structures, the crystal system and space group remained as monoclinic $P2_1/c$, however significant structural changes were observed, see Figure 3.5 and Table 3.5.

At ambient and 1.8(2) kbar the structure obtained was consistent with the room temperature structure i.e. both Fe centres were in the HS state. At 7.5(2) kbar the Fe2-N bond lengths, Σ and V_p had reduced significantly indicating that Fe2 had mostly undergone a spin crossover, which appeared to be essentially complete at 9.6(2) kbar. The structure at 7.5(2) kbar is therefore very similar to the low temperature structure obtained for **D**. What is noticeable at 9.6(2) kbar is that the Fe1-N bond lengths, Σ and V_p have started to reduce significantly, and this continues until the 15.0(2) kbar dataset where the transition appears to be nearly but probably not quite complete as the change in Fe-N bond lengths (~0.13-0.2 Å) is slightly less than the expected ~0.2 Å reduction. It is possible looking at the plot of bond length versus pressure for Fe1 that the spin transition has begun at 7.5(2) kbar however this is not totally clear. Alongside the changes in structural parameters relating to the Fe centres there was a small reduction of ~0.1 Å in the *a* axis length and a slightly larger decrease in the *b* and *c* axes of ~0.6 Å and ~1 Å respectively. The *β* angle initially increased by ~1° as the pressure increased up to 9.6(2) kbar before dropping to ~1° below the value seen at ambient pressure. The cell volume showed an ~12.5% reduction between ambient pressure and 15.0(2) kbar.

After reaching 17.0 kbar, at which pressure the data quality were poor, the pressure in the DAC was released and another dataset collected at ambient pressure. This showed that the transition was reversible with both Fe centres having reverted back to the HS state with the cell parameters and Fe parameters consistent with those at the start of the experiment (Table 3.5 and Appendix 3, Table S3.3). It was noted that the quality of the crystal had reduced as a result of the change in pressure.

This result is particularly interesting as applying pressure to **D** has resulted in the occurrence of a spin transition at both Fe1 and Fe2, a situation that is inaccessible thermally.

3.4.6 Summary of the four [Fe(abpt)$_2$(NCS)$_2$] polymorphs

As discussed in the introduction, the four reported polymorphs of [Fe(abpt)$_2$(NCS)$_2$] are particularly interesting as they show quite different spin crossover behaviour despite having very similar structures. Some of these properties along with selected structural parameters are detailed in Table 3.6.

Examining an overlay of the unique molecules shows that the molecular confirmations are relatively similar, as would be expected. The largest differences are seen in the relative orientations of the two pyridyl rings on the abpt ligand for **B** (green) and **D** Fe2 (grey), see Figure 3.6. These happen to be two of the Fe centres that don't undergo a thermal spin crossover, however this may well just be coincidental for these structures and it is most likely that it is a function of the resultant packing. It is widely recognised that intermolecular interactions play a significant role in the spin crossover behaviour of compounds[19, 58]. Table 3.7 summarises the reported spin crossover behaviour of Fe(abpt)$_2$X$_2$ compounds found in the Cambridge Structural Database, along with details of π-π interactions. The main points to note are that all of the Fe centres that do undergo at least a partial thermal spin crossover display π-π interactions between their adpt ligands, while and all of the Fe centres for which the attached abpt ligands are not involved in π-π interactions are not reported to undergo a thermal spin crossover. There are of course a couple of anomalies, in addition to **B** discussed herein, there are also two complexes that are not reported to undergo a thermal spin crossover that do have π-π interactions Fe(abpt)$_2$[N(CN)$_2$]$_2$[59] and Fe(abpt)$_2$(NCSe)$_2$ polymorph **B**[42], the latter of which is isostructural with **B** reported herein. As discussed herein **B** does undergo a pressure induced spin crossover and also a thermal spin crossover at pressure above 4.4 kbar.[42]

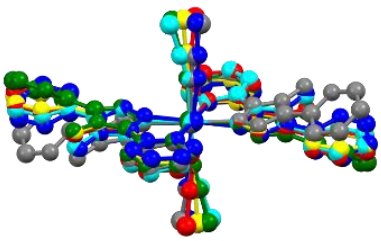

Figure 3.6 - Overlay of each of the unique Fe centres at room temperature, constructed in Mercury by selecting the Fe1/Fe2, N1/N8, N2/N9 and N3/N10 and calculating the overlay. Two different views of overlay shown (cyan) **A**, (green) **B**, (red) **C** Fe1, (blue) **C** Fe2, (yellow) **D** Fe1, (grey) **D** Fe2.

Table 3.6 - Summary of the behaviour and selected structural parameters for the four polymorphs of $[Fe(abpt)_2(NCS)_2]$.

Polymorph	**A**	**B**	**C**		**D**	
			Fe1	Fe2	Fe1	Fe2
Z’	0.5	0.5	2 x 0.5		2 x 0.5	
Thermal spin crossover	Yes	No	Yes	No	No	Yes
T1/2 (K)	188	-	86		162	
LIESST	Yes	-	Yes commensurate modulated structure	-	-	Yes
Pressure induced spin crossover	Yes	Yes by 23.6(2) kbar, after phase transition (11.5(2) - 13.5(2) kbar) giving Z’ = 2 x 0.5	unknown		Yes > ~15.0(2) kbar	Yes > ~9.6(2) kbar

Table 3.7 - Summary of the spin crossover behaviour of the $[Fe(abpt)_2X_2]$ compounds for which a structure has been reported.

Structure[i]	Temperature		Thermal spin crossover?	$T_{1/2}$	π-π[ii]
A[37-39]	275		Y	188	Both ends
B[42]	300		N	-	One end
C[39, 40]	RT	Fe1	Y	86	Both ends
		Fe2	N		-
D[39, 41]	300	Fe1	N		-
$Fe(abpt)_2(C(CN)_3)_2$[58]	RT		Y	336	Both ends
$Fe(abpt)_2((NC)_2CC(OCH_3)C(CN)_2)_2$[58]	RT		N	-	-
$Fe(abpt)_2((NC)_2CC(OC_2H_5)C(CN)_2)_2$[58]	RT		Y: magnetic data indicates ~60% spin crossover	377	Both ends
$Fe(abpt)_2((NC)_2CC(OC_2H_5)C(CN)_2)_2$[58]	RT	Fe1	Y: magnetic data indicates ~60% crossover	383	Both ends
		Fe2			Both ends
$Fe(abpt)_2[N(CN)_2]_2$[60]	RT		N: redetermined see paper[59]	-	Both ends
$Fe(abpt)_2[N(CN)_2]_2$[59]	RT	Fe1	Y	~86 stepped Fe1 then Fe2	Both ends
		Fe2			Both ends
$Fe(abpt)_2(C_{16}SO_3)_2$[61]	92		Y	Unknown	One end
$Fe(abpt)_2Cl_2$[62]	85		N	-	-
$Fe(abpt)_2(NCSe)_2$ A[37, 43]	375		Y		Both ends
$Fe(abpt)_2(NCSe)_2$ B[42]	RT		N	-	One end

[i] If multiple structures are reported for a compound only one structure has been selected for each unique polymorph to avoid duplication. [ii] Both ends means that both the pyridyl rings on the abpt are involved in π-π interactions with the two pyridyl rings on an abpt on another molecule while one end means only one pyridyl ring on an abpt interacts with a pyridyl on an abpt in another molecule.

3.5 Conclusions

In summary, the spin crossover behaviour of $[Fe(abpt)_2(NCS)_2]$ polymorph **B** and **D** have been structurally characterised. In the case of **B**, it does not undergo a thermal spin crossover but was found to undergo a pressure induced spin crossover. Somewhere between 11.5(2) and 13.5(2)

kbar it undergoes a phase transition from a monoclinic to triclinic crystal system with Z' increasing from 0.5 to 2 x 0.5. At the same point the Fe centres start to display a spin crossover which by 23.4(2) kbar is approximately complete.

Polymorph **D** has previously been reported to undergo a thermal spin crossover in one of the two unique Fe centres, the second Fe centre remains HS upon cooling. Herein the cell parameters and structural parameters were monitored from 300(2) to 30(2) K. A LIESST structure was also obtained at 30(2) K. In addition, a high pressure single crystal study showed that **D** underwent a stepped pressure induced spin crossover. The Fe centre that undergoes a thermal spin transition underwent a pressure induced spin crossover by ~9.6(2) kbar while the second Fe centre began to undergo the spin crossover at a higher pressure and was essentially LS by ~15.0(2) kbar.

In all cases the spin crossover upon cooling or increasing pressure resulted in the expected reduction in the Fe-N bond lengths, Σ and V_p for the Fe centre that underwent the spin crossover.

The ability to undergo a spin crossover for general $Fe(abpt)_2X_2$ complexes could be linked to the presence of intermolecular π-π interactions. All of the complexes that undergo at least a partial thermal spin crossover displayed π-π interactions between pyridyl rings on abpt ligands and all of the complexes that did not have π-π interactions did not undergo a thermal spin crossover. There were three complexes identified with π-π interactions but that do not undergo a thermal spin crossover, however **B** does undergo a pressure induced spin transition.

It was particularly interesting to note within this study that high pressure was able to induce a thermally inaccessible spin crossover at Fe centres in both **B** and **D**.

3.6 References

1. L. Cambi and L. Szegö, *Berichte Der Deutschen Chemischen Gesellschaft*, 1931, **64 (10)**, 2591-2598.
2. P. Gütlich, V. Ksenofontov and A. B. Gaspar, *Coordination Chemistry Reviews*, 2005, **249**, 1811-1829.
3. A. Hauser, *Light-Induced Spin Crossover and the High-Spin→Low-Spin Relaxation. Spin Crossover in Transition Metal Compounds II, Top. Curr. Chem., 234, 155-198*, Springer-Verlag: Berlin, Heidelberg, New York, 2004.
4. M. Nakaya, R. Ohtani, L. F. Lindoy and S. Hayami, *Inorganic Chemistry Frontiers*, 2021, **8**, 484-498.
5. P. Gütlich, A. B. Gaspar and Y. Garcia, *Beilstein Journal of Organic Chemistry*, 2013, **9**, 342-391.
6. S. De, L. M. Chamoreau, H. El Said, Y. L. Li, A. Flambard, M. L. Boillot, S. Tewary, G. Rajaraman and R. Lescouezec, *Frontiers in Chemistry*, 2018, **6**.
7. T. Matsuyama, K. Nakata, H. Hagiwara and T. Udagawa, *Crystals*, 2019, **9**.
8. D. Sertphon, P. Harding, K. S. Murray, B. Moubaraki, S. M. Neville, L. Liu, S. G. Telfer and D. J. Harding, *Crystals*, 2019, **9**.
9. T. Houari, E. Cuza, D. Pinkowicz, M. Marchivie, S. Yefsah and S. Triki, *Crystals*, 2018, **8**.
10. A. R. Craze, N. F. Sciortino, M. M. Badbhade, C. J. Kepert, C. E. Marjo and F. Li, *Inorganics*, 2017, **5**.
11. M. Nihei, T. Shiga, Y. Maeda and H. Oshio, *Coordination Chemistry Reviews*, 2007, **251**, 2606-2621.
12. K. Takahashi, K. Yamamoto, T. Yamamoto, Y. Einaga, Y. Shiota, K. Yoshizawa and H. Mori, *Crystals*, 2019, **9**.
13. W. Phonsri, L. C. Darveniza, S. R. Batten and K. S. Murray, *Inorganics*, 2017, **5**.
14. T. Nakanishi, A. Okazawa and O. Sato, *Inorganics*, 2017, **5**.

15. A. B. Gaspar, M. C. Muñoz, V. Niel and J. A. Real, *Inorganic Chemistry*, 2001, **40**, 9-10.
16. P. Nielsen, H. Toftlund, A. D. Bond, J. F. Boas, J. R. Pilbrow, G. R. Hanson, C. Noble, M. J. Riley, S. M. Neville, B. Moubaraki and K. S. Murray, *Inorganic Chemistry*, 2009, **48**, 7033-7047.
17. A. Ondo and T. Ishida, *Crystals*, 2018, **8**.
18. O. A. Qamar, C. Cong and H. B. Ma, *Dalton Transactions*, 2020, **49**, 17106-17114.
19. P. Guionneau, *Dalton Transactions*, 2014, **43**, 382-393.
20. K. S. Kumar and M. Ruben, *Angewandte Chemie-International Edition*, 2021, **60**, 7502-7521.
21. O. Sato, *Nature Chemistry*, 2016, **8**, 644-656.
22. J. Linares, E. Codjovi and Y. Garcia, *Sensors*, 2012, **12**, 4479.
23. P. Gütlich and H. A. Goodwin, eds., *Spin Crossover in Transition Metal Compounds I, II and III*, Springer-Verlag: Berlin, Heidelberg, New York, 2004.
24. M. A. Halcrow, ed., *Spin-Crossover Materials: Properties and Applications*, John Wiley & Sons, Ltd.: Chichester, UK, 2013.
25. M. Griffin, S. Shakespeare, H. J. Shepherd, C. J. Harding, J.-F. Létard, C. Desplanches, A. E. Goeta, J. A. K. Howard, A. K. Powell, V. Mereacre, Y. Garcia, A. D. Naik, H. Mueller-Bunz and G. G. Morgan, *Angewandte Chemie-International Edition*, 2011, **50**, 896-900.
26. J. A. Real, B. Gallois, T. Granier, F. Suezpanama and J. Zarembowitch, *Inorganic Chemistry*, 1992, **31**, 4972-4979.
27. T. Granier, B. Gallois, J. Gaultier, J. A. Real and J. Zarembowitch, *Inorganic Chemistry*, 1993, **32**, 5305-5312.
28. A. B. Gaspar, G. Molnar, A. Rotaru and H. J. Shepherd, *Comptes Rendus Chimie*, 2018, **21**, 1095-1120.
29. Z. Yan, L. F. Zhu, L. W. Zhu, Y. Meng, M. N. Hoque, J. L. Liu, Y. C. Chen, Z. P. Ni and M. L. Tong, *Inorganic Chemistry Frontiers*, 2017, **4**, 921-926.
30. J.-F. Létard, P. Guionneau, L. Rabardel, J. A. K. Howard, A. E. Goeta, D. Chasseau and O. Kahn, *Inorganic Chemistry*, 1998, **37**, 4432-4441.
31. E. Collet and P. Guionneau, *Comptes Rendus Chimie*, 2018, **21**, 1133-1151.
32. J. A. Wolny, V. Schunemann, Z. Nemeth and G. Vanko, *Comptes Rendus Chimie*, 2018, **21**, 1152-1169.
33. S. Chorazy, T. Charytanowicz, D. Pinkowicz, J. H. Wang, K. Nakabayashi, S. Klimke, F. Renz, S. Ohkoshi and B. Sieklucka, *Angewandte Chemie-International Edition*, 2020, **59**, 15741-15749.
34. T. Kosone, S. Okuda, M. Kawata, S. Arai, R. Kosuge and T. Kawasaki, *Acs Omega*, 2021, **6**, 12187-12193.
35. C. Lochenie, W. Bauer, A. P. Railliet, S. Schlamp, Y. Garcia and B. Weber, *Inorganic Chemistry*, 2014, **53**, 11563-11572.
36. J. Tao, R.-J. Wei, R.-B. Huang and L.-S. Zheng, *Chemical Society Reviews*, 2012, **41**, 703-737.
37. N. Moliner, M. C. Muñoz, S. Létard, J.-F. Létard, X. Solans, R. Burriel, M. Castro, O. Kahn and J. A. Real, *Inorganica Chimica Acta*, 1999, **291**, 279-288.
38. H. E. Mason, W. Li, M. A. Carpenter, M. L. Hamilton, J. A. K. Howard and H. A. Sparkes, *New Journal of Chemistry*, 2016, **40**, 2466-2478.
39. C.-F. Sheu, S.-M. Chen, S.-C. Wang, G.-H. Lee, Y.-H. Liu and Y. Wang, *Chemical Communications*, 2009, 7512-7514.
40. C.-H. Shih, C.-F. Sheu, K. Kato, K. Sugimoto, J. Kim, Y. Wang and M. Takata, *Dalton Transactions*, 2010, **39**, 9794-9800.
41. C.-F. Sheu, C.-H. Shih, K. Sugimoto, B.-M. Cheng, M. Takata and Y. Wang, *Chemical Communications*, 2012, **48**, 5715-5717.

42. A. B. Gaspar, M. C. Mũnoz, N. Moliner, V. Ksenofontov, G. Levchenko, P. Gütlich and J. A. Real, *Monatshefte für Chemie*, 2003, **134**, 285-294.
43. H. E. Mason, M. L. Hamilton, J. A. K. Howard and H. A. Sparkes, *New Journal of Chemistry*, 2018, **42**, 18028-18037.
44. A. E. Goeta, L. K. Thompson, C. L. Sheppard, S. S. Tandon, C. W. Lehmann, J. Cosier, C. Webster and J. A. K. Howard, *Acta Crystallographica, Section C: Crystal Structure Communications*, 1999, **C55**, 1243-1246.
45. Bruker, *SMART-NT, Data Collection Software, Version 5.63, Bruker Analytical X-ray Instruments Inc., Madison, WI, USA*, 2000.
46. Bruker, *SAINT+ Integration Engine, Data Reduction Software, Bruker Analytical X-ray Instruments Inc., Madison, WI, USA, 2007*, 2007.
47. Bruker, *SAINT-NT, Data Reduction Software Ver. 6.14, Bruker Analytical X-ray Instruments Inc., Madison, WI, USA*, 2000.
48. Bruker, *SADABS, Bruker AXS area detector scaling and absorption correction, Bruker Analytical X-ray Instruments Inc., Madison, Wisconsin, USA*, 2001.
49. G. M. Sheldrick, *Acta Crystallographica, Section A: Foundations of Crystallography*, 2008, **A64**, 112-122.
50. L. Palatinus and G. Chapuis, *Journal of Applied Crystallography*, 2007, **40**, 786-790.
51. L. Palatinus, S. J. Prathapa and S. van Smaalen, *Journal of Applied Crystallography*, 2012, **45**, 575-580.
52. O. V. Dolomanov, L. J. Bourhis, R. J. Gildea, J. A. K. Howard and H. Puschmann, *Journal of Applied Crystallography*, 2009, **42**, 339-341.
53. G. J. Piermarini, S. Block, J. D. Barnett and R. A. Forman, *Journal of Applied Physics*, 1975, **46**, 2774-2780.
54. M. R. Probert, J. A. Coome, A. E. Goeta and J. A. K. Howard, *Acta Crystallographica, Section A: Foundations of Crystallography*, 2011, **A67, Supplement**, C528.
55. M. R. Probert, C. M. Robertson, J. A. Coome, J. A. K. Howard, B. C. Michell and A. E. Goeta, *Journal of Applied Crystallography*, 2010, **43**, 1415-1418.
56. T. Schulz, K. Meindl, D. Leusser, D. Stern, J. Graf, C. Michaelsen, M. Ruf, G. M. Sheldrick and D. Stalke, *Journal of Applied Crystallography*, 2009, **42**, 885-891.
57. Bruker, *APEX2, Data Collection Software, Version 1.08, Bruker Analytical X-ray Instruments Inc., Madison, WI, USA*, 2004.
58. G. Dupouy, M. Marchivie, S. Triki, J. Sala-Pala, J. Y. Salaun, C. J. Gomez-Garcia and P. Guionneau, *Inorganic Chemistry*, 2008, **47**, 8921-8931.
59. C. F. Sheu, S. Pillet, Y. C. Lin, S. M. Chen, I. J. Hsu, C. Lecomte and Y. Wang, *Inorganic Chemistry*, 2008, **47**, 10866-10874.

Chapter 4

$[Fe(abpt)_2(NCSe)_2]$ polymorph A: Structural studies into the spin crossover behaviour

Helen E. Mason, Michelle L. Hamilton, Judith A. K. Howard and Hazel A. Sparkes

Published *New Journal of Chemistry*, 2018, **42(22)**, 18028-18037, doi 10.1039/C8NJ03627F. Reproduced with permission for the Royal Society of Chemistry.

4.1 Abstract

The spin crossover behaviour of $[Fe(abpt)_2(NCSe)_2]$ (abpt = 4-amino-3,5-bis(pyridin-2-yl)-1,2,4-triazole) polymorph **A** has been examined using single crystal X-ray diffraction and variable temperature UV-Vis transmission spectroscopy. The crystal structure of **A** is reported at sixteen temperatures between 30 and 375 K, all of which are in the monoclinic space group $P2_1/n$ with Z' = 0.5. Changes in the crystallographic cell parameters, bond lengths, distortion parameters and intra and intermolecular interactions between 375 K and 30 K are discussed. Continuous irradiation with a 670 nm, 5 mW CW laser at 30 K enabled a light induced excited spin state trapping (LIESST) metastable high spin structure, HS*, to be obtained.

4.2 Introduction

Spin crossover in molecular compounds was first observed in the 1930s.[1] Despite having been extensively studied it still attracts significant research interest partly due to its potential for industrial applications,[2-4] for example in data storage devices,[5, 6] molecular magnets[7] and molecular switches.[8, 9] For a spin crossover compound changes in the physical environment,[10] including temperature,[11] pressure,[12, 13] magnetic field or light irradiation,[14, 15] can result in a reversible change in the spin state. Many of the spin crossover complexes that have been identified and studied are octahedral Fe(II) species[10, 16] but spin crossover is also relatively common for other octahedral $3d^4$-$3d^7$ metal centres such as Fe(III)[15, 17] or Co(II).[18, 19] In the solid state, spin crossover is a complex phenomenon and the abrupt or gradual nature, completeness and temperature at which it occurs have been linked to the presence of intermolecular interactions within the crystal lattice. Indeed different polymorphs of the same compound can show different spin crossover behaviour.[20-23] Spin crossover complexes with limited cooperative communication between metal centres display very gradual changes in spin state, while species with significant molecular cooperativity show abrupt changes in spin state often with hysteresis. In addition, spin crossovers can be complete, partial or stepped.[24, 25] Insights into spin crossover materials and their behaviour are coming from a range of techniques including magnetic data,[13, 26] X-ray crystallography,[11, 27] spectroscopic techniques including UV-Vis,[26, 28] Resonant Ultrasound,[29] Mossbauer[11, 30] and X-ray photoelectron spectroscopy.[27] Given the complexity of spin crossover behaviour,[26, 31] it is important to study such systems in detail to further our understanding and allow the customised design of spin crossover materials for desired applications.

Spin crossover behaviour has been identified in various Fe(II) complexes containing 3,5-bis(pyridin-2-yl)-1,2,4-triazole derivatives with *trans* NCS or NCSe ligands: for example, *trans*-$[Fe(MBPT)_2(NCS)_2]$[32] (MBPT = 4-*p*-methylphenyl-3,5-bis(pyridine-2-yl)-1,2,4-triazole), $T_{1/2}$ ~ 231 K; $[Fe(L^{pz})_2(NCS)_2]$[33] (L^{pz} = 4-*p*-tolyl-3-(2-pyrazinyl)-5-(2-pyridyl)1,2,4-triazole) which exhibits an incomplete change in spin state $T_{1/2}$ (cooling) = 142 K, $T_{1/2}$ (warming) = 149 K; and $[Fe(L^{pz})_2(NCSe)_2]$,[33] $T_{1/2}$ (cooling) = 172 K, $T_{1/2}$ (warming) = 177 K. $[Fe(pldpt)_2(NCS)_2]$[34] (pldpt = N^4-

pyrrol-3,5-di(2-pyridyl)-1,2,4-triazole), which has both *cis* and *trans* coordinated (2:1 ratio) NCS ligands around the Fe centre, displays interesting spin crossover behaviour. Only the Fe centres which have *trans* coordinate NCS ligands (i.e. one-third of the Fe centres) display a thermal spin crossover, with $T_{1/2}$ being affected by the presence of solvent (solvent free $T_{1/2}$ = 180 K, solvated $T_{1/2}$ < 89 K). In addition, four polymorphs of $[Fe(abpt)_2(NCS)_2]$ (abpt = 4-amino-3,5-bis(pyridin-2-yl)-1,2,4-triazole) (**2**) have been identified (Table 4.1); three of which, polymorphs **A**,[29, 35, 36] **C**[37] and **D**[38] (herein referred to as **2A**, **2C** and **2D**), display thermal spin crossover. **2A** exhibits a gradual thermal spin crossover without hysteresis and with $T_{1/2}$ = 180 K[36] (re-measured as $T_{1/2}$ = 188 K for crystals prepared using a different method).[39] **2C** and **2D** have two crystallographically unique Fe centres and display more complicated spin crossover behaviour. In **2C**, one of the Fe centres undergoes a thermal spin crossover with $T_{1/2}$ = 86 K. Both temperature and light induced excited spin state trapping (TIESST and LIESST) have been observed and result in a commensurate modulated structure with four crystallographically independent Fe centres.[37] In the case of **2D**, thermal spin crossover of one of the crystallographically independent Fe centres has been reported with $T_{1/2}$ = 162 K. At low temperature, as well as the occurrence of LIESST, photoinduced linkage isomerism of the NCS ligand is observed.[38] The final polymorph, **B**[40] (herein referred to as **2B**), undergoes a thermal spin crossover at pressures >4.4 kbar but not at ambient pressure.[40]

Two polymorphs of the title compound, $[Fe(abpt)_2(NCSe)_2]$ **A**[36] and **B**,[40] have been reported previously (Table 4.1). While polymorph **B** does not undergo thermal spin crossover between 2 - 300 K,[40] polymorph **A** has been shown to undergo a thermal spin crossover without hysteresis and with $T_{1/2}$ = 224 K.[36] Magnetic studies on precipitated microcrystalline or single crystal samples of **A** have shown either a residual HS fraction, γ_{HS}, of 14%[35] or a virtually complete spin crossover[36] respectively. Both polymorphs have a six-coordinate Fe(II) centre with the NCSe ligands *trans* to each other. The structures of $[Fe(abpt)_2(NCSe)_2]$ polymorphs **A** and **B** are isostructural to those of the sulphur analogue, **2A**[36] and **2B**.[40] The 293 K HS structure of **A** is known, however LS and LIESST HS* structures have not been previously characterised and are reported herein alongside a detailed crystallographic study of structural changes occurring during the spin crossover. Single crystal variable temperature UV-Vis transmission spectroscopy, which has been used to monitor spectral changes across the thermal spin crossover temperature range, supports the crystallographic evidence and helps to provide further insight into the spin crossover behaviour of **A**.

4.3 Experimental

4.3.1 Synthesis

X-ray diffraction quality single crystals of $[Fe(abpt)_2(NCSe)_2]$ polymorph **A** were produced using the slow diffusion method previously reported for the synthesis of $[Fe(abpt)_2(NCS)_2]$.[39] All precursor materials are commercially available and were used as received, solvents were degassed and manipulations carried out under a nitrogen atmosphere. $FeSO_4.7H_2O$ (0.5 mmol, 0.139 g) and KNCSe (1 mmol, 0.144g) were stirred in MeOH (8 ml) for 15 min, the resulting pale yellow K_2SO_4 precipitate removed by filtration and deionised H_2O (8 ml) added to the remaining clear solution. abpt [4-amino-3,5-bis(pyridin-2-yl)-1,2,4-triazole] (1 mmol, 0.238 g) dissolved in MeOH (10 ml) was transferred to a narrow (<5 cm) Schlenk tube and the $Fe^{2+}/2(NCSe)^-$ solution carefully injected into the bottom of the Schlenk to form a layer underneath the abpt solution. A red coloured band immediately formed at the interface between the two layers. Single crystals of polymorph **A** suitable for X-ray diffraction studies were formed within 1-4 weeks but no crystals of polymorph **B** were produced.[40]

Table 4.1 - Brief summary of the spin crossover behaviour of $[Fe(abpt)_2(NCSe)_2]$ and $[Fe(abpt)_2(NCS)_2]$ (2) polymorphs.

Complex	Polymorph colour and habit	Reference number herein	Spin crossover behaviour
$[Fe(abpt)_2(NCSe)_2]$	**A** red block	**A**	Gradual complete thermal spin crossover without hysteresis, $T_{1/2}$ = 224 K, residual Y_{HS} = ~0% at low temperature. LIESST observed with T_{LIESST} = 32 K.[36]
	B orange prism	**B**	Thermal spin crossover not observed at ambient pressure.[40]
$[Fe(abpt)_2(NCS)_2]$	**A** dark red block	**2A**	Gradual thermal spin crossover without hysteresis, $T_{1/2}$ = 180 K[36] (188 K),[39] residual Y_{HS} = 23% (~0%)[39] at low temperature. LIESST observed with T_{LIESST} = 40 K.
	B orange prism	**2B**	Incomplete thermal spin crossover at >4.4 kbar, $T_{1/2}$ = 65 K, becoming more complete with increased pressure.[40]
	C red block	**2C**	Thermal spin crossover of one Fe centre in the asymmetric unit, $T_{1/2}$ = 86 K. Commensurate modulated structure with the *c*-axis length tripled observed in TIESST and LIESST metastable states and between 170 - 86 K upon slow cooling.[37, 39]
	D red needle	**2D**	Thermal spin crossover of one Fe centre in the asymmetric unit, $T_{1/2}$ = 162 K. Two low temperature light induced metastable processes: LIESST, T_{LIESST} = 36 K, and photoinduced NCS to SCN linkage isomerism.[38, 39]

4.3.2 X-ray Crystallography - Variable temperature and LIESST measurements

A Bruker Smart 1K CCD diffractometer was used to collect single crystal X-ray diffraction data using graphite monochromated Mo*Kα* (λ = 0.71073 Å) X-ray radiation. Cooling was achieved using either an Oxford Instruments open flow nitrogen Cryostream or an Oxford Cryosystems HeliX[41] for datasets collected at temperatures >105 K or <105 K respectively. Data collection was carried out using SMART software,[42] integration performed using SAINT[43, 44] and face indexed numerical absorption corrections applied using SADABS-2012/1.[45] The structures were solved by direct methods in SHELXS[46] and refined by full matrix least squares on F^2 in SHELXL[46] in Olex2.[47] Non-hydrogen atoms were refined anisotropically and all hydrogen atoms were located geometrically and refined using a riding model except for the N6 hydrogen atoms which were located in the difference map. A LIESST HS* structure was obtained at 30 K by irradiating a crystal *in-situ* using a 670 nm, 5 mW CW laser. To establish and maintain a photostationary state (i.e. the metastable LIESST HS* structure) for the duration of the data collection, the crystal was irradiated for 60 min prior to and also throughout the data collection. Due to deterioration of the crystal quality during heating-cooling cycles and upon irradiation, different crystals were used for data collections with the HeliX (Crystal 1; full datasets at 30, 50, 75, 100 and 30 K under laser irradiation) and Cryostream (Crystal 2; full datasets at 108, 125, 150, 175, 225, 275, 325 and 375 K). Full structure determinations were carried out at sixteen temperatures these structures and the structure at 30 K under irradiation are published herein, see Table 4.2 and Appendix 4, Table S4.1.

Relaxation of the LIESST HS* state was examined by monitoring the evolution of unit cell parameters with time. Immediately after switching off the laser, omega scans consisting of 30 frames (scan width 0.4°) at alternating phi positions of 0 and 90° were collected continuously until the crystal had relaxed back to the LS state. SMARTreduce,[48] a script which automates reflection harvesting, unit cell indexation and least squares refinement in SMART,[42] was used to iteratively determine a unit cell from each consecutive set of two runs.

Table 4.2 - Crystal data and refinement results for A at 375 K, 30 K and 30 K after irradiation.

Spin state (temperature)	HS [375(2) K]	LS [30(2) K]	LIESST HS* [30(2) K]
Empirical formula	$C_{26}H_{20}FeN_{14}Se_2$	$C_{26}H_{20}FeN_{14}Se_2$	$C_{26}H_{20}FeN_{14}Se_2$
Formula weight	742.33	742.33	742.33
Temperature / K	375(2)	30(2)	30(2)
Crystal system	monoclinic	monoclinic	monoclinic
Space group	$P2_1/n$	$P2_1/n$	$P2_1/n$
a / Å	8.6568(4)	8.4320(6)	8.5189(7)
b / Å	10.2722(5)	9.9499(7)	10.0940(8)
c / Å	16.6275(8)	16.3484(12)	16.4616(13)
β / °	93.5349(9)	93.1202(14)	93.1989(15)
Volume / Å^3	1475.78(12)	1369.6(2)	1413.3(2)
Z	2	2	2
ρcalc / (g/cm^3)	1.671	1.800	1.744
μ / mm-1	3.022	3.256	3.155
F(000)	736.0	736.0	736.0
Radiation	MoKα (λ = 0.71073 Å)	MoKα (λ = 0.71073 Å)	MoKα (λ = 0.71073 Å)
2θ range for data collection / °	4.664 to 52.738	4.794 to 56.554	4.736 to 55.756
Index ranges	-10 ≤ h ≤ 10, -12 ≤ k ≤ 12, -19 ≤ l ≤ 20	-11 ≤ h ≤ 11, -12 ≤ k ≤ 13, -21 ≤ l ≤ 19	-11 ≤ h ≤ 11, -13 ≤ k ≤ 13, -20 ≤ l ≤ 21
Reflections collected	14338	9605	11585
R_{int}	0.0396	0.0353	0.0428
Data/restraints/parameters	3018/0/202	3381/0/202	3362/0/202
Goodness-of-fit on F^2	1.076	1.035	1.092
Final R indexes [I>=2σ (I)]	R_1 = 0.0410, wR_2 = 0.0953	R_1 = 0.0362, wR_2 = 0.0726	R_1 = 0.0452, wR_2 = 0.0922
Final R indexes [all data]	R_1 = 0.0716, wR_2 = 0.1094	R_1 = 0.0459, wR_2 = 0.0754	R_1 = 0.0523, wR_2 = 0.0949
Largest diff. peak/hole / (e Å-3)	0.85/-0.70	0.90/-0.74	2.14/-1.21

4.3.3 Variable temperature UV-Vis transmission spectroscopy

Variable temperature single crystal UV-Vis transmission spectroscopy was carried out using a custom built setup[29] (Figure 4.1) based on a cassegrain system (Bruker). Radiation from a Hamamatsu high power UV-VIS fiber broadband light source (L10290) was transferred via fibre optic cables to the cassegrain optics and into an Andor Shamrock SR-303i imaging spectrograph coupled with a Newton EMCCD camera (150 lines/mm grating groove density; specifications quote

a resolution of 0.88 nm at a centre wavelength of 500 nm). The spot size at the focus of the cassegrain optics is determined by the input fibre optic cable core size; this was chosen such that a ~50 µm diameter region of the crystal was sampled by UV-Vis radiation.

A single crystal fragment (<100×100×25 µm), mounted using perfluoropolyether oil onto a 100 µm aperture UV-Vis MicroLoop (MiTeGen, LLC) fixed on an XRD goniometer head, was positioned at the focus of the cassegrain system in the orientation giving the cleanest spectroscopic signal. The crystal was observed using a high-magnification zoom lens system mounted on a Thorlabs CMOS camera. An Oxford Cryosystems non-liquid nitrogen Cobra Cryostream was used to control the sample temperature.

To monitor spectral changes with temperature, Andor's Solis software was used to collect spectra in kinetic series mode (100 ms exposure, 30 s kinetic cycle time) while cooling from 290 K to 83 K at 150 K/hr. Spectra were presented by the Solis software in absorbance mode by collecting background (no light source) and reference (light source on a MicroLoop without sample) spectra. All data were normalised for comparison because the % transmission, but not the spectral shape, is dependent on the crystal orientation within the light beam. A Savitzky-Golay smoothing filter (polynomial order 2, frame size 13) was applied to the normalised data using MATLAB.[49] MATLAB[49] functions "polyfit" and "polyval" were used to give an estimate of the standard error in the Savitzky-Golay fitted value at a chosen wavelength of interest.

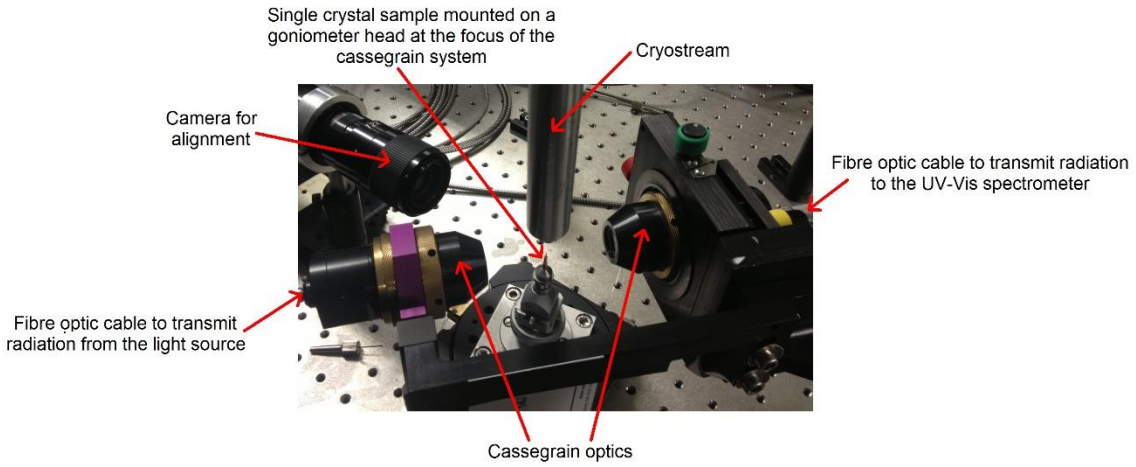

Figure 4.1 - Annotated photograph showing the custom built system used to collect variable temperature single crystal UV-Vis transmission spectra.

4.4 Results and discussion

4.4.1 Thermal spin crossover and cell parameter changes

The reported magnetic data for $[Fe(abpt)_2(NCSe)_2]$ polymorph **A** shows a gradual thermal spin crossover without hysteresis between ~265 – 175 K with $T_{1/2}$ = 224 K[36]. The occurrence of this spin crossover was also clearly indicated, over the expected region, through changes in the crystallographic cell parameters of **A** upon cooling from 375 to 30 K, with an ~0.3 Å decrease in the length of all of the cell axes and an ~0.4° decrease in the θ-angle (Figure 4.2, Table 4.2 and Appendix 4, Table S4.1). This resulted in an ~8% decrease in the unit cell volume over the full temperature range investigated.

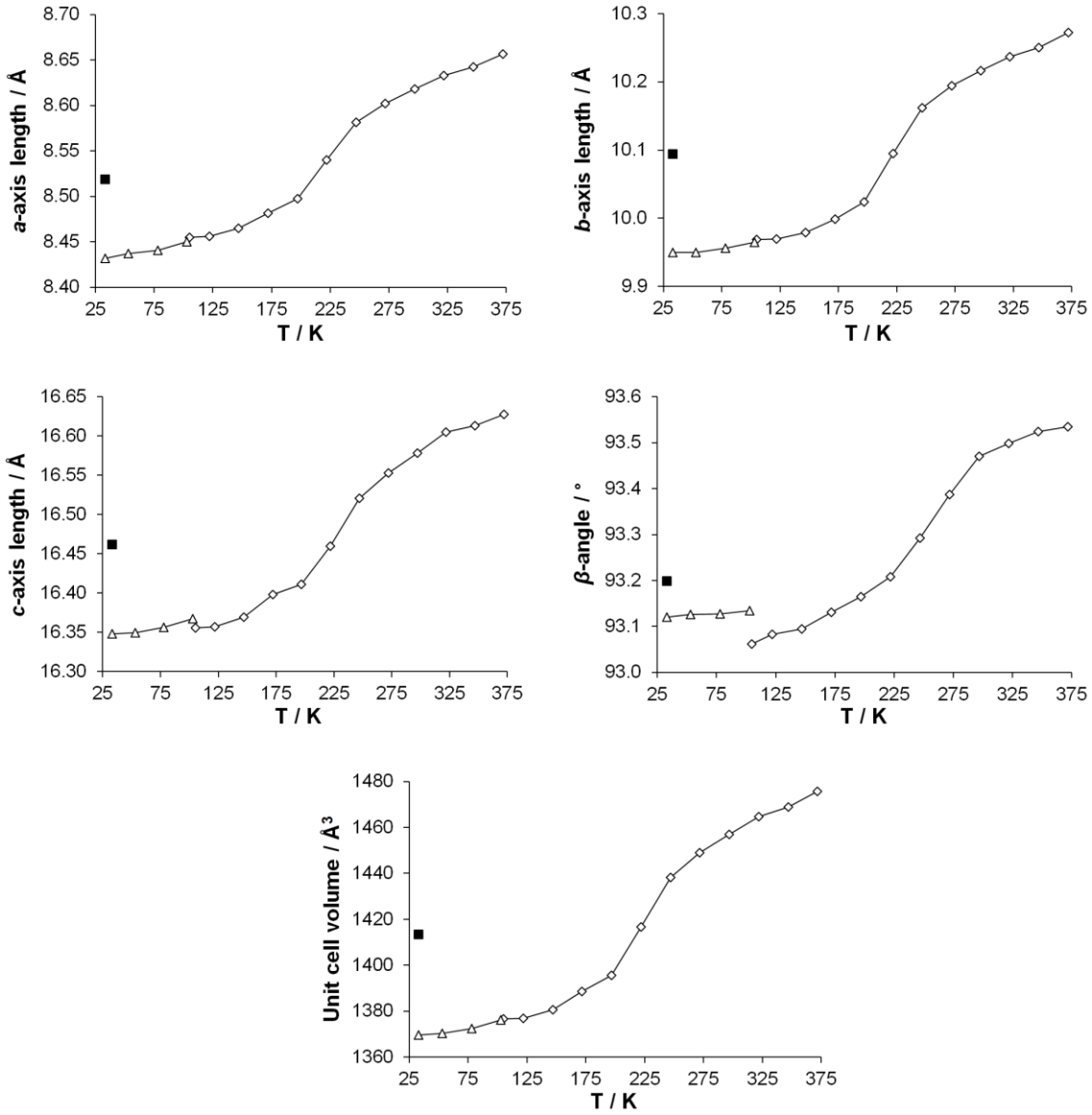

Figure 4.2 -Cell parameters for **A** measured as a function of temperature: (◊) and (Δ) data collected using the Cryostream (Crystal 2) and HeliX (Crystal 1) respectively; (■) cell parameters for the LIESST HS* state (Crystal 1). Error bars are included but obscured by the data point markers.

The HS structure of **A** described in this paper is consistent with the previously reported structure of **A** at 293 K[36, 40], since all of the structures determined herein have significant similarities the 125 K structure is used for the following discussion of the key structural features (Figure 4.3). **A** crystallises in the monoclinic space group $P2_1/n$ with half a molecule in the asymmetric unit (Z' = 0.5, Z = 2); the full molecule consists of a 6-coordinate iron metal centre bound to two abpt (each coordinated through both a pyridyl and a tiazole nitrogen) and two NCSe ligands. The two NCSe ligands are coordinated *trans* to each other and are approximately linear with an N1-C1-Se1 bond angle of 177.8(2)°, however the NCSe is slightly bent with respect to the iron metal centre with an Fe1-N1-C1 bond angle of 171.4(2)°. The N-Fe-N angles between the NCSe and abpt ligands range from 87.96(8) - 92.03(8)°. The abpt ligands are slightly distorted from planarity; there is an angle of 10.8(1)° between planes calculated through the two 6-membered pyridyl rings and angles of 9.0(1)° and 11.4(1)° between the 5-membered triazole ring and either of the pyridyl (N7, C9-C13) or (N2, C2-C6) rings respectively. An intramolecular hydrogen bond is present between N6-H6B···N7 for which D-H = 0.94(3) Å, H···A = 2.09(3) Å, D···A = 2.853(3) Å, <DHA = 138(2)º, along

with a weak intramolecular C2-H2···N4#1 (#1 = 1-*x*, 1-*y*, 1-*z*) interaction with D-H = 0.95 Å, H···A = 2.35 Å, D···A = 3.132(3) Å, <DHA = 140º. In addition, a short intermolecular N6-H6A···Se1#2 (#2 = 1/2+*x*, 3/2-*y*, 1/2+*z*) interaction for which D-H = 0.96(3) Å, H···A = 2.65(3) Å, D···A = 3.476(2) Å, <DHA = 145(2)º was identified. The structure also contains π-π contacts with a centroid (N2, C2-C6) to centroid (N7#3, C9#3-C13#3, #3 = 1-*x*, 2-*y*, 1-*z*) distance of 3.684(1) Å and an offset of 1.432(4) Å. These π-π contacts create a 1-dimensional chain through the lattice in the approximate direction of the *b*-axis (Figure 4.4).

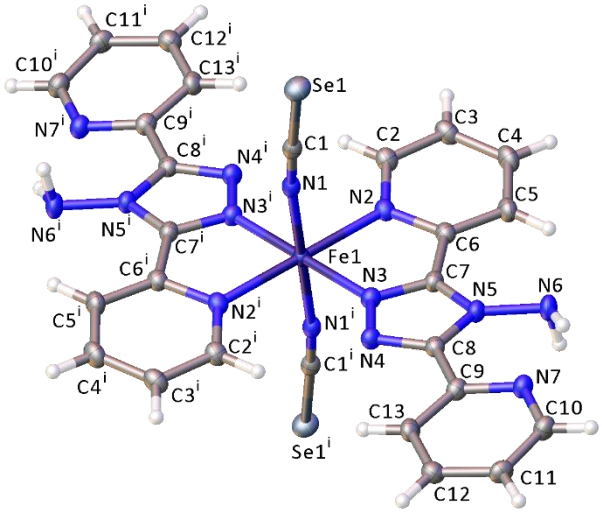

Figure 4.3 - Crystal structure of $[Fe(abpt)_2(NCSe)_2]$ polymorph **A** at 125 K with ellipsoids depicted at 50% probability level. The asu consists of half a molecule and 'i' represents the other half of the molecule which is related by the symmetry operator 1-*x*, 1-*y*, 1-*z*.

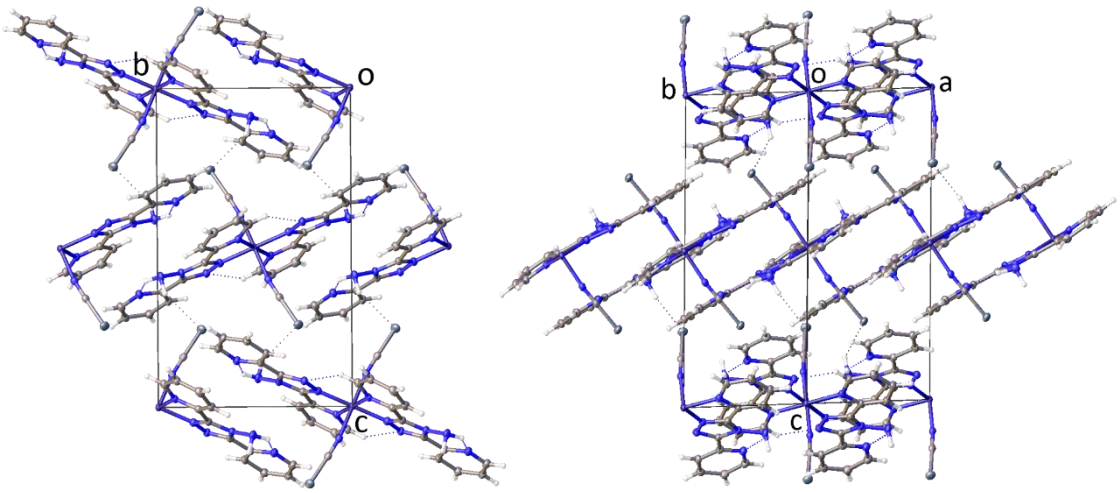

Figure 4.4 - Diagrams showing the packing of $[Fe(abpt)_2(NCSe)_2]$ polymorph **A** at 30 K viewed along the (left) (100) and (right) (110) directions.

The structure determined at temperatures between 375 - 30 K (Appendix 4, Table S4.1,S4.3-S4.5) show that, although the key structural features of **A** discussed above are not significantly altered as a result of the spin crossover, there are changes in some of the geometric parameters which

are worth noting. As is commonly observed for spin crossover compounds, all the Fe-N bond distances decrease by ~0.2 Å as the structure goes from HS to LS. In this case the range of Fe-N bond lengths in **A** decreases from 2.127(3) - 2.218(3) Å at 375 K to 1.955(2) - 2.014(2) Å at 30 K with the change in each unique Fe-N bond length through the spin crossover temperature range (Figure 4.5) following the trend observed in the magnetic data.[35, 36] The thermal HS to LS crossover for **A** is accompanied by a decrease in the distortion parameter (Σ) and volume of the Fe octahedron (V_p), see Table 4.3 and Appendix 4, Table S4.3. There is no significant change in unit cell parameters, Σ and V_p between crystal structures of **A** collected at 225 K (~ $T_{1/2}$) during cooling (↓) and warming (↑) cycles through the spin crossover (ramp rate 120 K/hr) (Appendix 4, Table S4.2). This is consistent with the magnetic data,[36] and indicates that thermal hysteresis is not observed for **A**. A gradual reduction in the diffraction quality occurs as a result of the spin crossover and after prolonged irradiation fracturing of the crystal was visible to the eye. The spin crossover in **2A** caused no apparent reduction in crystallinity[29] so it is unclear why the structural integrity of the crystal lattice of **A**, which is isostructural to **2A**, is more sensitive to the spin crossover.

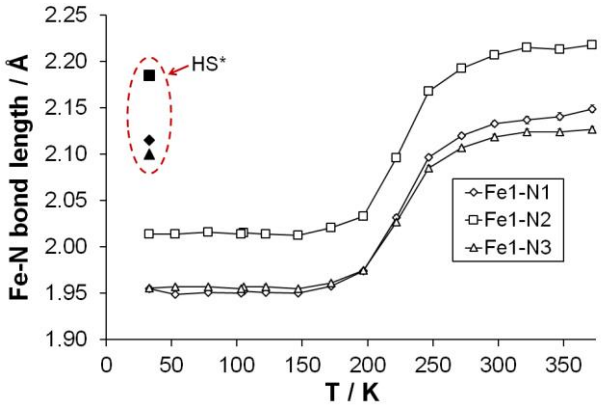

Figure 4.5 - Change in Fe-N bond lengths as a function of temperature, LIESST HS* values are contained within the dashed oval. Error bars are included but obscured by the data point markers.

In both **A** and the isostructural sulfur complex, $[Fe(abpt)_2(NCS)_2]$ polymorph **A** (**2A**), the HS to LS spin crossover results in a shortening of the intramolecular C2-H2···N4#1 (#1 = 1-*x*, 1-*y*, 1-*z*) interaction distance.[29] As indicated by the reduction in Σ, all the N-Fe-N bond angles get closer to 90° upon cooling through the HS to LS spin crossover. The N2-Fe1-N3 angle increases from 74.8(1)° at 375 K to 79.9(1)° at 30 K and there is a concomitant decrease in the N2-Fe-N3#1 (#1 = 1-*x*, 1-*y*, 1-*z*) angle from 105.2(1)° at 375 K to 100.1(1)° at 30 K. Similar changes in the N-Fe-N bond angles with temperature are observed for **2A**.[29] The π-π contacts between symmetry related pyridyl rings (N2, C2-C6) and (N7#3, C9#3-C13#3, #3 = 1-*x*, 2-*y*, 1-*z*), the intramolecular N6-H6B···N7 hydrogen bond and intermolecular N6-H6A···Se1#2 (#2 = 1/2+*x*, 3/2-*y*, 1/2+*z*) interaction all show either limited or no change across the investigated temperature range (Appendix 4, Table S4.4 and S4.5).

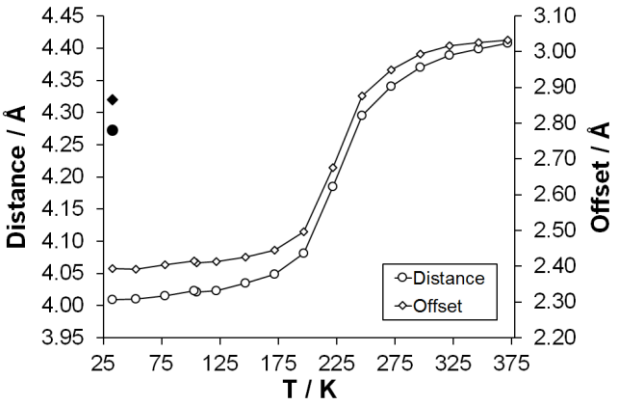

Figure 4.6 - Change in centroid-centroid separation between (N2, C2-C6) and (N2#4, C2#4-C6#4, #4 = 2-*x*, 1-*y*, 1-*z*) pyridyl rings: (○) distances and (◊) offsets as a function of temperature; (●) distance and (♦) offset for the LIESST HS* structure. Note: The values for these interaction parameters lie beyond those typically associated with a π-π interaction. Error bars are included but obscured by the data point markers.

As a result of the spin crossover significant shifting of adjacent molecules is observed. This can be illustrated nicely by looking at the change in the centroid-centroid distance between two of the adpt ligands pyridyl rings (N2, C2-C6) and (N2#4, C2#4-C6#4, #4 = 2-*x*, 1-*y*, 1-*z*) in neighbouring molecules. Clearly, the separation and offset of these rings are beyond those typically associated with π-π interactions and hence no inference of a significant interaction is intended (Figure 4.6, Figure 4.7), however, it is worth noting that a similar change is also observed for **2A** as a result of the spin crossover.[29]

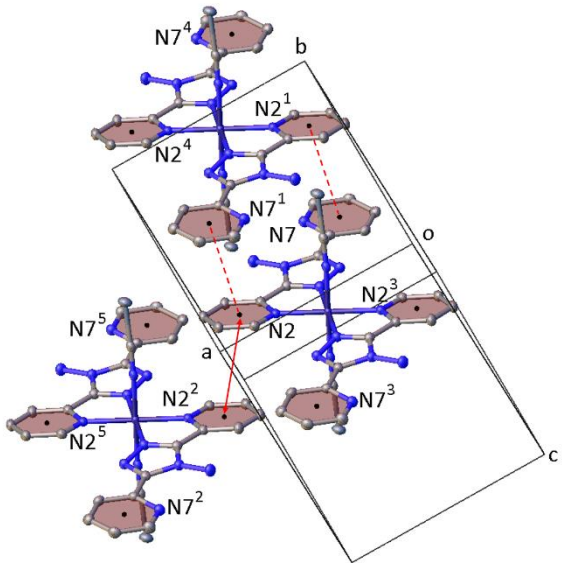

Figure 4.7 - Illustration of (red dashed lines) the π-π contact between (N2, C2-C6) and (N7[1], C9[1]-C13[1]) and (red solid arrow) the centroid-centroid separation distance between (N2, C2-C6) and (N7[2], C9[2]-C13[2]) that decreases as a function of temperature. Symmetry codes: [1] 1-*x*, 2-*y*, 1-*z*; [2] 2-*x*, 1-*y*, 1-*z*; [3] 1-*x*, 1-*y*, 1-*z*; [4] +*x*, 1+*y*, +*z*; [5] 1+*x*, +*y*, +*z*.

4.4.2 LIESST metastable HS* structure at 30 K

A critical LIESST temperature, T_{LIESST}, of ~32 K has been reported for **A** from magnetic measurements on a microcrystal sample.[36] The sulfur analogue, **2A**, which displays T_{LIESST} ~ 40 K, relaxes from the HS* state back to the LS state within ~4000 s[29, 36] at 30 K whereas **A** relaxes on a much quicker timescale. At 10 K, less than 20% of the HS* state of **A** exists beyond 500 - 1000 s and complete conversion back to the LS state is observed within <4000 s.[36] As the T_{LIESST} is only just above the minimum temperature of 30 K achievable on the in-house HeliX and given the rapid relaxation times in order to try and maintain a photostationary LIESST HS* structure throughout the data collection, the sample was subjected to continuous *in-situ* laser irradiation (670 nm, 5 mW CW laser). The structural changes observed in the resultant structure were consistent with those expected for a LS to HS* state spin crossover, i.e. the geometric parameters were similar to those seen in the HS structures collected around room temperature, indicating the successful formation of the LIESST metastable HS* state of **A**. Since the key structural features of the HS* structure are very similar to those of the 275 K HS structure (Table 4.3) only a few key points are highlighted here. The HS* structure maintains the same monoclinic space group, $P2_1/n$, found in the HS and LS structures, with an ~3% increase in the unit cell volume relative to the 30 K LS structure. As expected the Fe-N bond lengths in the 30 K HS* structure [2.100(3) - 2.185(3) Å] are almost 0.2 Å longer than those in the 30 K LS structure [1.955(2) - 2.014(2) Å]. In addition, the distortion parameter and Fe octahedron volume also increase as a result of the LS to HS* spin crossover: from Σ = 49.5(6)° and V_p = 10.105(8) Å^3 (LS, 30 K) to Σ = 67.4(8)° and V_p = 12.524(11) Å^3 (HS*, 30 K). It is worth noting that it is unknown whether the crystals used in this study retained a residual ground state, LS, fraction even during continuous irradiation at 30 K and the potential for any resulting bias in the HS* structural parameters was not investigated.[50]

Table 4.3 - Fe-N bond lengths for all structures, along with the distortion parameter, Σ, and the volume of the Fe octahedron, V_p.

	30(2) K LIESST HS*	30(2) K	125(2) K	150(2) K	175(2) K
Fe1-N1 / Å	2.115(3)	1.955(2)	1.951(2)	1.950(2)	1.958(2)
Fe1-N2 / Å	2.185(3)	2.014(2)	2.014(2)	2.013(2)	2.021(2)
Fe1-N3 / Å	2.100(3)	1.956(2)	1.957(2)	1.955(2)	1.961(2)
Σ[a] / º	67.4(8)	49.5(6)	50.0(5)	49.8(6)	51.0(6)
V_p[b] / Å^3	12.524(11)	10.105(8)	10.087(6)	10.067(6)	10.174(7)

[a] Σ, the angle distortion parameter, is the sum of the absolute value of the deviation of all 12 *cis* N-Fe-N angles from 90°. [b] V_p is the volume of the Fe octahedron calculated in Olex2.[47]

Table 4.3 continued - Fe-N bond lengths for all structures, along with the distortion parameter, Σ, and the volume of the Fe octahedron, V_p.

	225(2) K	275(2) K	325(2) K	375(2) K
Fe1-N1 / Å	2.032(3)	2.120(3)	2.137(4)	2.149(4)
Fe1-N2 / Å	2.096(2)	2.193(2)	2.215(3)	2.218(3)
Fe1-N3 / Å	2.027(2)	2.107(2)	2.124(3)	2.127(3)
Σ[a] / º	59.0(6)	68.3(6)	69.4(8)	70.2(8)
V_p[b] / Å^3	11.234(8)	12.629(9)	12.939(12)	13.029(12)

[a] Σ, the angle distortion parameter, is the sum of the absolute value of the deviation of all 12 *cis* N-Fe-N angles from 90°. [b] V_p is the volume of the Fe octahedron calculated in Olex2.[47]

4.4.3 Variable temperature UV-Vis transmission spectroscopy

Single crystals of **A** are an intense red colour in the HS state and gradually change to darker red upon cooling and, similar to **2A**,[29, 36] a residual HS fraction may remain in the predominantly LS state at low temperature. It is therefore challenging to collect good quality transmission spectra, particularly at low temperature, and assignment of the UV-Vis absorption bands to particular transitions is beyond the scope of this study. Figure 4.8 shows normalised UV-Vis transmission spectra obtained from a single crystal fragment of **A** at 290 K (HS state), 190 K and 110 K (LS state) collected as part of a kinetic series slow cooling through the spin crossover. At 290 K, where **A** is purely in the HS state, the spectrum shows one main band at ~524 nm and an absorbance edge ~580 nm. Below 190 K the spin crossover is virtually complete, **A** is essentially in the LS state and there is very little further spectral change. The one featureless band shown in the 190 K and 110 K spectra sits at a slightly longer wavelength than that observed at 290 K, resulting is movement of the absorption edge to longer wavelengths, ~610 nm and is consistent with the darker red colour of the crystal. Magnetic studies on **A** have shown a residual γ_{HS} at low temperature of 16% for a precipitated polycrystalline sample[35] and 0% for a sample consisting of single crystals.[36] The crystal preparation method used in this study differs from previous reports[35, 36] and it is unknown whether there is any residual HS contribution to the low temperature LS spectra. The crystal mount contracts during cooling and the crystal was repositioned in the beam several times during the experiment to maintain consistent illumination, therefore calculation of the percentage HS to LS conversion is not possible from the UV-Vis spectra.

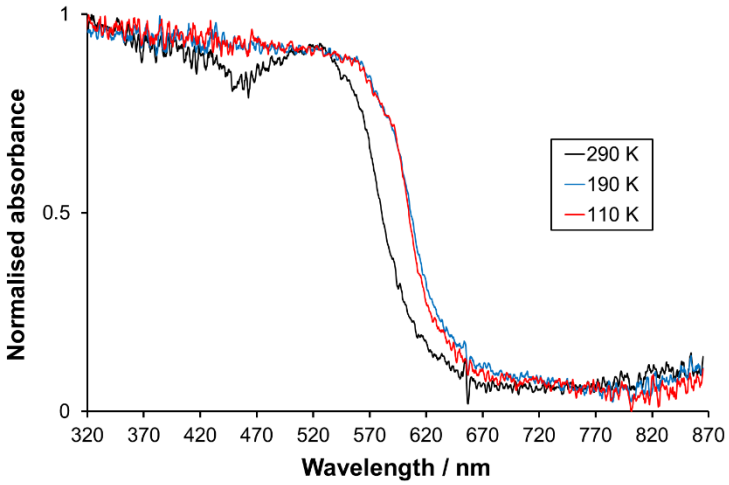

Figure 4.8 - Normalised UV-Vis absorbance spectra for $[Fe(abpt)_2(NCSe)_2]$ polymorph **A** at 290 K, 190 K and 110 K collected as part of a kinetic series cooling at 150 K/hr.

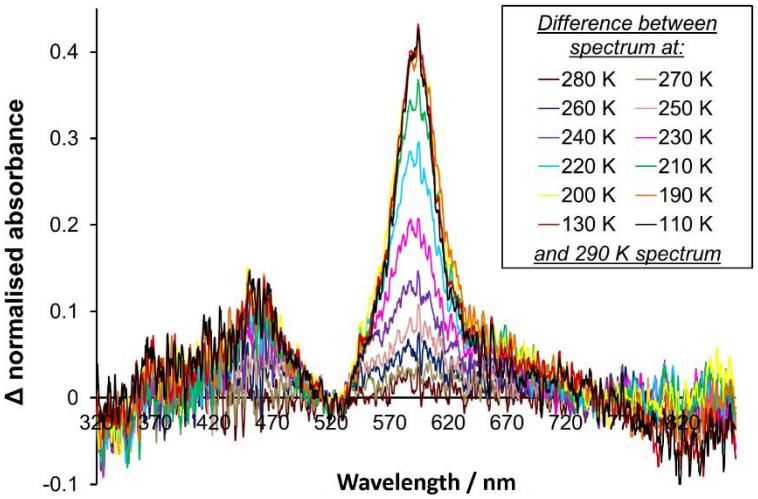

Figure 4.9 - Difference spectra for **A** calculated by ratioing the normalised absorbance spectrum at 290 K with spectra at various temperatures across the spin transition temperature range.

Figure 4.9 shows that, in the wavelength region investigated, the largest change in absorbance with temperature occurs in the ~530 - 710 nm region with a maximum at 594 nm. It is difficult to distinguish any other small systematic changes with temperature from the noise, although there is a suggestion of a second transition centred around ~460 nm.

The transition shape and $T_{1/2}$ value reported from magnetic data for the thermal spin crossover in single crystals of **A**,[36] are closely mirrored in both the profile of the absorbance change with temperature at 594 nm (Figure 4.10) and the variable temperature crystallographic studies in this paper.

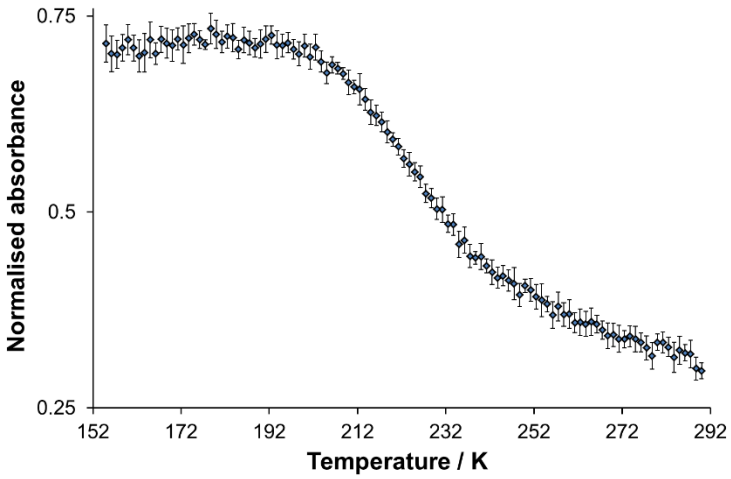

Figure 4.10 - Normalised absorbance spectrum for **A** showing the change in absorbance at 594 nm upon cooling at 150 K/hr through the thermal spin crossover temperature range. Note: Lower transmission intensity was observed between 154 - 132 K due to contraction of the crystal mount; at 132 K the mount was adjusted and spectra obtained between 132 - 83 K are consistent with those at 154 K, hence only data above 154 are presented.

4.5 Structural comparison of polymorphs A and B

Unlike **A**, polymorph **B** does not undergo a thermal spin crossover at ambient pressure.[40] The previously published structure of polymorph **B**[40] is used for the following discussions and comparison with polymorph **A** presented in this paper. Polymorph **B**, for which data were collected at 300 K, also crystallised in the monoclinic space group $P2_1/n$ with half a molecule in the asymmetric unit (Z' = 0.5, Z = 2). There are a number of similarities between the two polymorphs and in **B** the NCSe ligands are also approximately linear with an N-C-Se bond angle of ~179°, the NCSe ligands are also slightly bent with respect to the iron metal centre with an Fe-N-C angle of ~170°. In addition, the N-Fe-N angles between the NCSe and adpt ligands are in line with those seen for **A** ranging from ~87-93°. However, in **B** the adpt ligands are significantly distorted from planarity and there is an angle of ~36° between planes calculated through the two pyridyl ligands and ~7° and 31° between the 5 membered triazole ring and the two 6 membered rings respectively. This compares to values in **A** at 300(2) K of 9.4(2)° between the two pyridyl rings and 7.9(2)° and 7.5(2)° between the 5 membered and each of the pyridyl rings. This difference in configuration of the adpt rings may explain significant differences in the packing of the two polymorphs. In **A**, the three rings of the adpt ligands of adjacent molecules are aligned above each other with π-π interactions at each end between the pyridyl rings (at 300(2) K centroid to centroid distance 3.688(2), offset 1.339(6) Å) creating a 1-dimensional chain in approximately the *b*-axis direction. In **B**, each of the pyridyl rings on an adpt ligand forms π-π interactions (centroid to centroid distance ~3.73 Å, offset ~1.26 Å) with the pyridyl ring of adpt ligands that are on different molecules, creating a 2-dimensional network approximately parallel to the *ac* plane. Given the relatively gradual nature of the spin crossover in **A** it seems reasonable to suggest that there is limited communication between the molecules. The influence of intermolecular interactions and communication between the metal centres on the spin crossover behaviour of a compound is well documented. In this case it would appear reasonable to suggest that the lack of spin crossover in **B** is as a result of the 2-dimensional nature of the π-π interactions in **B** having affected communication between the metal centres as compared to **A** which forms a 1-

dimensional chain as result of the pi-pi interactions involving the two pyridyl rings of both adpt ligands.

4.6 Conclusions

Structural and spectral changes associated with the spin crossover behaviour of $[Fe(abpt)_2(NCSe)_2]$ polymorph **A** have been successfully characterised. A clear shift is observed between the absorbance spectra obtained for the high and low spin complexes, monitoring the spectral changes in this region as a function of temperature shows a change consistent with the spin crossover observed in the previously published magnetic data. Likewise, the unit cell parameters change as a function of temperature with a profile that matches those observed in the magnetic data and supports the occurrence of spin crossover. The Fe-N bond lengths, distortion parameter (Σ) and volume of the Fe octahedron (V_p) all decrease as a result of the HS to LS spin crossover and follow the trends commonly associated with spin crossover complexes. It is interesting to note that for both **A** (NCSe) and **2A** (NCS),[29] the HS to LS spin crossover causes a shifting of adjacent molecules towards each other. This change was apparent in **A** through a change in distance between two of the adpt ligands pyridyl rings (N2, C2-C6) and (N2#4, C2#4-C6#4, #4 = 2-*x*, 1-*y*, 1-*z*) in neighbouring molecules, although it should be noted that the separation distance between pyridyl rings remains beyond that associated with significant π-π interactions. A LIESST HS* structure for $[Fe(abpt)_2(NCSe)_2]$ polymorph **A** at 30 K is also reported and shown to have similar features to the HS structure at approximately room temperature. Comparing the structures of polymorphs **A** to **B** (which had been previously published and does not show a thermal spin transition at ambient pressure), shows clear differences in the relative orientations of the pyridyl rings on the same adpt ligand with twist angles of 9.4(2)° and ~36° respectively. The packing was found to be quite different for the two polymorphs with **A** having 1-dimensional chains created by π-π interactions between pairs of adpt ligands on adjacent molecules in which both pyridyl groups were involved while in **B** the π-π interactions formed a 2-dimensional network as a result of each pyridyl ring on an adpt ligand forming an interaction to the pyridyl ring on an adpt ligand in different molecules. Given the importance of intermolecular interactions on the spin crossover behaviour of compounds it seems reasonable to suggest that the nature of the interactions in **B** have affected the communication between metal centres and thus accounts for the lack of spin crossover for this polymorph.

4.7 References

1. L. Cambi and L. Szegö, *Berichte Der Deutschen Chemischen Gesellschaft*, 1931, **64 (10)**, 2591-2598.
2. A. Bousseksou, G. Molnar, L. Salmon and W. Nicolazzi, *Chem. Soc. Rev.*, 2011, **40**, 3313-3335.
3. M. A. Halcrow, *Chem. Soc. Rev.*, 2011, **40**, 4119-4142.
4. M. D. Manrique-Juarez, S. Rat, F. Mathieu, D. Saya, I. Seguy, T. Leichle, L. Nicu, L. Salmon, G. Molnar and A. Bousseksou, *Applied Physics Letters*, 2016, **109**.
5. P. Gütlich and H. A. Goodwin, eds., *Spin Crossover in Transition Metal Compounds I, II and III*, Springer-Verlag: Berlin, Heidelberg, New York, 2004.
6. M. A. Halcrow, ed., *Spin-Crossover Materials: Properties and Applications*, John Wiley & Sons, Ltd.: Chichester, UK, 2013.
7. O. V. Farberovich and V. L. Mazalova, *Journal of Magnetism and Magnetic Materials*, 2016, **405**, 169-173.
8. M. D. Manrique-Juarez, S. Rat, L. Salmon, G. Molnar, C. M. Quintero, L. Nicu, H. J. Shepherd and A. Bousseksou, *Coord. Chem. Rev.*, 2016, **308**, 395-408.
9. B. Doistau, L. Benda, B. Hasenknopf, V. Marvaud and G. Vives, *Magnetochemistry*, 2018, **4**.

10. P. Gütlich, A. B. Gaspar and Y. Garcia, *Beilstein J. Org. Chem.*, 2013, **9**, 342-391.
11. B. Fei, X. Q. Chen, Y. D. Cai, J. K. Fang, M. L. Tong, J. Tucek and X. Bao, *Inorganic Chemistry Frontiers*, 2018, **5**, 1671-1676.
12. P. Gütlich, V. Ksenofontov and A. B. Gaspar, *Coord. Chem. Rev.*, 2005, **249**, 1811-1829.
13. J. Laisney, H. J. Shepherd, L. Rechignat, G. Molnar, E. Riviere and M. L. Boillot, *Phys. Chem. Chem. Phys.*, 2018, **20**, 15951-15959.
14. A. Hauser, *Light-Induced Spin Crossover and the High-Spin→Low-Spin Relaxation.*, Springer-Verlag: Berlin, Heidelberg, New York, 2004.
15. A. Tsukiashi, M. Nakaya, F. Kobayashi, R. Ohtani, M. Nakamura, J. M. Harrowfield, Y. Kim and S. Hayami, *Inorg. Chem.*, 2018, **57**, 2834-2842.
16. H. S. Scott, R. W. Staniland and P. E. Kruger, *Coord. Chem. Rev.*, 2018, **362**, 24-43.
17. M. Nihei, T. Shiga, Y. Maeda and H. Oshio, *Coord. Chem. Rev.*, 2007, **251**, 2606-2621.
18. A. B. Gaspar, M. C. Muñoz, V. Niel and J. A. Real, *Inorg. Chem.*, 2001, **40**, 9-10.
19. P. Nielsen, H. Toftlund, A. D. Bond, J. F. Boas, J. R. Pilbrow, G. R. Hanson, C. Noble, M. J. Riley, S. M. Neville, B. Moubaraki and K. S. Murray, *Inorg. Chem.*, 2009, **48**, 7033-7047.
20. J. Tao, R.-J. Wei, R.-B. Huang and L.-S. Zheng, *Chem. Soc. Rev.*, 2012, **41**, 703-737.
21. I. Salitros, L. Pogany, M. Ruben, R. Boca and W. Linert, *Dalton Trans.*, 2014, **43**, 16584-16587.
22. H. Hang, B. Fei, X. Q. Chen, M. L. Tong, V. Ksenofontov, I. A. Gural'skiy and X. Bao, *Journal of Materials Chemistry C*, 2018, **6**, 3352-3361.
23. A. I. Vicente, L. P. Ferreira, M. D. Carvalho, V. H. N. Rodrigues, M. M. Dirtu, Y. Garcia, M. J. Calhorda and P. N. Martinho, *Dalton Trans.*, 2018, **47**, 7013-7019.
24. M. Griffin, S. Shakespeare, H. J. Shepherd, C. J. Harding, J.-F. Létard, C. Desplanches, A. E. Goeta, J. A. K. Howard, A. K. Powell, V. Mereacre, Y. Garcia, A. D. Naik, H. Mueller-Bunz and G. G. Morgan, *Angew. Chem., Int Ed.*, 2011, **50**, 896-900.
25. W. Liu, Y. Y. Peng, S. G. Wu, Y. C. Chen, M. N. Hoque, Z. P. Ni, X. M. Chen and M. L. Tong, *Angew. Chem., Int Ed.*, 2017, **56**, 14982-14986.
26. A. Schober, S. Demeshko and F. Meyer, *Zeitschrift Fur Anorganische Und Allgemeine Chemie*, 2018, **644**, 719-728.
27. L. Li, A. R. Craze, R. Akiyoshi, A. Tsukiashi, S. Hayami, O. Mustonen, M. M. Bhadbhade, S. Bhattacharyya, C. E. Marjo, Y. Wang, L. F. Lindoy, J. R. Aldrich-Wright and F. Li, *Dalton Trans.*, 2018, **47**, 2543-2548.
28. S. De, L. M. Chamoreau, H. El Said, Y. L. Li, A. Flambard, M. L. Boillot, S. Tewary, G. Rajaraman and R. Lescouezec, *Frontiers in Chemistry*, 2018, **6**.
29. H. E. Mason, W. Li, M. A. Carpenter, M. L. Hamilton, J. A. K. Howard and H. A. Sparkes, *New J Chem*, 2016, **40**, 2466-2478.
30. A. I. Rykov, J. Wang, T. Zhang and K. Nomura, *Hyperfine Interactions*, 2013, **218**, 139-143.
31. L. Pogany, B. Brachnakova, J. Moncol, J. Pavlik, I. Nemec, Z. Travnicek, M. Mazur, L. Bucinsky, L. Suchanek and I. Salitros, *Chem. -Eur. J.*, 2018, **24**, 5191-5203.
32. D. R. Zhu, Y. Xu, Z. Yu, Z. J. Guo, H. Sang, T. Liu and X. Z. You, *Chem. Mat.*, 2002, **14**, 838-843.
33. R. W. Hogue, R. G. Miller, N. G. White, H. L. C. Feltham, G. N. L. Jameson and S. Brooker, *Chem. Commun.*, 2014, **50**, 1435-1437.
34. J. A. Kitchen, G. N. L. Jameson, J. L. Tallon and S. Brooker, *Chem. Commun.*, 2010, **46**, 3200-3202.
35. N. Moliner, M. C. Muñoz, P. J. van Koningsbruggen and J. A. Real, *Inorg. Chim. Acta*, 1998, **274**, 1-6.
36. N. Moliner, M. C. Muñoz, S. Létard, J. F. Létard, X. Solans, R. Burriel, M. Castro, O. Kahn and J. A. Real, *Inorg. Chim. Acta*, 1999, **291**, 279-288.
37. C.-H. Shih, C.-F. Sheu, K. Kato, K. Sugimoto, J. Kim, Y. Wang and M. Takata, *Dalton Trans.*, 2010, **39**, 9794-9800.

38. C.-F. Sheu, C.-H. Shih, K. Sugimoto, B.-M. Cheng, M. Takata and Y. Wang, *Chem. Commun.*, 2012, **48**, 5715-5717.
39. C.-F. Sheu, S.-M. Chen, S.-C. Wang, G.-H. Lee, Y.-H. Liu and Y. Wang, *Chem. Commun.*, 2009, 7512-7514.
40. A. B. Gaspar, M. C. Muñoz, N. Moliner, V. Ksenofontov, G. Levchenko, P. Gütlich and J. A. Real, *Monatsh. Chem.*, 2003, **134**, 285-294.
41. A. E. Goeta, L. K. Thompson, C. L. Sheppard, S. S. Tandon, C. W. Lehmann, J. Cosier, C. Webster and J. A. K. Howard, *Acta Crystallogr., Sect. C: Cryst. Struct. Commun.*, 1999, **55**, 1243-1246.
42. Bruker, *SMART-NT, Data Collection Software, Version 5.63, Bruker Analytical X-ray Instruments Inc., Madison, WI, USA*, 2000.
43. Bruker, *SAINT-NT, Data Reduction Software Ver. 6.14, Bruker Analytical X-ray Instruments Inc., Madison, WI, USA*, 2000.
44. Bruker, *SAINT+ Integration Engine, Data Reduction Software, Bruker Analytical X-ray Instruments Inc., Madison, WI, USA*, 2007.
45. Bruker, *SADABS, Bruker AXS area detector scaling and absorption correction, Bruker Analytical X-ray Instruments Inc., Madison, Wisconsin, USA*, 2001.
46. G. M. Sheldrick, *Acta Crystallogr., Sect. A: Found. Crystallogr.*, 2008, **64**, 112-122.
47. O. V. Dolomanov, L. J. Bourhis, R. J. Gildea, J. A. K. Howard and H. Puschmann, *J. Appl. Crystallogr.*, 2009, **42**, 339-341.
48. M. R. Probert, *SMARTreduce, Durham University, UK*, 2009.
49. *MathWorks, MATLAB and Statistics Toolbox Release 2013a. 8.1.0.604 ed.; The MathWorks, Inc.: Natick, Massachusetts, United States*, 2013, **Vol. 2013a**.
50. V. Legrand, S. Pillet, H.-P. Weber, M. Souhassou, J.-F. Létard, P. Guionneau and C. Lecomte, *J. Appl. Crystallogr.*, 2007, **40**, 1076-1088.

Chapter 5

$Co(abpt)_2(NCS)_2$ and $Ni(abpt)_2(NCS)_2$: Structural Characterisation of Polymorphs A and B

Helen E. Mason, Judith A. K. Howard and Hazel A. Sparkes

Published *Acta Crystallographica C*, 2021, in publication, doi.org/10.1107/S2053229621010251. Reproduced with permission of the International Union of Crystallography.

5.1 Abstract

The synthesis and structures of $Co(abpt)_2(NCS)_2$ and $Ni(abpt)_2(NCS)_2$ are reported. In both cases two polymorphs, **A** and **B**, were identified and structurally characterised. For both polymorphs the structures obtained with the different metals, *i.e.* Co(II) or Ni(II), were found to be isostructural. All of the structures contained an intramolecular N-H···N hydrogen bond, C-H···N interactions and π-π stacking interactions. No structural evidence for a thermal spin crossover was observed for either of the $Co(abpt)_2(NCS)_2$ polymorphs between 300(2) and 120(2) K.

5.2 Introduction

The bidentate ligand 4-amino-3,5-bis(pyridine-2-yl)-1,2,4-triazole (abpt) has been found to form mononuclear complexes as well as single or double bridged dinuclear complexes with a variety of metals.[1-3] Amongst these a number of Fe(II) complexes have been synthesised and studied, because of their interesting polymorphism and spin crossover behaviour. Perhaps the most studied is the $Fe(abpt)_2(NCS)_2$ complex of which there are four known polymorphs assigned **A**-**D**, all of which display different magnetic behaviour. Three of the polymorphs **A**,[4-6] **C**[5, 7] and **D**[5, 8, 9] undergo at least a partial thermal spin crossover at ambient pressure, while **B**[10] only undergoes a thermal spin crossover at pressures above 4.4 kbar. All of the three polymorphs which display at least a partial thermal spin crossover also show light induced excited spin state trapping (LIESST) at low temperature. While three of the polymorphs, **A**, **B** and **D** are known to undergo a pressure induced spin crossover at room temperature,[6, 9] polymorph **C** has not been studied under pressure at room temperature. To date $Co(abpt)_2(NCS)_2$ is the only other $M(abpt)_2(NCS)_2$ complex containing a transition metal for which any structures have been reported. Like the Fe analogue this has also been found to display polymorphism with two different polymorphs of $Co(abpt)_2(NCS)_2$ reported at room temperature. These will be referred to as $Co(abpt)_2(NCS)_2$ polymorphs **B**[11] and **D**[12] throughout as they are isostructural with $Fe(abpt)_2(NCS)_2$ polymorphs **B** and **D**. The structures of two polymorphs, **A** and **B**, of $Co(abpt)_2(NCS)_2$ and $Ni(abpt)_2(NCS)_2$, are reported herein, see Scheme 5.1.

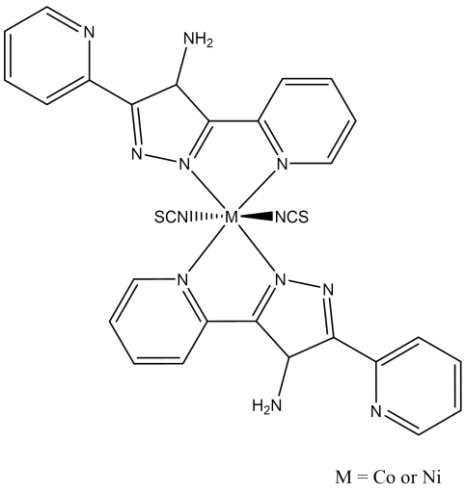

Scheme 5.1 - Schematic of the compounds studied.

5.3 Experimental

5.3.1 Synthesis

Synthesis of $[M(abpt)_2(NCS)_2$ where M=Co or Ni was carried out using a slow diffusion method with methanol-water solutions as previously reported.[5]

All chemicals were obtained from Sigma-Aldrich and used as supplied. $CoSO_4.7H_2O$ (1 mmol, 0.281 g) or $NiSO_4.6H_2O$ (1 mmol, 0.263 g) and KNCS (2 mmol, 0.194 g) were stirred in methanol (10 ml) for 15 min. Pale yellow insoluble K_2SO_4 precipitate was removed by filtration and deionised water (10 ml) was added to the remaining clear solution. abpt (2 mmol, 0.477 g) ligand was dissolved in methanol (20 ml) and placed in a narrow (<5 cm) Schlenk tube. The M^{2+}/NCX^- solution was very carefully pipetted at the bottom of the Schlenk to form a lower more dense layer below the abpt solution. Immediately a coloured band formed at the interface between the two layers containing the target complex. The Schlenk was left static and within one week to one month later single crystals suitable for X-ray diffraction studies are formed.

5.3.2 X-ray Crystallography

A Bruker Smart 1K CCD or Bruker D8 Venture diffractometer was used to collect single crystal X-ray diffraction data using graphite monochromated Mo*Kα* (λ = 0.71073 Å) X-ray radiation. Cooling was achieved using an Oxford Instruments open flow nitrogen Cryostream. Data collection was carried out using SMART software,[13] integration performed using SAINT[14] and absorption corrections applied using SADABS.[15] The structures were solved by direct methods in SHELXS[16] and refined by full matrix least squares on F^2 in SHELXL[16] in Olex2.[17] Non-hydrogen atoms were refined anisotropically and all hydrogen atoms were located geometrically and refined using a riding model except the NH hydrogen atoms which were located in the Fourier difference map (FDM) wherever feasible. Details of the crystallographic data collections are given in Table 5.1.

Table 5.1 - Crystal data and structure refinement details.

	$Co(abpt)_2(NCS)_2$		$Ni(abpt)_2(NCS)_2$	
	Polymorph **A**	Polymorph **B**	Polymorph **A**	Polymorph **B**
Empirical formula	$C_{26}H_{20}CoN_{14}S_2$	$C_{26}H_{20}CoN_{14}S_2$	$C_{26}H_{20}N_{14}NiS_2$	$C_{26}H_{20}N_{14}NiS_2$
Formula weight	651.61	651.61	651.39	651.39
Temperature/K	120(2)	120(2)	120(2)	120(2)
Crystal system	monoclinic	monoclinic	monoclinic	monoclinic
Space group	$P2_1/n$	$P2_1/n$	$P2_1/n$	$P2_1/n$
a/Å	8.4792(6)	11.4978(5)	8.4041(7)	11.5860(14)
b/Å	10.1307(7)	9.5235(4)	10.0681(9)	9.5489(12)
c/Å	16.3774(11)	12.7179(5)	16.2360(14)	12.8132(16)
α/°	90	90	90	90
β/°	93.4850(10)	100.7710(10)	93.060(2)	100.806(2)
γ/°	90	90	90	90
Volume/$Å^3$	1404.22(17)	1368.07(10)	1371.8(2)	1392.4(3)
Z	2	2	2	2
$\rho_{calc}g/cm^3$	1.541	1.582	1.577	1.554
μ/mm^{-1}	0.806	0.827	0.907	0.893
F(000)	666.0	666.0	668.0	668.0
Crystal size/mm^3	0.24 × 0.16 × 0.11	0.48 × 0.22 × 0.1	0.2 × 0.12 × 0.08	0.2 × 0.13 × 0.04
Radiation	MoKα (λ = 0.71073)	MoKα (λ = 0.71073)	MoKα (λ = 0.71073)	MoKα (λ = 0.71073)
2Θ range for data collection/°	4.73 to 52.724	4.386 to 52.72	4.762 to 52.744	4.352 to 50.682
Index ranges	-10 ≤ h ≤ 10, -12 ≤ k ≤ 12, -20 ≤ l ≤ 20	-14 ≤ h ≤ 14, -11 ≤ k ≤ 11, -15 ≤ l ≤ 15	-10 ≤ h ≤ 10, -12 ≤ k ≤ 12, -20 ≤ l ≤ 20	-13 ≤ h ≤ 13, -11 ≤ k ≤ 11, -14 ≤ l ≤ 15
Reflections collected	13341	13084	15450	12077
Independent reflections	2884 [R_{int} = 0.0440, R_{sigma} = 0.0354]	2799 [R_{int} = 0.0367, R_{sigma} = 0.0284]	2819 [R_{int} = 0.0459, R_{sigma} = 0.0400]	2552 [R_{int} = 0.1158, R_{sigma} = 0.0938]
Data/restraints/parameters	2884/1/202	2799/0/202	2819/0/202	2552/0/202
Goodness-of-fit on F^2	1.062	1.029	1.022	1.055
Final R indexes [I>=2σ (I)]	R_1 = 0.0391 wR_2 = 0.0874	R_1 = 0.0283 wR_2 = 0.0618	R_1 = 0.0365 wR_2 = 0.0777	R_1 = 0.0582 wR_2 = 0.1195
Final R indexes [all data]	R_1 = 0.0531 wR_2 = 0.0928	R_1 = 0.0378 wR_2 = 0.0647	R_1 = 0.0595 wR_2 = 0.0851	R_1 = 0.1047 wR_2 = 0.1361
Largest diff. peak/hole / e $Å^{-3}$	0.58/-0.27	0.26/-0.39	0.48/-0.27	0.61/-0.66

5.4 Results and Discussion

The structure of $Co(abpt)_2(NCS)_2$ polymorph **B** has already been published at room temperature and was consistent with that reported here (Peng *et. al.*, 2006).[11] The main structural features of all four structures are very similar, they all crystallised in the monoclinic space group $P2_1/n$ with half a molecule in the asymmetric unit (Z' = 0.5), see Figure 5.1. Each of the four complexes consists of an approximately octahedrally coordinated metal centre (Co(II) or Ni(II)) coordinated to six nitrogen atoms: one from each of the NCS ligands and two from each abpt ligand (one pyridyl and one triazole nitrogen). Each of the structures contains an intramolecular N-H···N hydrogen bond exists between the NH_2 group on the triazole and the N of the uncoordinated pyridyl ring, as well as two intramolecular C-H···N interactions one between a pyridyl C-H and the N of the NH_2

group attached to the triazole, and a second between a pyridyl C-H and the uncoordinated N on the triazole group, see Table 5.2.

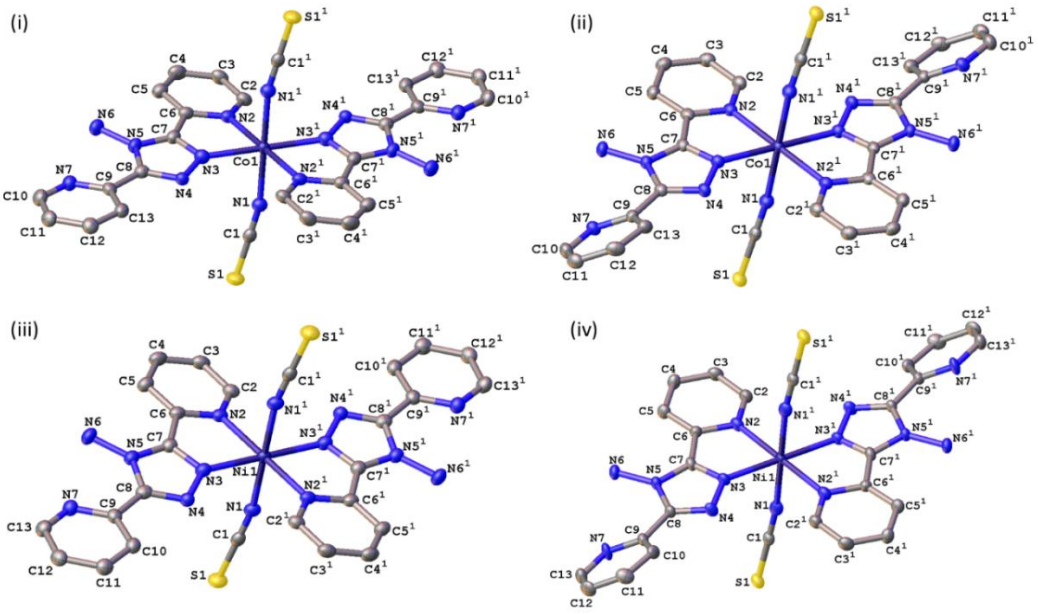

Figure 5.1 - Illustration of the structures of $Co(abpt)_2(NCS)_2$ (i) **A** (ii) **B** and $Ni(abpt)_2(NCS)_2$ (iii) **A** (iv) **B** with atomic numbering scheme depicted. Hydrogen atoms omitted for clarity. Symmetry code [1] = 1-*x*, 1-*y*, 1-*z*.

Table 5.2 - Hydrogen-bond geometry (Å, º) for $Co(abpt)_2(NCS)_2$ and $Ni(abpt)_2(NCS)_2$ at 120(2) K.

Structure	Polymorph	*D*—H···*A*	*D*—H	H···*A*	*D*···*A*	*D*—H···*A*
$Co(abpt)_2(NCS)_2$	**A**	N6—H6*B*···N7	0.90 (3)	2.14 (3)	2.861 (3)	136 (3)
		C5—H5···N6	0.95	2.53	3.135 (4)	122
		C2—H2···N4^{i}	0.95	2.67	3.467(3)	142
	B	N6—H6*B*···N7	0.90 (2)	2.41 (2)	2.914 (2)	115.6 (16)
		C5—H5···N6	0.95	2.46	3.084 (2)	123
		C2—H2···N2^{i}	0.95	2.66	3.482(2)	145
$Ni(abpt)_2(NCS)_2$	**A**	N6—H6*B*···N7	0.88 (3)	2.14 (3)	2.848 (3)	137 (3)
		C5—H5···N6	0.95	2.52	3.124 (4)	122
		C2—H2···N4^{ii}	0.95	2.55	3.347 (3)	141
	B	N6—H6*B*···N7	0.84 (6)	2.52 (5)	2.950 (6)	112 (4)
		C5—H5···N6	0.95	2.48	3.104 (7)	123
		C2—H2···N4^{ii}	0.95	2.59	3.403 (7)	144

(i) 1-*x*, 1-*y*, 1-*z*; (ii) −*x*+1, −*y*+1, −*z*+1.

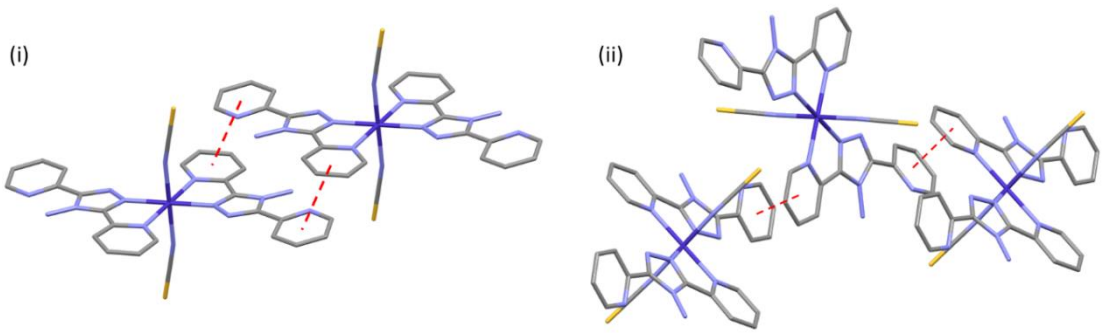

Figure 5.2 - Illustration of the π-π stacking interactions as red dashed lines for one abpt ligand in (i) polymorph **A** (ii) polymorph **B**.

The pair of polymorph **A**, Co(II) or Ni(II), structures are isostructural with each other and also isostructural with the previously published $Fe(abpt)_2(NCS)_2$ polymorph **A** structure.[4-6] In addition to the previously mentioned N-H···N hydrogen bonding and C-H···N interactions, the structures contain intermolecular π-π stacking between pairs of molecules and involving the two pyridyl rings at each end of the abpt ligand interacting with the two pyridyl rings on an adjacent abpt ligand creating a 1-dimensional chain through the structure, see Table 5.3, Figure 5.2.

Table 5.3 - π-π stacking interactions (Å) for $Co(abpt)_2(NCS)_2$ and $Ni(abpt)_2(NCS)_2$ at 120(2) K.

Structure	Polymorph	Plane 1	Plane 2	Centroid to centroid distance	Shift distance
$Co(abpt)_2(NCS)_2$	**A**	N2,C2-C6	N7,C9-C13^{i}	3.63	1.31
		N7,C9-C13	N2,C2-C6^{i}	3.63	1.31
	B	N2,C2-C6	N7,C9-C13^{ii}	3.68	1.34
		N7,C9-C13	N2,C2-C6^{iii}	3.68	1.34
$Ni(abpt)_2(NCS)_2$	**A**	N2,C2-C6	N7,C9-C13^{i}	3.64	1.34
		N7,C9-C13	N2,C2-C6^{i}	3.64	1.34
	B	N2,C2-C6	N7,C9-C13^{ii}	3.72	1.41
		N7,C9-C13	N2,C2-C6^{iii}	3.72	1.41

(i) 1-*x*, 2-*y*, 1-*z*; (ii) ½+*x*, 3/2-*y*, ½+*z*; (iii) –½+*x*, 3/2-*y*, -½+*z*;

As seen for the pair of polymorph **A** structures, the two polymorph **B** structures were also isostructural with each other and the previously published $Fe(abpt)_2(NCS)_2$ polymorph **B** structure.[9, 10] The structures of polymorph **B** also have π-π interactions but in this case each of the pyridyl rings on the abpt ligand is involved in a π-π interaction to a pyridyl ring on a different abpt ligand, creating a 3-dimensional network of interactions in the structure, see Table 5.3, Figure 5.2. Along with the difference in the form of the π-π interactions between the polymorph **A** and polymorph **B** structures, the other main difference is the twist between the two rings on the abpt ligands. In the case of **A** the twist between the rings is ~9°, while for **B** the twist between the rings is ~35°, see Table 5.4. This is likely to be the reason for the significantly different π-π stacking as

the larger twist in **B** would prevent both rings on one abpt ligand being correctly orientated to interact with both rings on a single abpt ligand on an adjacent molecule.

Table 5.4 - Twist and fold angles between planes calculated through the 6 atoms of the two rings on the abpt ligand at 120(2) K.

Compound	Polymorph	Twist angle (°)	Fold angle (°)
$Co(abpt)_2(NCS)_2$	**A**	8.99(8)	99.0(8)
	B	35.25(6)	142.50(19)
$Ni(abpt)_2(NCS)_2$	**A**	9.39(8)	96.7(8)
	B	34.64(17)	142.8(6)

The Hirshfeld fingerprint plots[18] for the two polymorphs highlight the differences between the two structures, see Figure 5.3. The plots are only shown for the Co polymorph **A** and **B** as the plots for the Ni polymorphs **A** and **B** were essentially identical to the respective Co polymorph. The shape of the two plots are clearly slightly different although given the structures are polymorphs it is unsurprising that they show the same main short contacts. For both polymorphs the S···H contacts are quite pronounced, with a similar shape and position. However, in the case of **A** the C···H contacts are more pronounced than seen for **B**, while the H···H contacts for **A** are less pronounced than observed for **B**. Examining the Hirshfeld surfaces for both compounds, the greater number of red spots on the surface of **A** than for **B** indicating that **A** has more short contacts.

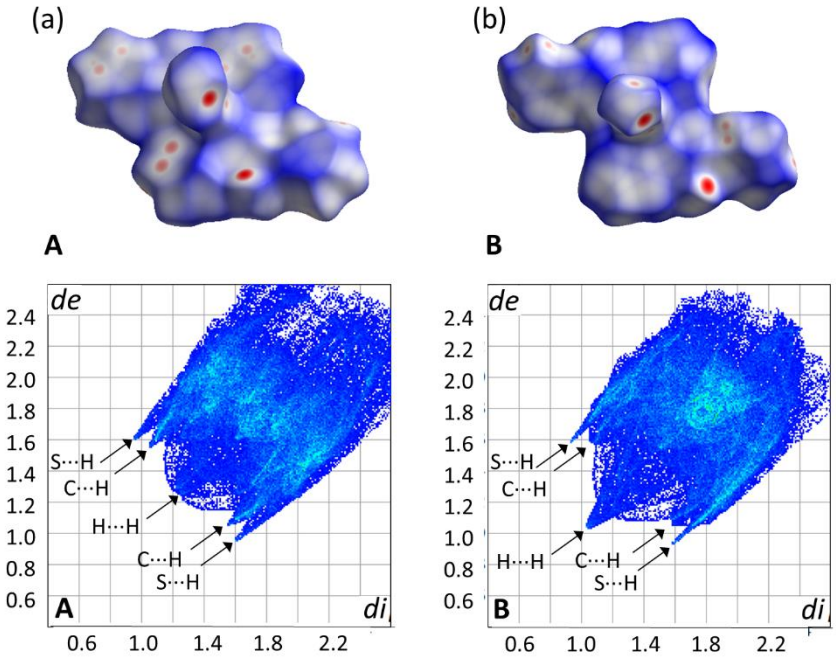

Figure 5.3 - The Hirshfeld Surface plot and fingerprint plot for (a) Polymorph **A**, (b) Polymorph **B**. Shown for Co but the Ni plots for the same respective polymorphs are essentially identical.

Given that $Fe(abpt)_2(NCS)_2$ polymorph **A** was shown to have a spin transition upon cooling,[4-6] data for Co(II) d^7 polymorph **A** and **B** were also measured at 300(2) K, see Appendix 5, Table S5.1. Examining the Co-N bond lengths showed them to be essentially identical to the 120(2) K structure and indicate that no spin transition had occurred over this temperature range, see Table 5.5. In the case of Ni(II) the complex is d^8 so no spin transition would be possible.

Table 5.5 - Co-N distances for $Co(abpt)_2(NCS)_2$ at 120(2) and 300(2) K.

Structure	Polymorph	Temperature (K)	Co1-N1	Co1-N2	Co1-N3
$Co(abpt)_2(NCS)_2$	**A**	120	2.116(2)	2.166(2)	2.088(2)
		300	2.113(5)	2.164(4)	2.093(5)
	B	120	2.0987(15)	2.1616(15)	2.1138(14)
		300	2.102(2)	2.166(2)	2.1161(18)

5.5 Conclusions

The synthesis and structures of $Co(abpt)_2(NCS)_2$ and $Ni(abpt)_2(NCS)_2$ are reported. Two polymorphs were identified for each of the complexes, A and B, and the pairs of polymorphs with the different metal centres were found to be isostructural. All of the structures contained intramolecular N-H···N hydrogen bonding, intramolecular C-H···N interactions and π-π stacking. There are identifiable differences between the two polymorphs structures. Firstly, the twist angle between the two six membered rings on one abpt ligand was ~9° for polymorph A and ~35° for polymorph B. Secondly the nature of the π-π stacking interactions was significantly different, presumably due to the differing twist angles of the rings. In the case of A both rings on one abpt ligand form π-π stacking interactions with both rings on an abpt ligand on an adjacent molecule, while for B each of the rings on the abpt ligand forms π-π stacking interactions with a ring on different abpt ligands in adjacent molecules. Variable temperature studies on the d^7 $Co(abpt)_2(NCS)_2$ did not show any evidence of a thermally induced spin crossover for either of the polymorphs between 300(2) and 120(2) K.

5.6 References

1. G. Dupouy, M. Marchivie, S. Triki, J. Sala-Pala, J. Y. Salaun, C. J. Gomez-Garcia and P. Guionneau, *Inorganic Chemistry*, 2008, **47**, 8921-8931.
2. N. G. White, J. A. Kitchen and S. Brooker, *European Journal of Inorganic Chemistry*, 2009, 1172-1180.
3. C. P. Li, J. M. Wu and M. Du, *Inorganic Chemistry*, 2011, **50**, 9284-9289.
4. N. Moliner, M. C. Muñoz, S. Létard, J. F. Létard, X. Solans, R. Burriel, M. Castro, O. Kahn and J. A. Real, *Inorganica Chimica Acta*, 1999, **291**, 279-288.
5. C. F. Sheu, S. M. Chen, S. C. Wang, G. H. Lee, Y. H. Liu and Y. Wang, *Chemical Communications*, 2009, 7512-7514.
6. H. E. Mason, W. Li, M. A. Carpenter, M. L. Hamilton, J. A. K. Howard and H. A. Sparkes, *New Journal of Chemistry*, 2016, **40**, 2466-2478.
7. C.-H. Shih, C.-F. Sheu, K. Kato, K. Sugimoto, J. Kim, Y. Wang and M. Takata, *Dalton Transactions*, 2010, **39**, 9794-9800.
8. C.-F. Sheu, C.-H. Shih, K. Sugimoto, B.-M. Cheng, M. Takata and Y. Wang, *Chemical Communications*, 2012, **48**, 5715-5717.

9. H. E. Mason, J. R. C. Musselle-Sexton, J. A. K. Howard, M. R. Probert and H. A. Sparkes, *New Journal of Chemistry*, 2021, **45**, 14014-14023.
10. A. B. Gaspar, M. C. Muñoz, N. Moliner, V. Ksenofontov, G. Levchenko, P. Gütlich and J. A. Real, *Monatshefte Fur Chemie*, 2003, **134**, 285-294.
11. M. X. Peng, C. G. Hong, C. K. Tan, J. C. Chen and M. L. Tong, *Journal of Chemical Crystallography*, 2006, **36**, 703-707.
12. Z. Y. Chen and M. X. Peng, *Chinese Journal of Inorganic Chemistry*, 2007, **23**, 2091-2096.
13. Bruker, *SMART-NT, Data Collection Software, Version 5.63, Bruker Analytical X-ray Instruments Inc., Madison, WI, USA*, 2000.
14. Bruker, *SAINT-NT, Data Reduction Software Ver. 6.14, Bruker Analytical X-ray Instruments Inc., Madison, WI, USA*, 2000.
15. Bruker, *SADABS, Bruker AXS area detector scaling and absorption correction, Bruker Analytical X-ray Instruments Inc., Madison, Wisconsin, USA*, 2001.
16. G. M. Sheldrick, *Acta Crystallogr., Sect. A: Found. Crystallogr.*, 2008, **64**, 112-122.
17. O. V. Dolomanov, L. J. Bourhis, R. J. Gildea, J. A. K. Howard and H. Puschmann, *J. Appl. Crystallogr.*, 2009, **42**, 339-341.
18. J. R. Turner, D. A. Resendiz-Lara, T. Jurca, A. Schafer, J. R. Vance, L. Beckett, G. R. Whittell, R. A. Musgrave, H. A. Sparkes and I. Manners, *Macromolecular Chemistry and Physics*, 2017, **218**.

Chapter 6

Selected structural studies of photochromic systems

Helen E. Mason

Submitted as the literature review for her first year PhD report.

6.1 Abstract

This review will give a brief introduction to photochromic compounds, particularly focussing on their solid-state properties. A variety of compounds will be discussed to assess their suitability for future development and compound design to enhance their properties towards potential applications.

6.2 An introduction to photochromism

Photochromism is a reversible photoreaction, involving a reversible change in molecular structure induced in one or both directions by electromagnetic radiation, with the two species showing distinctly different absorption spectra.[1, 2] Commonly, the transformation is caused by UV or visible light and a visible colour change is observed, but these are not necessary conditions. The two different species will exist in unimolecular equilibrium which is reversed either by irradiation at a different wavelength or thermally. These systems have attracted research interest for many years due to their potential technological applications. Upon conversion, changes in geometrical structure, refractive index, oxidation and reduction potential and dielectric constant can also occur and are thought to be essential for practical applications including optical switching devices, display systems and memory media.[3-6]

6.2.1 Related types of chromism

Photochromism often occurs in conjunction with other types of chromism, which are classified according to the type of external stimuli involved, examples include heat, charge flow, solvent polarity, pressure, mechanical friction or pH. The transformation mechanisms for certain compounds are complex making it difficult to obtain conclusive results for an individual chromism type. The main focus of this review will be photochromism but thermochromism (heat induced colour change) will also be briefly mentioned, because it often occurs in photochromic compounds. Common classifications and chromism types that may take place in photochromic compounds are described below:

Gated photochromism occurs in photochromic systems when one or more components can be reversibly transformed to a "locked" non-photochromic form either chemically or electrochemically.[2] Therefore, no further change can occur until the system is "unlocked" allowing the previously blocked photoinduced reaction to occur like the flow through a gate. Gated photochromism has been observed in specially designed diarylethene derivatives.[7]

Dual-mode photochromism arises when two different switching processes can be mutually alternated by different stimuli, for example light and electric current. The systems involved are complex but show potential for applications in write-read-erase applications including dual-mode optoelectrical molecular switching devices.[8]

Piezochromism and tribochromism are colour changes induced by mechanical grinding. Piezochromism involves the formation of a metastable form which reverts back to the original colour when dissolved in organic solvent or left in the dark. Tribochromic compounds do not revert back under either of these

conditions.[2] Imidazole derivatives are well known solid-state piezochromic compounds; upon mechanical grinding colour change occurs due to formation of radical species.[9-11]

Thermochromism is a reversible thermally induced colour change which can be slight or very dramatic, for example di-*β*-naphthospiran changes from colourless to blue-violet upon heating.[12] The switching speed and fading rate is dependent upon the compound. Many inorganic[13] and organic[12] compounds have been found to display thermochromism, including anils,[14] spiro compounds,[15] VO_2,[16] bistricyclic aromatic enes (BAEs)[17] and some iron(II) complexes.[18] Thermochromic paints, dyes and plastics are now in common usage.

Solvatochromism is induced by altering solvent polarity, resulting in a reversible colour change. Positive or negative solvatochromism occurs depending on the direction of spectral shift with increasing solvent polarity, either bathochromic (red shift) or hypsochromic (blue shift) respectively. Common solvatochromic compounds include cyanine dyes, which could be used as photosensitizers[19] and poly(3-alkylthiophenes).

Halochromism occurs upon formation of a new chromophore induced by pH change.[2] Common halochromic compounds include pH indicators, which show distinct colour change after addition of acid or base, and quinoxaline dyes.[20]

Electrochromism is a colour change that occurs upon electrochemically induced charge-transfer between redox states showing distinctly different absorption bands. Switching is often between an initial colourless state and one or more coloured states (polyelectrochromism). Common electrochromic compounds are the viologens,[21, 22] conducting polymers and metallophthalocyanines.[23] Electrochromic materials are used for 'smart glass' in switchable windows and future applications could include optical storage using controllable light-reflective or transmittive systems.

6.2.2 Photochromic properties of organic, inorganic and biological compounds

Photochromism occurs in a wide range of organic,[24] organometallic,[25] inorganic[26] and biological compounds[1, 2] with each group having unique characteristics. All undergo conversion via different mechanisms and show different properties including excitation wavelength, fatigue, colouration and bleaching rates.

The majority of organic compounds are excited by UV light between 200 nm and 400 nm but positive photochromism induced by visible light is rare even if the energy gap is correct. The photoexcited form commonly absorbs in the visible or UV region because the structure of most organic compounds is incompatible with strong electronic transitions in the infrared region. Exceptions have been found for some holopolar cyanine dyes and phthalocyanine dyes. Organic photochromic compounds include fulgides,[27] spiropyrans and spirooxazines,[28] cyanines,[19] azo compounds,[29] anils,[14, 30] viologens[21, 22] and diarylethenes.[31, 32] Inorganic compounds in the crystalline state can be excited by any wavelength in the electromagnetic spectrum, but again the most regularly observed is UV light induced excitation. The photoproduct usually absorbs in the visible or infrared region. This is due to the different structure of these materials with the energy levels determined by the crystal lattice and different mechanisms including spin crossover,[33, 34] *F*-centre formation or photoionization. Inorganic photochromic compounds include transition metal complexes,[26] alkali halides, alkali metal azides, metal oxides and complex minerals.[1, 2] Biological systems are often photochromic but few retain this property when isolated from the living cell. For example, retinal proteins, which bind to a protein via lysine, and phytochrome, which controls plants photomorphogenesis.[1, 2]

6.2.3 Solution versus solid-state studies

In solution, molecular motion is less restricted than in solid-state, therefore photochromism is more common and switching happens on a much quicker timescale. Solution state studies often display distinct solvatochromism, halochromism and/or thermochromism in conjunction with photochromism, making

comparison of results difficult. For example, a betaine dye derivative in ethanol can be blue-violet at +78°C but red at -78°C[35] and the open-forms of spiropyrans and spirooxazines exhibit either positive or negative solvatochromic shifts depending on the substituents.[36] For industrial usage, the photochromic molecules need to be confined in a support matrix, for example a polymer structure, but this often decreases the photochromic properties. The ideal matrix is a single-crystal, where no extra components have been added. Side reactions are restricted and the photoproduct quantum yield is often higher, therefore compounds displaying solid-state photochromism are of greatest use for practical applications. The solid-state photochromic mechanism cannot be obtained from solution studies and until the structural transformation has been unequivocally observed by X-ray crystallography doubts often remain about the hypothesized mechanism.

This review will focus mainly on solid-state organic photochromic compounds[24] and where applicable their single-crystal to single-crystal photoinduced transformations. These compounds show potential for applications including multifunctional,[8, 37, 38] photomagnetic[39] and optical switching systems and storage media[3, 6, 40] as well as ophthalmics.

6.3 Organic photochromic compounds

6.3.1 History of photochromism

The phenomenon that is now called “photochromism” was first considered as an entirely physical reversible photoreaction in 1899[41] and named "phototropy", several years after it was originally reported by Fritzsche.[42] Early work was limited to the synthesis of new compounds and determination of the excitation speed, wavelength and fatigue rate with only a few mechanisms proposed. Between 1940 and 1960 interest in the field increased and Hirshberg suggested the term “photochromism” derived from the Greek words “*phos*” meaning light and “*chroma*” meaning colour, to describe the phenomenon.[43] This replaced “phototropy” which is no-longer used today due to its similarity with phototropism, which describes light dependent growth of an organism. In the 1960s technological advancements in experimental techniques, including Porter's discovery of time-resolved spectroscopy[44] and improvements in synthesis techniques allowed further development. The first photochromic lens was manufactured by Corning Glass Works and applications, including the photochromic micro image (PCMI) process, attracted industrial and academic interest. The discovery of fatigue resistant spirooxazine and chromene derivatives in the 1980s prompted a new era for development allowing commercial photochromic ophthalmic lenses to be developed. Since then the field of photochromism has expanded exponentially with many other photochromic compounds discovered, studied both theoretically and experimentally and advanced towards suitable commercial applications.[1, 2]

6.3.2 Basic mechanism for photochromism

Photochromism is distinguishable from other photochemical reactions due to its reversibility criterion.[1, 2] Notably, similar to other photochemical reactions, the species exist in equilibrium hence the photoproduct is not distinctly separate. This leads to problems isolating and characterizing the photoproduct, but methods previously applied to other photochemical reactions have allowed continued development in this area. A lot of organic photochromic systems involve a unimolecular equilibrium between two different species, **A** and **B**, showing absorption bands in different regions of the spectrum (Figure 6.1).

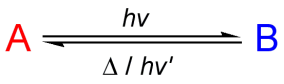

Figure 6.1 - Unimolecular equilibrium between two different species, A and B, with distinctly different absorption spectra.

A, the thermodynamically stable form, undergoes a photoinduced reaction upon irradiation with wavelength λ_1 to form **B**. **B** can either revert back to **A** thermally (T-type photochromism) or photochemically (P-type photochromism) by irradiation at a different wavelength, λ_2. Compounds often display both T- and P-type photochromism with the dominating type depending on the reaction conditions. Generally, λ_{max}(**A**) < λ_{max}(**B**) with form **A** pale yellow or colourless and form **B** deeper coloured, this is called positive photochromism. Negative or inverse photochromism, where λ_{max}(**A**) > λ_{max}(**B**), occurs less frequently. Bimolecular processes with either mono- or binuclear back reactions can also occur, for example in electron transfer processes or reversible photocycloadditions.[1, 2]

Photochromism is a wavelength specific kinetic photoreaction. It is usually a one-photon process but two-photon processes can also occur. The number of photons absorbed determines the extent of photoconversion and this is dependent on factors like the excitation wavelength, the photochromic molecule's concentration and extinction coefficients and the effect of other system components. The exciting radiation must have sufficient energy to overcome the energy barrier for conversion between the two species. Spiropyrans, spirooxazines[45] and dihydroindolizines display kinetic behaviour characteristic of unimolecular photochromic systems (Figure 6.2).[1, 2]

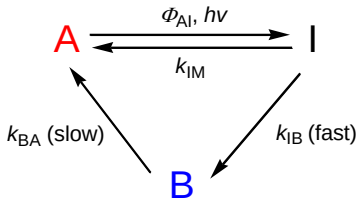

Figure 6.2 - Basic kinetic behaviour of a unimolecular photochromic system: A, is the colourless thermodynamically stable form, B the coloured long-lived non-isolable photoproduct and I an intermediate transient short-lived species.[2]

The *quantum yields*, Φ, for colouration and bleaching for a photochemical reaction are calculated using in Equation 1 and are simply the probability that absorption of one-photon will cause *n* (the stoichiometric coefficient) reactant molecules to react.

$$\Phi = \frac{\text{amount of reactant consumed or product formed}}{\text{amount of photons absorbed}}$$

Equation 1: Definition of quantum yield for a photochemical reaction.[2]

The values obtained are generally a lot less than 1 due to conflicting pathways hindering full conversion of the excited molecules to the photoproduct, for example conversion to heat, fluorescence, phosphorescence or other chemical changes.[1, 2]

Fatigue resistance in photochromic compounds is the reduction of photochromic performance upon repeated cycles by side reactions (oxidation being one of the most prominent) causing irreversible damage to the photochromic material.[1, 2] A basic unimolecular photochromic reaction with a side-reaction forming the unwanted product, B', irreversibly is illustrated by Equation 2.

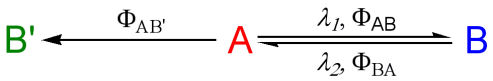

Equation 2: Photochromic equilibrium between A and B with a major side reaction to form product B'.

The lower the side-reaction quantum yield, $\Phi_{AB'}$, the greater the fatigue resistance of the compound and to carry out at least 10000 cycles, $\Phi_{AB'}$, needs to be less than 0.0001.[1, 2]

6.4 Single-crystal to single-crystal transformations

Single-crystal to single-crystal transformations occurring upon application of an external stimulus are important for understanding the solid-state properties of a particular compound, which can often be very different from those observed in gas, solution, amorphous solids or other solid matrices.

In the 1970s, Schmidt *et al.* carried out a comprehensive study of solid-state transformations, particularly focussing on the [2+2] cycloaddition reactions of cinnamic acids, based on the hypothesis that "*a reaction in the solid-state occurs with a minimum amount of atomic or molecular movement*".[46-48] This suggests that reactions occur within particular distances and orientations of the reactive centre with upper limits for reactivity for each mechanism; reactions with large molecular motion are unlikely to proceed and the original isomer and photoproduct usually closely resemble each other in structure. Detailed studies of the molecular and packing structures are required to understand whether a solid-state transformation can occur. *Inter*- and *intra*molecular interactions and free volume in the crystal are particularly important, because strong interactions may hinder the transformation whereas a large reaction cavity may allow it to proceed. These rules are generally true but occasionally reactions that would not be expected to proceed in the solid-state have been reported.[49] Several different reaction pathways that minimize molecular movement and are volume conserving for different transformations have been proposed. These include the hula-twist (HT), one bond flip (OBF) and pedal-motion mechanisms. Destruction of the crystal lattice also commonly occurs during phototransformation, either due to the internal strain caused by the molecular change or harsh reaction conditions.

X-ray diffraction is the best way to obtain the molecular structure in the solid-state. To resolve the structure of a disordered crystal the minor occupancy must generally be >10% and occur coherently in the crystal. This means that for many chromic transformations, even though a visible colour change is observed, the crystal structure change cannot be detected by X-ray diffraction. New experimental techniques for the application of the external stimuli to the crystal have allowed continued development in the area; including diamond anvil cells for increased pressure, techniques for extreme low / high temperature studies[50] and laser irradiation studies including two-photon excitation.

6.5 Photocrystallography

Historically, X-ray crystallography has provided only a time averaged picture of molecular structure in a crystal because data collection occurred on a much slower timescale than X-ray scattering. In the last few years, in line with advances in laser technology and synchrotron sources, a new method termed "photocrystallography" has allowed the dimension of time into X-ray crystallography.[51-53] A time-resolved pump-probe technique is utilized with high power pulsed lasers, for example Ti: Sapphire, providing the "pump" pulse to excite the compound and a well synchronized synchrotron beam pulse as the "probe" to look at the excited structure. This technique allows structural information of photoinduced transient species down to picosecond timescales to be obtained for the first time and the progress of photoreactions to be monitored. This will provide better mechanistic understanding of photoexcitable systems, which will be very important for developments in opto-electronics and photonics and will aid "crystal engineering" to produce materials with particular properties to suit certain applications. This method has already been successful for studying photoinduced structural paraelectric to ferroelectric

phase change in an organic charge-transfer material,[54] photoinduced geometry changes[55] and structural reorganization[56] in excited states of metal complexes, metastable states formed by linkage isomerization[57] and spin crossover in various metal complexes.[58]

6.6 Two-photon excitation

6.6.1 Theory

Two-photon absorption, the simultaneous absorption of two-photons in a single atomic or molecular transition, was predicted by Maria Göppert-Mayer in 1931[59] but was not proved experimentally until 1961 by Kaiser *et al.*.[60] The selection rules for one and two-photon transitions are different therefore two-photon absorption can be used to probe "forbidden" one-photon transitions. Since the development of sub-picosecond lasers, two-photon absorption has become widely used in spectroscopy, fluorescence microscopy, photochemistry, chemical analysis, three dimensional optical data storage and *in vivo* sampling.[61, 62]

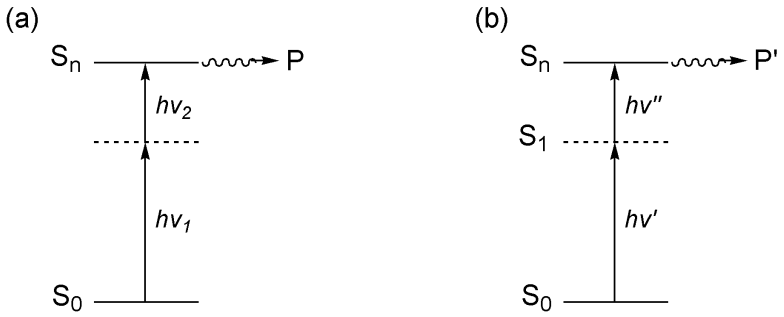

Figure 6.3 - Absorption of two-photons (a) simultaneously via a virtual level to form product P and (b) stepwise via a real level to form product P'.[2]

Two-photon absorption by an atom or molecule to reach a higher energy electronic state can occur in two different ways; either the two-photons are absorbed in a step-wise manner via a real level (perhaps a metastable intermediate), with some energy from the first photon remaining before absorption of the second photon, or simultaneously (biphotonic excitation) via a “virtual” (non-resonant) level (Figure 6.3). The two-photons can have either identical or different frequencies and the two-photon process will trigger a photochemical or photophysical response. Energy is inversely proportional to wavelength, therefore the two absorbed photons (if identical frequency) must have a wavelength twice that required for the one-photon process.

A two-photon transition is a non-linear optical process unlike a one-photon transition where rate is linearly dependent on the intensity of light irradiation. A two-photon process can be described in several ways, including rate equations which show a simple description of the process’ non-linear dependence on intensity and Maxwell's description of electromagnetic waves in dielectric materials. The rate of a two-photon reaction with equal energy photons can be written as the simultaneous interaction of two-photons with photon number density [$h\nu$] where the concentration of excited state molecules is [M*]. When $I\delta$ is small Equation 3 is obtained.[63]

$$\frac{d[M^*]}{dt} = \delta I_0^2 N$$

Equation 3: The concentration of excited state molecules produced per second. [I_0 is the incident laser intensity, $\delta = k_2/c^2$ ($cm^4.sec.molecule^{-1}.photon^{-1}$), where k_2 is the rate constant and c the speed of light, is defined as the two-photon "cross section" in analogy with that obtained for one-photon spectroscopy from the Beer-Lambert Law].[63]

The rate of two-photon excitation therefore increases with the square of light intensity. Strong one-photon absorptions have cross sections of $\sigma \approx 10^{-17}$ $cm^2.molecule^{-1}$ while the analogous absorptivity for a strong two-photon transition is $\delta \approx 10^{-48}$ $cm^4.sec.molecule^{-1}.photon^{-1}$. This means the two-photon absorption is many orders of magnitude smaller than the one-photon absorption with the same laser intensity. Hence, for two-photon absorption to occur intense pulsed laser sources are needed, for example pulsed Ti: Sapphire or Nd: YAG lasers.[63]

6.6.2 Two-photon excitation applied to photochromic systems

Most photochromic systems convert via a one-photon absorption process but two-photon excitation can also be used. Conversion will occur if the product of the two exciting photon energies is equal to the energy gap between the two states. In one-photon optical memory or imaging systems the information is easily erased under visible light or by repeated cycles, therefore gated or two-photon photochromism is necessary. Parthenopoulos *et al.* used simultaneous two-photon absorption to design a potential binary format two-photon write, read, erase system using spirobenzopyran embedded in a polymer matrix.[64] True three dimensional information storage is achieved by simultaneous two-photon absorption because the two-photon process requires the two beams to overlap within the memory volume in both time and space. A yellow naphthopyran derivative was reported by Uchida *et al.* to undergo a stepwise two-photon transition via a thermally unstable intermediate to form the bicyclohexane isomer (Figure 6.4). [65]

Recently two-photon excitation has been utilized to establish the photoproduct structure for a variety of compounds. As previously discussed (Section 6.4), to resolve the structure of the minor component in a crystal, significant and coherent conversion must occur but there are two common problems; (1) low conversion to the photoproduct and (2) destruction of the crystal lattice. To induce significant conversion the light used for excitation must meet certain conditions. Firstly, the absorbance of the crystal at the excitation wavelength must be small and secondly, the coloured species produced must not strongly absorb the excitation light. Unfortunately, the properties of many organic photoreversible systems make it difficult to fulfil both criteria simultaneously. When the photoreaction is carried out by one-photon irradiation at λ_{max} of the original isomer, the light is strongly absorbed, intensity falls off drastically in the crystal bulk and the photoreaction only takes place at the crystal surface. Hence, even if significant surface conversion does occur, the bulk of the crystal remains unconverted meaning that the observed Bragg reflections are from the original crystal lattice. Light of a longer wavelength than λ_{max} readily penetrates the crystal but often lies within the newly formed photoproduct's absorption band accelerating the reverse reaction and thus erasing the colour. These difficulties can be solved by using two-photon excitation. Irradiation at a wavelength longer than the photoexcited form's absorption band but with the correct energy to excite to the photoproduct allows the light to penetrate into the bulk crystal. This is because the probability of a two-photon transition is much lower than that of a one-photon transition. A more homogeneous spread of the photoproduct occurs in the crystal, hopefully allowing structural analysis by X-ray diffraction. This method has been successfully applied to find the structures of anil[66] and fulgide[27] compounds where one-photon irradiation had previously been unsuccessful.

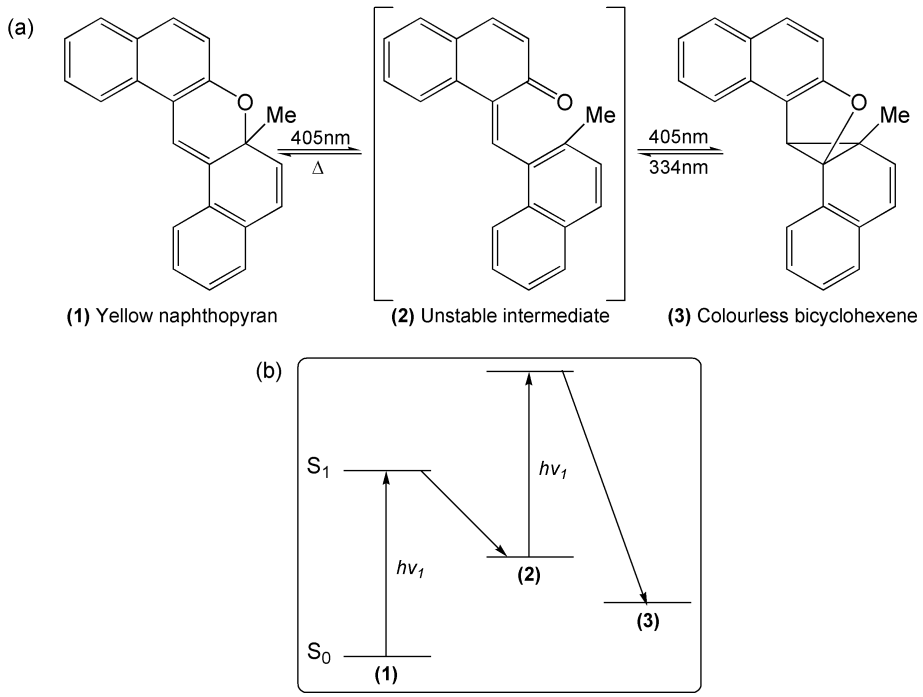

Figure 6.4 - Stepwise two-photon transition between the (1) yellow naphthopyran, (2) thermally unstable intermediate and (3) colourless bicyclohexene forms, illustrated by (a) the photochromic mechanism and (b) an energy level diagram.[2, 65]

6.7 Photochromic mechanisms

A large amount of literature is available discussing both organic and inorganic photochromic compounds.[1, 2] In this section various mechanisms for photochromic transformations in organic compounds will be discussed and compared by drawing on examples from the literature. The main focus will be on single-crystal to single-crystal transformations in these compounds.

6.7.1 "E - Z" isomerization

Photochromism that occurs through an *E* – *Z* isomerism mechanism around double bonds has been reported for a lot of compounds including those with ethylenic (-C=C-) or azo (-N=N-) groups.[1, 2] The *E*-form is generally more thermodynamically stable, therefore the back reaction happens thermally, but the *Z*-form is kinetically stabilized by the isomerization activation energy. Interest in these compounds has been generated because of their potential for fast optical switching applications in liquid crystals, microelectronic and non-linear optical devices,[67] ease of immobilization and inclusion into organic and inorganic systems. The azo and olefin photochromic mechanisms have been intensively studied in solution using time-resolved spectroscopy measurements.[68, 69, 70] However, reports of their solid-state properties are mainly limited to structural studies of the individually isolated isomers rather than *in situ* studies of the solid-state transformation. This is due to the large structural change in the transformation, which will generally be restricted in the crystalline state.[46]

The azo group can be attached to a variety of different moieties and is present in organic,[71] inorganic[72] and organometallic[73] compounds. Azobenzene can be used as an efficient actinometer because it is one of the cleanest photo reactions known.[2] *E* - *Z* (*trans-cis*) isomerization of the azo group (Figure 6.5) occurs upon irradiation with UV light (320 – 350 nm) and is reversed by irradiation with blue light (400 - 450nm) or thermally. The *Z*-form is generally more deeply coloured than the *E*-form.[1, 2]

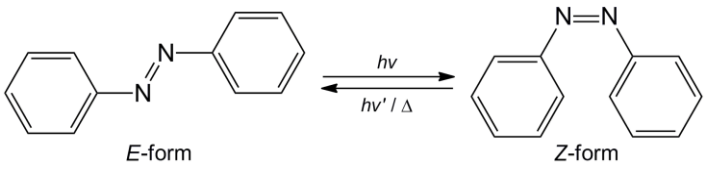

Figure 6.5 - The photochromic mechanism for azobenzene.

In the solid-state the crystal structures of several *trans*-azo compounds and a few of the isolated *cis*-azo form have been reported. *Trans*-azobenzene molecules are almost planar to maximize π-delocalization and pack in a herringbone-type pattern[29] whereas in the *cis*-form the molecules are distinctly distorted from planarity.[74] It appears that the photoisomerization of azo compounds has not yet been reported in the solid-state but is predicted to occur via a pedal-motion mechanism.[29]

In 2009, Harada *et al.* succeeded in observing the photoinduced *cis-trans* structure change for (*Z*)-2-(9-anthrylmethylene)-1-indanone (**1**) and (*E*)-2-(9-anthrylmethylene)-6-methyl-1-indanone (**2**).[49] Compound (**1**) is one of the first purely organic compounds to undergo a single-crystal photoisomerization to the *trans*-form with 100% conversion (within 90 hours of irradiation) without crystal degradation.

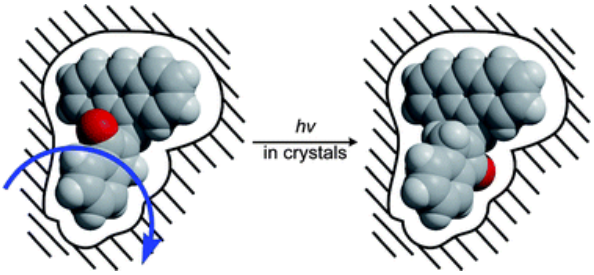

Figure 6.6 - Spacefill diagram to illustrate the photoisomerization of (**1**) in the single-crystal by the one-bond flip pathway. Reproduced with permission from the Royal Society of Chemistry.[49]

The conversion was lower for (**2**) [*trans*-form occupancy of 93.1(2) %], this is thought to be due to greater dissimilarity between the *cis* and *trans* isomers molecular structures than for compound (**1**). Interestingly, the orientation of the indanonyl group means the reaction volume conserving pathway is a one bond flip mechanism (OBF), where half the molecule flips around the double bond (Figure 6.6). Previously this reaction pathway was thought to require a large reaction cavity, but these results indicate that structural similarity between the original and photoexcited isomers is more important.[49]

6.7.2 Bond cleavage

6.7.2.1 Spirans

Spiropyrans and spirooxazines can display both thermo- and photochromism depending on the presence and position of substituents, solvent polarity, temperature and irradiation wavelength.[36, 45] The thermo- and photoproducts are thought to be identical. Their resistance to fatigue, high reversibility, large two-photon cross section and colourability make them a suitable candidate for applications including optical memories, displays, switching devices,[3] actinometry, optical sensors,[75] self-developing photography and ophthalmic lenses.

The photochromic mechanism for spiropyrans and spirooxazines involves a 6π 6-atom pericyclic process with the photoinduced cleavage of the spiro C–O bond. The colourless or weakly coloured closed (spiro) form usually absorbs in the 200 nm – 400 nm region and is converted to the open planar (photomerocyanine) deeply coloured form by UV light irradiation. The open form is thought to exist as a resonance hybrid of two canonical forms, a dipolar zwitterionic form and a polyenic or quinoidal neutral form (Figure 6.7). The closed form is usually the thermodynamically stable form and the open form will convert back either thermally or by photoirradiation.[1, 2]

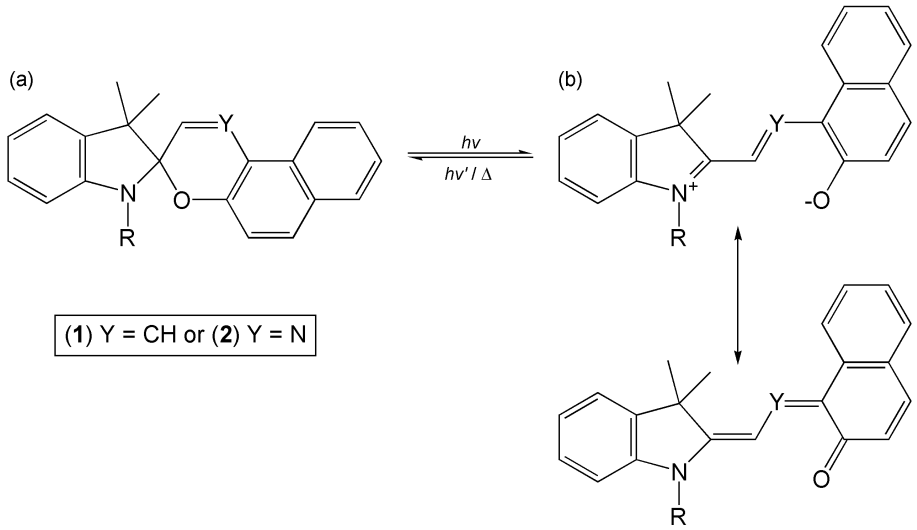

Figure 6.7 - The photochromic mechanism for (**1**) a spiropyran and (**2**) a spirooxazine showing (a) the closed (spiro) form and (b) the open (photomerocyanine) forms.

It was thought that the photochromic mechanism in spirans was restricted in the solid-state due to lack of free-volume. Photochromism was only reported when a larger void existed around the molecules for example in solution, amorphous molecular solids,[76] polymer films[77, 78] or in cationic compounds.[79] Femtosecond laser pulse irradiation has been used to induce photocolouration in microcrystalline powder of spironaphthoxazine[80, 81] and its chloro substituted analogue[82, 83] where steady UV irradiation does not cause a photochromic change.[81] A cooperative photochemical reaction model was suggested for the photochromism of spironaphthoxazines in the crystalline state.[81, 83] Recently, it has been discovered that steady UV light can actually induce photochromism in solid-state spirans. The temperature dependence of photochromism in these compounds has previously been hinted at in solution[45, 84] but not really been discussed in the solid-state. In 2010 Harada *et al.*[28] found that a variety of spirans previously reported as displaying limited or no photochromic properties in the solid-state at room temperature actually display conversion at low temperatures with the photocolouration yield enhanced by decreasing temperature (Figure 6.8). When irradiated at 90 K the photoinduced colour does not fade until the crystal is warmed to room temperature.

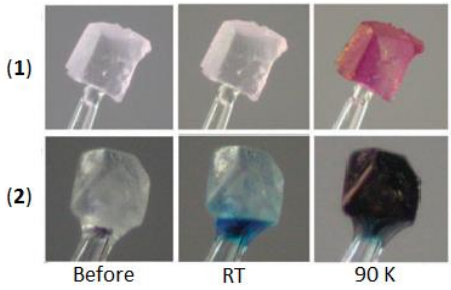

Figure 6.8 - Photographs of (1) 1,3,3-trimethylspiro[indoline-2,3'-[*3H*]-naphtho[2,1-*b*]pyran] and (2) 1,3,3-trimethylspiro[indoline-2,3'-[*3H*]-naphtho[2,1-*b*]-[1,4]-oxazine], (left) before irradiation, (middle) after UV irradiation at room temperature and (right) after UV irradiation at 90 K. Reproduced with permission from the Royal Society of Chemistry.[28]

It is now suggested that the back reaction rate at room temperature may be the limiting factor for photochromism of spirans in the crystalline state rather than rigid lattice restrictions.[28]

6.7.2.2 Hexaarylbiimidazole (HABI) derivatives

Hexaarylbiimidazole (HABI) compounds display chromic responses to several different stimuli, including heat, light and pressure and show potential for fast switching light modulator applications. The reaction mechanism involves the formation of paramagnetic radical species, triarylimidazolyl (iophyl) radicals, through photo- or thermally induced homolytic cleavage of the C-N bond between the two imidazole rings in the iophine dimer, the recombination reaction occurs thermally and visible light irradiation does not increase the rate (Figure 6.9).[24]

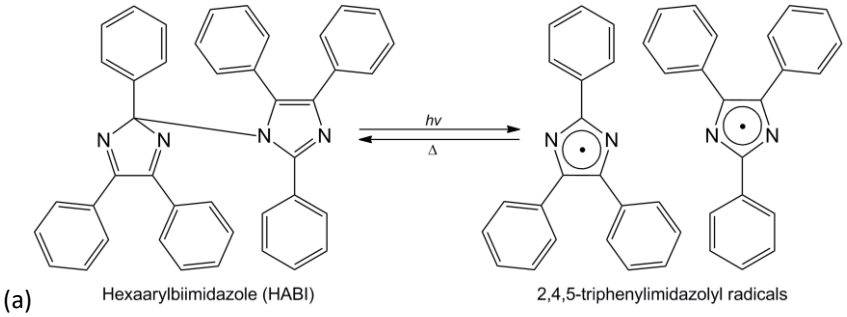

(a)

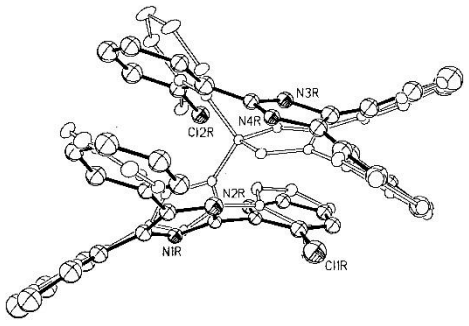

(b)

Figure 6.9 - (a) Photochromic mechanism for hexaarylbiimidazole (HABI) and (b) ORTEP plot of the disordered crystal structure of *o*-Cl-HABI after irradiation; *o*-Cl-HABI is displayed with open bonds and its corresponding radical pair (10% occupancy) displayed with solid bonds. Molecule A and hydrogen atoms are omitted for clarity. Ellipsoids are shown at 30% probability. Reprinted with permission. Copyright 1999 American Chemical Society.[85]

Kawano *et al.* succeeded in observing the structural change that occurs upon irradiation for *ortho*-Cl-HABI using *in situ* X-ray crystallography with the cryotrapping method [Figure 6.9(b)].[85] The asymmetric unit contains two iophine dimers, **A** and **B,** but only **B** underwent bond cleavage to form radical species upon irradiation. The photoreaction in **A** is thought to be sterically suppressed because its reaction cavity is 26 $Å^3$ smaller than that of **B**.[85]

6.7.3 Electrocyclization reactions

6.7.3.1 Fulgides

Fulgides, derivatives of dimethylene succinic anhydrides, display fatigue resistance of up to ~ 100 cycles[86] and thermal irreversibility meaning there has been much interest in fulgides as organic materials for optical storage devices, for example rewritable photon mode optical memory.[1, 2]

The fulgide photochromic mechanism involves a UV induced 6π-electrocyclization (pericyclic reaction) between two species, a pale coloured, open *E*-form and darker coloured, closed *C*-form, existing in equilibrium (Figure 6.10). This is a stereospecific reaction obeying the Woodward-Hoffmann rules for conserving orbital symmetry.[87] If disrotatory ring-opening is sterically restricted the back reaction cannot occur thermally and only happens via a visible light induced conrotatory ring-opening.[87]

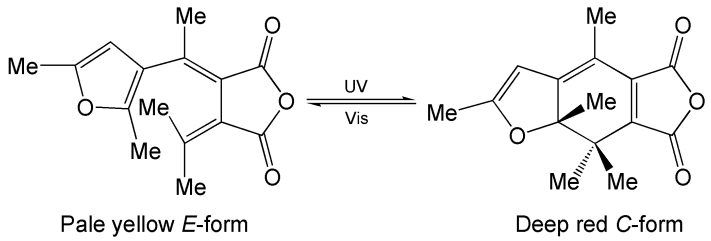

Figure 6.10 - The photochromic mechanism for (*E*)-α-(2,5-dimethyl-3-furylethylidene)(isopropylidene)succinic anhydride.

Until 2008 the photoinduced transformation in a fulgide single-crystal had not been observed.[27] In the solid-state unwanted *E-Z* photoisomerization is nearly always restricted, therefore increasing the quantum yield of the desired photoproduct. Two fulgide compounds; (*E*)-2-[1-(2,5-dimethyl-3-furyl)-ethylidene]-3-isopropylidenesuccinic anhydride (**3**) and (*E*)-2-[1-(2,5-dimethyl-3-furyl)-2-methylpropylidene]-3-isopropylidenesuccinic anhydride (**4**) were studied. The authors conclude the inability to resolve the *C*-form upon steady light irradiation is not due to lack of conversion [(**4**) shows ~13% conversion to the *C*-form upon steady 365 nm irradiation in single-crystal], but high conversion at the crystal surface causing loss of crystal lattice structure in this region and limited conversion in the bulk crystal. When a single-crystal of (**3**) was irradiated using two-photon excitation at room temperature by a 742 nm (twice the λ_{max} of the *E*-form) pulsed laser for 90 mins, it became dark red, nearly black. Figure 6.11 clearly shows that only the two-photon light causes a homogeneous population of the photocoloured state in the single-crystal.

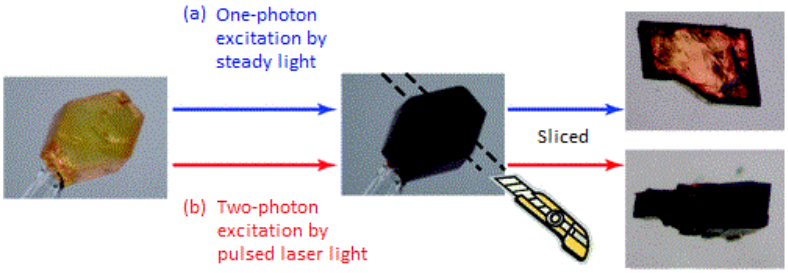

Figure 6.11 - Photographs indicating the differences observed in a crystal of (**3**) that has been irradiated by (a) steady 405 nm light and (b) 742 nm pulsed laser light. Reprinted with permission. Copyright 2008 American Chemical Society.[27]

New electron density peaks in the Fourier Difference Map could be assigned to the *C*-form of the fulgide and the *C*-form of (**3**) was found to have an occupancy of 5.5(3)% after 90 mins of irradiation at 300 mJ/cm^2 (Figure 6.12). This suggests a loss of crystallinity upon irradiation because (**4**) showed a much higher occupancy of 27.8(2)% after 75 mins of irradiation at 100 mJ/cm^2.[27]

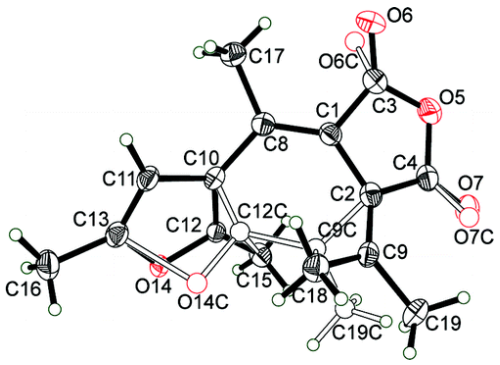

Figure 6.12 - The crystal structure of (**3**) after pulsed 742nm laser irradiation for 90 mins. The *E*-form is displayed as filled bonds and the *C*-form as open bonds. Reprinted with permission. Copyright 2008 American Chemical Society.[27]

6.7.3.2 Diarylethenes

A lot of research interest is currently focussed on photochromic diarylethene derivatives with heterocyclic aryl groups, in particular diarylperfluorocyclopentenes. These compounds display unique physical properties, including thermal irreversibility (some derivatives have a half-life of up to 470,000 years at room temperature), fatigue resistance of more than 10^4 cycles, fast switching in both directions in less than 10 ps, colouration quantum yields of ~1, good wavelength separation of the two forms absorption bands, dual-mode and gated photochromism.[31] For applications in optical memory systems sensitivity in the 650 – 830 nm region is desirable. By substitution of different electron donating / withdrawing groups on the thiophene rings or by changing the cycloalkene ring for maleic anhydride or maleimide derivatives the sensitivity region can be shifted.[40, 88, 89] These properties are necessary if applications in photonic devices including 3-D optical memory, switching devices and display systems are to be realized.[5, 40]

The basic photochromic mechanism involves a reversible photoinduced cyclization (Figure 6.13),[32] similar to fulgides and spirans. The colourless open-ring hexatriene form transforms upon UV irradiation to the

coloured (yellow, red, blue or green) closed-ring cyclohexadiene form and reverts back upon visible light irradiation following Woodward-Hoffman rules.[87]

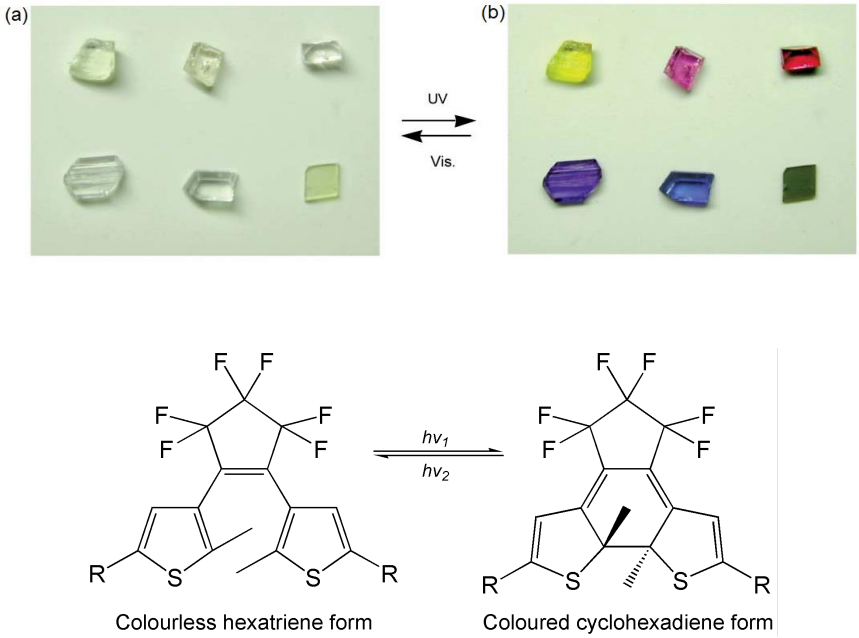

Figure 6.13 - Photographs of single-crystals of six diarylperfluorocyclopentene derivatives (a) before irradiation and (b) after UV light irradiation[32] and the photochromic mechanism for a diarylethene derivative, R is an aryl group. Reproduced with permission from the Royal Society of Chemistry.[32]

In diarylethenes the solid-state reaction can occur because the geometrical change is small. Side reactions (including *E-Z* isomerization) are prohibited, making diarylethenes extremely fatigue resistant in the solid-state, with undetectable by-product formation and crystallinity retained even after 10^4-10^5 cycles.[32, 90] A larger conversion to the photoproduct is usually observed compared with other organic photochromic compounds. The photoproduct is stable up to 100°C and shows extremely good thermal stability at room temperature in the dark, never returning to the original form. The molecular structure dictates the solid-state diarylethene photoreactivity. The majority of diarylethene molecules crystallize in the anti-parallel (C_2) photoactive conformation rather than the non-photoactive parallel (C_s) conformation, but not all are photochromic. The distance between the two carbon atoms involved in the photocyclization (the reactive carbons) is thought to be the limiting factor for photochromism; if this distance is larger than 0.42 nm the photoreaction will not occur but if it is under 0.40 nm it will proceed efficiently with a colouration quantum yield of ~1.[91]

The *intra*conversion between the open and closed forms has been observed by X-ray diffraction using *in-situ* photoirradiation. Irie *et al.* carried out extensive investigations of 1,2-bis(2,5-dimethyl-3-thienyl)perfluorocyclopentene (**5**) and 1,2-bis(2-methyl-5-phenyl-3-thienyl)perfluorocyclopentene (**6**) looking at the conversion in both directions using different irradiation conditions.[92-95] Irradiation of the closed form of (**5**) with 680 nm light for 100 hours achieved a 9% conversion to the open isomer.[93] In the reverse reaction, irradiation of the (100) crystal face of the open isomer with 360 nm light (linearly polarised parallel to the *c*-axis) for 24 hours caused an 8% conversion to the closed form (Figure 6.14).[94]

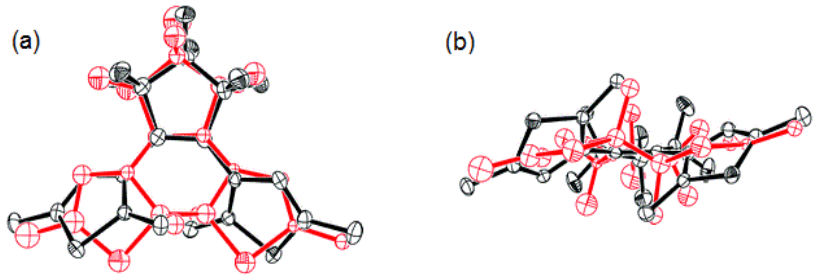

Figure 6.14 - ORTEP plot showing the disordered crystal structure of (**5**) after irradiation with 360 nm UV light (a) top view and (b) side view. The open-ring isomer is displayed in black and the closed-ring isomer in red with occupancy 92: 8. Reproduced with permission from the Royal Society of Chemistry.[32]

The open form of compounds (**5**) and (**6**) crystallized with molecules in the anti-parallel conformation. During the photoreaction the molecule's centre of gravity remains the same with only the sulphur and reactive carbon atoms found to move significant distances, hence explaining why the reaction can proceed in less than 10 ps. The distances between reactive carbons in molecules of (**5**) and (**6**) were less than 0.40 nm thus explaining the high photocyclization efficiency of both compounds.[94,95]

A lot of photochromic systems display a linear response to irradiation and are not suitable for optical memory devices because they do not provide a non-destructive readout method. Diarylethenes have capability for gated[7] and dual-mode photochromism.[8] Dual-mode photochromism can occur due to mutual photochromic and electrochromic switching (light switches the electrochromism 'on' and 'off' and vice versa) between three distinct stable states distinguishable by their absorption spectra. These characteristics make diarylethene systems suitable for read-write-erase applications with non-destructive output.[8]

6.7.4 Redox systems

Inorganic compounds that display photochromism due to a charge-transfer mechanism are well known, for example the silver halides which are commonly used in ophthalmic lenses are active due to a photoreduction mechanism. Redox active organic compounds are less well known but a few groups have been reported, including the viologens,[21, 22] quinones and biindenylidenedione derivatives.[96] The photochromic mechanism in viologens involves photoreduction of the colourless viologen cation to the coloured monocation radical via electron transfer from the counter anion upon UV irradiation. The reverse reaction happens thermally and is very rapid in solution but in solid matrices it is much slower and more easily controlled.[21] Photochromism in biindenylidenediones was first reported in 1992 and has generated interest because the photochromic mechanism involves the formation of a stable biradical system upon UV irradiation meaning photomagnetic properties are also observed.[96] Research is still in its early stages with the nature of the photoproduced radical species still under debate.[97-99] Unusually photochromism is not displayed in solution due to quenching of the radical species, but does occur in solid matrices including crystalline state.

6.7.5 Hydrogen transfer

Photoinduced tautomerism involving hydrogen transfer occurs in many different organic compounds between different groups, including aci-nitro, and as keto-enol tautomerism in hydroxyl-azo, alkyl-carbonyl and hydroxyl-carbonyl groups.[1, 2] Photochromism through excited state hydrogen transfer between hydroxyl and imine nitrogen groups occurs in anil compounds and is discussed in detail in Section 6.8.[14, 30]

6.7.5.1 Nitrobenzylpyridine (NBP) derivatives

The generally accepted basic mechanism for photochromism in nitrobenzylpyridines derivatives involves three-species, but there are also many other side reaction pathways that are not yet fully understood. Proton transfer occurs from the colourless CH form to produce a long lived blue enamine, NH, form either directly or via the metastable aci-nitro, OH, form [Figure 6.15(a)].[100]

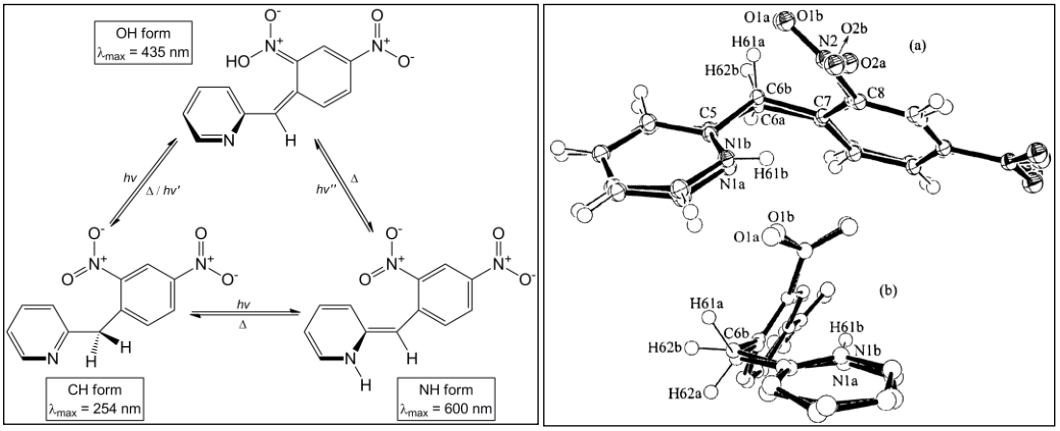

Figure 6.15 - (Left) Basic reaction mechanism for the photochromism of 2-(2',4'-dinitrobenzyl)pyridine (DNBP). (Right) ORTEP plot showing the disordered crystal structure of DNBP after irradiation (ellipsoids at 50% probability), the CH and NH forms have occupancies of 67.2% and 32.8% respectively (H atoms on the NH form are omitted for clarity). Reprinted with permission. Copyright 2002 American Chemical Society.[101]

The structure of the CH form has been known for a while but the structure of the NH form has only recently been obtained. Naumov *et al.* used two-photon excitation to irradiate the crystal with 502nm pulsed laser light for 0.5 hours and achieved a conversion of 32.8% to the NH form [Figure 6.15(b)].[101] The structure of the OH form is still unknown due to its instability but it is suggested time-resolved studies could be used to establish the structure and mechanism of conversion between the three species.[100]

6.8 Anils

6.8.1 Introduction to the chromic properties of anils

Anils, Schiff bases of salicylaldehyde derivatives with aniline derivatives, (also known as Schiff bases or *N*-salicylidene-anilines) have been known to display both thermo- and photochromism in solution and solid-state for many years. They are easy to prepare in the solid-state meaning they have been studied extensively and a lot of literature ranging over many years exists including some conflicting results.[1, 2, 14, 24, 30, 102-104] Their photochromic mechanism involves an excited state proton transfer and some anils display switchable non-linear optical properties[105] giving them potential for devices that require fast optical switching.[106] There is still indecision regarding the origin of these compounds' chromic properties due to the complexity of the mechanism which is influenced by many different factors.

Cohen *et al.* carried out the first systematic study of photochromism in anils and discovered that the *ortho*-hydroxy group was essential for thermo- and / or photochromism in anil compounds (Figure 6.16). [102, 107, 108]

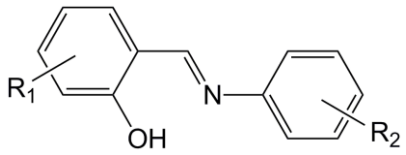

Figure 6.16 - General structure of an *ortho*-hydroxy anil compound, R_1 and R_2 can be any substituent.

When prepared anils range in colour from pale yellow to red and some exist in more than one polymorphic form[109] with each polymorph displaying different properties. The darker coloured orange / red anils are found to display thermochromism; upon cooling a reversible lightening in colour is observed. Some of the yellow coloured anils are photochromic, showing a darkening in colour to orange or red upon irradiation. This colour fades either by heating or irradiation with visible light, with the fading rate characteristic to a particular compound or polymorph.

Anils have a particular temperature range for photochromic activity, imposed by low yield below a certain temperature (the "low temperature limit") and rapid thermal fading above another temperature (the "high temperature limit"). Many anils display a large usable temperature range with stable colour and high yield, for example *N*-salicylidene-2-chloroaniline displays no change in photoproduct yield between 113 K and 298 K. However, some anils only have a small photochromic temperature range, for example *N*-salicylidene-4-bromoaniline has a range of 60 K, which implies low yields and also rapid fading rates at most temperatures.[102, 107] When a compound is irradiated at a temperature with high photoyield and then is cooled below the lower temperature limit the colour is maintained. This property has been utilized in the "cryotrapping" or "flash freezing" method to find the structures of photoexcited anils and other photochromic compounds by X-ray diffraction.[66]

Thermo- and photochromism were long believed to be mutually exclusive properties in anils and distinct differences between the compound's absorption spectra led to the classification into two categories: α-type; pale yellow, photochromic but not thermochromic and β-type; dark yellow or orange, thermochromic but not photochromic.[107] The thermochromic anils displayed an absorption band in the visible region, which altered in intensity with changing temperature. The photochromic anils displayed no such band (Figure 6.17).[107] The absorption spectra of the irradiated photochromic compounds was thought to resemble that of the thermochromic compounds at higher temperature in the region of ~490 nm, but show different features at higher wavelength.[102]

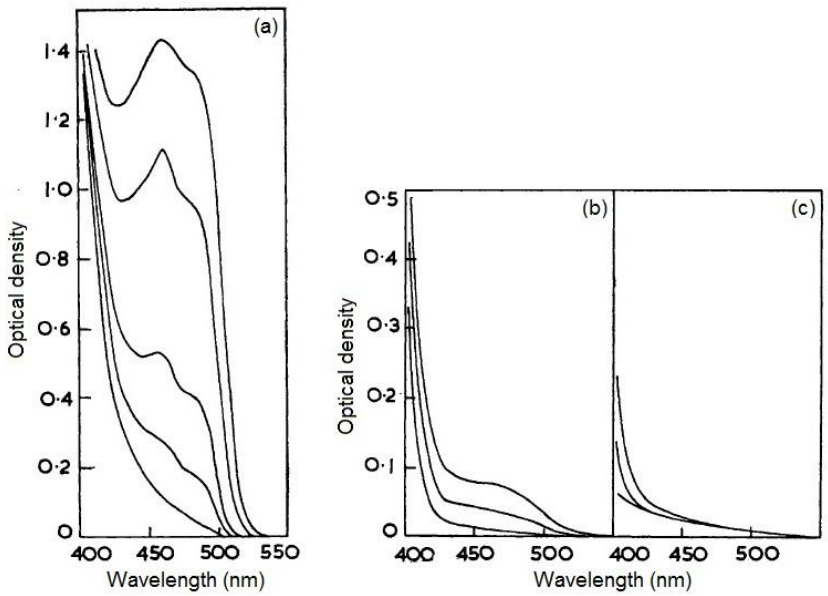

Figure 6.17 - Absorption spectra changes observed upon decreasing temperature (highest-lowest curve) in (a) *N*-salicylidene-5-chloroaniline, a thermochromic compound, (b) *N*-salicylidene-3-chloroaniline, a thermochromic compound but showing less obvious colour change and (c) *N*-salicylidene-2-chloroaniline, a non-thermochromic compound.[107]

Fluorescence was observed upon UV irradiation for the thermochromic compounds; the luminescence was yellow at room temperature but changed to green at lower temperatures. Photochromic compounds displayed no fluorescence above their lower temperature limit, but upon lowering of temperature fluorescence was observed.[107] However, it is now believed that all anils are thermochromic to some extent with some also displaying photochromism, although this new classification is based on slightly different criteria.[110]

6.8.2 Mechanisms

The thermo- and photochromism in anils are thought to be due to a thermal or photo- induced tautomeric equilibrium shift between the colourless enol (OH) and coloured (red or orange) keto (NH) forms (Figure 6.18). The forward photochromic reaction is induced by UV light (365 nm) and the reverse reaction can happen thermally or upon visible light irradiation >560 nm. The enol absorbs at ~340 nm (outside the visible region) and the keto form is orange / red due to an extra absorption band at ~500 nm. The final long lived thermoproduct is the *cis*-keto form whereas the photoproduct is the *trans*-keto form.[14, 24, 30, 104] Photoinduced conversion between the *cis*-keto and *trans*-keto forms can also occur upon irradiation with 436 nm light at room temperature, showing that the photoproduct can not only be produced by irradiation of the enol form but also by irradiation of the cis-keto form.[110]

Both thermo- and photochromism involve an *intra*molecular proton shift from the *ortho*-hydroxy group, which is essential for the mechanism to occur,[102] to the imine nitrogen passing through a quasi six-membered ring transition state. In most cases the enol form is more stable than the keto form. The mechanism for the photoreaction in anils has been investigated in the gas phase, by ultrafast spectroscopic techniques in solution and less prominently in crystalline state.[111-113]

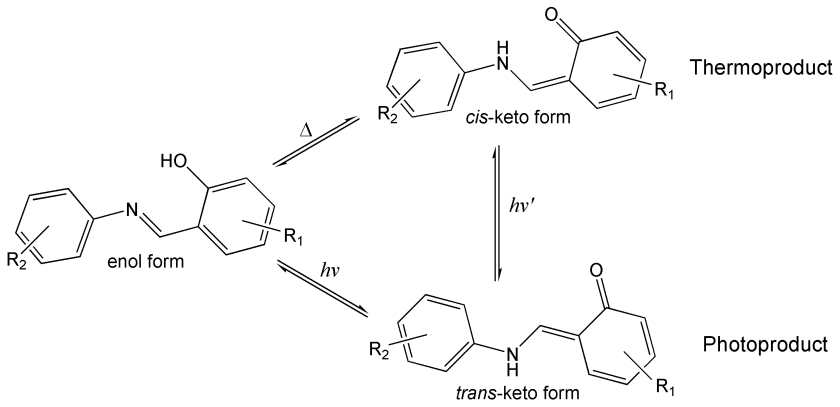

Figure 6.18 - The basic thermo- and photochromic mechanism for anil compounds.

The mechanistic behaviour of the anils can be split into two groups mirroring the chromic properties displayed. Class A: Compounds that display photochromism in both solution and the solid-state, are not fluorescent and generally pack with enough free volume to allow conversion to the *trans*-keto form. Class B: Compounds display photochromism in solution (similar to class A) but in crystalline state are exclusively thermochromic and the molecular packing is compact restricting *cis*-*trans* isomerization. The generally accepted mechanism involves the excitation of the stable ground state (S_0) enol form to the excited (S_1) enol* form, followed by excited state *intra*molecular proton transfer (ESIPT) to a *cis*-keto* form. ESIPT occurs within 1 ps in solution and 50 fs in solid-state.[111] The final metastable photoproduct, the *trans*-keto form, is then formed through *cis*-*trans* isomerization.[113] Each compound displays a distinctive thermal fading, which can range from seconds to over a year in solid-state. *N*-(3,5-di-*tert*-butylsalicylidene)-4-aminopyridine displays a particular long lifetime of 460 days, this is the longest time currently reported for an anil compound.[105] If *cis*-*trans* isomerization is hindered, for example in class B compounds, the *cis*-keto* form relaxes down to the ground state by strong fluorescence and then undergoes proton transfer back to the enol form.[111] There are still questions regarding the kinetics, exact nature and number of the *cis*-keto* species produced upon ESIPT for different compounds and the form of the precursor species to the *trans*-keto form. Further investigation is also needed to establish information regarding the enol* isomer and the possible influence of quinoidal of zwitterionic forms of the enol, *cis*-keto or *trans*-keto in different reaction environments.[112]

Sliwa *et al.* recently investigated the solid-state mechanism using steady and transient state optical spectroscopy for two anil compounds, *N*-(3,5-di-tert-butylsalicylidene)-4-aminopyridine (**7**), a class A compound showing potential for photoswitching applications[105, 114] and *N*-(3,5-di-tert-butylsalicylidene)-2-aminopyridine (**8**), a class B compound showing potential for thermoswitching applications.[115]

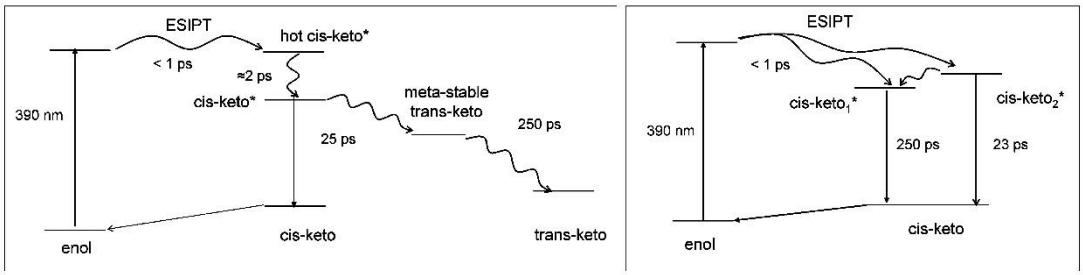

(a) **Class A**: *N*-(3,5-ditert-butylsalicylidene)-4-aminopyridine (b) **Class B**: *N*-(3,5-ditert-butylsalicylidene)-2-aminopyridine

Figure 6.19 - Possible photodynamic schemes for microcrystalline powders of (a) compound (**7**), a class A compound and (b) compound (**8**), a class B compound upon 390 nm irradiation. Reprinted with permission. Copyright 2009 American Chemical Society.[111]

For compound (**7**), an intermediate species between the *cis*-keto* and *trans*-keto forms was observed which displayed absorption characteristics of the photoproduct. It is thought that in the solid-state, steric restrictions may hinder direct formation of the photoproduct and introduce a two-step mechanism where relaxation of the *cis*-keto* produces a metastable ground state form with *trans*-keto like properties [Figure 6.19(a)]. For compound (**8**), biexponential kinetics were observed for the decay of the *cis*-keto* band, indicating the presence of two fluorescent species, *cis*-keto$_1$* and *cis*-keto$_2$*. As expected for compound (**8**) in the solid-state, after decay of the *cis*-keto* band no other absorption band remained, showing the *trans*-keto form was not produced [Figure 6.19(b)].[111]

In 2004, Fujiwara *et al.*[110] provided a new perspective on the thermo- and photochromism of anils. Variable temperature diffuse reflectance spectra of crystalline powders of *N*-salicylideneaniline (**9**) and *N*-salicylidene-2-chloroaniline (**10**) were collected at temperatures between 298 K and 80 K to investigate the thermochromic properties. UV-vis Kubelka-Munk spectra were obtained by transformation of diffuse reflectance spectra of the crystalline powders diluted with NaCl using the Kubelka-Munk function.[116] The enol form, which has long been thought to be pale yellow, was actually discovered to be white at lower temperatures. This colour change was observed by eye [Figure 6.20(a)] and also evidenced by a decrease in the *cis*-keto and increase in the enol band absorption with decreasing temperature [Figure 6.20(b)]. This study indicates that photochromic anils generally do display a temperature dependent colour change which can be detected by diffuse reflectance spectroscopy, hence they are also thermochromic. Therefore, this suggests that all anils display thermochromism in the solid-state with some also displaying photochromism and mutual exclusiveness does not exist.[110]

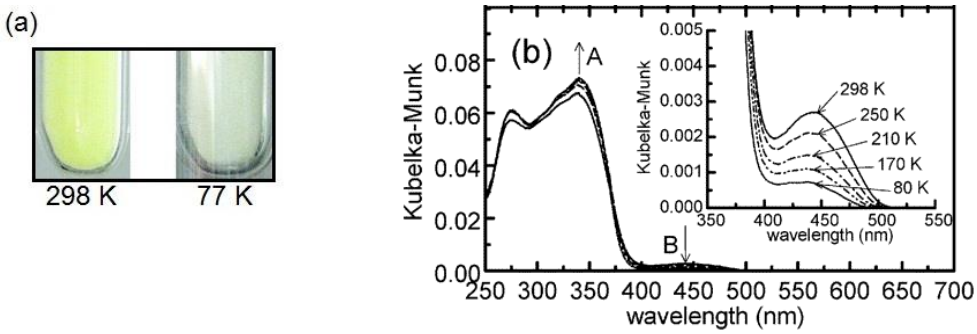

Figure 6.20 - (a) Colour change observed for compound (**9**) upon temperature change from 298 K to 77 K and (b) corresponding Kubelka-Munk spectra; band A is assigned to the enol form and band B the *cis*-keto form. Reprinted with permission. Copyright 2004 American Chemical Society.[110]

In 2007 the same group re-examined the thermochromic changes in three thermochromic anil compounds.[117] They concluded the colour changes could not be completely explained by the tautomeric equilibrium between enol and *cis*-keto forms and that the observed colour changes are mainly caused by the effect of temperature on the fluorescence. The chromaticity coordinate,[118] which gives the perceived colour taking into account the spectrum of the illumination source, the spectral sensitivity of the eye and the material's diffuse reflectance spectrum, was calculated. For *N*-(5-chlorosalicylidene)-aniline, the chromaticity coordinate calculated from the collected variable temperature diffuse reflectance spectra indicated that the colours should be orange at room temperature and pale yellow at 80 K but the colours actually observed were orange and yellowish green respectively. When the chromaticity coordinate was re-calculated taking into account the sample's fluorescence, the expected and perceived colours agreed. Similar results were obtained for *N*-(5-chlorosalicylidene)-4-hydroxyaniline and *N*-(salicylidene)-4-methylaniline. This suggests that the low temperature colour can only be correctly interpreted by taking into account the fluorescence and that this is the dominant effect rather than the shift in tautomeric equilibrium. Hence, in thermochromic compounds at high temperatures (above room temperature) and

photochromic compounds where fluorescence is weak the thermochromic colour change is due to the tautomeric equilibrium shift but at lower temperatures in thermochromic compounds fluorescence cannot be ignored because it dominates the colour change.[117]

6.8.3 Molecular structure and packing

In the crystalline state the thermo- and photochromic properties of anils are thought to be directly related to the molecular and packing structures. Cohen *et al.*[107] suggested that certain molecular structure and packing features were characteristic for the anils they classified as α- and β-type.

In both thermochromic and photochromic anils the quasi six-membered ring created by the *intra*molecular hydrogen bond between *ortho*-hydroxy group and imine nitrogen is close to planarity despite other structural differences in the molecule. Thermochromic anils are thought to have distinctly planar molecules which pack in a herringbone-type structure of offset π-π stacks with distances of 3.3 - 3.5 Å between molecules [Figure 6.21(a)]. This so called "close packed" structure provides stabilization for the *cis*-keto form but sterically restricts the *cis-trans* isomerization required for photochromism. The basicity of the imine nitrogen atom is increased by molecular planarity through decreased overlap between the imine nitrogen lone pair and the aniline ring. The O-H···N *intra*molecular hydrogen bond is therefore stronger and hydrogen transfer can occur more easily in the ground state.[14] Photochromic anils are thought to have distinctly non-planar molecular structures, with the aniline moiety rotated out of plane with the salicylaldimine moiety, sometimes as much as 50°. This decreases the basicity of the nitrogen atom, meaning hydrogen transfer is less likely to occur in the ground state, but upon excitation to the excited state hydrogen transfer is possible. This means the packing structure is distinctly different to that of the thermochromic compounds and molecules pack in a more "open packed" structure with fewer strong *inter*molecular interactions and *cis-trans* isomerization can occur [Figure 6.21(b)].[14]

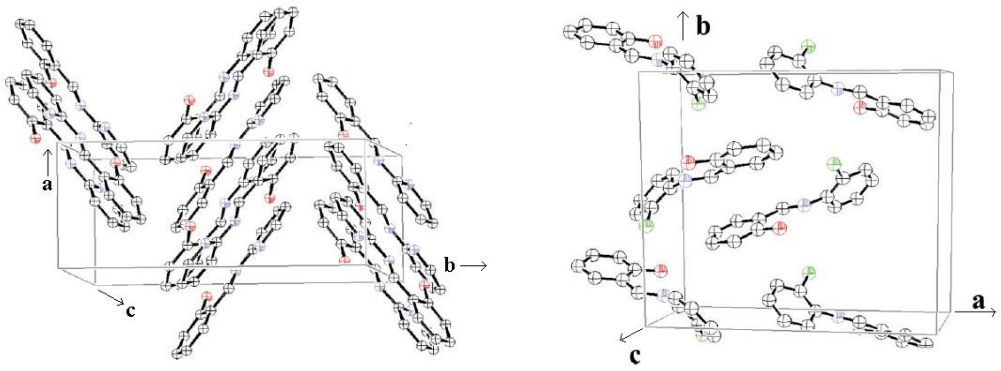

Figure 6.21 - (a) Herringbone-type "close" packing structure typical for thermochromic compounds and (b) more "open" packing structure typical for photochromic compounds. Reproduced with permission from the Royal Society of Chemistry.[14]

Since Cohen *et al.* proposed this classification, the effect of substitution of different groups onto the salicyl and aniline moieties has been widely investigated. In 1987, Mavridis *et al.* carried out an extensive study of mono-, di- and tri-substitution of different groups, including methoxy, hydroxy, methyl, amino and different halogens, onto *N*-salicylidene-aniline, *N*-salicylidene-2, 3 or 4-aminopyridines and *N*-salicylidene-benzyamines.[119] *N*-salicylidene-2-aminopyridine derivatives all displayed thermochromism and packed in the typical herringbone-type structure. The nitrogen in the 2-position of the aniline is thought to effectively "lock" the molecule in a planar configuration through hydrogen bonding with the hydrogen on the carbon adjacent to the imine nitrogen. Since then, different groups have reported different behaviour for the same compounds, particularly in reports published over 50 years ago. This

could be attributed either to differences in experimental technique, for example more intense irradiation sources, or perhaps different polymorphs were produced. Planarity is now known not to be crucial for thermochromism, with many non-planar anils also displaying strong thermochromic properties, but it is thought to be unfavourable for photochromism. Thermochromism is now believed to rely on the imine nitrogen atom's electron density, which can be dramatically altered by different substituents, assisting easy hydrogen transfer. Substituents which weaken the O-H bond but increase the electron density on the imine nitrogen will enhance thermochromic properties. Hence, thermo- and photochromism may be exhibited simultaneously[14] if the molecular packing allows *cis*-*trans* isomerization to occur, this agrees with the suggestion that they are not mutually exclusive properties.[110] Bulky groups, for example *tert*-butyl, substituted on the aromatic rings can act as space openers in the crystal lattice. This method has been successful in producing photochromic compounds from previously non-photochromic ones.

The colour changes exhibited in thermo- and/or photochromic anils are caused by very small conversions to the keto form. Therefore, for many years the structures of neither keto form could be established using X-ray diffraction. In 1998 and 1999 the structural changes accompanying the transformation from the enol to the *cis*-keto[120] and *trans*-keto[66] forms respectively were observed for the first time. *N*-(5-chlorosalicylidene)-4-hydroxyaniline is yellowish orange at room temperature and yellowish green at 77 K.[117] The population of the *cis*-keto form increased with decreasing temperature, at 299 K the ratio of OH to NH forms was 31: 69, at 90 K 10: 90[120] and at 15 K this compound is thought to exist purely in the NH form (Figure 6.22).[121]

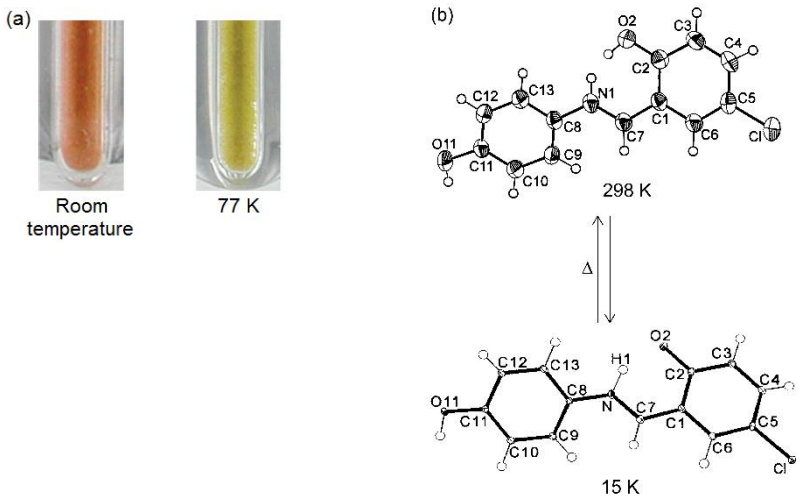

Figure 6.22 - *N*-(5-chlorosalicylidene)-4-hydroxyaniline: (a) Colour change observed upon cooling from room temperature to 77 K[117] and (b) ORTEP plots showing the molecular structure change occurring between 298 K[120] and 15 K[121] (ellipsoids at 50% probability level).

The observed bond lengths for the *cis*-keto form were significantly different to those calculated using density functional theory (Becke3LYP/6-31G) calculations. Hence, it is predicted that in the crystalline phase the *cis*-keto form is distinctly zwitterionic but in the gas phase more quinoidal in character. The stabilization of the *cis*-keto form is attributed to *inter*molecular hydrogen bonding which is enhanced due to the zwitterionic character in crystals increasing molecular polarity. The proposed thermochromic mechanism predicts a higher occupancy of the *cis*-keto form at higher temperature, which is contrary to these reported results. Harada *et al.* explain this by concluding that the colour change in this compound is not caused by the tautomeric equilibrium but due to the change in fluorescence with lowering temperature.[117]

Two-photon excitation of a single-crystal of *N*-3,5-di-*tert*-butylsalicylidene-3-nitroaniline (**11**) at 730 nm was used to excite the bulk crystal and obtain enough conversion to the dark-red *trans*-keto form for structural analysis.[66] This provides the same energy as one-photon excitation at 365 nm and is close to the absorption maximum of the enol form for this compound. At 90 K, before irradiation, the compound existed purely in the enol form. After 4 hours of irradiation at room temperature, the structure was recollected at 90 K and the enol and *trans*-keto forms were observed to coexist in a ratio of 90:10 in the crystal. The space group was retained in the transformation but small changes in the unit cell dimensions and a small increase in the unit cell volume was observed.[66] Subsequent irradiation with λ > 530 nm at room temperature caused the original pale yellow colour to return and X-ray crystallography confirmed the structure had returned to the enol form (Figure 6.23).

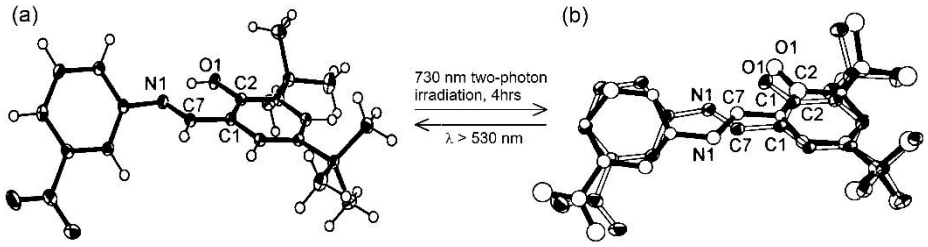

Figure 6.23 - Phototranformation occurring in (**11**). (a) Molecular structure before irradiation and (b) disordered structure after two-photon irradiation at 730 nm for 4hrs; the enol and *trans*-keto forms (10% occupancy) are drawn with white and black bonds respectively. Ellipsoids are shown at 50% probability and hydrogen atoms are omitted for clarity. Reprinted with permission. Copyright 1999 American Chemical Society.[66]

The photocoloured form has a lifetime of 1200 minutes.[122] It is proposed that the *trans*-keto form is stabilized by dimer formation in the photoexcited structure, with *inter*molecular hydrogen bonding occurring between the NH group of the photoproduct on one molecule and an oxygen atom of the nitro group on a second molecule [Figure 6.24(a)].

Ten years later, in 2009, the same group investigated three different polymorphs (α, β and γ) of *N*-3,5-di-*tert*-butylsalicylidene-3-carboxyaniline (**12**) (Table 6.1) to try to establish why different anils display different photoproduct lifetimes.[122]

Table 6.1 - Properties of three polymorphs of *N*-3,5-di-*tert*-butylsalicylidene-3-carboxyaniline.[122]

Polymorph	Colour	Morphology	Photochromic ?	Lifetime of photoproduct (mins)	Dihedral angle between two phenyl rings (°)
α	Colourless	Needle	Yes	17	60.95
β	Pale yellow	Parallelepiped	Yes	780	37.34
γ	Orange	Block	No	N/A	28.90

All three polymorphs were found to crystallize in the enol form before irradiation. The structure of α at 93 K was found to be disordered with the *trans*-keto form observed at 11.7(2)% occupancy after UV light

irradiation at 267 K for 40 minutes. *Inter*molecular hydrogen bonding between the *trans*-keto forms does not occur [Figure 6.24(b)], possibly explaining why the photoproduct lifetime (17 mins) is less that of (**11**) (1200 mins).[122]

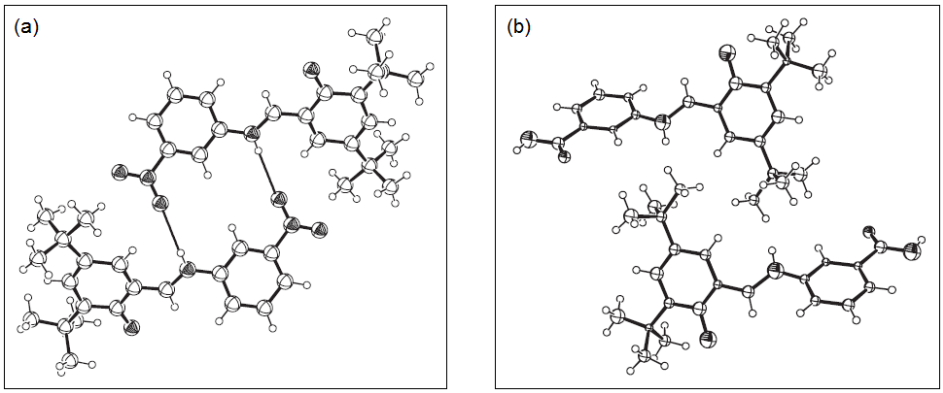

Figure 6.24 - (a) *Inter*molecular hydrogen bonding between *trans*-keto forms in (**11**) and (b) *inter*molecular contact between neighbouring *trans*-keto molecules of polymorph α of (**12**). Reproduced with permission from the Bulletin of the Chemical Society of Japan.[122]

The crystal structure of the photoproduct of polymorph β could not be obtained due to low conversion. The photoinduced transformation in both anil compounds is thought to occur through a "pedal-motion" movement (similar to azobenzene derivatives)[29] where the benzene rings remain almost static and the transformation occurs through rotation of the central section of the molecule.[66, 122] The size of the reaction cavity around the central imine group is thought to be important for the stability of the *trans*-keto form; the larger the reaction cavity the more easily photoisomerization can proceed.[123] The reaction cavities for (**11**) and polymorphs α and β of (**12**) were calculated to be 1.3 Å, 3.5 Å and 1.6 Å respectively.[122]

6.9 Crystal engineering toward applications

6.9.1 Characteristics of photochromic systems suitable for applications

An "ideal" photochromic system would display high yield, thermal stability (important for optical switching applications[3, 6, 40]), good fatigue resistance, few by-products, high sensitivity with quick switching in both directions and stable, isolable starting materials and photoproduct. Photochromic properties need to be retained in solid matrices, display appropriate wavelength sensitivity, a method for non-destructive readout and durability to allow diode lasers to be used for excitation. In reality few systems satisfy all these qualities simultaneously meaning their technological viability is currently limited

The applications of photochromic materials can be separated into two basic groups. Firstly, those directly dependent on absorption or emission spectra changes and secondly, those that utilize changes in other chemical or physical properties, for example refractive index, oxidation or reduction potential, conductivity, dielectric constant, viscosity, solubility or phase transition. Some of the important applications envisioned are optical switching devices and data storage media,[3, 6, 40] actinometers,[124] photoswitchable multicolour displays and multi-state recording[37, 38] and photomechanical actuators.[125, 126] Currently one of the most common usages for photochromic compounds is in ophthalmic lenses for photochromic sunglasses.

Crystal engineering[127] of photochromic compounds[128] through studying structure-property relationships is a rapidly expanding research area motivated by the desire to deeply understand their properties. The eventual aim is to design compounds with the desired properties to match specific applications.

Substitution of different electronic groups, formation of metal complexes and other supramolecular structures are some methods being utilized.

6.9.2 Formation of metal complexes

Inorganic photochromic compounds can be formed in two ways; either by attachment of organic photochromic compounds onto metal centres[129] (or other inorganic groups) or by the inorganic compound's intrinsic structural or electronic properties. The second group will not be discussed in detail here but many reviews are available and mechanisms include spin crossover, linkage isomerism and valence tautomerism.[25, 26, 34, 130]

When an organic photochromic compound is attached to a metal centre the compound's photochromic properties and the electromagnetic and electronic properties of the original metal complex can both be changed. The photoproduct is often stabilized upon complexation, therefore improving the durability of the system. The absorption bands for the photochrome can be shifted by different metals and this can be used to tune the excitation wavelength to suit applications. The electronics and sterics of both the photochrome and metal complex and also metal-metal interactions through the photochromic compound can influence the properties. Another area of interest is multi-photoresponsive systems; by combining metal complexes that show photo-, electro- or chemical response to stimuli with photochromic compounds, gated or dual photochromic materials can be designed for non-destructive readout.[129] Recently, reversible photochromism in a ferrocenylazobenzene monolayer controlled by a single green light source has been reported. The system contains four states which can be reversibly switched due to a combination of azo photoisomerization, electrochemical and chemical redox reactions.[131]

Photochromic organometallics using diarylethene molecules as ligands or linkers, due to their excellent fatigue resistance and durability, have been developed for potential non-linear optical (NLO) materials, smart chemical systems and molecular switching applications.[129] Coordination to the metal centre does not unduly affect the structure of the diarylethene ligands, which still arrange in anti-parallel conformations with the reactive carbons a suitable distance apart for photochromism to occur.[132] Dipolar (bipyridyl)zinc(II) complexes displayed photochromism and efficient switching of NLO properties due to increased π-delocalization in the system upon conversion to the closed form.[133] Ruthenium complexes with metal centres linked by a diethynylated dithienylethene bridge displayed dual photo- and electrochromic behaviour and analogous iron complexes displayed reversible redox switching behaviour via effective communication along the bridging linker between the metal centres.[132]

6.9.3 Formation of other supramolecular structures

Development of supramolecular structures[134] including host-guest compounds, those formed through hydrogen bonding[135] and other interactions[128] have been investigated. These structures display unique photochromic properties, and by utilizing non-covalent *inter*molecular interactions many different structures can be designed for use in novel photonic devices.[128] The formation of clathrate complexes with host molecules, including deoxycholic acid (DCA), crown-ether and cyclodextrin, enhances photochromism usually limited by reaction cavity size, for example in anils.[24]

Diarylethenes with carboxylic acid groups on the perfluoro rings form one dimensional chain-like photochromic structures linked by *inter*molecular hydrogen bonding interactions between adjacent molecules. The chains have two-fold helical symmetry with different helical pitches and absorption maxima depending on the carboxylic acid substitution position and therefore the degree of π-conjugation in the molecule.[135] Co-crystallization of different diarylethenes or a diarylethene and another aromatic, for example benzene or naphthalene, in different stoichiometric ratios can form periodic nano-layered or mosaic structures, with the photoreaction occurring selectively in particular layers due to excited state energy transfer.[128]

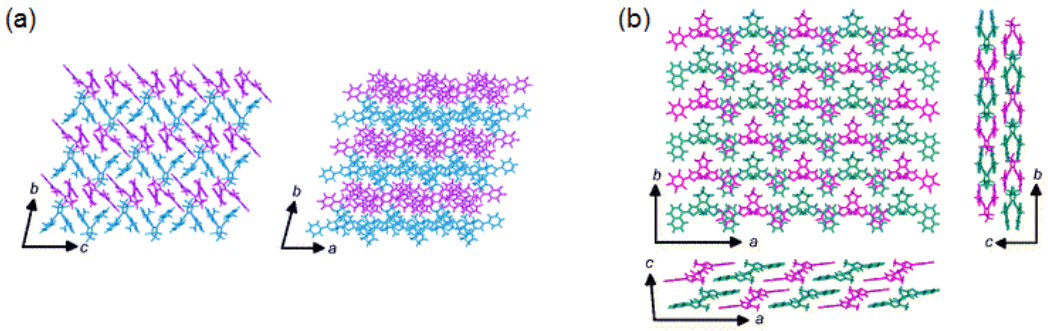

Figure 6.25 - Periodic layered packing structures of two different co-crystals (a) and (b) containing different dithienylethene derivatives. Reproduced with permission from John Wiley and Sons.[128]

Non-photochromic anils have been shown to exhibit photochromism upon inclusion into host DCA-, β- or γ-cyclodextrin molecules.[136-139] This is attributed to the increased space around the anil molecule allowing the *cis-trans* isomerization required for the photochromic mechanism to occur.[139, 140] MCM-41 mesoporous silica, a porous material with a large surface area, has been used to entrap thermochromic *N*-(5-chlorosalicylidene)-aniline by grinding in a 1:1 ratio in the solid-state. The anil is thought to absorb on the inner walls of this inorganic matrix, and now displays photochromism but not thermochromism.[141] Inclusion of viologens in crown ether cavities alters the photochromic behaviour of the polymer film due to *inter*molecular interactions with the host crown ether.[142]

6.10 Conclusions of literature review

The phenomenon of photochromism in the solid-state has been introduced with particular interest in single-crystal to single-crystal transformations in organic photochromic compounds. The problems associated with observing the transformation using photocrystallographic methods have been discussed and two-photon excitation has been presented as a technique for increasing conversion to the photoproduct. The phototransformation mechanisms for different organic photochromic compounds have been introduced by drawing on examples from the literature. Anils have been known for many years to display both solid-state thermo- and photochromism but it has been identified that few reports show systematic analysis of the effect of different substituents, there are conflicting results for the same compounds and many exceptions to general rules. The basic mechanisms for thermo- and photochromism are generally accepted, but the influence of fluorescence on thermochromism of anils needs further investigation and there are only limited reports of the thermo- or photo-induced transformation in single-crystals. The properties required in photochromic compounds for potential applications and crystal design methods being utilized to produce “ideal” photochromic compounds are identified and discussed.

6.11 References

1. G. H. Brown, "*Photochromism*", Wiley-Interscience, New York, 1971.
2. H. Dürr and H. Bouas-Laurent, "*Photochromism: Molecules and Systems*", Revised Edition edn., Elsevier, Amsterdam, 2003.
3. G. Berkovic, V. Krongauz and V. Weiss, *Chem. Rev.*, 2000, **100**, 1741-1753.
4. S. Kawata and Y. Kawata, *Chem. Rev.*, 2000, **100**, 1777-1788.
5. H. Tian and S. Yang, *Chem. Soc. Rev.*, 2004, **33**, 85-97.
6. Y. Yokoyama, *Chem. Rev.*, 2000, **100**, 1717-1740.
7. M. Irie, O. Miyatake and K. Uchida, *J. Am. Chem. Soc.*, 1992, **114**, 8715–8716.
8. S. H. Kawai, S. L. Gilat and J.-M. Lehn, *J. Chem. Soc., Chem. Commun.*, 1994, 1011-1013.
9. T. Hayashi and K. Maeda, *Bull. Chem. Soc. Jpn.*, 1965, **38**, 685-686.
10. N. Fridman, S. Speiser and M. Kaftory, *Cryst. Growth Des.*, 2006, **6** 1653–1662.

11. A. M. A. Asiri, G. A. Baghaffar, K. O. Badahdah, A. G. M. Al-Sehemi, S. A. Khan and A. A. Bukhari, *J. Chem. Sci.*, 2009, **121**, 983-987.
12. J. H. Day, *Chem. Rev.*, 1962, **63**, 65-80.
13. J. H. Day, *Chem. Rev.*, 1968, **68**, 649-657.
14. E. Hadjoudis and I. M. Mavridis, *Chem. Soc. Rev.*, 2004, **33**, 579-588.
15. M. R. di Nunzio, P. L. Gentili, A. Romani and G. Favaro, *J. Phys. Chem. C*, 2010, **114**, 6123–6131.
16. J. B. Goodenough, *J. Solid State Chem.*, 1971, **3**, 490-500.
17. P. U. Biedermann, J. J. Stezowski and I. Agranat, *Chem. --Eur. J.*, 2006, **12**, 3345 – 3354.
18. L. G. Lavrenova, N. G. Yudina, V. N. Ikorskii, V. A. Varnek, I. M. Oglezneva and S. V. Larionov, *Polyhedron*, 1995, **14**, 1333-1337.
19. H. A. Shindy, *Color. Technol.*, 2007, **123**, 298–305.
20. J.-Y. Jaung, *Dyes Pigm.*, 2006, **71**, 245-250.
21. H. Kamogawa and T. Suzuki, *J. Chem. Soc., Chem. Commun.*, 1985, 525-526.
22. H. Kamogawa and T. Suzuki, *Bull. Chem. Soc. Jpn.*, 1987, **60**, 794-796.
23. R. J. Mortimer, *Electrochim. Acta*, 1999, **44**, 2971-2981.
24. K. Amimoto and T. Kawato, *J. Photochem. Photobiol., C*, 2005, **6**, 207-226.
25. H. Nakai and K. Isobe, *Coord. Chem. Rev.*, 2010, **254**, 2652–2662.
26. J. G. Vos and M. T. Pryce, *Coord. Chem. Rev.*, 2010, **254**, 2519–2532.
27. J. Harada, R. Nakajima and K. Ogawa, *J. Am. Chem. Soc.*, 2008, **130**, 7085–7091.
28. J. Harada, Y. Kawazoe and K. Ogawa, *Chem. Commun.*, 2010, **46**, 2593–2595.
29. J. Harada, K. Ogawa and S. Tomoda, *Acta Crystallogr., Sect. B: Struct. Sci.*, 1997, **B53**, 662-672.
30. E. Hadjoudis, S. D. Chatziefthimiou and I. M. Mavridis, *Curr. Org. Chem.*, 2009, **13**, 269-286.
31. K. Matsuda and M. Irie, *Chem. Lett.*, 2006, **35**, 1204-1209.
32. M. Irie, *Photochem. Photobiol. Sci.*, 2010, **9**, 1535-1542.
33. K. S. Murray, *Eur. J. Inorg. Chem.*, 2008, **2008**, 3101–3121.
34. M. A. Halcrow, *Coord. Chem. Rev.*, 2009, **253**, 2493–2514.
35. C. Reichardt, *Chem. Soc. Rev.*, 1992, 147-153.
36. G. Favaro, F. Masetti, U. Mazzucato, G. Ottavi, P. Allegrini and V. Malatesta, *J. Chem. Soc., Faraday Trans.*, 1994, **90**, 333-338.
37. K. Higashiguchi, K. Matsuda and M. Irie, *Angew. Chem., Int. Ed.*, 2003, **42** 3537 –3540.
38. M. Morimoto, S. Kobatake and M. Irie, *J. Am. Chem. Soc.*, 2003, **125** 11080–11087.
39. S. i. Nakatsuji, *Chem. Soc. Rev.*, 2004, **33**, 348-353.
40. M. Irie, *Chem. Rev.*, 2000, **100**, 1685-1716.
41. W. Marckwald, *Z. Phys. Chem (Leipzig)*, 1899, **30**, 140.
42. J. Fritzsche, *Compt. Rend. Acad. Sci., Paris*, 1867, **69**, 1035.
43. Y. Hirshberg, *Compt. Rend. Acad. Sci., Paris*, 1950, **231**, 903.
44. G. Porter, *Angew. Chem.*, 1968, **80**, 882-891.
45. M. R. di Nunzio, P. L. Gentili, A. Romani and G. Favaro, *ChemPhysChem*, 2008, **9**, 768-775.
46. M. D. Cohen and G. M. J. Schmidt, *J. Chem. Soc.*, 1964, 1996-2000.
47. G. M. J. Schmidt, *Pure Appl. Chem.*, 1971, **27**, 647-678.
48. M. D. Cohen, *Angew. Chem., Int. Ed. Engl.*, 1975, **14**, 386–393.
49. J. Harada, M. Harakawa, S. Sugiyama and K. Ogawa, *CrystEngComm*, 2009, **11**, 1235-1239.
50. A. E. Goeta and J. A. K. Howard, *Chem. Soc. Rev.*, 2004, **33**, 490-500.
51. J. M. Cole, *Chem. Soc. Rev.*, 2004, **33**, 501-513.
52. P. Coppens, I. I. Vorontsov, T. Graber, M. Gembicky and A. Y. Kovalevsky, *Acta Crystallogr., Sect. A: Found. Crystallogr.*, 2005, **61**, 162-172.
53. J. M. Cole, *Acta Crystallogr., Sect. A: Found. Crystallogr.*, 2008, **A64**, 259–271.
54. E. Collet, M.-H. Lemée-Cailleau, M. Buron-Le Cointe, H. Cailleau, M. Wulff, T. Luty, S.-Y. Koshihara, M. Meyer, L. Toupet, P. Rabiller and S. Techert, *Science*, 2003, **300**, 612-615.
55. P. Coppens, I. I. Vorontsov, T. Graber, A. Y. Kovalevsky, Y.-S. Chen, G. Wu, M. Gembicky and I. V. Novozhilova, *J. Am. Chem. Soc.*, 2004, **126**, 5980-5981.

56. L. X. Chen, G. Jennings, T. Liu, D. J. Gosztola, J. P. Hessler, D. V. Scaltrito and G. J. Meyer, *J. Am. Chem. Soc.*, 2002, **124**, 10861-10867.
57. M. R. Warren, S. K. Brayshaw, A. L. Johnson, S. Schiffers, P. R. Raithby, T. L. Easun, M. W. George, J. E. Warren and S. J. Teat, *Angew. Chem., Int. Ed.*, 2009, **48**, 5711-5714.
58. J. Kusz, H. Spiering and P. Gütlich, *J. Appl. Crystallogr.*, 2001, **34**, 229-238.
59. M. Göppert-Mayer, *Ann. Phys. (Leipzig)*, 1931, **9**, 273.
60. W. Kaiser and C. G. B. Garrett, *Phys. Rev. Lett.*, 1961, **7**, 229-231.
61. F. Terenziani, C. Katan, E. Badaeva, S. Tretiak and M. Blanchard-Desce, *Adv. Mater.*, 2008, **20**, 4641–4678.
62. M. Pawlicki, H. A. Collins, R. G. Denning and H. L. Anderson, *Angew. Chem., Int. Ed.*, 2009, **48**, 3244-3266.
63. D. M. Friedrich, *J. Chem. Educ.*, 1982, **59**, 472-481.
64. D. A. Parthenopoulos and P. M. Rentzepis, *Science*, 1989, **245**, 843-845.
65. M. Uchida and M. Irie, *J. Am. Chem. Soc.*, 1993, **115**, 6442–6443.
66. J. Harada, H. Uekusa and Y. Ohashi, *J. Am. Chem. Soc.*, 1999, **121**, 5809-5810.
67. N. Tamai and H. Miyasaka, *Chem. Rev.*, 2000, **100**, 1875-1890.
68. T. Fujino, S. Y. Arzhantsev and T. Tahara, *J. Phys. Chem. A*, 2001, **105** 8123–8129.
69. T. Schultz, J. Quenneville, B. Levine, A. Toniolo, T. J. Martínez, S. Lochbrunner, M. Schmitt, J. P. Shaffer, M. Z. Zgierski and A. Stolow, *J. Am. Chem. Soc.*, 2003, **125** 8098–8099.
70. C. Dugave and L. Demange, *Chem. Rev.*, 2003, **103**, 2475–2532.
71. H. Zollinger, "*Azo and Diazo Chemistry*", Interscience, New York and London, 1961.
72. H. Bock, G. Rudolph, E. Baltin and J. Kroner, *Angew. Chem.*, 1965, **77**, 469-484.
73. M. I. Bruce, *Angew. Chem.*, 1977, **89**, 75–89.
74. A. Mostad and C. Rømming, *Acta Chemica Scandinavica*, 1971, **25**, 3561-3568.
75. K. Fries, S. Samanta, S. Orski and J. Locklin, *Chem. Commun.*, 2008, 6288–6290.
76. A. Zelichenok, F. Buchholtz, J. Ratner, E. Fischer and V. Krongauz, *J. Photochem. Photobiol., A*, 1994, **77**, 201-206.
77. N. Malic, J. A. Campbell and R. A. Evans, *Macromolecules*, 2008, **41**, 1206-1214.
78. W. Du and H. Y. Tam, *Opt.Commun.*, 1996, **126**, 223-229.
79. S. Bénard and P. Yu, *Chem. Commun.*, 2000, 65-66.
80. T. Asahi and H. Masuhara, *Chem. Lett.*, 1997, **26**, 1165-1166.
81. T. Asahi, M. Suzuki and H. Masuhara, *J. Phys. Chem. A*, 2002, **106**, 2335-2340.
82. M. Suzuki, T. Asahi, K. Takahashi and H. Masuhara, *Chem. Phys. Lett.*, 2003, **368**, 384–392.
83. M. Suzuki, T. Asahi and H. Masuhara, *ChemPhysChem*, 2005, **6**, 2396 – 2403.
84. E. Fischer and Y. Hirshberg, *J. Chem. Soc.*, 1952, 4522-4524.
85. M. Kawano, T. Sano, J. Abe and Y. Ohashi, *J. Am. Chem. Soc.*, 1999, **121**, 8106–8107.
86. A. Kaneko, A. Tomoda, M. Ishizuka, H. Suzuki and R. Matsushima, *Bull. Chem. Soc. Jpn.*, 1988, **61**, 3569-3573.
87. R. Hoffmann and R. B. Woodward, *Acc. Chem. Res.*, 1968, **1**, 17–22.
88. M. Irie, K. Sakemura, M. Okinaka and K. Uchida, *J. Org. Chem.*, 1995, **60** 8305–8309.
89. G. Hohlneicher, M. Müller, M. Demmer, J. Lex, J. H. Penn, L.-X. Gan and P. D. Loesel, *J. Am. Chem. Soc.*, 1988, **110**, 4483–4494.
90. M. Irie, T. Lifka, K. Uchida, S. Kobatake and Y. Shindo, *Chem. Commun.*, 1999 747-750.
91. S. Kobatake, K. Uchida, E. Tsuchida and M. Irie, *Chem. Commun.*, 2002, 2804-2805
92. S. Kobatake, T. Yamada, K. Uchida, N. Kato and M. Irie, *J. Am. Chem. Soc.*, 1999, **121** 2380–2386.
93. T. Yamada, S. Kobatake, K. Muto and M. Irie, *J. Am. Chem. Soc.*, 2000, **122** 1589–1592.
94. T. Yamada, S. Kobatake and M. Irie, *Bull. Chem. Soc. Jpn.*, 2000, **73**, 2179-2184.
95. T. Yamada, K. Muto, S. Kobatake and M. Irie, *J. Org. Chem.*, 2001, **66**, 6164–6168.
96. J. Han and J.-B. Meng, *J. Photochem. Photobiol., C*, 2009, **10**, 141–147.
97. K. Tanaka, Y. Yamamoto and M. R. Caira, *CrystEngComm*, 2004, **6**, 1-4.
98. K. Tanaka and F. Toda, *J. Chem. Soc., Perkin Trans. 1*, 2000, 873-874.

99. L. Xu, T. Sugiyama, H. Huang, Z. Song, J. Meng and T. Matsuura, *Chem. Commun.*, 2002, 2328-2329.
100. P. Naumov, *J. Mol. Struct.*, 2006, **783**, 1–8.
101. P. Naumov, A. Sekine, H. Uekusa and Y. Ohashi, *J. Am. Chem. Soc.*, 2002, **124**, 8540–8541.
102. M. D. Cohen and G. M. J. Schmidt, *J. Phys. Chem.*, 1962, **66**, 2442-2446.
103. W. Luck and H. Sand, *Angew. Chem., Int. Ed.*, 1964, **3**, 570-580.
104. F. Robert, A. D. Naik, B. Tinant, R. Robiette and Y. Garcia, *Chem. --Eur. J.*, 2009, **15**, 4327-4342.
105. M. Sliwa, S. Létard, I. Malfant, M. Nierlich, P. G. Lacroix, T. Asahi, H. Masuhara, P. Yu and K. Nakatani, *Chem. Mater.*, 2005, **17**, 4727-4735.
106. T. Elsaesser and H. J. Bakker, "*Ultrafast Hydrogen Bonding Dynamics and Proton Transfer Processes in the Condensed Phase (Understanding Chemical Reactivity)*", Kluwer Academic Publishers, Dordrecht, The Netherlands, 2002.
107. M. D. Cohen, G. M. J. Schmidt and M. Flavian. S., *J. Chem. Soc.*, 1964, 2041-2051.
108. M. D. Cohen, Y. Hirshberg and G. M. J. Schmidt, *J. Chem. Soc.*, 1964, 2060-2067.
109. F. Arod, P. Pattison, K. J. Schenk and G. Chapuis, *Cryst. Growth Des.*, 2007, **7**, 1679-1685.
110. T. Fujiwara, J. Harada and K. Ogawa, *J. Phys. Chem. B*, 2004, **108**, 4035-4038.
111. M. Sliwa, N. Mouton, C. Ruckebusch, S. Aloïse, O. Poizat, G. Buntinx, R. Métivier, K. Nakatani, H. Masuhara and T. Asahi, *J. Phys. Chem. C*, 2009, **113**, 11959-11968.
112. M. Sliwa, N. Mouton, C. Ruckebusch, L. Poisson, A. Idrissi, S. Aloïse, L. Potier, J. Dubois, O. Poizat and G. Buntinx, *Photochem. Photobiol. Sci.*, 2010, **9**, 661-669.
113. C. Ruckebusch, N. Mouton, T. Gladytz, A. Rendelmann, G. Buntinx and M. Sliwa, *Sci China Phys Mech Astron*, 2010, **53**, 1024–1035.
114. M. Sliwa, A. Spangenberg, R. Métivier, S. Létard, K. Nakatani and P. Yu, *Res. Chem. Intermed.*, 2008, **34**, 181-190.
115. M. Sliwa, A. Spangenberg, I. Malfant, P. G. Lacroix, R. Métivier, R. B. Pansu and K. Nakatani, *Chem. Mater.*, 2008, **20**, 4062–4068.
116. P. Kubelka and F. Munk, *Z. Tech. Phys. (Leipzig)*, 1931, **12**, 593-601.
117. J. Harada, T. Fujiwara and K. Ogawa, *J. Am. Chem. Soc.*, 2007, **129**, 16216-16221.
118. G. Wyszechi, "*Color science: concepts and methods, quantitative data and formulae*", 2nd Edition edn., Wiley, New York, 2001.
119. E. Hadjoudis, M. Vittorakis and I. Moustakali-Mavridis, *Tetrahedron*, 1987, **43**, 1345-1360.
120. K. Ogawa, Y. Kasahara, Y. Ohtani and J. Harada, *J. Am. Chem. Soc.*, 1998, **120**, 7107-7108.
121. K. Ogawa, J. Harada, I. Tamura and Y. Noda, *Chem. Lett.*, 2000, **29**, 528-529.
122. K. Johmoto, A. Sekine, H. Uekusa and Y. Ohashi, *Bull. Chem. Soc. Jpn.*, 2009, **82**, 50-57.
123. Y. Ohashi, K. Yanagi, T. Kurihara, Y. Sasada and Y. Ohgo, *J. Am. Chem. Soc.*, 1981, **103**, 5805-5812.
124. H. G. Heller and J. R. Langan, *J. Chem. Soc., Perkin Trans. 2*, 1981, 341-343.
125. S. Kobatake, S. Takami, H. Muto, T. Ishikawa and M. Irie, *Nature*, 2007, **446**, 778-781.
126. Y. Yu, M. Nakano and T. Ikeda, *Nature*, 2003, **425**, 145.
127. C. B. Aakeröy, *Acta Crystallogr., Sect. B: Struct. Sci.*, 1997, **B53**, 569-586.
128. M. Morimoto, S. Kobatake and M. Irie, *Chem. Rec.*, 2004, **4**, 23–38.
129. V. Guerchais, L. Ordronneau and H. Le Bozec, *Coord. Chem. Rev.*, 2010, **254**, 2533–2545.
130. O. Sato, A. Cui, R. Matsuda, J. Tao and S. Hayami, *Acc. Chem. Res.*, 2007, **40**, 361-369.
131. K. Namiki, A. Sakamoto, M. Murata, S. Kume and H. Nishihara, *Chem. Commun.*, 2007, 4650–4652.
132. Y. Tanaka, T. Ishisaka, A. Inagaki, T. Koike, C. Lapinte and M. Akita, *Chem. --Eur. J.*, 2010, **16**, 4762 – 4776.
133. V. Aubert, V. Guerchais, E. Ishow, K. Hoang-Thi, I. Ledoux, K. Nakatani and H. Le Bozec, *Angew. Chem., Int. Ed.*, 2008, **47**, 577 –580.
134. J. W. Steed and J. L. Atwood, "*Supramolecular Chemistry*", 2nd Edition edn., John Wiley & Sons, Ltd. (UK), Chichester, UK 2009.
135. S. Yamamoto, K. Matsuda and M. Irie, *Chem. --Eur. J.*, 2003, **9**, 4878-4886.

136. H. Koyama, T. Kawato, H. Kanatomi, H. Matsushita and K. Yonetani, *J. Chem. Soc., Chem. Commun.*, 1994, 579-580.
137. T. Kawato, H. Koyama, H. Kanatomi, K. Yonetani and H. Matsushita, *Chem. Lett.*, 1994, **23**, 665-668.
138. G. Pistolis, D. Gegiou and E. Hadjoudis, *J. Photochem. Photobiol., A*, 1996, **93**, 179-184.
139. E. Hadjoudis, K. Yannakopoulou, S. D. Chatziefthimiou, A. Paulidou and I. M. Mavridis, *J. Photochem. Photobiol., A*, 2011, **217**, 293-298.
140. E. Giglio, J. L. Atwood, J. E. D. Davies and D. D. MacNicol, "*Inclusion Compounds, vol. 2"*, Academic Press, London, 1984
141. E. Hadjoudis, A. B. Bourlinos and D. Petridis, *J. Inclusion Phenom. Macrocyclic Chem.*, 2002, **42**, 275-279.
142. T. Kuwabara, M. Sugiyama and M. Nanasawa, *Photochem. Photobiol.*, 2001, **73**, 469–472.

Chapter 7

Structural studies of *N*-(methoxysalicylidene)-fluoroaniline, *N*-(methoxysalicylidene)-chloroaniline and *N*-(methoxysalicylidene)-bromoaniline derivatives

Helen E. Mason, Jane L. R. Yates, Rachael J. Potts, Matthias J. Gutmann, Judith A. K. Howard and Hazel A. Sparkes

Published *Acta Crystallographica B*, 2021 in publication, doi.org/10.1107/S2052520621009835. Reproduced with permission of the International Union of Crystallography.

7.1 Abstract

Twenty-seven *N*-(methoxysalicylidene)-haloaniline (halo = F, Cl or Br) compounds were synthesised. The crystal structures of all twenty-seven compounds have been determined at low temperature and are reported herein, along with a variable temperature neutron diffraction study on two of the compounds. New polymorphs were identified for two of the compounds along with a temperature induced phase transition for one of the other compounds. Visual observations on the thermochromism of the 27 compounds are also reported. The *inter*planar angle between the two aromatic rings and the *inter*molecular interactions in the structures are examined and linked to the visual observations on the thermochromism.

7.2 Introduction

The relatively easy synthesis of a wide range of Schiff bases makes them versatile ligands and consequently they have found widespread use in many areas including organometallic chemistry,[1] polymer synthesis,[2] anticancer drugs,[3] catalysts[4] and sensors.[5] In addition, Schiff bases themselves have been found to display interesting properties with anils, Schiff bases of salicylaldehyde derivatives with aniline derivatives, having been found to exhibit both thermo- and photochromism in the solid-state.[6-8] Originally the thermochromism and photochromism of anils were thought to be mutually exclusive[7, 8] but this has since been found not to be the case and it is thought they all display thermochromism with some also displaying photochromism.[9] The colour change was initially attributed to a light or thermally induced tautomeric equilibrium shift between colourless enol(-imine) and coloured keto(-amine) forms,[10, 11] see Figure 7.1. In both cases the chromism involves an intramolecular proton shift from the ortho-hydroxy group, crucial for the mechanism to occur, to the imine nitrogen atom. Evidence for the thermochromic mechanism was first observed in N-(5-chlorosalicylidene)-4-hydroxyaniline with the population of the cis-keto form increasing with decreasing temperature, with the ratio of OH to NH forms changing from 31:69 at 299 K to 10:90 at 90 K[12] and at 15K it is believed to be solely the NH form.[13] The photochromic mechanism has been observed in single crystals of N-3,5-di-tert-butylsalicylidene-3-nitroaniline.[14] After 4 hours irradiation at room temperature, using 2-photon excitation at 730 nm, the structure of the dark-red photo product at 90 K was found to contain both the enol and trans-keto form at a ratio of 90:10. Irradiation at room temperature using light with $\lambda > 530$ nm caused the crystal to return to the pale yellow colour of the enol form and demonstrated the reversibility of the mechanism.

The enol to keto tautomerism isn't the whole picture, Harada et al. identified that thermochromism in anils can only be explained by taking into account the fluorescence and not just the tautomeric equilibrium between enol and cis-keto forms.[15] The impact of the

fluorescence becomes particularly significant for thermochromic compounds at lower temperatures and can in fact dominate as the cause of the thermochromic colour change. While at higher temperatures the keto-enol tautomerism is dominant for thermochromic compounds.

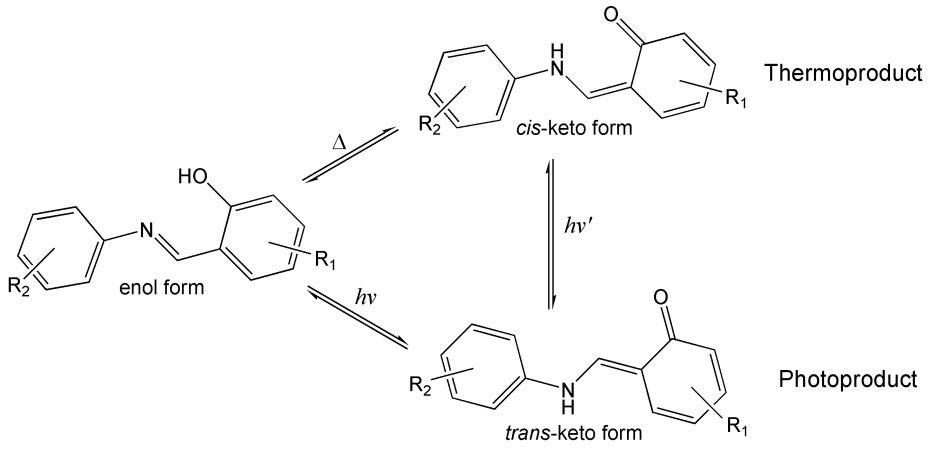

Figure 7.1 - Illustration of the enol to keto tautomerism mechanism which affects that colour change in anils.

The synthesis of twenty-seven *N*-(methoxysalicylidene)-haloaniline (halo = F, Cl or Br) compounds are reported. The crystal structures of all of the compounds are reported at low temperature. Ten of the structures had previously been reported at room temperature, however they are reported herein at low temperature for completeness. For two other compounds new polymorphs were identified herein while a further compound was found to undergo a temperature induced phase transition. Visual observations were made of the thermochromic colour change upon cooling for all of the compounds. These were linked to the structural properties of the various compounds.

Table 7.1 - Studied compounds and their reference numbers

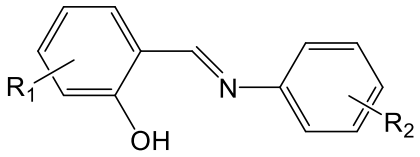

R_1 = OMe
R_2 = Br, Cl, F

Compound reference number	Substituents		Compound reference number	Substituents
1-F	R_1 = 3-OMe, R_2 = 2-F		**1-Br**	R_1 = 3-OMe, R_2 = 2-Br
2-F	R_1 = 4-OMe, R_2 = 2-F		**2-Br**	R_1 = 4-OMe, R_2 = 2-Br
3-F	R_1 = 5-OMe, R_2 = 2-F		**3-Br**	R_1 = 5-OMe, R_2 = 2-Br
4-F	R_1 = 3-OMe, R_2 = 3-F		**4-Br**	R_1 = 3-OMe, R_2 = 3-Br
5-F	R_1 = 4-OMe, R_2 = 3-F		**5-Br**	R_1 = 4-OMe, R_2 = 3-Br
6-F	R_1 = 5-OMe, R_2 = 3-F		**6-Br**	R_1 = 5-OMe, R_2 = 3-Br
7-F	R_1 = 3-OMe, R_2 = 4-F		**7-Br**	R_1 = 3-OMe, R_2 = 4-Br
8-F	R_1 = 4-OMe, R_2 = 4-F		**8-Br**	R_1 = 4-OMe, R_2 = 4-Br
9-F	R_1 = 5-OMe, R_2 = 4-F		**9-Br**	R_1 = 5-OMe, R_2 = 4-Br
1-Cl	R_1 = 3-OMe, R_2 = 2-Cl		**6-Cl**	R_1 = 5-OMe, R_2 = 3-Cl
2-Cl	R_1 = 4-OMe, R_2 = 2-Cl		**7-Cl**	R_1 = 3-OMe, R_2 = 4-Cl
3-Cl	R_1 = 5-OMe, R_2 = 2-Cl		**8-Cl**	R_1 = 4-OMe, R_2 = 4-Cl
4-Cl	R_1 = 3-OMe, R_2 = 3-Cl		**9-Cl**	R_1 = 5-OMe, R_2 = 4-Cl
5-Cl	R_1 = 4-OMe, R_2 = 3-Cl			

7.3 Experimental

7.3.1 Synthesis

All reagents were used as supplied from Aldrich. Compounds were synthesized by direct condensation of the appropriate salicylaldehyde and aniline derivatives in ethanol. 0.0025 moles of the salicylaldehyde and aniline were each dissolved in 25 ml of ethanol, the resulting solutions combined and refluxed with stirring for four hours. Any precipitate was filtered off rinsed with ethanol and left to dry, the (remaining) solution was then rotary evaporated until (further) precipitate formed. Re-crystallization was carried out from ethanol and acetonitrile for all compounds. The compounds synthesised along with the reference numbers used to refer to them throughout this paper are listed in Table 7.1.

7.3.2 X-ray Crystallography

Single crystal X-ray diffraction measurements for **1**-**F** to **9**-**F**, **7**-**Cl** to **9**-**Cl** and **1**-**Br** to **9**-**Br** were collected at 120(2) K, **9**-**Br** was also collected at 220(2) K on Bruker Smart 1K diffractometer, **1**-**Cl** to **3**-**Cl** were collected at 120(2) K, **4**-**Cl** and **6**-**Cl** were collected at 100(2) K and **5**-**Cl** was collected at 150(2) K on a Bruker ApexII diffractometer. All datasets were collected using graphite monochromated Mo Kα radiation (λ = 0.71073 Å) and recorded on a CCD detector. Unit cell parameters were also checked at 300(2) K for all structures. Structures **1**-**F** to **9**-**F**, **7**-**Cl** to **9**-**Cl** and **1**-**Br** to **9**-**Br** were solved using direct methods in ShelXS[16] and **1**-**Cl** to **6**-**Cl** were solved using Superflip.[17-19] All structures were refined by full matrix least squares on F^2 using SHELXL[16, 20] in Olex2.[21] All hydrogen atoms, apart from the OH hydrogen involved in the intramolecular hydrogen bonding with the imine nitrogen atom were positioned geometrically (aromatic and C8-H8 C-H

0.95 Å, methyl C-H 0.98 Å) and refined using a riding model. The isotropic displacement parameter of the hydrogen atom was fixed at U_{iso}(H) = 1.2 times U_{eq} of the parent carbon atom for the aromatic hydrogen atoms and C8-H8, while U_{iso}(H) = 1.5 times U_{eq} for the parent carbon atom for the methyl hydrogens. The hydrogen atoms involved in the intramolecular hydrogen bond were located in the Fourier difference map (FDM) wherever feasible or fixed geometrically (O-H 0.84 Å, U_{iso}(H) = 1.2 times U_{eq} of the parent oxygen atom) for **6**-**F**, **5**-**Br** and **6**-**Br** where this was not possible. Crystal packing diagrams were created and analyzed using Mercury.[22] The *inter*planar dihedral angle was calculated by measuring the angle between planes computed through the six carbon atoms of the two aromatic rings. See Appendix 7, Tables S7.1-S7.3 for further details of the crystallographic data collections.

Single crystal neutron diffraction data for 3-Cl and 3-Br were collected at 120 and 300 K on SXD at ISIS,[23] by mounting a single crystal on a closed cycle refrigerator and using 4-5 crystal settings. Data were processed using SXD2001.[24]

7.3.3 Diffuse reflectance spectroscopy

Diffuse reflectance spectra were measured for **1-Br** to **9-Br**. The sample was ground to give uniform particle distribution and placed in a 40 x 10 x 2 mm quartz cuvette to ensure optical thickness. A cuvette sample holder with a white polytetrafluoroethylene (PTFE) block spacer was used to load the sample into an Oxford Instruments Cryostat. The sample was irradiated with an Ocean Optics halogen light source and an Avantes AvaSpec-2048-2 CCD detector (placed at an acute angle to minimize detection of specular reflectance) collected the reflectance spectra which were recorded using AvaSoft basic software. Cryostat temperature control was achieved using an Oxford Intelligent Temperature Controller, each temperature was stabilized by leaving for 10 min or waiting until a temperature variation of ±0.1 K before recording the spectrum. A white PTFE block was used to record a reference spectrum before each data set collection. The diffuse reflectance spectra are illustrated as % reflectance versus wavelength and Kubelka-Munk function, *F(R)*, versus wavelength. If *S* is independent of λ, then *F(R)* versus λ is equivalent to the absorption spectrum for a diffuse reflector. To allow basic trends to be easily observed moving averages were applied to data during analysis.

7.4 Results and Discussion

7.4.1 Crystal Structures

The crystal structures of compounds **1-F**,[25] **1-Cl**,[26] **2-Cl**,[27] **3-Cl**,[28] **6-Cl**,[29] **8-Cl**,[27] **9-Cl**,[30] **3-Br**,[31] **6-Br**[31] and **7-Br**[32] have previously been reported. The structures obtained herein were consistent with the previously published structures. Different polymorphs, to those previously published, were obtained in this study for **8-F**[33] and **7-Cl**[34] and a phase transition upon cooling was observed for **9-Br**.[31] The structures reported herein will be denoted as **8-F(2)**, **7-Cl(2)** and **9-Br(LT)**. The structures of the remaining compounds are included here at low temperature for completeness as the published structures are at room temperature. They also demonstrate that for the majority of them no structural changes are observed upon cooling.

The 27 compounds all crystallised with one molecule in the asymmetric unit (Z'=1) with the exception of **7**-**Cl(2)** which contained two unique molecules in the asymmetric unit (Z'=2) in this study. However, the previously published polymorph of **7-Cl(1)** had one molecule in the asymmetric unit (Z'=1).[34] The basic structure of the 27 compounds is the same containing a methoxy substituted hydroxy-phenyl group and a halogen substituted phenyl group joined by an imine group (Figure 7.2). The imine group C8=N1 bond lengths range from 1.263(12) Å in **6**-**Br** to 1.299(10) Å in **9**-**Br(LT)**, while the hydroxyl-phenyl C2-O2 bond lengths range from 1.343(4) Å in

8-Cl to 1.364(7) Å in **5-Br**. These C8=N1 and C2-O2 are consistent with the bonds being double and single bonds respectively,[35] indicating that the crystal structures are all in the enol form. An *intra*molecular hydrogen bond creates a quasi-six-membered ring O2-H2···N1-C8-C7-C2, which shows only small deviations from planarity (maximum 0.0293 Å for **2-F**, calculated as deviations from the plane through the five non-hydrogen atoms, this value was less for the other compounds).

Examining the intermolecular interactions in the structures showed the presence of C-H···O,[36] and also in the case of **1-F** to **9-F** C-H···F,[37, 38] interactions in all of the structures. In addition, a small number of the structures also contained π-π interactions (Appendix 7, Tables S7.4-S7.8). The C-H···O interactions involve the methoxy oxygen (O1) and/or hydroxy oxygen (O2) atoms interacting mainly with aromatic C-H, although in the case of **5-F**, **8-F(2)**, **5-Cl** and **8-Br** only methyl C-H are involved (Appendix 7, Tables S7.4-S7.6). The C-H···F interactions also mainly involve aromatic hydrogen atoms, except **9-F** which also involved a methyl hydrogen atom and **6-F** which contains either short aromatic or methyl C-H···F interactions due to the disorder in the fluorine atoms (Appendix 7, Table S7.7).

7.4.2 Polymorph 8-F(2)

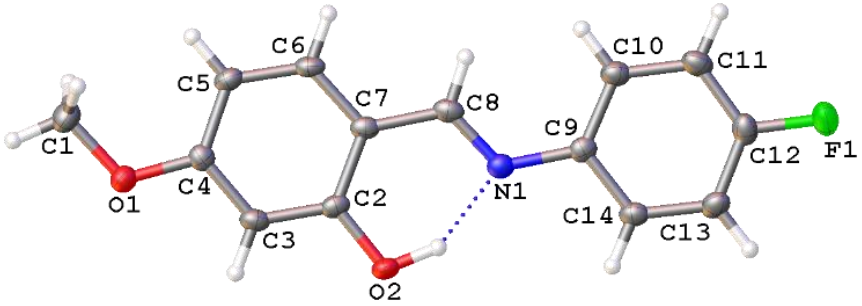

Figure 7.2 - Structure of **8-F(2)** at 120(2) K with atomic numbering scheme depicted. Intramolecular hydrogen bond shown with dashed line.

The structure of **8-F** obtained in the current study, **8-F(2)**, see Figure 7.2, differs significantly from the previously published structure, denoted **8-F(1)**.[33] Both polymorphs crystallised in the monoclinic crystal system, with **8-F(1)** in the space group *Pc* while **8-F(2)** was in the space group $P2_1/c$. However, there are key differences in the molecular conformations of the two polymorphs. Firstly while both polymorphs have the methyl group of the -OMe group in approximately the same plane as the phenyl group to which it is attached, for **8-F(1)** it is on the same side as the OH group while for **8-F(2)** it is on the opposite side to the OH group. Secondly, the two phenyl rings are orientated differently with respect to each, in **8-F(1)** the dihedral angle between the two phenyl rings is 48.17(1)° while for **8-F(2)** it is 2.07(9)° see Figure 7.3.

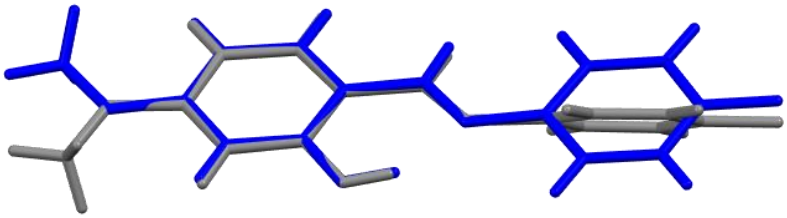

Figure 7.3 - Overlay of molecule of (grey) **8-F(1)** at room temperature on (blue) **8-F(2)** at 120(2) K.

The packing and intermolecular interactions for the two polymorphs are also quite different. In the case of **8-F(1)** all of the molecules are orientated in the same direction, and the structure shows C-H···F interactions between the methyl group and the fluorine atom of adjacent molecules. While in the case of **8-F(2)**, C-H···F interactions exist between an aromatic H adjacent to the F on one molecule and the F on an adjacent molecule. The structure also contains π-π interactions between adjacent molecules forming a stack in approximate the *a* axis direction.

7.4.3 Polymorph 7-Cl(2)

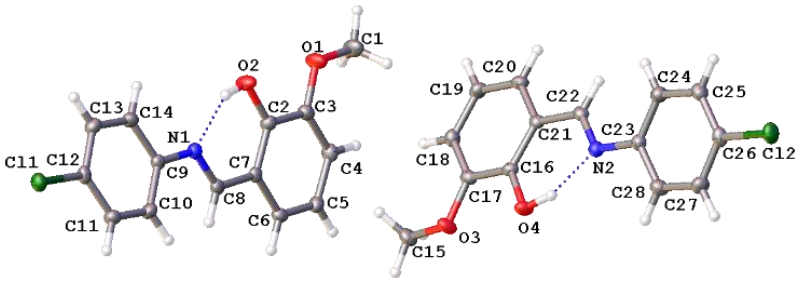

Figure 7.4 - Structure of **7-Cl(2)** at 120(2) K shown with the atomic numbering scheme. Intramolecular hydrogen bonding shown with dashed lines.

In the case of **7-Cl**, the previously published structure (**7-Cl(1)**)[34] was obtained in the orthorhombic space group $P2_12_12_1$ with one molecule in the asymmetric unit. The dihedral angle between the two rings was ~11.9°. The structure of **7-Cl(2)** obtained herein crystallised in the monoclinic space group $P2_1/c$ with two molecules in the asymmetric unit, see Figure 7.4. The dihedral angles between the two phenyl rings were 11.75(11)° and 16.73(11)° for the two independent molecules, very similar to that seen for **7-Cl(1)**. The structure of **7-Cl(2)**, unlike **7-Cl(1)**, contains Cl···Cl interactions with Cl···Cl distances of 3.3618(7) Å and 3.3845(7) Å. Examining the packing of the two polymorphs shows that **7-Cl(1)** forms a herring bone type motif. While **7-Cl(2)** has a herring bone type motif in the *ab* plane, however it is two molecules wide in the *c*-axis direction and then as a result of the *c*-glide the zig-zag is the opposite direction still in the *ab* plane, see Figure 7.5.

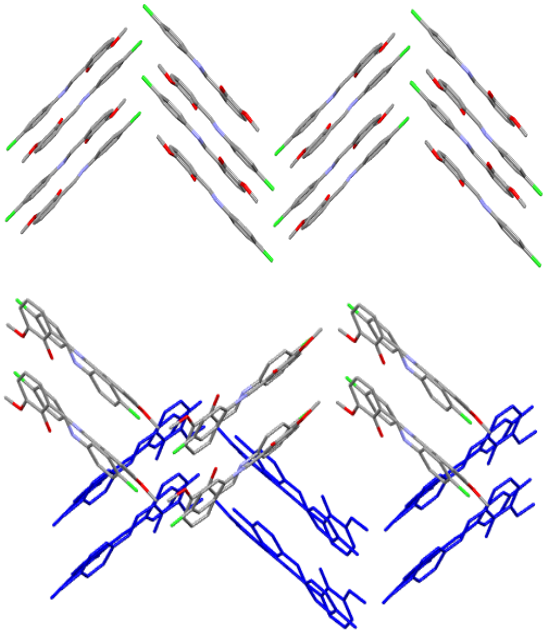

Figure 7.5 - Packing for (top) **7-Cl(1)**, (bottom) **7-Cl(2)** with front pair of molecules with different colours for the different elements and next pair behind in blue to show opposite zig-zag direction.

7.4.4 Temperature induced phase transition 9-Br

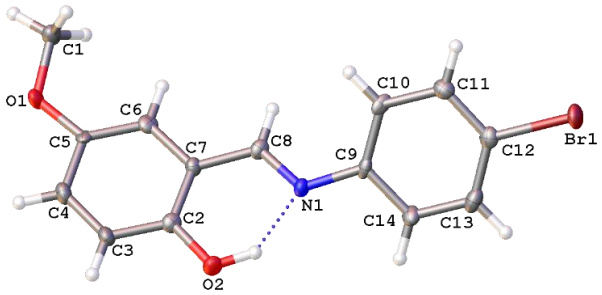

Figure 7.6 - Structure of 9-Br at 120(2) K with atomic numbering scheme shown. Intramolecular hydrogen bond shown with dashed line.

The structure of 9-Br[31] has previously been published at room temperature in the monoclinic space group *Pc*, see Figure 7.6. The structures obtained herein at 300(2) K and 220(2) K were consistent with the previously published structure. However, the structure was found to undergo a thermal phase transition upon cooling with no significant loss of crystallinity. At 120(2) K the structure was found to be in the monoclinic space group *Cc*, with an approximate doubling of the *a* -axis length from 14.112(3) Å at 300(2) K to 27.874(5) Å at 120(2) K and a reduction in the β angle from 98.326(4)° at 300(2) K to 95.091(4)° at 120(2) K. The orientation of the molecule did not change significantly as a result of the phase transition, see Figure 7.7, and the packing in both cases was almost identical.

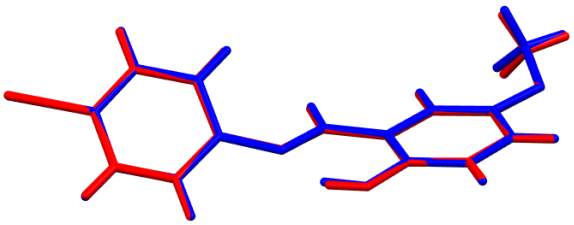

Figure 7.7 - Overlay of one molecule of **9-Br** at (red) 300(2) K on **9-Br** at (blue) 120(2) K.

7.4.5 Thermochromic observations

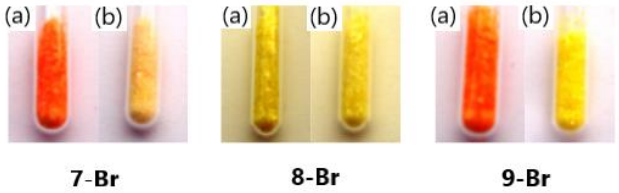

Figure 7.8 - Microcrystalline powders of (left) **7-Br**, (middle) **8-Br** and (right) **9-Br** at (a) room temperature (b) after dipping in liquid nitrogen.

The anils are known to display thermochromism. Here all of the 3- or 5-methoxysalicylaldimine derivatives were found to be orange/red at room temperature and showed a reversible colour change to yellow when dipped in liquid nitrogen temperature (~77 K). The 4-methoxysalicylaldimine derivatives appear yellow at room temperature and show little or no colour change to the naked eye with decreasing temperature (see Figure 7.8 for a representative example). The colour change for the strongly thermochromic compounds can also be followed clearly by eye as a function of temperature, see Figure 7.9.

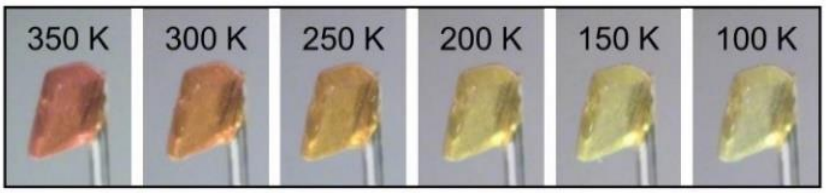

Figure 7.9 - Illustration of the colour change upon cooling for **4-F**.

The thermochromic colour change was initially believed to be due solely to an enol to cis-keto tautomerism with the enol form being colourless and the keto form being coloured.[10,11] However, it has also been found that temperature-induced fluorescence also plays a significant role in the colour change observed, particularly upon cooling.[15] Diffuse reflectance spectra were collected for 1-Br to 9-Br and are available in the Appendix 7, Figures S7.1-S7.9. No account was taken of the potential effect of fluorescence, however the spectra are presented to support the visually observed trends. In the reflectance spectra for the more strongly thermochromic complexes (1, 3, 4, 6, 7 and 9) the reflectance decreases rapidly below ~580 nm as the temperature is reduced, which is consistent with a lightening in colour. While for the weakly thermochromic compounds (2, 5 and 8) much smaller decreases in reflectance were observed upon cooling below ~490 nm.

To look for evidence of proton transfer in two of the crystals showing significant colour changes, **3-Cl** and **3-Br**, variable temperature neutron diffraction was carried out. However, no evidence of the proton shifting was identified and the O-H proton was located at essentially the same position at both 300(2) and 120(2) K for both structures. It is possible that the level of the cis-keto form was too small to be detected crystallographically.

7.4.6 Structural analysis

A packing similarity tree diagram for the structures, calculated using CSD Materials in Mercury[22] and allowing for structural variations, highlights both links between structures with similar packing and the wide range of packing observed, Figure 7.10. The point at which structures meet at a node highlights the number of molecules in a cluster around the central molecule that are similar so for example **1**-**F** and **7**-**Br** have twelve molecules in common while **1**-**Cl** and **1**-**Br** are essentially isostructural with fifteen molecules in common. For completeness the location of the three published structures differing to the structures determined in this study have been included on the diagram. Unsurprisingly for **9**-**Br** which undergoes a space group change upon cooling (*Pc* to *Cc*) the packing in the room temperature structure[31] has a very high similarity to the 120(2) K structure. In general, it is worth noting that the structures showing high similarity in their packing with ≥ 12 molecules in common, tend to be pairs or groups that are either moderately/strongly thermochromic or weakly thermochromic. The main exception to this rule is that the weakly thermochromic **8-F** and **8**-**Br** have very similar structures to **9**-**Br** which by eye show a larger colour change.

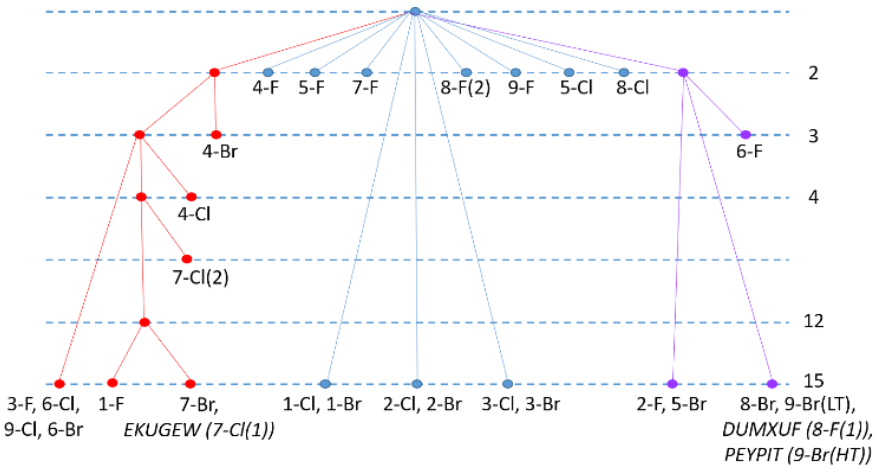

Figure 7.10 - Packing similarity diagram calculated using CSD Materials in Mercury[22] and allowing for structural variations. Both polymorphs of **8-F** and **7-Cl** are included along with the 300 K (HT) and 120 K (LT) structures of **9-Br**.

The dihedral angles between the two phenyl rings are given in Table 7.2 and show wide variations from 2.07(9)° in **8**-**F(2)** to 56.74(7)° in **2**-**F**. In some Schiff bases a link between the dihedral angle and chromic behaviour has been proposed,[10, 11] compounds with φ < 25° are expected to be strongly thermochromic due to the higher basicity of the imine nitrogen and as φ increases the degree of thermochromism is expected to reduce. In the compounds studied here there is some variation from this expected trend with three of the strongly thermochromic compounds **4**-**F**, **6**-**F** and **9**-**Br** having large φ values of 30.60(8)°, 29.53(4)° and 38.42(16)° respectively, while three of the weakly thermochromic compounds **5-F**, **8**-**F(2)** and **8**-**Cl** have very small or small φ values of

2.40(11)°, 2.07(9)° and 16.33(20)° respectively. No significant correlation between the halogen substituent position and the thermochromic behaviour was identified in this study.

Table 7.2 - Dihedral angles between the two phenyl rings for all of the compounds. Both polymorphs of **7-Cl** and **8-F** are included. Note **7-Cl(2)** has *Z'*=2.

Compound prefix	Halogen position	OMe position	F	Cl	Br
1	2	3	6.19(11)	7.20(10)	6.88(21)
2	2	4	56.75(7)	24.15(5)	23.70(8)
3	2	5	5.66(7)	11.13(7)	13.86(13)
4	3	3	30.60(8)	0.60(11)	24.09(11)
5	3	4	2.40(11)	28.38(5)	42.72(12)
6	3	5	29.52(4)	5.64(15)	5.43(74)
7	4	3	10.48(5)	**7-Cl(1)**[34] 11.9°	10.88(36)
				7-Cl(2) 11.75(11) 16.73(11)	
8	4	4	**8-F(1)**[33] 48.17(1)	16.26(21)	48.67(7)
			8-F(2) 2.07(9)		
9	4	5	20.60(4)	7.71(9)	38.42(16)

7.5 Conclusions

The structures of 27 *N*-(methoxysalicylidene)-haloaniline (halo = F, Cl or Br) are reported at 150(2), 120(2) or 100(2) K. Ten of these structures had previously been reported at room temperature and the structures herein were the same. While in the case of **8-F** and **7-Cl** new polymorphs are reported which show significant differences in their packing compared to the previously reported polymorphs. In addition, a phase transition was identified for **9-Br**, which occurs somewhere between 200(2) and 120(2) K. No phase transitions were identified between 300(2) and 120(2) K for any of the other compounds.

The 4-methoxysalicyl derivatives are yellow at room temperature and display very little colour change by eye when dipped in liquid nitrogen, ~77 K, whereas the 3 or 5-methoxysalicyl compounds are orange / red at room temperature and show a dramatic colour change with decreasing temperature down to yellow at liquid nitrogen temperatures. The colour change has previously been associated with the occurrence of a temperature induced enol to *cis*-keto tautomerism with temperature induced fluorescence also having a significant impact. Herein neutron diffraction studies on **3-Cl** and **3-Br** showed no evidence of proton shifting, so it is possible that the level of the *cis*-keto form was too small to be detected crystallographically but also no investigation was made into the effect of fluorescence on the or the colour change in the complexes.

While both the nature of the packing and the compounds' *inter*planar angle are believed to affect the thermo- and photochromic properties of the anils, the type and position of substituents can also be important. The position of the strongly electron donating methoxy group on the salicyl

moiety appears to have a stronger influence on the colour and thermochromic properties of the anils than the location of the weakly electron withdrawing halogen on the aniline moiety. The 3- and 5- methoxy compounds visually showed significant colour changes upon cooling, while the 4-methoxy compounds showed relatively small colour changes. While the majority of the 3- and 5-methoxy compounds had dihedral angles φ of < 25° there were several exceptions to the rule.

7.6 References

1. H. Kargar, V. Torabi, A. Akbari, R. Behjatmanesh-Ardakani, A. Sahraei and M. N. Tahir, *Journal of Molecular Structure*, 2020, **1205**, 127642.
2. H. Mighani, *Journal of Polymer Research*, 2020, **27**.
3. S. Parveen, *Applied Organometallic Chemistry*, 2020, **34**, e5687.
4. S. Kumari, B. Das and S. Ray, *Dalton Transactions*, 2019, **48**, 15942-15954.
5. M. Sahu, A. K. Manna, K. Rout, J. Mondal and G. K. Patra, *Inorganica Chimica Acta*, 2020, **508**.
6. A. Senier and F. G. Shepheard, *J. Chem. Soc., Trans.*, 1909, **95**, 1943-1955.
7. M. D. Cohen and G. M. J. Schmidt, *Journal of Physical Chemistry*, 1962, **66**, 2442-2446.
8. M. D. Cohen, G. M. J. Schmidt and S. Flavian, *Journal of the Chemical Society*, 1964, 2041-2051.
9. T. Fujiwara, J. Harada and K. Ogawa, *Journal of Physical Chemistry B*, 2004, **108**, 4035-4038.
10. E. Hadjoudis and I. M. Mavridis, *Chemical Society Reviews*, 2004, **33**, 579-588.
11. F. Robert, A. D. Naik, B. Tinant, R. Robiette and Y. Garcia, *Chemistry-a European Journal*, 2009, **15**, 4327-4342.
12. K. Ogawa, Y. Kasahara, Y. Ohtani and J. Harada, *Journal of the American Chemical Society*, 1998, **120**, 7107-7108.
13. K. Ogawa, J. Harada, I. Tamura and Y. Noda, *Chemistry Letters*, 2000, 528-529.
14. J. Harada, H. Uekusa and Y. Ohashi, *Journal of the American Chemical Society*, 1999, **121**, 5809-5810.
15. J. Harada, T. Fujiwara and K. Ogawa, *Journal of the American Chemical Society*, 2007, **129**, 16216-16221.
16. G. M. Sheldrick, *Acta Crystallographica Section A*, 2008, **64**, 112-122.
17. L. Palatinus and G. Chapuis, *Journal of Applied Crystallography*, 2007, **40**, 786-790.
18. L. Palatinus and A. van der Lee, *Journal of Applied Crystallography*, 2008, **41**, 975-984.
19. L. Palatinus, S. J. Prathapa and S. van Smaalen, *Journal of Applied Crystallography*, 2012, **45**, 575-580.
20. G. M. Sheldrick, *Acta Crystallographica Section C-Structural Chemistry*, 2015, **71**, 3-8.
21. O. V. Dolomanov, L. J. Bourhis, R. J. Gildea, J. A. K. Howard and H. Puschmann, *Journal of Applied Crystallography*, 2009, **42**, 339-341.
22. C. F. Macrae, I. J. Bruno, J. A. Chisholm, P. R. Edgington, P. McCabe, E. Pidcock, L. Rodriguez-Monge, R. Taylor, J. van de Streek and P. A. Wood, *Journal of Applied Crystallography*, 2008, **41**, 466-470.
23. D. A. Keen, M. J. Gutmann and C. C. Wilson, *Journal of Applied Crystallography*, 2006, **39**, 714-722.
24. M. J. Gutmann, *SXD2001, ISIS Facility, Rutherford Appleton Laboratory, Didcot, OX11 OQX, United Kingdom*, 2005.
25. H. Unver, E. Kendi, K. Guven and T. N. Durlu, *Zeitschrift Fur Naturforschung Section B-a Journal of Chemical Sciences*, 2002, **57**, 685-690.
26. S. Francis, P. T. Muthiah, G. Venkatachalam and R. Ramesh, *Acta Crystallographica Section E*, 2003, **59**, o1045-o1047.

27. B. Kosar, C. Albayrak, M. Odabasoglu and O. Buyukgungor, *Acta Crystallographica Section C*, 2009, **65**, o517-o520.
28. A. Ozek, O. Buyukgungor, C. Albayrak and M. Odabasoglu, *Acta Crystallographica Section E*, 2008, **64**, o1579-o1580.
29. A. Özek, Ç. Albayrak, M. Odabaşoğlu and O. Büyükgüngör, *Journal of Chemical Crystallography*, 2008, **39**, 353-357.
30. A. Ozek, O. Buyukgungor, C. Albayrak and M. Odabasoglu, *Acta Crystallographica Section E*, 2008, **64**, o1613-o1614.
31. A. Ozek, C. Albayrak, M. Odabasoglu and O. Buyukgungor, *Acta Crystallographica Section C-Crystal Structure Communications*, 2007, **63**, O177-O180.
32. C. S. Zheng, N. Yang, M. Li and Z. L. Jing, *Acta Crystallographica Section E-Structure Reports Online*, 2005, **61**, O3613-O3614.
33. C. Albayrak, A. Ozek, B. Kosar, M. Odabasoglu and O. Buyukgungor, *Acta Crystallographica Section E*, 2010, **66**, o315.
34. G.-Y. Yeap, S.-T. Ha, N. Ishizawa, K. Suda, P.-L. Boey and W. A. Kamil Mahmood, *Journal of Molecular Structure*, 2003, **658**, 87-99.
35. F. H. Allen, O. Kennard, D. G. Watson, L. Brammer, A. G. Orpen and R. Taylor, *J. Chem. Soc., Perkin Trans 2*, 1987, S1-S19.
36. Y. L. Gu, T. Kar and S. Scheiner, *Journal of the American Chemical Society*, 1999, **121**, 9411-9422.
37. E. D'Oria and J. J. Novoa, *Crystengcomm*, 2008, **10**, 423-436.
38. V. R. Thalladi, H. C. Weiss, D. Blaser, R. Boese, A. Nangia and G. R. Desiraju, *Journal of the American Chemical Society*, 1998, **120**, 8702-8710.

Chapter 8

Selected solid state behaviour of three di-tertiary butyl substituted *N*-salicylideneaniline derivatives: temperature induced phase transitions and chromic behaviour

Helen E. Mason, Judith A. K. Howard and Hazel A. Sparkes

Published *Acta Crystallographica*, 2021, **C77**, 659-667, doi.org/10.1107/S2053229621008780. Reproduced with permission of the International Union of Crystallography.

8.1 Abstract

The synthesis, single crystal structures and chromic behaviour of three related Schiff bases (E)-2,4-di-tert-butyl-6-(((4-fluorophenyl)imino)methyl)phenol, (E)-2,4-di-tert-butyl-6-(((4-chlorophenyl)imino)methyl)phenol, and (E)-2,4-di-tert-butyl-6-(((4-bromophenyl)imino)methyl)phenol are reported. Two polymorphs of (E)-2,4-di-tert-butyl-6-(((4-fluorophenyl)imino)methyl)phenol were obtained which were found to have different photochromic properties. (E)-2,4-di-tert-butyl-6-(((4-chlorophenyl)imino)methyl)phenol, and (E)-2,4-di-tert-butyl-6-(((4-bromophenyl)imino)methyl)phenol were found to be isostructural and underwent a phase transition upon cooling which was attributed to the dynamic disorder in one of the tertiary butyl groups resolving at low temperature. All of the structures were found to exist in the enol rather than keto form based on the C-O(H) and imine C=N bond lengths and contained an intramolecular O-H···N hydrogen bond alongside weaker intermolecular C-H···O contacts.

8.2 Introduction

Compounds which display reversible property changes upon some sort of stimulus are of interest due to potential applications including optical switches,[1] sensors,[2] or optical data storage.[3] Within these are compounds displaying temperature dependent, thermochromic,[4, 5] or light induced, photochromic,[6] colour changes. One such class of compounds that have been found to exhibit both thermochromism and photochromism in the solid-state are N-salicylideneanilines, Schiff bases of salicylaldehyde derivatives with aniline derivatives.[7-9] Typically, their thermochromism involves a lightening of colour from red/orange to orange/yellow upon cooling while their photochromic colour changes usually result in a darkening of colour from yellow to orange/red upon irradiation with UV light. Initially the two properties were thought to be mutually exclusive,[8, 9] however now it is believed that most, if not all, of N-salicylideneanilines display thermochromism with some also showing photochromism.[10]

The mechanism for the thermochromic colour change is believed to be due to an enol to cis-keto tautomerism while the photochromism involves a *cis* to *trans* isomerism of the keto form,[11, 12] see Figure 8.1. The enol form is believed to be colourless while the keto form is coloured.[10, 13, 14] Evidence of the thermoproduct has been observed for *N*-(5-chlorosalicylidene)-4-hydroxyaniline, where the population of the *cis*-keto form was found to increase upon cooling,[13, 15] while the photoproduct has been seen crystallographically for *N*-3,5-di-tert-butylsalicylidene-3-nitroaniline using two photon irradiation.[16] However, the thermochromism cannot be fully explained by the keto-enol tautomerism alone, in order to fully explain the thermochromism it is necessary to take into account fluorescence.[14] The impact of fluorescence is particularly significant for thermochromic compounds at lower temperature and can in fact be the dominant cause of colour change, while at higher temperatures fluorescence is negligible. The presence of fluorescence at

lower temperature results in different perceived colours to those observed from the diffuse reflectance spectra e.g. *N*-(5-chloro-2-hydroxylbenzylidene)aniline appears yellowish green at 80 K but from the diffuse reflectance suggests the colour to be pale yellow since fluorescence was eliminated in the measurement of diffuse reflectance spectra. The extent of the thermochromism of the *N*-salicylideneanilines has been linked to the dihedral angle (Φ) between the two aromatic rings with those with a Φ < 25° being generally strongly thermochromic as a smaller *inter*planar or dihedral angle results in reduced overlap between the nitrogen atom lone pair and the aromatic aniline moiety. This allows for easier hydrogen atom transfer and creates a stronger intramolecular hydrogen bond. While a larger dihedral angle increases overlap between the nitrogen atom lone pair and the aromatic aniline moiety giving greater delocalization into the π-system and reducing the basicity of the nitrogen and thus the thermochromism.[11, 12] For photochromism the link to dihedral angle is more complicated and compounds with Φ < 20° are generally non-photochromic, Φ > 30° are more likely to be photochromic and those in between can be either photochromic or non-photochromic.[17] Other factors have also been found to influence the chromic behaviour of the *N*-salicylideneanilines including substituents that weaken the O-H bond or increase the nitrogen atoms basicity tending to result in more strongly thermochromic compounds.[11] In addition, crystal packing also affects chromic behaviour with more closely packed structures tending to be more strongly thermochromic and more open packed structures more likely to be photochromic.[11, 12] The latter is likely to be due to the large conformational change required for the transition, with tightly packed structures having greater steric restrictions to conformational change. The presence of bulky groups, such as tertiary butyl substituents, or creating cavities using hosts can help to increase space in the lattice of a structure and favour photochromism, as more space presumably reduces the steric restraint on the molecule for the significant conformational change required for *cis* to *trans* isomerism to occur.[18-20]

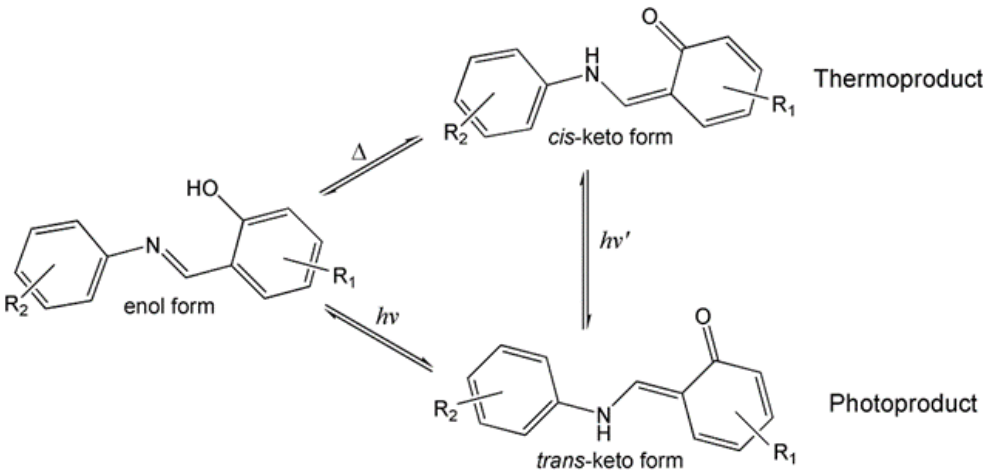

Figure 8.1 - Illustration of the proposed mechanism for the thermo or photochromism in *N*-salicylideneaniline derivatives.

The structures of three related *N*-salicylidineanlines (E)-2,4-di-tert-butyl-6-(((4-fluorophenyl)imino)methyl)phenol, **1**, (E)-2,4-di-tert-butyl-6-(((4-chlorophenyl)imino)methyl)phenol, **2** and (E)-2,4-di-tert-butyl-6-(((4-bromophenyl)imino)methyl)phenol, **3** are reported alongside a study into their chromic properties, see Scheme 8.1. The structure of **2** has been previously reported at 273 K[21] but no investigation into the chromic properties or thermal behaviour has been reported. The structure

of **3** has also been reported and is known to be photochromic, however the thermal behaviour was not studied.[18]

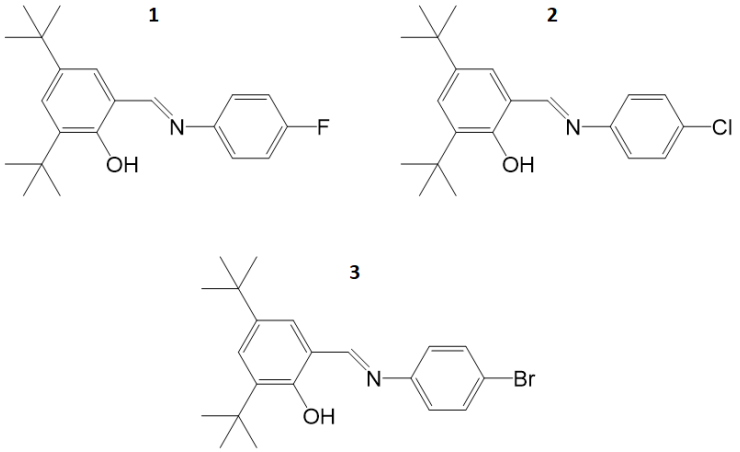

Scheme 8.1 Molecular structures of (E)-2,4-di-tert-butyl-6-(((4-fluorophenyl)imino)methyl)phenol, **1**, (E)-2,4-di-tert-butyl-6-(((4-chlorophenyl)imino)methyl)phenol, **2** and (E)-2,4-di-tert-butyl-6-(((4-bromophenyl)imino)methyl)phenol, **3**.

8.3 Experimental

8.3.1 Synthesis

All reagents were used as supplied from Aldrich. Compounds were synthesized by direct condensation of the appropriate salicylaldehyde and aniline derivatives in ethanol. 1.25 mmoles (**1** and **3**) or 2.5 mmoles (**2**) of the salicylaldehyde and aniline were each dissolved in 25 ml of ethanol, the resulting solutions combined and refluxed with stirring for four hours. Any precipitate was filtered, rinsed with ethanol and left to dry, the (remaining) solution was then removed under reduced pressure using a rotary evaporator until (further) precipitate formed. Re-crystallization was carried out by slow evaporation from ethanol.

8.3.2 Characterisation

Elemental C, H and N content analysis was carried out by the Durham University Analytical service using an Exeter Analytical E-440 Elemental Analyzer.

8.3.3 Single Crystal X-ray Diffraction Data Collection

X-ray diffraction data were collected on an Oxford Diffraction Gemini or Oxford Diffraction SuperNova using monochromated Mo-*Kα* (λ = 0.71073 Å) radiation. Data collection, integration and absorption corrections were carried out using CrysAlisPro.[22] The structures were solved either by direct methods in SHELXS[23] or using olex2Solve[24] and refined by full matrix least squares on F^2 in SHELXL[23] using Olex2.[25] All non-hydrogen atoms were refined anisotropically and all hydrogen atoms were located geometrically and refined using a riding model with the exception of the hydrogen atoms involved in the intramolecular hydrogen bonding which were located in the Fourier difference map (FDM) wherever feasible. In **2** and **3** one of the tert-butyl groups was disordered (apart from at 120(2) K and 100(2) K for **2** and 100(2) K for **3**) the sum of the

occupancies of the disordered parts were set to equal 1. The data for **2** at 300(2) K, 250(2) K and 200(2) K drop of at high angle, presumably due to the presence of the disorder in the tert-butyl group, as a consequence the data are cut at a resolution limit of 0.95 Å, 0.91 Å and 0.89 Å respectively. Likewise the data for **3** were also weak at 300(2)K and consequently cut at a resolution limit of 0.86 Å. The interplanar dihedral angle and fold angles were calculated in Olex2 (Dolomanov et. al., 2012) by measuring the angles between planes computed through the six non-hydrogen atoms of the two rings. For the acentric structure of **1B** at 120 K, the diffraction data did not establish the absolute structure. Crystal structure and refinement details are provided in Table 8.1.

Table 8.1 - Crystal data and structure refinement for **1A**, **1B**, **2** and **3** at 100 or 120 K**.**

Identification code	**1A** 100 K	**1B** 120K	**2** 100K	**3** 100K
Empirical formula	$C_{21}H_{26}FNO$	$C_{21}H_{26}FNO$	$C_{21}H_{26}ClNO$	$C_{21}H_{26}BrNO$
Formula weight	327.43	327.43	343.88	388.34
Temperature/K	100(2)	120(2)	100(2)	100(2)
Crystal system	triclinic	orthorhombic	monoclinic	monoclinic
Space group	*P*-1	*Pna*2$_1$	*P*2$_1$/*c*	*P*2$_1$/*c*
a/Å	6.5324(3)	12.2569(3)	17.3011(11)	17.4450(3)
b/Å	10.6141(8)	8.9658(2)	10.6780(7)	10.69412(16)
c/Å	14.1675(9)	16.5739(4)	10.1200(6)	10.15010(17)
α/°	80.364(5)	90	90	90
β/°	81.094(4)	90	90.252(6)	90.1557(16)
γ/°	74.507(5)	90	90	90
Volume/Å^3	926.97(10)	1821.35(7)	1869.6(2)	1893.58(5)
Z	2	4	4	4
ρ_{calc}g/cm^3	1.173	1.194	1.222	1.362
μ/mm^{-1}	0.078	0.079	0.211	2.178
F(000)	352.0	704.0	736.0	808.0
Crystal size/mm^3	0.38 × 0.36 × 0.26	0.46 × 0.43 × 0.10	0.35 × 0.31 × 0.10	0.3 × 0.05 × 0.05
Radiation	Mo Kα (λ = 0.71073)	Mo Kα (λ = 0.71073)	Mo Kα (λ = 0.71073)	Mo Kα (λ = 0.71073)
2θ range for data collection/°	5.282 to 52.742	5.166 to 52.736	5.546 to 52.744	6.002 to 55.748
Index ranges	-7 ≤ h ≤ 8, -13 ≤ k ≤ 13, -15 ≤ l ≤ 17	-15 ≤ h ≤ 15, -11 ≤ k ≤ 11, -20 ≤ l ≤ 20	-21 ≤ h ≤ 21, -13 ≤ k ≤ 12, -12 ≤ l ≤ 12	-22 ≤ h ≤ 22, -9 ≤ k ≤ 14, -13 ≤ l ≤ 13
Reflections collected	7178	25510	13865	28200
Independent reflections	3792 [R_{int} = 0.0380, R_{sigma} = 0.0647]	3712 [R_{int} = 0.0494, R_{sigma} = 0.0298]	3830 [R_{int} = 0.0866, R_{sigma} = 0.0875]	4491 [R_{int} = 0.0358, R_{sigma} = 0.0262]
Data/restraints/parameters	3792/0/227	3712/1/226	3830/0/227	4491/22/227
Goodness-of-fit on F^2	1.043	1.046	1.078	1.037
Final R indexes [I>=2σ (I)]	R_1 = 0.0541, wR_2 = 0.0988	R_1 = 0.0341, wR_2 = 0.0749	R_1 = 0.0709, wR_2 = 0.1574	R_1 = 0.0261, wR_2 = 0.0558
Final R indexes [all data]	R_1 = 0.0843, wR_2 = 0.1101	R_1 = 0.0371, wR_2 = 0.0765	R_1 = 0.1023, wR_2 = 0.1761	R_1 = 0.0364, wR_2 = 0.0595
Largest diff. peak/hole / e Å^{-3}	0.28/-0.20	0.16/-0.16	0.78/-0.33	0.46/-0.22

8.3.4 Raman

Irradiation was carried out using two UV LED sources (λ~365 nm) in the dark to minimize conversion back to the ground state and measurements were recorded with the 764 nm laser on a Horiba Jobin Yvon LabRAM HR Raman spectrometer.

8.3.5 Diffuse reflectance spectroscopy

The sample was ground to give uniform particle distribution and placed in a 40 x 10 x 2 mm quartz cuvette to ensure optical thickness. A cuvette sample holder with a white polytetrafluoroethylene (PTFE) block spacer was used to load the sample into an Oxford Instruments Cryostat. The sample was irradiated with an Ocean Optics halogen light source and an Avantes AvaSpec-2048-2 CCD detector (placed at an acute angle to minimize detection of specular reflectance) collected the reflectance spectra which were recorded using AvaSoft basic software. Cryostat temperature control was performed using an Oxford Intelligent Temperature Controller, each temperature was stabilized for 10 min or until ±0.1 K before recording the spectrum. A white PTFE block was used to record a reference spectrum before each data set collection. Irradiation was carried out using a 405 nm laser pointer or UV LEDs after an initial ground state spectrum was collected. The diffuse reflectance spectra are illustrated as % reflectance versus wavelength and Kubelka-Munk function, *F(R)*, versus wavelength. If *S* is independent of λ, then *F(R)* versus λ is equivalent to the absorption spectrum for a diffuse reflector. To allow basic trends to be easily observed moving averages were applied to data during analysis.

8.4 Results

8.4.1 Structural Characterisation

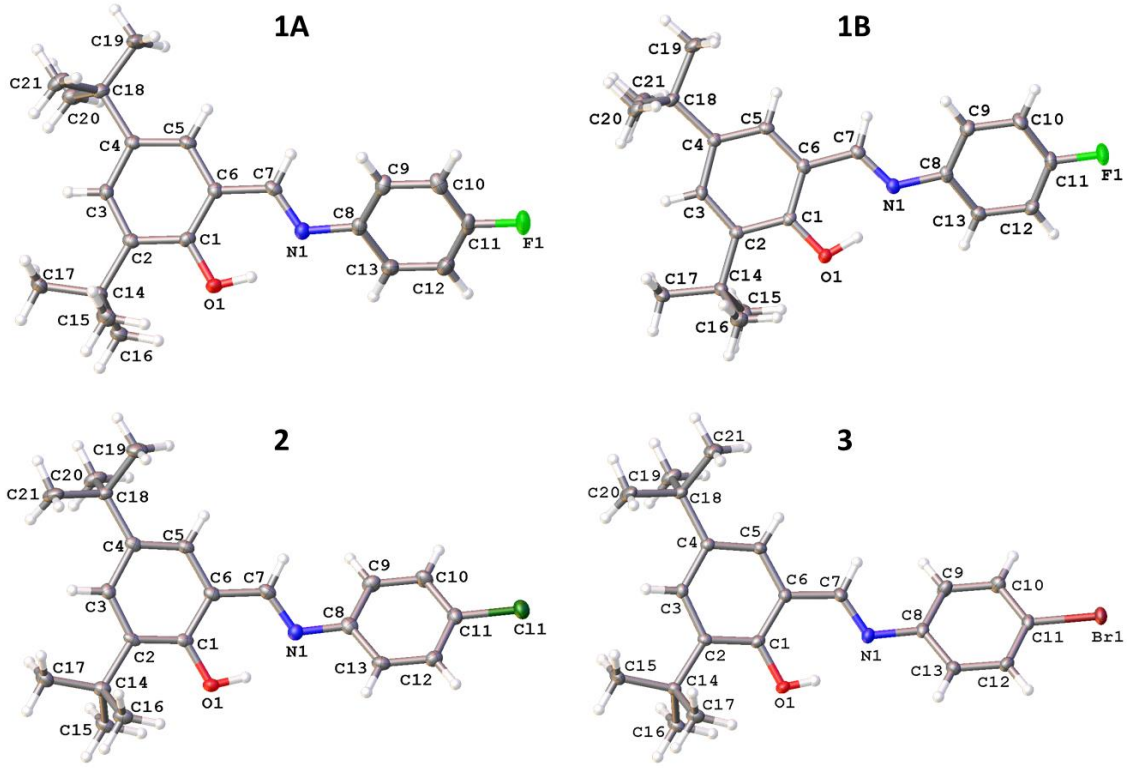

Figure 8.2 - Illustration of the structures of **1A** (100(2) K), **1B** (120(2) K), **2** (100(2) K) and **3** (100(2) K) with atomic numbering scheme depicted. Ellipsoids shown at the 50% probability level.

Compound **1** was found to produce two different polymorphs upon recrystallisation, **1A** and **1B**, which had different morphologies and structures. **1A** formed yellow rectangular block like crystals and crystallised in the triclinic space group *P*-1 while **1B** formed bright yellow octahedral shaped crystals and crystallised in the orthorhombic space group $Pna2_1$. Only one polymorph was identified during these studies for **2** and **3** which were both yellow.

Table 8.2 - Hydrogen-bond geometry (Å, °)

Compound	Temperature	*D*—H···*A*	*D*—H	H···*A*	*D*···*A*	*D*—H···*A*
1A	100	O1—H1···N1	0.94 (3)	1.72 (3)	2.587 (2)	151 (2)
1B	120	O1—H1···N1	0.96 (3)	1.64 (3)	2.544 (2)	155 (2)
2	300	O1—H1···N1	0.84 (4)	1.84 (4)	2.612 (4)	151 (4)
	250	O1—H1···N1	0.91 (3)	1.76 (4)	2.615 (4)	155 (3)
	200	O1—H1···N1	0.90 (3)	1.78 (3)	2.611 (3)	153 (3)
	150	O1—H1···N1	0.92 (3)	1.77 (3)	2.615 (3)	151 (3)
	120	O1—H1···N1	0.86 (4)	1.82 (4)	2.633 (3)	157 (4)
	100	O1—H1···N1	0.94 (4)	1.77 (4)	2.626 (3)	150 (3)
3	300	O1—H1···N1	0.83 (5)	1.84 (5)	2.614 (4)	154 (5)
	250	O1—H1···N1	0.84 (3)	1.83 (3)	2.612 (3)	154 (3)
	200	O1—H1···N1	0.82 (3)	1.85 (3)	2.611 (2)	153 (3)
	150	O1—H1···N1	0.86 (1)	1.83 (2)	2.612 (2)	152 (3)
	120	O1—H1···N1	0.86 (1)	1.84 (2)	2.622 (2)	151 (3)
	100	O1—H1···N1	0.85 (1)	1.84 (1)	2.6257 (18)	152 (2)

The four structures are all similar in that they have the same basic backbone with a phenyl group substituted with a hydroxy and two tert-butyl groups joined to halogen substituted phenyl group via an imine group (Figure 8.2). The structures all exist in the enol form at low temperature rather than the less common keto form with C7=N1 bond lengths ranging from 1.279(3) Å - 1.286(2) Å and C1-O1 bond lengths ranging from 1.353(3) Å - 1.358(2) Å which are consistent with double C=N (typically ~1.279 Å) and single C-O (typically ~1.362 Å) bonds respectively (Allen *et. al.*, 1987). In all cases the hydrogen atom was also located in the Fourier difference map in the vicinity of the oxygen atom supporting the presence of the enol form of the anil. All the structures contain an intramolecular hydrogen bond between O1-H1···N1 with similar parameters e.g. O1···N1 distances ranging from 2.544(2) Å to 2.632(2) Å, see Table 8.2. The structures also contain weaker intermolecular C-H···O interactions, see Table 8.3.

Table 8.3 – C-H···O interaction geometry (Å, °)

Compound	Temperature	*D*—H···*A*	*D*—H	H···*A*	*D*···*A*	*D*—H···*A*
1A	100	C12—H12···O1^{i}	0.95	2.62	3.345 (2)	133
1B	120	C10—H10···O1^{ii}	0.95	2.60	3.523 (3)	165
		C19—H19B···O1^{iii}	0.98	2.72	3.522(3)	140
		C17—H17*A*···F1^{iv}	0.98	2.57	3.453 (3)	150
2	300	C12—H12···O1^{v}	0.93	2.71	3.461 (4)	138
	250	C12—H12···O1^{v}	0.94	2.68	3.438 (3)	138
	200	C12—H12···O1^{v}	0.95	2.65	3.415 (2)	138
	150	C12—H12···O1^{v}	0.95	2.63	3.396 (3)	138
	120	C12—H12···O1^{vi}	0.95	2.56	3.359 (3)	142
	100	C12—H12···O1^{vi}	0.95	2.54	3.343 (4)	142
3	300	C12—H12···O1^{vii}	0.93	2.76	3.522 (3)	140
	250	C12—H12···O1^{vii}	0.94	2.73	3.500 (2)	140
	200	C12—H12···O1^{vii}	0.94	2.71	3.483 (3)	140
	150	C12—H12···O1^{vii}	0.95	2.67	3.458 (2)	140
	120	C12—H12···O1^{vii}	0.95	2.62	3.425 (2)	142
	100	C12—H12···O1^{vii}	0.95	2.61	3.415 (2)	143

Symmetry code: (i) −*x*, −*y*+2, −*z*; (ii) *x*+½, −*y*+3/2, *z*; (iii) 3/2-*x*, ½+*y*, ½+*z*; (iv) −*x*+2, −*y*+1, *z*+½; (v) −*x*+2, −*y*+1, −*z*+1; (vi) −*x*+2, −*y*, −*z*+1; (vii) −*x*, −*y*, −*z*

The structure of **1A** consists of molecules oriented such that the plane of the molecules is in approximately the *-101* plane with short aromatic C-H···O contacts between pairs of adjacent molecules. The tertiary butyl groups within these pairs are at opposite ends to each other, see Figure 8.3. Examining the structure of **1B** shows that the molecules are packed in a completely different manner to **1A**, in **1B** alternate molecules in the *c* axis direction are orientated in either the *101* or *10-1* direction, see Figure 8.3. Intermolecular interactions in this case are (i) short C-H···O contacts involving the hydrogen atoms on a methyl group and an aromatic H, (ii) C-H···F contacts involving methyl group hydrogen atoms (see Figure 8.4, Table 8.3). The structures of **2** and **3** were found to be isostructural crystallising in the monoclinic space group $P2_1/c$. All of the molecules are oriented such that the plane of the molecules is in approximately the *101* plane with short aromatic C-H···O contacts between pairs of adjacent molecules. Within these pairs the molecules are arranged such that the tertiary butyl groups are at opposite ends to each other, see Appendix 8, Figure S8.1. Although in a different crystal system and space group, the structures of **2** and **3** are similar to that of **1A** in terms the packing and intermolecular interactions.

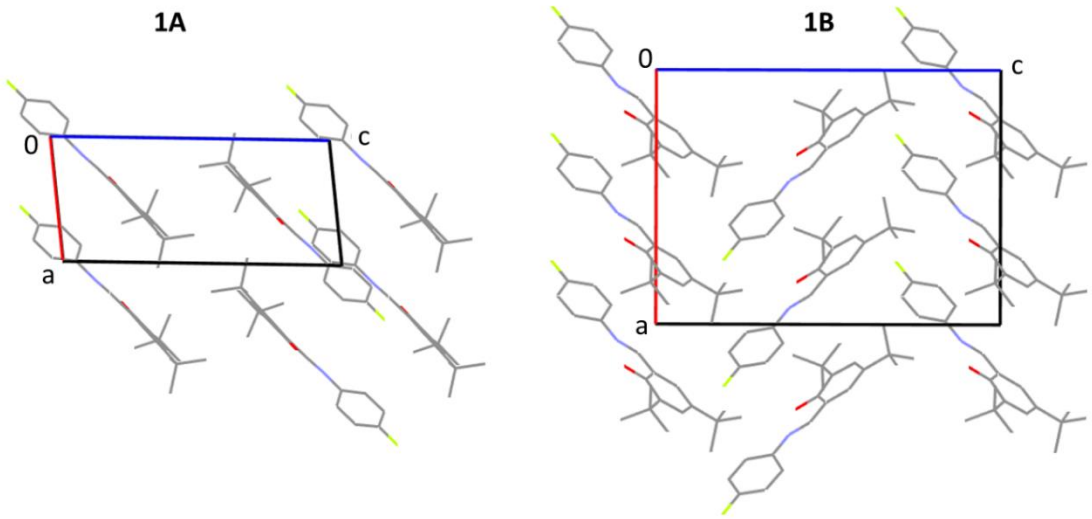

Figure 8.3 - Illustration of the packing of 1A at 100(2) K and 1B at 120(2) K looking down the *b* axis. Hydrogen atoms omitted for clarity.

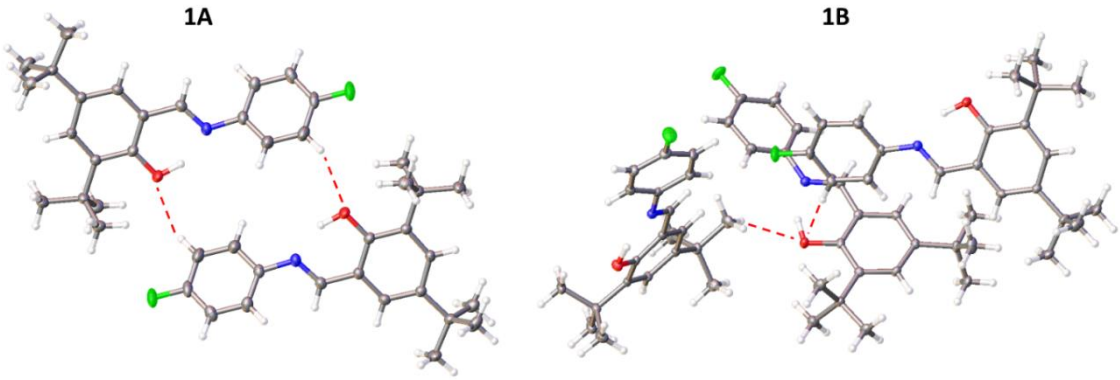

Figure 8.4 - Intermolecular hydrogen bonding in **1A** at 100(2) K and **1B** at 120(2) K.

8.4.2 Thermal behaviour

The structures of **2** and **3** are isostructural and upon cooling both undergo a phase transition somewhere between 150 and 120 K during which the *a*-axis length decreases by ~0.37 Å for **2** and ~0.27 Å for **3**, while the *b* axis increases by ~0.20 Å for **2** and ~0.10 Å for **3**. These changes are accompanied by a decrease in the beta angle of just over 1° in both cases, see Appendix 8 Figure S8.2 and S8.3. Across the full temperature range measured the behaviour of the cell parameters is slightly different for the two compounds but shows many similarities. For **2**, the *a*-axis decreases almost linearly until 150 K and then shows a sharp decrease after the phase transition, the *b*-axis decreases approximately linearly until 200 K, increases slightly to 150 K and then increases sharply by 120 K, the beta angle decreases approximately linearly until 150 K, then shows a sharp decrease to 120 K before increasing slightly at 100 K while the *c*-axis and unit cell volume decrease almost linearly throughout with slight inflections at around 175 and 150 K. For **3** overall across the temperature range upon cooling *a* and *c* cell axes lengths, beta angle and unit cell volume decrease approximately linearly prior to phase transition and continue to decrease after the phase transition. In the case of the *b* axis it initially decreases until ~200 K, increases slightly at 150 K and then increases sharply through the phase transition.

Examining the crystal structures above and below the transition the cause of the phase transition appears to be due to dynamic disorder in one of the tertiary butyl groups, at higher temperature the group is disordered while at low temperature the disorder resolves. In the case of **2** the disordered tertiary butyl group is modelled over three positions at 150(2) K but is fully ordered at 120(2) K, while for **3** at 150(2) K the tertiary butyl group is also modelled over three positions, at 120(2) K it was modelled over two positions and it was only at 100(2) K that it was fully ordered.

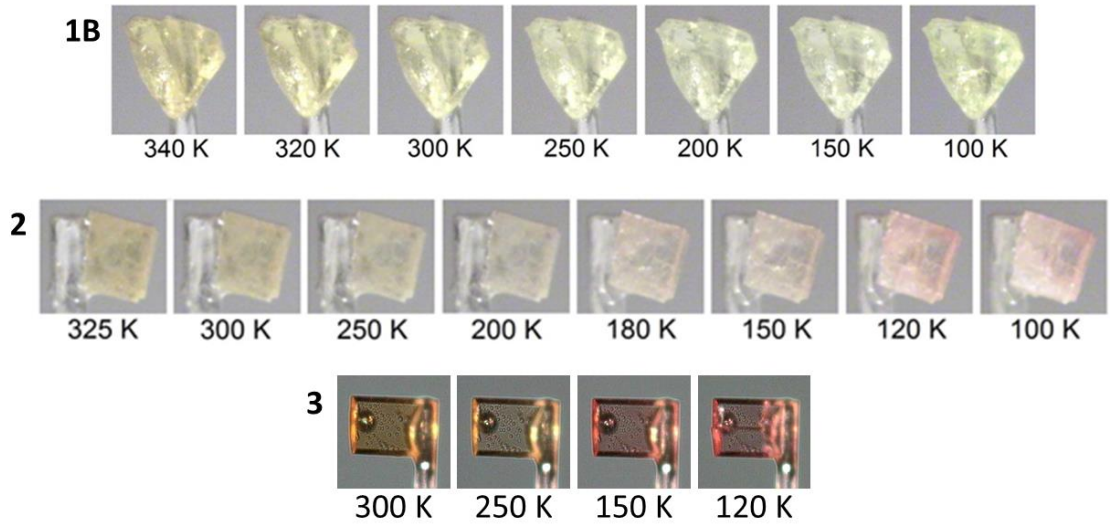

Figure 8.5 - Illustration of the colour change of **1B**, **2** and **3** upon cooling.

The majority of the *N*-salicylideneanilines show thermochromism upon cooling with compounds that are red/orange at room temperature becoming paler or yellow and those that are yellow at room temperature becoming paler. However, it was interesting to note that upon cooling the crystals of **2** and **3** showed an apparent 'reverse thermochromism' around the phase transition temperature with the crystals becoming more red, see Figure 8.5 and Appendix 8 Figure S8.4. Diffuse reflectance spectra were also collected for all of the compounds and are available in the Appendix 8, Figures S8.5 and S8.6. No account was taken of the potential effect of fluorescence, which can affect the observed colour upon cooling (Harada *et. al.*, 2007), however the spectra are presented to support the visually observed trends. In the case of the reflectance spectra for **1**, which is likely to be a mixture of both polymorphs, the shoulder shifts to lower wavelengths upon cooling suggesting a lightening in colour. In the case of **2** and **3** there is also a shift in the position of the main shoulder to lower wavelengths upon cooling, but this is also accompanied by additional changes in the spectra. The spectrum for **2** shows additional changes in the ~500-580nm region with additional shoulders appearing. These appear to start by around 200 K and become more pronounced upon further cooling which is consistent with results observed visually in Figure 8.5. A similar situation, although less pronounced, is observed for **3** where additional shoulders appear between ~500-580 nm for the spectra at 200 K and below. The apparent 'reverse thermochromism' is believed to be related to the phase transition that has occurred rather than the normal thermochromism seen in *N*-salicylideneanilines. It was noted that the dihedral angle between the two six membered rings decreases by around 1.2-1.9° as the temperature is reduced and in the case of **2** there is a noticeably larger step around the phase transition between 150(2) and 120(2) K. In both cases the fold angle increases as the temperature is reduced and there is a large step increase of ~2.3-2.5° between 150(2) and 120(2) K, see Table 8.4. Although relatively small it is possible that these structural changes may be related to the

observed colour change as structures with smaller dihedral angles have reduced overlap between the nitrogen atom lone pair and the aromatic aniline allowing for a stronger O-H···N hydrogen bond favoured by the strongly thermochromic compounds.[11, 12] In the case of *N*-salicylideneaniline a similar reverse thermochromism has been seen upon heating above 306 K the colour changes from red to yellow. This was associated with the planar *β* form transitioning to the non-planar disordered α_1 form, however the change in structure in this case was much more significant with a change in the dihedral angle from (β) ~2° to (α_1) ~49°.[26] More examples and further studies would be required to confirm a correlation between the colour change observed here and the phase transition having occurred.

Table 8.4 - Dihedral angles between planes calculated through the 6 atoms of the two rings.

Compound	Temperature (K)	Dihedral angle (°)	Fold angle (°)
1A	100	39.03(5)	8.68(5)
1B	120	20.61(7)	3.24(7)
2	300	26.75(7)	9.01(9)
	250	26.56(8)	8.87(8)
	200	26.33(6)	9.09(6)
	150	25.80(9)	9.28(9)
	120	24.96(10)	11.84(10)
	100	24.83(9)	12.05(9)
3	300	25.83(8)	9.29(9)
	250	25.49(6)	9.45(6)
	200	25.33(8)	9.69(7)
	150	24.88(7)	10.16(7)
	120	24.70(7)	12.49(7)
	100	24.63(5)	13.20(5)

8.4.3 Photochromism

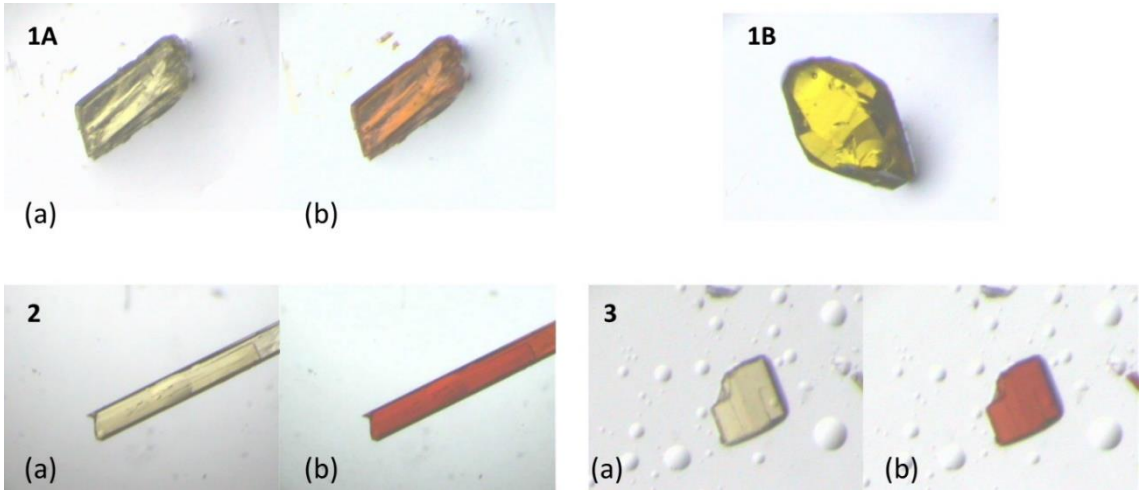

Figure 8.6 - Illustration of the behaviour of each of the crystal structures at room temperature upon irradiation with a UV LED (λ ~ 365nm) (a) unirradiated, (b) irradiated.

Upon irradiation three of the crystals 1A, 2 and 3 were found to display photochromism becoming much darker in colour when irradiated with a UV light. On the other hand, polymorph 1B did not show a colour change even upon prolonged irradiation, see Figure 8.6. The occurrence of photochromism for 3 had previously been reported.[18]

Raman data were collected before irradiation and after irradiation with a UV LED, see Figure 8.7. The three crystals displaying photochromism, **1A**, **2** and **3** all showed the appearance of new peaks upon irradiation, the main peak positions are given in Table 8.5. As expected, the spectrum of **1B** showed no change in the Raman spectra upon irradiation. It is clear that only a small amount of the photoproduct has been formed which is not uncommon as photo yield is often low, particularly without 2-photon excitation, and the change is often restricted to the surface of the crystal.[27] Therefore, it is unsurprising that even after irradiation with a UV laser no changes were observed in the single crystal X-ray structures. Diffuse reflectance spectra before and after irradiation for samples of **2** and **3** are presented in the Appendix 8, Figure S8.7, these support the observation by eye and from the Raman with significant changes in the spectra upon irradiation. In both case the position of the shoulder in the reflectance spectra shifts to higher wavelengths upon irradiation. No diffuse reflectance spectra upon irradiation are presented for **1** due to the sample likely being a mixture of polymorphs.

Table 8.5 - Position of main peaks that appear in Raman upon irradiation

Compound	New peaks (cm^{-1})
1A	1651, 1525, 1373, 1302 and 1143
2	1528, 1423, 1311 and 1152
3	1518, 1418, 1301 and 1134

It has also been found that compounds with more 'space' in the crystal lattice are more likely to show photochromism as it is easier for the compound to undergo the necessary *cis* to *trans* isomerism. The presence of bulky tertiary butyl groups can help create space and potentially enable photochromism to be displayed.[18] However, only three of the structures reported herein **1A**, **2** and **3** display photochromism. The packing and intermolecular interaction in **1A**, **2** and **3** are relatively similar as discussed earlier, however **1B** has significantly different packing and intermolecular interactions. It seems reasonable to suggest that these differences may well link to the compounds' different photochromic behaviour. A link has been proposed between the interplanar or dihedral angle between the two aromatic rings and the likelihood of this type of compound showing photochromism with the observation that photochromic compounds tend to have larger dihedral angle, typically dihedral angles below 20° are associated with non-photochromic compounds, those above 30° are more likely to be photochromic and those between 20°-30° can display photochromism.[18] The structures reported here fit in with these general observations and those with the larger dihedral angles between the two aromatic rings are the ones displaying photochromism, see Table 8.4. It is possible that in order to form the aromatic C-H···O interaction present in **1A**, **2** and **3** requires a larger dihedral angle between the two rings, while the C-H···O interactions in **1B** do not require this twisting, hence photochromism may be favoured for **1A**, **2** and **3** with the larger dihedral angle but not seen for **1B** due to the smaller dihedral angle.

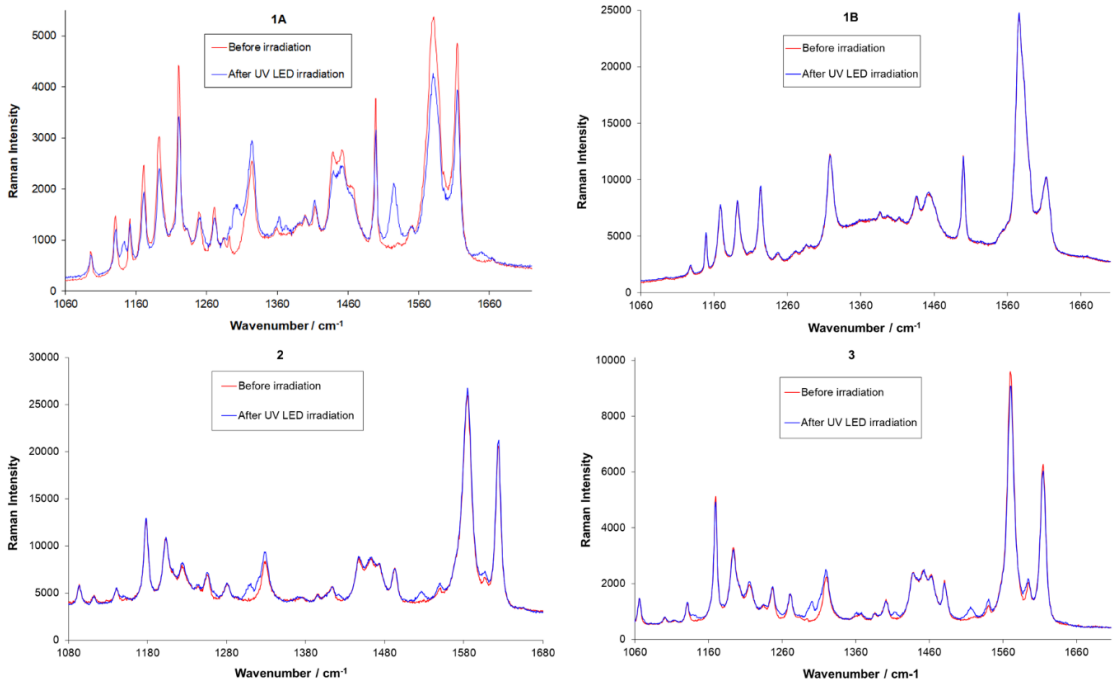

Figure 8.7 - Raman spectra of **1A**, **1B**, **2** and **3** (red) before irradiation (blue) after irradiation with UV LED's.

8.5 Conclusions

The structures of three related Schiff base compounds are reported, for one, E)-2,4-di-tert-butyl-6-(((4-fluorophenyl)imino)methyl)phenol, 1, two polymorphic structures are reported. The basic structures of the compounds are very similar all existing in the enol form and showing an

intermolecular O-H···N hydrogen bond and short C-H···O contacts. However, the packing of the two polymorphs of 1 were found to be significantly different. Compounds 2 and 3 were found to be isostructural with each other and displayed a temperature induced phase transition upon cooling, this was attributed to the disorder in one of the tertiary butyl groups resolving at low temperature, this was linked to a colour change from yellow to red around the phase transition. Three of the structures 1A, 2 and 3 were found to show photochromism upon irradiation with UV LED's, while 1B did not this was linked differences in the packing and to the interplanar or dihedral angle between the two aromatic rings being > 25 ° for the photochromic structures and < 25° for 1B. The presence of the photochromism was identified both by eye and using Raman spectroscopy.

8.6 References

1. M. Sliwa, S. Letard, I. Malfant, M. Nierlich, P. G. Lacroix, T. Asahi, H. Masuhara, P. Yu and K. Nakatani, *Chemistry of Materials*, 2005, **17**, 4727-4735.
2. M. Sahu, A. K. Manna, K. Rout, J. Mondal and G. K. Patra, *Inorganica Chimica Acta*, 2020, **508**.
3. H. Wang, X. F. Ji, Z. A. Page and J. L. Sessler, *Materials Chemistry Frontiers*, 2020, **4**, 1024-1039.
4. A. Seeboth, D. Lotzsch, R. Ruhmann and O. Muehling, *Chemical Reviews*, 2014, **114**, 3037-3068.
5. Y. Suzuki, T. Kato, H. Y. Huang, I. Yoshikawa, T. Mutai and H. Houjou, *Journal of Photochemistry and Photobiology a-Chemistry*, 2019, **385**.
6. L. Wu, R. J. Chen, Z. W. Luo and P. Wang, *Journal of Materials Science*, 2020, **55**, 12826-12835.
7. A. Senier and F. G. Shepheard, *Journal of the Chemical Society*, 1909, **95**, 1943-1955.
8. M. D. Cohen and G. M. J. Schmidt, *Journal of Physical Chemistry*, 1962, **66**, 2442-2446.
9. M. D. Cohen, G. M. J. Schmidt and S. Flavian, *Journal of the Chemical Society*, 1964, 2041-2051.
10. T. Fujiwara, J. Harada and K. Ogawa, *Journal of Physical Chemistry B*, 2004, **108**, 4035-4038.
11. E. Hadjoudis and I. M. Mavridis, *Chemical Society Reviews*, 2004, **33**, 579-588.
12. F. Robert, A. D. Naik, B. Tinant, R. Robiette and Y. Garcia, *Chemistry-a European Journal*, 2009, **15**, 4327-4342.
13. K. Ogawa, Y. Kasahara, Y. Ohtani and J. Harada, *Journal of the American Chemical Society*, 1998, **120**, 7107-7108.
14. J. Harada, T. Fujiwara and K. Ogawa, *Journal of the American Chemical Society*, 2007, **129**, 16216-16221.
15. K. Ogawa, J. Harada, I. Tamura and Y. Noda, *Chemistry Letters*, 2000, 528-529.
16. J. Harada, H. Uekusa and Y. Ohashi, *Journal of the American Chemical Society*, 1999, **121**, 5809-5810.
17. K. Johmoto, T. Ishida, A. Sekine, H. Uekusa and Y. Ohashi, *Acta Crystallographica Section B-Structural Science Crystal Engineering and Materials*, 2012, **68**, 297-304.
18. K. Johmoto, T. Ishida, A. Sekine, H. Uekusa and Y. Ohashi, *Acta Crystallographica Section B-Structural Science*, 2012, **68**, 297-304.
19. G. Pistolis, D. Gegiou and E. Hadjoudis, *Journal of Photochemistry and Photobiology a-Chemistry*, 1996, **93**, 179-184.
20. H. Koyama, T. Kawato, H. Kanatomi, H. Matsushita and K. Yonetani, *J. Chem. Soc., Chem. Commun.*, 1994, 579-580.
21. J. Li, R. Zhao and C. Ma, *Acta Crystallographica Section E-Crystallographic Communications*, 2007, **63**, O4923-U7094.

22. Agilent-Technologies, *CrysAlisPro Version 1.171.37.33c*, 2000.
23. G. M. Sheldrick, *Acta Crystallogr., Sect. A: Found. Crystallogr.*, 2008, **64**, 112-122.
24. L. J. Bourhis, O. V. Dolomanov, R. J. Gildea, J. A. K. Howard and H. Puschmann, *Acta Crystallographica a-Foundation and Advances*, 2015, **71**, 59-75.
25. O. V. Dolomanov, L. J. Bourhis, R. J. Gildea, J. A. K. Howard and H. Puschmann, *J. Appl. Crystallogr.*, 2009, **42**, 339-341.
26. F. Arod, P. Pattisont, K. J. Schenk and G. Chapuisl, *Crystal Growth & Design*, 2007, **7**, 1679-1685.
27. J. Harada, R. Nakajima and K. Ogawa, *Journal of the American Chemical Society*, 2008, **130**, 7085-7091.

Chapter 9

Synthesis and structures of three isoxazole containing Schiff bases

Helen E. Mason, Judith A. K. Howard and Hazel A. Sparkes

Published *Acta Crystallographica*, 2020, **C76**, 927-931, doi.org/10.1107/S2053229620010530. Reproduced with permission of the International Union of Crystallography.

9.1 Abstract

The synthesis and structures of three isoxazole containing Schiff bases are reported, namely (E)-2-((isoxazol-3-ylimino)methyl)phenol, (E)-2-(((5-methylisoxazol-3-yl)imino)methyl)phenol and (E)-2,4-di-tert-butyl-6-((isoxazol-3-ylimino)methyl)phenol. All three structures contain an intramolecular O-H···N hydrogen bond, alongside weaker intermolecular C-H···N and C-H···O contacts. The C-O(H) and imine C=N bond lengths were consistent with the structures existing in the enol rather than keto form. Despite having dihedral angles < 25° none of the compounds were observed to be strongly thermochromic, unlike their anil counterparts, however all three compounds showed a visible colour change upon irradiation with UV light.

9.2 Introduction

A wide range of Schiff bases can be relatively easily prepared making them versatile as ligands and consequently they have found widespread use over many years in areas such as organometallic chemistry,[1] polymer synthesis,[2] anticancer drugs,[3] catalysts[4] and sensors.[5] In addition, Schiff bases themselves have been found to display interesting properties with anils, Schiff bases of salicylaldehyde derivatives with aniline derivatives, having been first found to exhibit both thermo- and photochromism in the solid-state.[6-8] Originally the thermo and photo chromism of anils were thought to be mutually exclusive[7, 8] but it has since been found not to be the case and it is thought they all display thermochromism with some also displaying photochromism.[9] The colour change is believed to be due to a photo or to a thermally induced tautomeric equilibrium shift between colourless enol(-imine) and keto(-amine) forms.[10, 11]

The Schiff bases of salicylaldehyde (2-hydroxybenzaldehyde) derivatives with isoxazole derivatives have not been widely characterised structurally, with a search of the Cambridge Structural Database as of June 2020 revealing two structures (E)-2-Methoxy-6- (5-methylisoxazol-3-yl)iminomethyl phenol[12] and N-[5-Methylisoxazole amino-3-yl]-3,5-di-tert-butylsalicylaldimine.[13] Herein the synthesis and characterisation of three isoxazole containing Schiff bases are reported, namely (E)-2-((isoxazol-3-ylimino)methyl)phenol (**1**), (E)-2-(((5-methylisoxazol-3-yl)imino)methyl)phenol (**2**) and (E)-2,4-di-tert-butyl-6-((isoxazol-3-ylimino)methyl)phenol (**3**), see Scheme 9.1.

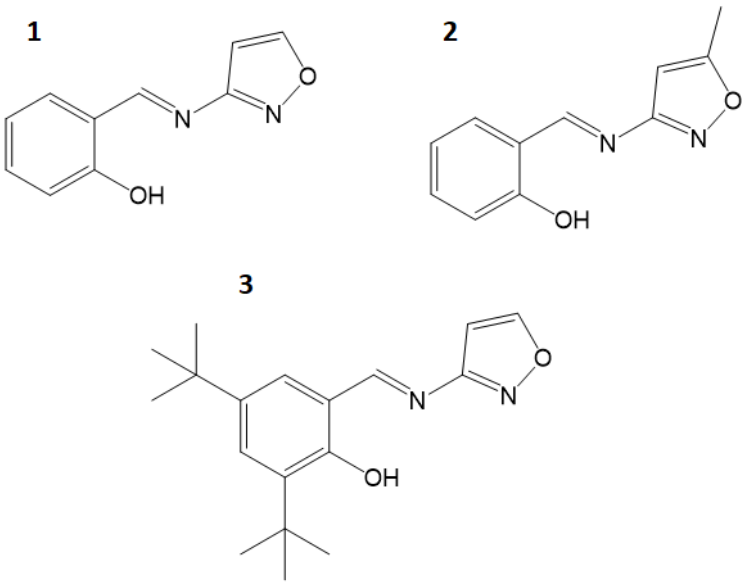

Scheme 9.1 - Compound structures of (E)-2-((isoxazol-3-ylimino)methyl)phenol (**1**), (E)-2-(((5-methylisoxazol-3-yl)imino)methyl)phenol (**2**) and (E)-2,4-di-tert-butyl-6-((isoxazol-3-ylimino)methyl)phenol (**3**)

9.3 Experimental

9.3.1 Synthesis

All reagents were used as supplied from Aldrich. Compounds were synthesized by direct condensation of the appropriate salicylaldehyde and isoxazole derivatives in ethanol. 0.0025 moles of the salicylaldehyde and aniline were each dissolved in 25 ml of ethanol, the resulting solutions combined and refluxed with stirring for six-eight hours. Any precipitate was filtered, rinsed with ethanol and left to dry, the (remaining) solution was then rotary evaporated until (further) precipitate formed. Re-crystallization was carried out from hexane-DCM (**1**), ethanol (**2**) or chloroform (**3**).

9.3.2 Characterisation

Elemental C, H and N content analysis was carried out using the Durham University Analytical services on the Exeter Analytical E-440 Elemental Analyzer. Mass spectrometry in positive electro-spray (ES+) mode was performed by the Durham University Mass Spectrometry service on a Waters TQD with an Acquity solvent system. See Appendix 9 for the results.

9.3.3 Single Crystal X-ray Diffraction Data Collection

X-ray diffraction data were collected on a Bruker Apex2 or Oxford Diffraction Gemini using monochromated Mo-*Kα* (λ = 0.71073 Å) radiation. Data collection, integration and absorption corrections were carried out using SAINT[14] or CrysAlisPro.[15] The structures were solved either by direct methods in SHELXT[16] or using SHELXS[17] and refined by full matrix least squares on F^2 in SHELXL[17] using Olex2.[18] All hydrogen atoms, apart from the OH hydrogen involved in the intramolecular hydrogen bonding with the imine nitrogen were positioned geometrically and refined using a riding model. The hydrogen atoms involved in the intramolecular hydrogen bond were located in the Fourier difference map (FDM) wherever feasible. Structures **1** and **2** crystallised in non-centrosymmetric space groups however the Flack parameters obtained here

were not meaningful as the data were collected with molybdenum radiation and there are no heavy atoms to facilitate anomalous dispersion. In **3**, which contained two independent molecules in the asymmetric unit, one of the tert-butyl groups was disordered the sum of the occupancies of the two parts were set to equal 1 and subsequently fixed at the refined values. The *inter*planar dihedral angle was calculated by measuring the angle between planes computed through the five or six non-hydrogen atoms of the two rings. See Table 9.1 for further details of the crystallographic data collections.

Table 9.1 - Crystal data and structure refinement for **1**, **2** and **3**.

Identification code	**1**	**2**	**3**
Empirical formula	$C_{10}H_8N_2O_2$	$C_{11}H_{10}N_2O_2$	$C_{18}H_{24}N_2O_2$
Formula weight	188.18	202.21	300.39
Temperature/K	210(2)	120(2)	120(2)
Crystal system	orthorhombic	orthorhombic	triclinic
Space group	$P2_12_12_1$	$Pna2_1$	P-1
a/Å	4.5999(5)	20.5584(7)	10.8955(5)
b/Å	10.2684(10)	10.0468(4)	10.9571(4)
c/Å	18.711(2)	4.6417(2)	14.8329(6)
α/°	90	90	82.335(3)
β/°	90	90	88.326(4)
γ/°	90	90	75.178(3)
Volume/Å^3	883.79(16)	958.73(7)	1696.56(12)
Z	4	4	4
ρ_{calc}g/cm^3	1.414	1.401	1.176
μ/mm^{-1}	0.101	0.099	0.077
F(000)	392.0	424.0	648.0
Crystal size/mm^3	0.3 × 0.08 × 0.05	0.49 × 0.24 × 0.09	0.6 × 0.31 × 0.18
Radiation	MoKα (λ = 0.71073)	Mo Kα (λ = 0.71073)	Mo Kα (λ = 0.71073)
2θ range for data collection/°	5.89 to 56.606	5.67 to 54.192	5.542 to 52.744
Index ranges	-5 ≤ h ≤ 6, -13 ≤ k ≤ 13, -24 ≤ l ≤ 23	-26 ≤ h ≤ 24, -7 ≤ k ≤ 12, -5 ≤ l ≤ 5	-13 ≤ h ≤ 13, -13 ≤ k ≤ 13, -17 ≤ l ≤ 18
Reflections collected	10497	6756	14901
Independent reflections	2166 [R_{int} = 0.0204, R_{sigma} = 0.0145]	2021 [R_{int} = 0.0395, R_{sigma} = 0.0381]	6942 [R_{int} = 0.0365, R_{sigma} = 0.0565]
Data/restraints/parameters	2166/0/131	2021/1/141	6942/0/447
Goodness-of-fit on F^2	1.078	1.050	1.018
Final R indexes [I>=2σ (I)]	R_1 = 0.0321, wR_2 = 0.0798	R_1 = 0.0365, wR_2 = 0.0775	R_1 = 0.0492, wR_2 = 0.1050
Final R indexes [all data]	R_1 = 0.0378, wR_2 = 0.0831	R_1 = 0.0428, wR_2 = 0.0808	R_1 = 0.0744, wR_2 = 0.1192
Largest diff. peak/hole / e Å^{-3}	0.18/-0.14	0.16/-0.17	0.26/-0.21

9.4 Results and Discussion

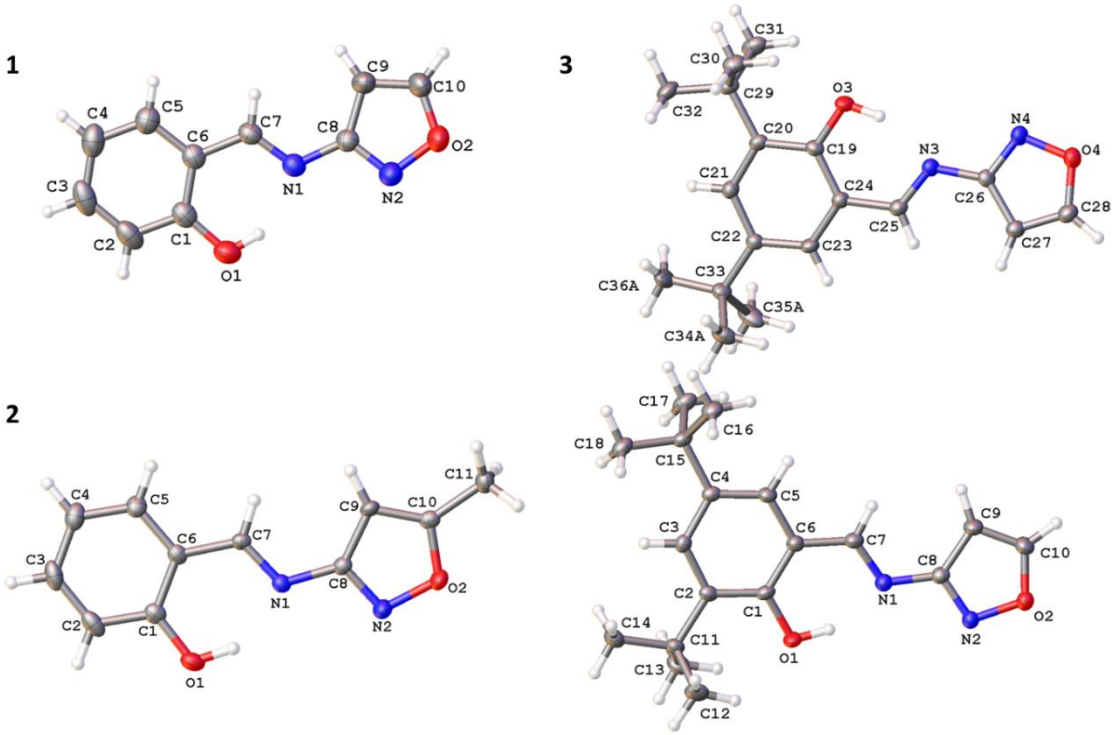

Figure 9.1 - Illustration of the structures of **1** (210(2)K), **2** (120(2) K) and **3** (120(2) K) with atomic numbering scheme depicted. Anisotropic displacement parameters at 50%. In the case of **3** only one position of the disordered tert-butyl group is shown for clarity.

9.4.1 Structural Discussion

The three structures all consist of the same basic backbone with a hydroxy substituted phenyl group joined to an isoxazole compound via an imine group (Figure 9.1). The C7=N1 bond lengths are consistent with the presence of a double bond (range 1.283(2) Å in **1** to 1.293(2) Å in **3**), while the C1-O1 bond lengths (range 1.350(2) Å in **1** to 1.3655(18) Å in **3**) are consistent with a single bond. Indeed, the hydroxy hydrogen atom was located in the Fourier difference map in the vicinity of the oxygen atom supporting the fact that the structure are all in the more commonly observed enol form rather than the keto form. All three structures contain an intramolecular hydrogen bond between O1-H1···N1 with similar parameters e.g. O1···N1 distances ranging from 2.6062(17) Å to 2.632(2) Å, see Table 9.2. The structures also contain weaker intermolecular C-H···N and C-H···O interactions, see Table 9.2.

Table 9.2 - Hydrogen-bond geometry (Å, °) for **1**, **2** and **3**.

Compound	*D*—H···*A*	*D*—H	H···*A*	*D*···*A*	*D*—H···*A*
1 (210(2) K)	O1—H1···N1	0.85 (3)	1.86 (3)	2.6110 (19)	146 (3)
	C7—H7···N2^{i}	0.93	2.71	3.599 (2)	159
	C9—H9···O1^{ii}	0.93	2.70	3.400 (2)	133
	C9—H9···N2^{i}	0.93	2.61	3.403 (2)	144
	C10—H10···O1^{i}	0.93	2.52	3.235 (2)	134
2 (120(2) K)	C7—H7···O2^{iii}	0.95	2.61	3.502 (3)	157
	C7—H7···N2^{iii}	0.95	2.49	3.394 (3)	159
	C9—H9···N2^{iii}	0.95	2.74	3.591 (3)	149
	C2—H2···O1^{iv}	0.95	2.62	3.496 (3)	153
	O1—H1···N1	0.95 (3)	1.80 (3)	2.632 (2)	145 (3)
3 (120(2) K)	C23—H23···O2^{v}	0.95	2.60	3.5232 (19)	165
	C25—H25···N2^{v}	0.95	2.70	3.637 (2)	169
	C5—H5···O4^{vi}	0.95	2.66	3.538 (2)	155
	C7—H7···N4^{vi}	0.95	2.82	3.708 (2)	156
	C18—H18*B*···N2^{vii}	0.98	2.67	3.559 (2)	152
	O1—H1···N1	0.92 (2)	1.76 (2)	2.6207 (18)	153 (2)
	O3—H3···N3	0.91 (3)	1.77 (2)	2.6062 (17)	151 (2)
	C10—H10···O3^{vi}	0.95	2.53	3.187 (2)	127
	C28—H28···O1^{v}	0.95	2.69	3.3370 (19)	126

Symmetry codes: (i) −*x*, *y*+1/2, −*z*+3/2; (ii) −*x*+1, *y*+1/2, −*z*+3/2; (iii) −*x*+3/2, *y*−1/2, *z*−1/2; (iv) −*x*+2, −*y*+2, *z*−1/2; (v) −*x*, −*y*+1, −*z*; (vi) −*x*+1, −*y*+1, −*z*; (vii) −*x*, −*y*, −*z*.

Examining the structure of **1** short π-π stacking type interactions exist between the six membered aromatic ring and the C=N (centroid to centroid distance 3.2905(3) Å)[19] creating 1-D stacks in approximately the *101* direction. The intermolecular interactions involving the isoxazole N and OH are: (i) bifurcated C-H···N interactions to another molecules, (ii) bifurcated C-H···O interactions to two different molecules. These interactions link a central molecule with four molecules in total, two molecules either side of itself creating chains in approximately the *b*-axis direction. Combining these interactions with the π-π stacking creates a 3-D network with a herringbone type packing structure, see Figure 9.2.

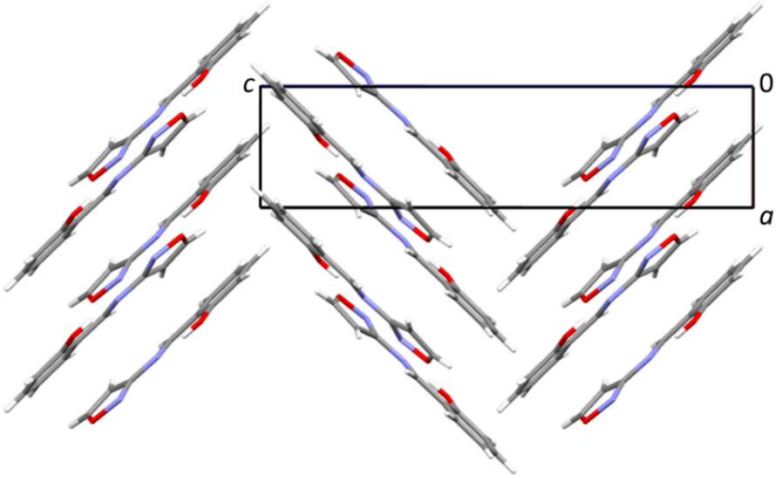

Figure 9.2 - Illustration of the packing for **1** looking down the *b*-axis direction.

The structure of **2** has short π-π stacking type interactions that exist between the six membered aromatic ring and the C=N (centroid to centroid distance 3.2772(1) Å) creating a 1-D stack up approximately the *101* direction. With all stacks in the *ac* plane in the same direction, however moving in the *b*-axis direction by one molecules the stacks in the *ac* plane are in a different directions due to the presence of the 2_1 screw axes and glide planes. The structure also contains: (i) C-H···N and a C-H···O interactions involving the N and O of the isoxazole (ii) C-H···O interactions involving the O of the OH group. These interactions link the central molecule to four others, two on each side of the molecule, this created a 3-D network. An illustration of the overall packing is shown in Figure 9.3.

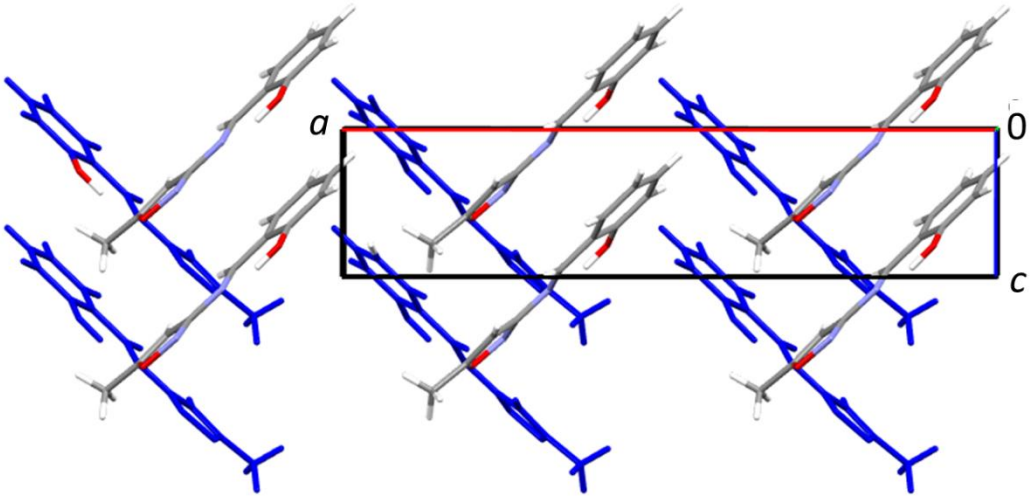

Figure 9.3 - Illustration of the packing in **2** looking down the *b*-axis. Molecules shown in elemental colours (C grey, O red, N blue, H white) are at the front, while molecules shown in blue are one molecule down the *b*-axis, showing the different orientations.

In **3** the two independent molecules show slightly different intermolecular interactions (i) C-H···N (bifurcated for the isoxazole containing N2 and O2, not for the isoxazole containing N4 and O4) and a C-H···O interactions involving the N and O of the isoxazole (ii) C-H···O interactions involving the O of the OH group. This creates a 3-D packing network, see Figure 9.4. There are no π-π stacking type interactions existing between the six membered aromatic ring and the C=N in this case presumably because of the presence of the bulky tert-butyl groups.

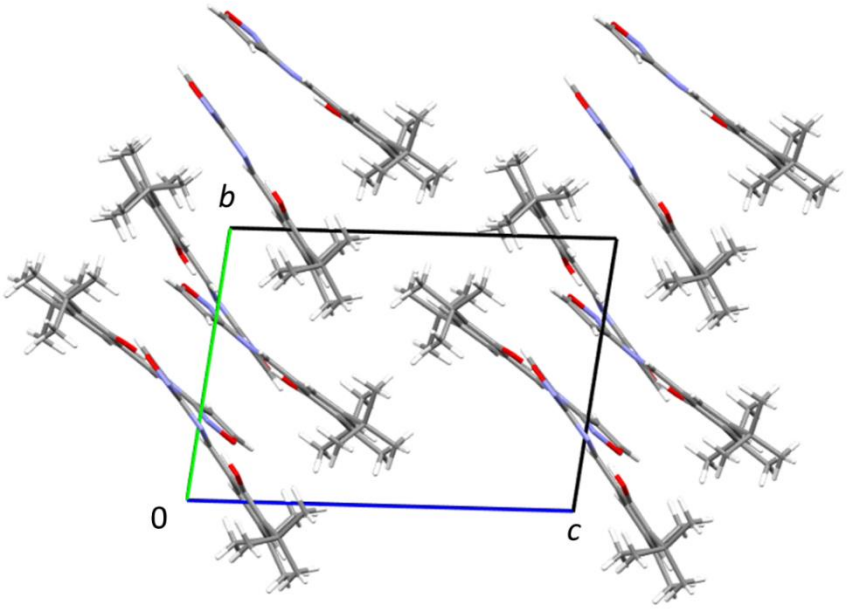

Figure 9.4 - Illustration of the packing in 3 looking down the *a*-axis.

9.4.2 Chromic studies

The chromic behaviour of these compounds was not fully investigated herein however some observations are worth reporting given the similarity of the structures to the widely studied anils. Schiff bases of salicylaldehyde derivatives with aniline derivatives, which exhibit both thermo- and photochromism in the solid-state.[7-9] In anils, a link has been proposed between the dihedral angle (Φ) and the chromic behaviour of some of the Schiff bases, with a suggestion that compounds with a Φ < 25° being expected to be strongly thermochromic, while those with Φ > 25° more likely to be photochromic.[10, 11] Clearly the dihedral angle is not the only factor that has been found to influence chromism in anils with thermochromic structures tending to be more closely packed than photochromic structures and substituents that weaken the O-H bond or strengthen the nitrogen atom's accepting ability often resulting in more strongly thermochromic complexes.[10, 11] The Schiff bases of salicylaldehyde derivatives with isoxazole derivatives presented here have not been widely studied in terms of their chromic behaviour and the three compounds presented herein appear to show some differences from the anils. The Φ were 6.95(12)° (**1**), 4.42(14)° (**2**) and 6.53(10)°/14.27(8)° (**3**), however none of the compounds were observed to be strongly thermochromic by eye when cooled to ~80 K. In the case of **2** and **3** this is perhaps not a major surprise as they are yellow at room temperature and while they did become paler in colour at lower temperatures the strongly thermochromic anil compounds are typically a red/orange colour at room temperature and change to yellow upon cooling. However, **1** which is orange at room temperature remained an orange colour at ~80 K also. All three compounds did show evidence of photochromism with a colour change, from orange to red for **1** and yellow to orange for **2** and **3**, upon irradiation with UV light.

9.5 Conclusions

The structures of three Schiff bases of salicylaldehyde derivatives with isoxazole derivatives, (E)-2-((isoxazol-3-ylimino)methyl)phenol (**1**), (E)-2-(((5-methylisoxazol-3-yl)imino)methyl)phenol (**2**) and (E)-2,4-di-tert-butyl-6-((isoxazol-3-ylimino)methyl)phenol (**3**), are reported. The three

structures all exist in the enol form with an intramolecular hydrogen bond between the O-H···N. All three structures contain intermolecular C-H···N and C-H···O contacts. In the structures of **1** and **2** π-π type contacts were identified between the C=N and the phenol ring. All three compounds had dihedral angles of < 25°, however none of the compounds were observed to be strongly thermochromic, even **1** which was orange at room temperature did not show a significant colour change upon cooling. This is in contract to the anils where the orange compounds with a dihedral angle of < 25° are normally strongly thermochromic. All three compounds did show evidence of photochromism upon irradiation with UV light.

9.6 References

1. H. Kargar, V. Torabi, A. Akbari, R. Behjatmanesh-Ardakani, A. Sahraei and M. N. Tahir, *Journal of Molecular Structure*, 2020, **1205**.
2. H. Mighani, *Journal of Polymer Research*, 2020, **27**.
3. S. Parveen, *Applied Organometallic Chemistry*, 2020, **34**, e5687.
4. S. Kumari, B. Das and S. Ray, *Dalton Transactions*, 2019, **48**, 15942-15954.
5. M. Sahu, A. K. Manna, K. Rout, J. Mondal and G. K. Patra, *Inorganica Chimica Acta*, 2020, **508**.
6. A. Senier and F. G. Shepheard, *Journal of the Chemical Society*, 1909, **95**, 1943-1955.
7. M. D. Cohen and G. M. J. Schmidt, *Journal of Physical Chemistry*, 1962, **66**, 2442-2446.
8. M. D. Cohen, G. M. J. Schmidt and S. Flavian, *Journal of the Chemical Society*, 1964, 2041-2051.
9. T. Fujiwara, J. Harada and K. Ogawa, *Journal of Physical Chemistry B*, 2004, **108**, 4035-4038.
10. E. Hadjoudis and I. M. Mavridis, *Chemical Society Reviews*, 2004, **33**, 579-588.
11. F. Robert, A. D. Naik, B. Tinant, R. Robiette and Y. Garcia, *Chemistry-a European Journal*, 2009, **15**, 4327-4342.
12. R. G. Zhao, J. Lu and J. K. Li, *Acta Crystallographica Section E-Crystallographic Communications*, 2008, **64**, O499.
13. O. Celik, M. Ulusoy, E. Tas and S. Ise, *Analytical Sciences: X-ray Structure Analysis Online*, 2007, **23**, x185-x186.
14. Bruker, *SAINT+ Integration Engine, Data Reduction Software, Bruker Analytical X-ray Instruments Inc., Madison, WI, USA*, 2007.
15. Agilent-Technologies, *CrysAlisPro Version 1.171.37.33c*, 2000.
16. G. M. Sheldrick, *Acta Crystallographica a-Foundation and Advances*, 2015, **71**, 3-8.
17. G. M. Sheldrick, *Acta Crystallogr., Sect. A: Found. Crystallogr.*, 2008, **64**, 112-122.
18. O. V. Dolomanov, L. J. Bourhis, R. J. Gildea, J. A. K. Howard and H. Puschmann, *J. Appl. Crystallogr.*, 2009, **42**, 339-341.
19. V. Corne, A. M. Sarotti, C. R. de Arellano, R. A. Spanevello and A. G. Suarez, *Beilstein Journal of Organic Chemistry*, 2016, **12**, 1616-1623.

Chapter 10

(*E*)-4-bromo-2-((phenylimino)methyl)phenol: A New Polymorph and Thermochromism

Helen E. Mason, Judith A. K. Howard and Hazel A. Sparkes

Published *Acta Crystallographica*, 2020, **76(11)**, 1001-1004, doi.org/10.1107/S2053229620011560. Reproduced with permission of the International Union of Crystallography.

10.1 Abstract

A new polymorph of (*E*)-4-bromo-2-((phenylimino)methyl)phenol is reported together with a low temperature structure determination of the previously published polymorph. Both polymorphs were found to have an intramolecular O—H···N hydrogen bond, between the phenol OH and imine N, forming an S(6) ring. The crystals were observed to be different colours at room temperature with the previously published polymorph being more orange and the new polymorph more yellow. The planarity of the molecule in the two polymorphs was found to be significantly different with dihedral angles (Φ) between the two aromatic rings for the previously published 'orange' polymorph of Φ = 1.8 (2)° at 120 K, while the new 'yellow' polymorph had Φ = 45.6 (1)° at 150 K. It was also observed that both polymorphs displayed some degree of thermochromism and upon cooling the 'orange' polymorph became more yellow, while the 'yellow' polymorph became paler upon cooling.

10.2 Introduction

A wide range of *N*-salicylideneanilines, Schiff bases of salicylaldehyde derivatives with aniline derivatives, have been synthesized.[1, 2] The *N*-salicylideneanilines derivatives are interesting as they have generally been found to display thermochromism with some also showing photochromism in the solid state.[3-5] The mechanism for the chromic colour change is believed to be due to a keto-enol tautomerism.[6, 7] The keto form is coloured while the enol form is colourless and the switch can be induced either by changes in temperature or by irradiation. A link has been proposed between the thermochromic behaviour of a compound and the dihedral angle (Φ) between the two aromatic rings with those with Φ < 25° being more likely to be strongly thermochromic.[6, 7] A larger *inter*planar angle allows increased orbital overlap and greater delocalization into the π-system which reduces the basicity of the nitrogen and thus the thermochromism. The substituents effect on the OH bond strength, nitrogen accepting ability and crystal packing have also been postulated as important in the chromic behaviour of the *N*-salicylideneanilines.[6, 7] It has also been observed that in general the *N*-salicylideneanilines, that are more strongly coloured, typically red/orange, at room temperature, tend to be more strongly thermochromic than those that are paler, typically yellow, at room temperature.[8, 9]

The structures of (*E*)-4-halogen-2-((phenylimino)methyl)phenol have been reported, F,[10] Cl,[11, 12] Br[13] and I.[14] Herein a new polymorph of (*E*)-4-bromo-2-((phenylimino)methyl)phenol, $C_{13}H_{10}BrNO$, **1B**, is reported together with a new low temperature determination of the previously reported

polymorph, **1A**,[13] see Scheme 10.1. Both polymorphs were found to be thermochromic to some extent.

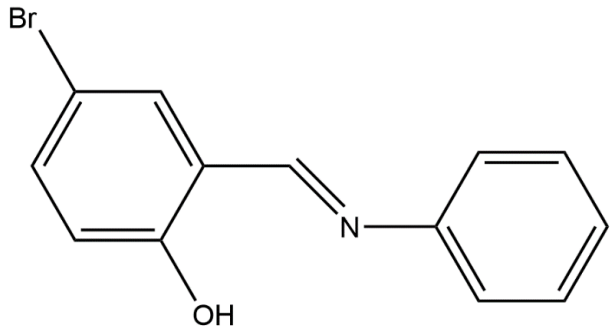

Scheme 10.1 - Molecular structure of **1**

10.3 Experimental

10.3.1 Synthesis and crystallization

(E)-4-bromo-2-((phenylimino)methyl)phenol was synthesized by direct condensation of the 5-bromosalicylaldehyde and aniline in ethanol. The two materials (0.005 mol of each, 1.000g 5-bromosalicylaldehyde, 0.466 g of aniline) were dissolved separately in ethanol (25 mL). The resultant solutions were combined and refluxed with stirring for 4 hrs. After removal of any precipitate, the solution was rotary evaporated until further precipitate formed, the solid filtered, rinsed with ethanol and left to dry, a yield of 94% (1.304 g, 0.0047mol) was obtained. Yellow single crystals (**1B**) crashed out of the crude reaction mixture and orange single crystals (**1A**) were produced by re-crystallization from ethanol.

10.3.2 X-ray Crystallography

Single crystal X-ray diffraction measurements for **1A** were collected at 120(2) K and **1B** were collected at 150(2) K on an Oxford Diffraction diffractometer. Both datasets were collected using Mo Kα radiation (λ = 0.71073 Å) and recorded on a CCD detector. The structures were solved using direct methods in ShelXS.[15] All structures were refined by full matrix least squares on F2 using SHELXL[15, 16] in Olex2.[17] All hydrogen atoms, apart from the OH hydrogen involved in the intramolecular hydrogen bonding with the imine nitrogen were positioned geometrically and refined using a riding model. The hydrogen atoms involved in the intramolecular hydrogen bond were located in the Fourier difference map (FDM) wherever feasible. In **1A**, the O-H distance was restrained to 0.86(1) Å. Crystal data, data collection and structure refinement details are summarized in Table 10.1.

Table 10.1 Crystal data and structure refinement for **1A** and **1B**.

Identification code	**1A**	**1B**
Empirical formula	$C_{13}H_{10}BrNO$	$C_{13}H_{10}BrNO$
Formula weight	276.13	276.13
Temperature/K	120(2)	150(2)
Crystal system	orthorhombic	monoclinic
Space group	$Pca2_1$	Cc
a/Å	12.2768(3)	25.8944(13)
b/Å	4.48290(10)	6.9439(4)
c/Å	19.6694(4)	6.1499(4)
α/°	90	90
β/°	90	91.381(5)
γ/°	90	90
Volume/Å^3	1082.52(4)	1105.48(11)
Z	4	4
ρ_{calc}g/cm^3	1.694	1.659
μ/mm^{-1}	3.772	3.694
F(000)	552.0	552.0
Crystal size/mm^3	0.45 × 0.20 × 0.05	0.58 × 0.49 × 0.22
Radiation	Mo Kα (λ = 0.71073)	Mo Kα (λ = 0.71073)
2θ range for data collection/°	6.638 to 52.74	6.074 to 52.724
Index ranges	-15 ≤ h ≤ 15, -5 ≤ k ≤ 5, -24 ≤ l ≤ 24	-32 ≤ h ≤ 32, -8 ≤ k ≤ 8, -7 ≤ l ≤ 7
Reflections collected	13133	7049
Independent reflections	2215 [R_{int} = 0.0425, R_{sigma} = 0.0260]	2254 [R_{int} = 0.0507, R_{sigma} = 0.0432]
Data/restraints/parameters	2215/2/149	2254/2/148
Goodness-of-fit on F^2	1.054	1.053
Final R indexes [I>=2σ (I)]	R_1 = 0.0219, wR_2 = 0.0518	R_1 = 0.0390, wR_2 = 0.0958
Final R indexes [all data]	R_1 = 0.0236, wR_2 = 0.0529	R_1 = 0.0420, wR_2 = 0.0995
Largest diff. peak/hole / e Å^{-3}	0.39/-0.23	0.95/-0.34
Flack parameter	-	-0.010(19)

10.4 Results and discussion

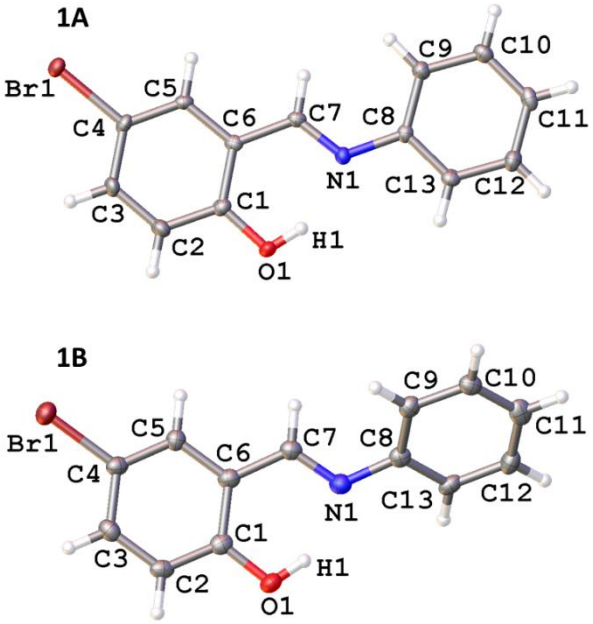

Figure 10.1 - Illustration of the structures of **1A** and **1B**, at 120 (2) K and 150 (2) K, respectively, with atomic numbering scheme depicted. Anisotropic displacement parameters shown at the 50% probability level.

The structures of **1A** and **1B** are shown in Figure 10.1. The structure of **1A** at 120 K was consistent with the previously published structure at room temperature.[13] The structure of **1A** was obtained in the orthorhombic space group $Pca2_1$ while **1B** was obtained in the monoclinic space group *Cc*. The compound consists of a hydroxy substituted phenyl ring linked *via* an imine group to a second unsubstituted phenyl group. An intramolecular hydrogen bond exists O1-H1···N1, see Table 10.2. In both polymorphs the structures were found to exist in the enol form with C7=N1 bond lengths of 1.282 (4) Å for **1A** and 1.284 (10) Å for **1B** indicating a double bond and C1—O1 bond lengths of 1.350 (5) Å for **1A** and 1.351 (9) Å for **1B** indicating a single bond. The structures showed quite different dihedral angles with **1A** having a Φ = 1.8 (2)° at 120 K and **1B** having Φ = 45.6 (1)° at 150 K. Upon cooling the structures were both found to display some degree of thermochromism with **1A** changing from orange at room temperature to yellow at 120 K and **1B** which was yellow at room temperature becoming slightly paler at 150 K, see Figure 10.2. The differences in the thermochromic behaviour of the two polymorphs is consistent with literature suggestions that a larger dihedral angle increases overlap of the π-system reducing the nitrogen basicity, disfavouring the keto form and thus also reducing the thermochromism of the compound.

Table 10.2 - Hydrogen-bond geometry (Å, °) for **1A** and **1B**.

Compound	Temperature	*D*—H···*A*	*D*—H	H···*A*	*D*···*A*	*D*—H···*A*
1A	120	O1—H1···N1	0.86 (1)	1.82 (3)	2.593 (4)	150 (5)
1B	150	O1—H1···N1	0.86 (11)	1.82 (11)	2.590 (10)	148 (10)

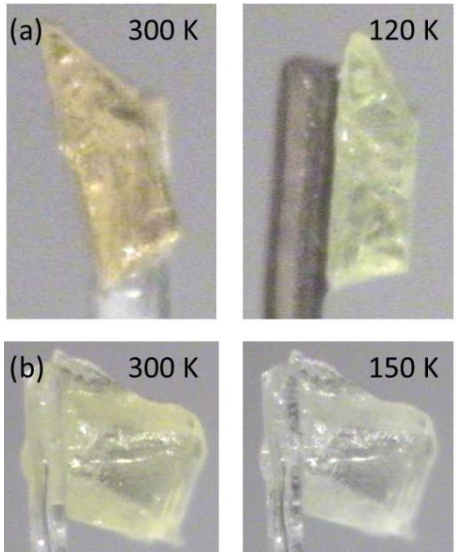

Figure 10.2 - Illustration of the colour change observed upon cooling (a) **1A**, (b) **1B** at 300 K and 120 K.

An intramolecular O1—H1···N1 hydrogen bond, involving the phenol OH and imine N, was identified in the structures of both polymorphs and creates an S(6) ring. The hydrogen bonding parameters were almost identical in the two structures with a D··A distance of ~2.59 Å and D—H···A angle of ~150°. The packing of the two polymorphs was unsurprisingly significantly different given the large difference in the dihedral angles. In **1A** the molecules are essentially planar and orientated diagonally such that the plane of the molecule is perpendicular to the *bc* plane and as a result of the 2_1 screw axis the diagonal slant of alternate molecules along the *a*-axis direction essentially align in opposite directions, see Figure 10.3a. It was also noted that there were short π type contacts between the C=N and the phenol ring in the 0–11 direction with a centroid to centroid (C=N) distance of 3.326 (1) Å. These can be seen on the Hirshfeld surface of **1A** as red dots, Figure 10.4a. In **1B**, although the molecules themselves are twisted, the molecules are orientated relative to each other such that they create planes parallel to the ac plane direction, see Figure 10.3b.

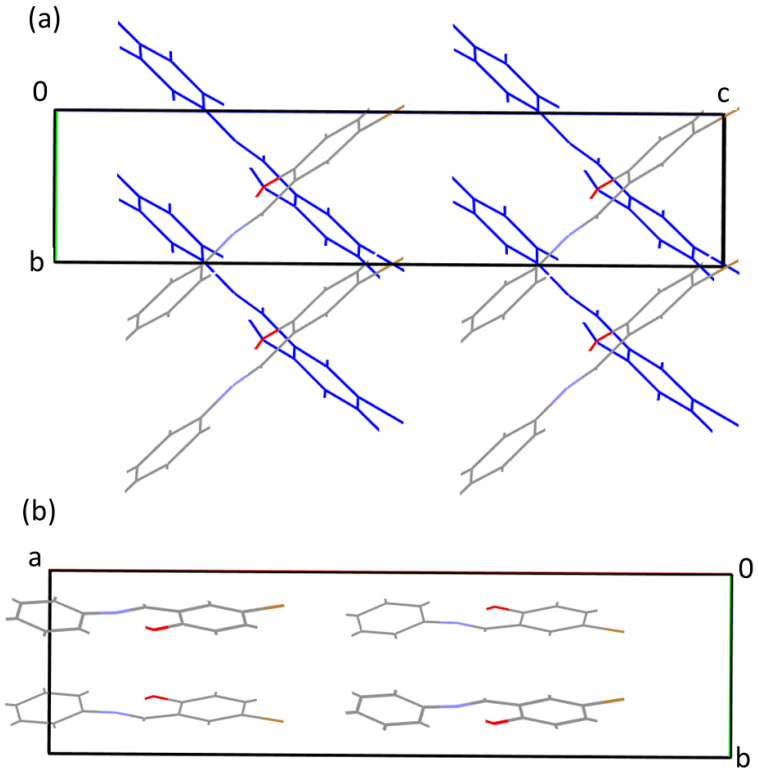

Figure 10.3 - Illustration of the packing for (a) **1A** looking down a-axis, molecules in blue are in plane behind those in element colours. (b) **1B** looking down the c-axis.

Examining the Hirshfeld fingerprint plots[18] for the two structures highlights the differences in the two structures, not least in the shapes of the two plots, see Figure 10.4. For **1A** the O···H and Br···H contacts are quite obvious, while in **1B** the H···H and C···H contacts are significantly more pronounced slightly masking the O···H and Br···H. These differences are very apparent on the Hirshfeld surface for both compounds with a greater number of red spots on the surface of **1A** that are more noticeable than for **1B** showing that **1A** has more short contacts.

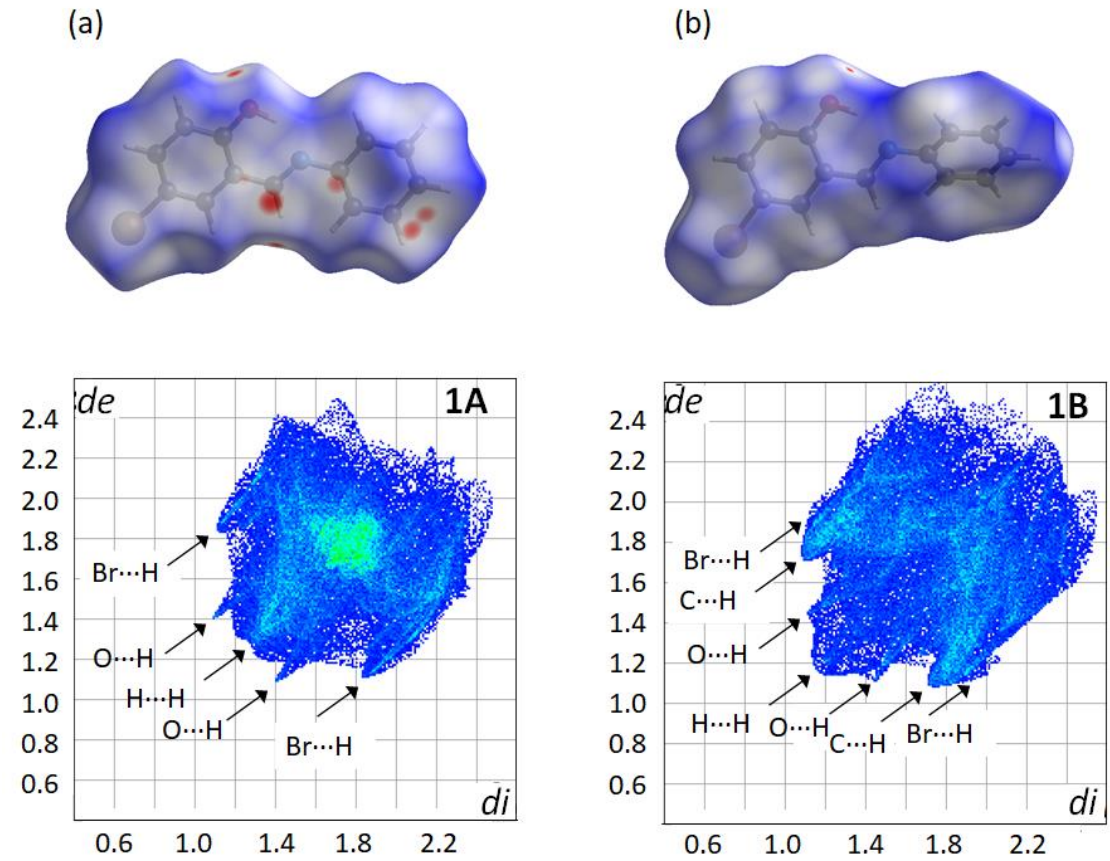

Figure 10.4 - The Hirshfeld Surface plot and fingerprint plot for (a) **1A**, (b) **1B**.

The two polymorphs of (E)-4-bromo-2-((phenylimino)methyl)phenol reported herein are particularly interesting as part of a study into the N-salicylideneanilines because they show significantly different molecular conformations and colours at room temperature. In line with the literature the extent of the thermochromism was found to be linked to the dihedral angle with **1A**, Φ = 1.8 (2)° showing a greater colour change upon cooling than observed for **1B**, Φ = 45.6 (1)°.

10.5 References

1. A. Özek, C. Albayrak, M. Odabaşoğlu and O. Büyükgüngör, *Acta Crystallogr., Sect. C: Cryst. Struct. Commun.*, 2007, **C63**, o177-o180.
2. K. Johmoto, T. Ishida, A. Sekine, H. Uekusa and Y. Ohashi, *Acta Crystallographica Section B-Structural Science Crystal Engineering and Materials*, 2012, **68**, 297-304.
3. M. D. Cohen and G. M. J. Schmidt, *Journal of Physical Chemistry*, 1962, **66**, 2442-2446.
4. M. D. Cohen, G. M. J. Schmidt and S. Flavian, *Journal of the Chemical Society*, 1964, 2041-2051.
5. T. Fujiwara, J. Harada and K. Ogawa, *Journal of Physical Chemistry B*, 2004, **108**, 4035-4038.
6. E. Hadjoudis and I. M. Mavridis, *Chemical Society Reviews*, 2004, **33**, 579-588.
7. F. Robert, A. D. Naik, B. Tinant, R. Robiette and Y. Garcia, *Chemistry-a European Journal*, 2009, **15**, 4327-4342.
8. K. Ogawa, J. Harada, T. Fujiwara and S. Yoshida, *Journal of Physical Chemistry A*, 2001, **105**, 3425-3427.
9. T. Fujiwara, J. Harada and K. Ogawa, *Journal of Physical Chemistry A*, 2009, **113**, 1822-1826.

10. G. Swetha, R. Ida Malarselvi, C. Ramachandra Raja, A. Thiruvalluvar and J. Priscilla, *Journal*, 2017, x171671.
11. J. Bregman, G. M. J. Schmidt and Leiserow.L, *Journal of the Chemical Society*, 1964, 2068-&.
12. K. Ogawa, Y. Kasahara, Y. Ohtani and J. Harada, *J. Am. Chem. Soc.*, 1998, **120**, 7107-7108.
13. X.-X. Yan, L.-P. Lu and M.-L. Zhu, *Journal*, 2014, **E70**, o853.
14. G. Swetha, R. Ida Malarselvi, C. Ramachandra Raja, A. Thiruvalluvar and J. Priscilla, *Journal*, 2019, x190788.
15. G. M. Sheldrick, *Acta Crystallographica Section A*, 2008, **64**, 112-122.
16. G. M. Sheldrick, *Acta Crystallographica Section C-Structural Chemistry*, 2015, **71**, 3-8.
17. O. V. Dolomanov, L. J. Bourhis, R. J. Gildea, J. A. K. Howard and H. Puschmann, *Journal of Applied Crystallography*, 2009, **42**, 339-341.
18. J. R. Turner, D. A. Resendiz-Lara, T. Jurca, A. Schafer, J. R. Vance, L. Beckett, G. R. Whittell, R. A. Musgrave, H. A. Sparkes and I. Manners, *Macromolecular Chemistry and Physics*, 2017, **218**.

Appendices

The appendices where they exist have been given the same number as the chapter to which they correspond.

Appendix 1

No Appendix for Chapter 1.

Appendix 2

Structural and spectroscopic characterisation of the spin crossover in $[Fe(abpt)_2(NCS)_2]$ polymorph A

Helen E. Mason, Wei Li, Michael A. Carpenter, Michelle L. Hamilton, Judith A. K. Howard and Hazel A. Sparkes

Published *New Journal of Chemistry*, 2016, **40(3)**, 2466-2478, doi 10.1039/C5NJ02359A.

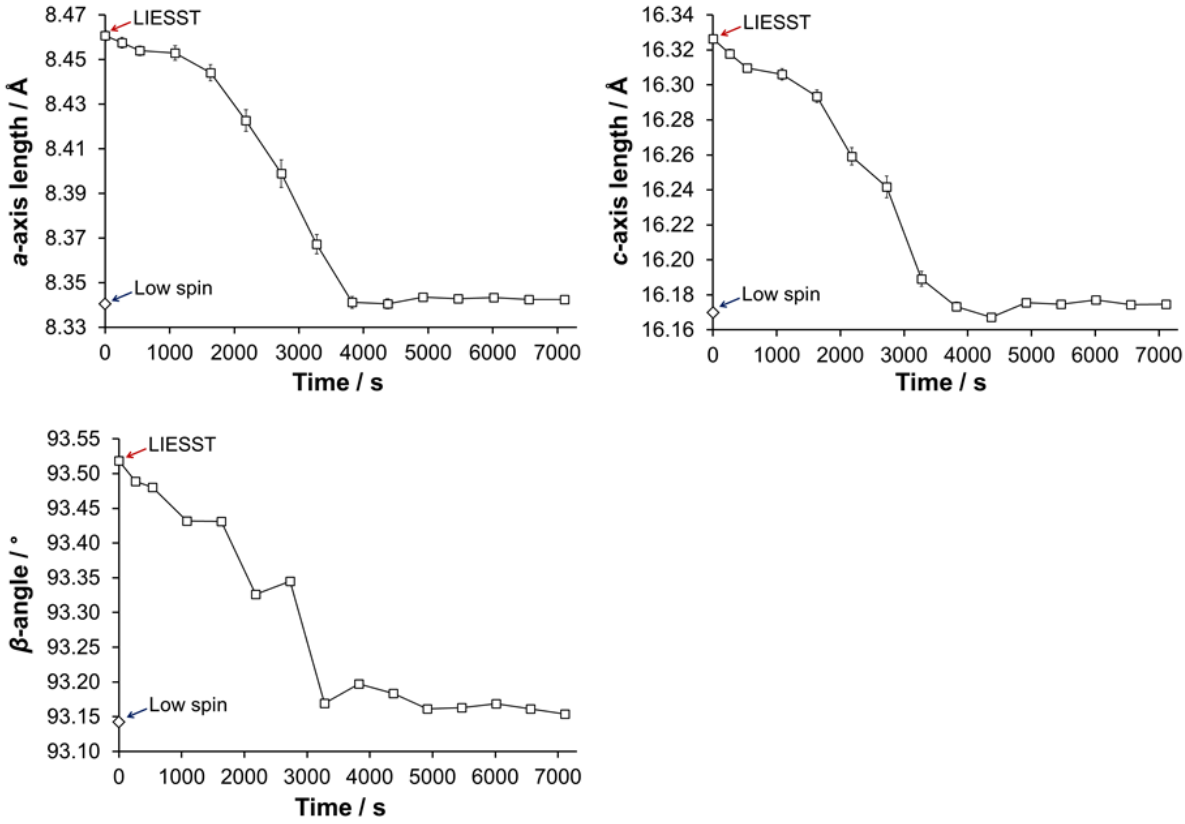

Figure S2.1 - Illustration of the change in the *a*-axis, *b*-axis and *β*-angle as a function of time at 30 K as a result of the relaxation of the LIESST HS* state. Note: each data point is plotted at the time mid-point of its two consecutive omega runs, therefore an error between +/-(535 to 538) s is associated with all data points except the 1st data point after turning the laser off (at 262 s) where the error is +/-262 s.

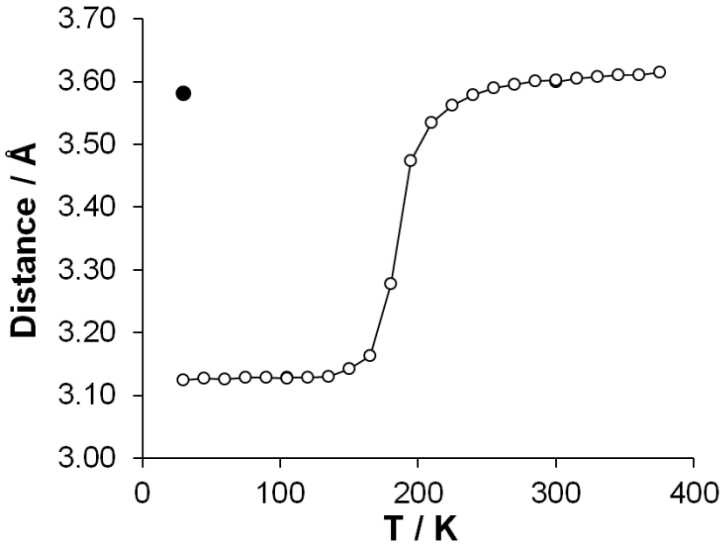

Figure S2.2 - Change in D···A distance for the C2-H2···N4#1 (#1 = -*x*+1, -*y*+1, -*z*+1) hydrogen bond in **A**: (o) as a function of temperature, (●) LIESST HS* structure.

Strain analysis

Values of the individual strains were obtained by first fitting a function of the form

$$a_o = a_1 + a_2 Q_s \coth\left(\frac{Q_s}{T}\right) \qquad \text{(S1)}$$

to lattice parameters in a temperature range well above the HS – LS transition. Extrapolation to low temperatures of the fit gives the reference parameters, a_o, b_o, $(c\sin\beta)_o$ and $(\cos\beta^*)_o$. The saturation temperature, Θ_s, gives the correct form for approaching T = 0 K with zero slope. Linear strains are then given by (after Carpenter *et al*., *Eur. J. Mineral.,* 1998, **10**, 621-691)

$$e_1 = \frac{a - a_o}{a_o} \qquad \text{(S2)}$$

$$e_2 = \frac{b - b_o}{b_o} \qquad \text{(S3)}$$

$$e_3 = \frac{c\sin\beta - \left(c\sin\beta\right)_o}{\left(c\sin\beta\right)_o} \qquad \text{(S4)}$$

and the non-zero shear strain is

$$e_5 \approx \frac{\cos\beta^* - \left(\cos\beta^*\right)_o}{\left(\cos\beta^*\right)_o}. \qquad \text{(S5)}$$

A value of Θ_s = 90 K was found to give a good representation of the four baselines shown in Figure S2.3(a)-(d) and ties in well with the single data point for the HS* state at 30 K. The same procedure can be followed for the volume strain, V_s, (Fig. S2.3e) which is given by

$$V_s = \frac{V - V_o}{V_o}. \qquad \text{(S6)}$$

The resulting values of all the strains are shown as a function of temperature in Figure S2.3(f).

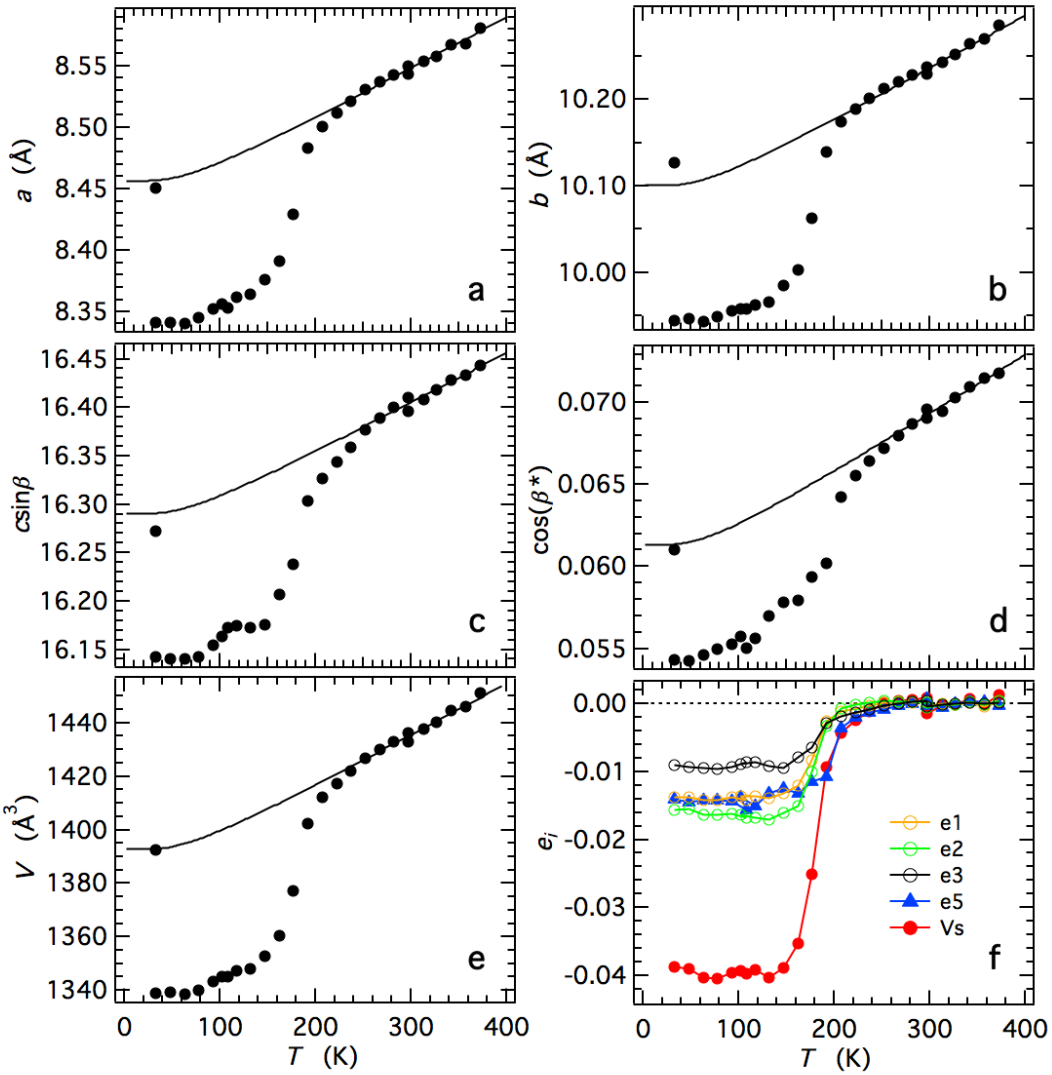

Figure S3 - Strain analysis from lattice parameter data. The solid curves in (a) – (e) are baseline (a_o, b_o, c_o, etc) fits to the highest temperature data using Equation S1, with the value of Θ_s = 90 K giving a good fit and passing through the 30 K data point for the high spin state induced by laser irradiation. (f) Strains determined using Equations S2-6.

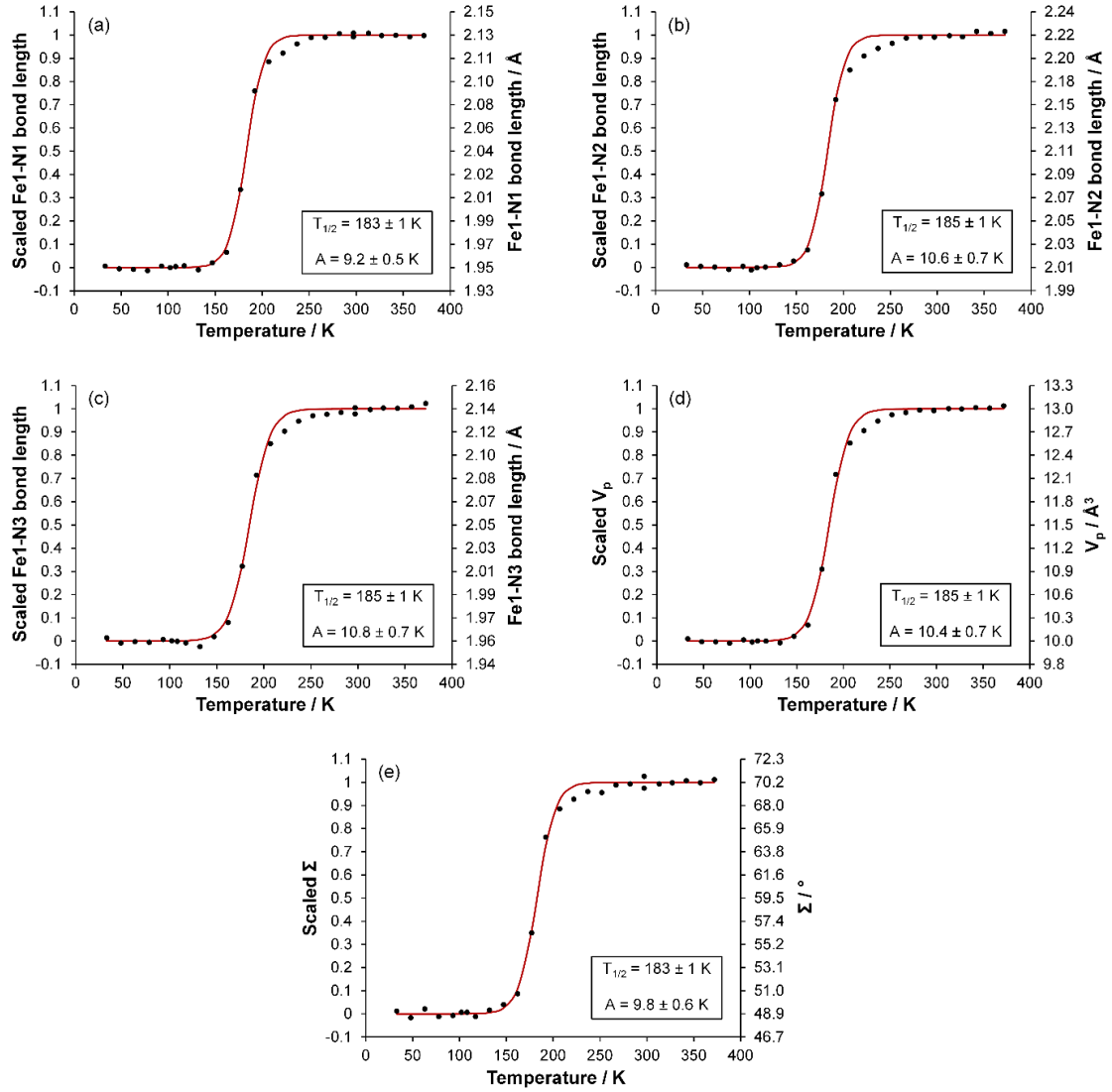

Figure S4 - Change in crystallographic parameters (rescaled to values between 0 and 1) as a function of temperature: (a)-(c) Fe-N bond lengths, (d) the volume of the Fe octahedron (V_p) and (e) the distortion parameter (Σ, the sum of the absolute value of the deviation of all 12 *cis* N-Fe-N angles from 90°). The red curve illustrates the fit of a sigmoidal function based on Equation 4 and the fit parameters, $T_{1/2}$ and A, are shown on each individual plot. Note: The sigmoid is not a perfect fit to the data, there is a slight deviation just above $T_{1/2}$ and this will influence the fit parameters.

Table S2.1 - Crystal data and refinement results for $[Fe(abpt)_2(NCS)_2]$ polymorph **A** at 120 K, 150 K, 180 K and 210 K.

	120(2) K (LS)	150(2) K	165(2) K	180(2) K	210(2) K
Empirical formula	$C_{26}H_{20}FeN_{14}S_2$	$C_{26}H_{20}FeN_{14}S_2$	$C_{26}H_{20}FeN_{14}S_2$	$C_{26}H_{20}FeN_{14}S_2$	$C_{26}H_{20}FeN_{14}S_2$
Formula weight	648.53	648.53	648.53	648.53	648.53
λ (Å)	0.71073	0.71073	0.71073	0.71073	0.71073
Crystal system	Monoclinic	Monoclinic	Monoclinic	Monoclinic	Monoclinic
Space group	$P2_1/n$	$P2_1/n$	$P2_1/n$	$P2_1/n$	$P2_1/n$
a (Å)	8.3636(8)	8.3770(9)	8.3913(4)	8.4290(4)	8.5008(3)
b (Å)	9.9597(10)	9.9820(11)	10.0025(5)	10.0626(5)	10.1744(4)
c (Å)	16.198(2)	16.198(2)	16.2339(8)	16.2671(8)	16.3606(6)
β (°)	93.114(2)	93.306(2)	93.321(1)	93.402(1)	93.684(1)
V (Å^3)	1347.3(2)	1352.2(3)	1360.29(12)	1377.31(12)	1412.11(9)
Z	2	2	2	2	2
Temperature (K)	120(2)	150(2)	165(2)	180(2)	210(2)
D_c (Mg/m^3)	1.599	1.593	1.583	1.564	1.525
μ (mm^{-1})	0.763	0.760	0.756	0.746	0.728
F(000)	664	664	664	664	664
Crystal size (mm^3)	0.36 x 0.30 x 0.26	0.36 x 0.30 x 0.26	0.36 x 0.30 x 0.26	0.36 x 0.30 x 0.26	0.36 x 0.30 x 0.26
ϑ range for data collection (°)	2.40 - 28.28	2.40 - 28.29	2.39 - 28.27	2.38 - 28.28	2.36 - 28.30
Ranges of h, k, l	$-10 \le h \le 11$, $-13 \le k \le 9$, $-21 \le l \le 15$	$-11 \le h \le 11$, $-13 \le k \le 12$, $-21 \le l \le 21$	$-10 \le h \le 11$, $-13 \le k \le 9$, $-21 \le l \le 15$	$-11 \le h \le 10$, $-13 \le k \le 9$, $-16 \le l \le 21$	$-11 \le h \le 11$, $-13 \le k \le 13$, $-21 \le l \le 21$
Refl. collected	9018	14820	9138	9303	15676
R_{int}	0.0312	0.0336	0.0288	0.0309	0.0340
Data/parameters	3333/202	3357/202	3374/202	3428/202	3521/202
Absorption coef. min/max	0.756/1.000	0.825/1.000	0.732/1.000	0.844/1.000	0.870/1.000
GooF (F^2)	1.040	1.043	1.022	1.034	1.044
Final R_1 [$I > 2\sigma(I)$]	0.0328	0.0293	0.0311	0.0335	0.0320
wR_2 [$I > 2\sigma(I)$]	0.0762	0.0700	0.0697	0.0760	0.0767
Largest diff. peak/hole (e Å^{-3})	0.36/-0.41	0.34/-0.33	0.33/-0.33	0.32/-0.27	0.37/-0.37

Table S2.2 - Hydrogen bonds for $[Fe(abpt)_2(NCS)_2]$ polymorph **A**. Symmetry transformations used to generate equivalent atoms: #1 = *x*+1/2, -*y*+3/2, *z*+1/2; #2 = -*x*+1, -*y*+1, -*z*+1.

D-H···A		270(2) K	210(2) K	180(2) K	165(2) K	150(2) K
N6-H6B···N7	d(D-H) (Å)	0.93(2)	0.89(2)	0.87(2)	0.89(2)	0.88(2)
	d(H···A) (Å)	2.12(2)	2.13(2)	2.17(2)	2.13(2)	2.16(2)
	d(D···A) (Å)	2.847(3)	2.851(2)	2.851(2)	2.850(2)	2.850(2)
	<(DHA) (°)	135(2)	137.4(19)	135(2)	138.4(19)	135.3(18)
N6-H6A···S1#1	d(D-H) (Å)	0.89(2)	0.93(2)	0.93(2)	0.93(2)	0.92(2)
	d(H···A) (Å)	2.69(2)	2.65(2)	2.60(2)	2.59(2)	2.61(2)
	d(D···A) (Å)	3.450(2)	3.4314(19)	3.403(2)	3.3958(18)	3.3890(17)
	<(DHA) (°)	143.1(19)	142.1(17)	144.2(18)	144.5(17)	142.4(17)
C2-H2···N4#2	d(D-H) (Å)	0.93	0.94	0.95	0.95	0.95
	d(H···A) (Å)	2.82	2.75	2.49	2.38	2.36
	d(D···A) (Å)	3.596(3)	3.536(3)	3.279(3)	3.163(2)	3.142(2)
	<(DHA) (°)	142.2	141.6	140.6	140	139.6

Table S2.2 continued - Hydrogen bonds for $[Fe(abpt)_2(NCS)_2]$ polymorph **A**. Symmetry transformations used to generate equivalent atoms: #1 = *x*+1/2, -*y*+3/2, *z*+1/2; #2 = -*x*+1, -*y*+1, -*z*+1.

D-H···A		120(2) K	30(2) K	30(2) K LIESST
N6-H6B···N7	d(D-H) (Å)	0.91(2)	0.88(2)	0.90(2)
	d(H···A) (Å)	2.13(2)	2.16(2)	2.11(2)
	d(D···A) (Å)	2.851(2)	2.853(2)	2.852(2)
	<(DHA) (°)	136.1(19)	134.5(19)	139.4(17)
N6-H6A···S1#1	d(D-H) (Å)	0.93(2)	0.89(2)	0.93(2)
	d(H···A) (Å)	2.61(2)	2.61(2)	2.63(2)
	d(D···A) (Å)	3.3862(18)	3.3814(18)	3.4170(15)
	<(DHA) (°)	142.1(18)	145.0(19)	143.0(15)
C2-H2···N4#2	d(D-H) (Å)	0.95	0.95	0.95
	d(H···A) (Å)	2.35	2.34	2.79
	d(D···A) (Å)	3.128(2)	3.124(2)	3.580(2)
	<(DHA) (°)	139.3	139.6	141.8

Table S2.2 continued - Hydrogen bonds for $[Fe(abpt)_2(NCS)_2]$ polymorph **A**. Symmetry transformations used to generate equivalent atoms: #1 = *x*+1/2, -*y*+3/2, *z*+1/2; #2 = -*x*+1, -*y*+1, -*z*+1.

D-H···A		296 K, ambient	296 K, 1.4(2) kbar	296 K, 5.1(2) kbar
N6-H6B···N7	d(D-H) (Å)	0.86(2)	0.87(2)	0.86(2)
	d(H···A) (Å)	2.12(6)	2.29(7)	2.22(5)
	d(D···A) (Å)	2.841(10)	2.839(8)	2.847(7)
	<(DHA) (°)	141(9)	122(6)	130(5)
N6-H6A···S1#1	d(D-H) (Å)	0.87(2)	0.867(19)	0.882(19)
	d(H···A) (Å)	2.80(7)	2.75(5)	2.70(5)
	d(D···A) (Å)	3.482(9)	3.437(7)	3.382(6)
	<(DHA) (°)	137(8)	138(6)	136(5)
C2-H2···N4#2	d(D-H) (Å)	0.93	0.93	0.93
	d(H···A) (Å)	2.81	2.77	2.44
	d(D···A) (Å)	3.579(13)	3.551(11)	3.215(11)
	<(DHA) (°)	141	142.7	140.4

Appendix 3

Structural Studies into the Spin Crossover Behaviour of $Fe(abpt)_2(NCS)_2$ Polymorphs B and D

Helen E. Mason, Jake R. C. Musselle-Sexton, Judith A. K. Howard, Michael R. Probert and Hazel A. Sparkes

Published *New Journal of Chemistry*, 2021, **45(31)**, 14014-14023, doi 10.1039/D1NJ02607K.

Table S3.1 Crystal data and structure refinement for Polymorph **B**.

Identification code	300(2) K	100(2) K	ambient	9 kbar
Empirical formula	$C_{26}H_{20}N_{14}S_2Fe$	$C_{26}H_{20}N_{14}S_2Fe$	$C_{26}H_{20}FeN_{14}S_2$	$C_{26}H_{20}FeN_{14}S_2$
Formula weight	648.53	648.53	648.53	648.53
Temperature/K	300(2)	100(2)	296.15	296.15
Crystal system	monoclinic	monoclinic	monoclinic	monoclinic
Space group	$P2_1/n$	$P2_1/n$	$P2_1/n$	$P2_1/n$
a/Å	11.5730(6)	11.47261(8)	11.5739(6)	11.3795(5)
b/Å	9.6589(5)	9.58685(8)	9.6588(8)	9.4118(7)
c/Å	12.8541(7)	12.72647(10)	12.8455(9)	12.4288(7)
α/°	90	90	90	90
β/°	101.2740(10)	100.5225(7)	101.244(4)	100.972(3)
γ/°	90	90	90	90
Volume/Å^3	1409.14(13)	1376.197(18)	1408.44(17)	1306.81(14)
Z	2	2	2	2
ρ_{calc}g/cm^3	1.528	1.565	1.529	1.648
μ/mm^{-1}	0.730	0.747	0.384	0.414
F(000)	664.0	664.0	664.0	664.0
Crystal size/mm^3	0.56 ×0.42 × 0.34	0.56 ×0.42 × 0.34	0.24 × 0.20 × 0.1	0.24 × 0.20 × 0.1
Radiation	MoKα (λ = 0.71073)	MoKα (λ = 0.71073)	AgKα (λ = 0.56086)	AgKα (λ = 0.56086)
2θ range for data collection/°	4.334 to 52.744	5.286 to 52.726	3.422 to 47.228	3.512 to 47.21
Index ranges	-14 ≤ h ≤ 14, -11 ≤ k ≤ 12, -16 ≤ l ≤ 11	-14 ≤ h ≤ 14, -11 ≤ k ≤ 11, -15 ≤ l ≤ 15	-16 ≤ h ≤ 16, -11 ≤ k ≤ 10, -16 ≤ l ≤ 13	-16 ≤ h ≤ 16, -9 ≤ k ≤ 10, -13 ≤ l ≤ 16
Reflections collected	8218	44396	20877	19633
Independent reflections	2875 [R_{int} = 0.0205, R_{sigma} = 0.0222]	2806 [R_{int} = 0.0342, R_{sigma} = 0.0113]	2101 [R_{int} = 0.0557, R_{sigma} = 0.0446]	1928 [R_{int} = 0.0540, R_{sigma} = 0.0423]
Data/restraints/parameters	2875/0/202	2806/0/202	2101/0/202	1928/0/202
Goodness-of-fit on F^2	1.029	1.073	1.081	1.054
Final R indexes [I>=2σ (I)]	R_1 = 0.0283, wR_2 = 0.0717	R_1 = 0.0221, wR_2 = 0.0552	R_1 = 0.0387, wR_2 = 0.0924	R_1 = 0.0369, wR_2 = 0.0946
Final R indexes [all data]	R_1 = 0.0352, wR_2 = 0.0754	R_1 = 0.0229, wR_2 = 0.0556	R_1 = 0.0800, wR_2 = 0.1159	R_1 = 0.0632, wR_2 = 0.1107
Largest diff. peak/hole / e Å^{-3}	0.19/-0.20	0.26/-0.25	0.25/-0.25	0.30/-0.28

Table S3.1 continued - Crystal data and structure refinement for Polymorph **B**.

Identification code	11.5 kbar	13.5 kbar	16 kbar	23.4 kbar
Empirical formula	$C_{26}H_{20}FeN_{14}S_2$	$C_{26}H_{20}FeN_{14}S_2$	$C_{26}H_{20}FeN_{14}S_2$	$C_{26}H_{20}FeN_{14}S_2$
Formula weight	648.53	648.53	648.53	648.53
Temperature/K	296.15	296.15	296.15	296.15
Crystal system	monoclinic	triclinic	triclinic	triclinic
Space group	$P2_1/n$	P-1	P-1	P-1
a/Å	11.3439(6)	9.2535(13)	9.1367(16)	8.985(4)
b/Å	9.3494(9)	11.3483(8)	11.3660(11)	11.328(3)
c/Å	12.3371(9)	12.2374(15)	12.1110(19)	12.013(5)
α/°	90	101.283(7)	101.644(9)	101.89(2)
β/°	100.984(4)	90.790(8)	91.715(10)	92.74(3)
γ/°	90	90.653(9)	90.844(11)	91.31(3)
Volume/Å^3	1284.49(17)	1260.0(3)	1231.0(3)	1194.4(8)
Z	2	2	2	2
ρ_{calc}g/cm^3	1.677	1.709	1.750	1.803
μ/mm^{-1}	0.421	0.429	0.439	0.453
F(000)	664.0	664.0	664.0	664.0
Crystal size/mm^3	0.24 × 0.20 × 0.1	0.24 × 0.20 × 0.1	0.24 × 0.20 × 0.1	0.24 × 0.20 × 0.1
Radiation	AgKα (λ = 0.56086)	AgKα (λ = 0.56086)	AgKα (λ = 0.56086)	AgKα (λ = 0.56086)
2θ range for data collection/°	4.278 to 47.346	2.888 to 45.82	2.888 to 47.076	2.9 to 47.216
Index ranges	-15 ≤ h ≤ 16, -10 ≤ k ≤ 10, -16 ≤ l ≤ 14	-10 ≤ h ≤ 9, -15 ≤ k ≤ 15, -12 ≤ l ≤ 15	-9 ≤ h ≤ 10, -15 ≤ k ≤ 15, -15 ≤ l ≤ 13	-9 ≤ h ≤ 9, -15 ≤ k ≤ 15, -12 ≤ l ≤ 12
Reflections collected	17152	17608	14154	6813
Independent reflections	1924 [R_{int} = 0.0512, R_{sigma} = 0.0404]	1985 [R_{int} = 0.0564, R_{sigma} = 0.0445]	1805 [R_{int} = 0.0607, R_{sigma} = 0.0551]	1305 [R_{int} = 0.0679, R_{sigma} = 0.0866]
Data/restraints/parameters	1924/0/202	1985/346/375	1805/346/369	1305/346/363
Goodness-of-fit on F^2	1.079	1.060	1.006	1.075
Final R indexes [I>=2σ (I)]	R_1 = 0.0362, wR_2 = 0.0800	R_1 = 0.0399, wR_2 = 0.0994	R_1 = 0.0364, wR_2 = 0.0817	R_1 = 0.0514, wR_2 = 0.1196
Final R indexes [all data]	R_1 = 0.0615, wR_2 = 0.0884	R_1 = 0.0699, wR_2 = 0.1127	R_1 = 0.0756, wR_2 = 0.0947	R_1 = 0.0980, wR_2 = 0.1373
Largest diff. peak/hole / e Å^{-3}	0.22/-0.24	0.20/-0.21	0.22/-0.19	0.23/-0.27

Table S3.2 - Crystal data and structure refinement for Polymorph **D** variable temperature.

Identification code	300(2) K	275(2) K	250(2) K	225(2) K
Empirical formula	$C_{26}H_{20}FeN_{14}S_2$	$C_{26}H_{20}N_{14}S_2Fe$	$C_{26}H_{20}FeN_{14}S_2$	$C_{26}H_{20}FeN_{14}S_2$
Formula weight	648.53	648.53	648.53	648.53
Temperature/K	300(2)	275(2)	250(2)	225(2)
Crystal system	monoclinic	monoclinic	monoclinic	monoclinic
Space group	$P2_1/c$	$P2_1/c$	$P2_1/c$	$P2_1/c$
a/Å	10.8097(3)	10.8017(4)	10.7949(3)	10.7881(3)
b/Å	15.9326(4)	15.9218(5)	15.9119(5)	15.9005(5)
c/Å	17.4617(5)	17.4303(6)	17.3979(5)	17.3637(5)
α/°	90	90	90	90
β/°	106.8470(10)	106.8250(10)	106.8040(10)	106.8010(10)
γ/°	90	90	90	90
Volume/Å^3	2878.30(14)	2869.38(17)	2860.78(15)	2851.36(15)
Z	4	4	4	4
ρ_{calc}g/cm^3	1.497	1.501	1.506	1.511
μ/mm^{-1}	0.714	0.717	0.719	0.721
F(000)	1328.0	1328.0	1328.0	1328.0
Crystal size/mm^3	0.4 × 0.24 × 0.16	0.4 × 0.24 × 0.16	0.4 × 0.24 × 0.16	0.4 × 0.24 × 0.16
Radiation	MoKα (λ = 0.71073)	MoKα (λ = 0.71073)	MoKα (λ = 0.71073)	MoKα (λ = 0.71073)
2θ range for data collection/°	3.532 to 52.744	3.536 to 52.744	3.54 to 52.744	3.544 to 52.74
Index ranges	-13 ≤ h ≤ 13, -19 ≤ k ≤ 19, -21 ≤ l ≤ 21	-13 ≤ h ≤ 13, -19 ≤ k ≤ 19, -21 ≤ l ≤ 21	-13 ≤ h ≤ 13, -19 ≤ k ≤ 19, -17 ≤ l ≤ 21	-13 ≤ h ≤ 13, -19 ≤ k ≤ 19, -17 ≤ l ≤ 21
Reflections collected	23130	28078	17086	17075
Independent reflections	5880 [R_{int} = 0.0340, R_{sigma} = 0.0298]	5863 [R_{int} = 0.0340, R_{sigma} = 0.0255]	5831 [R_{int} = 0.0296, R_{sigma} = 0.0320]	5818 [R_{int} = 0.0291, R_{sigma} = 0.0311]
Data/restraints/parameters	5880/1/407	5863/0/403	5831/1/407	5818/1/407
Goodness-of-fit on F^2	1.018	1.025	1.021	1.013
Final R indexes [I>=2σ (I)]	R_1 = 0.0340, wR_2 = 0.0792	R_1 = 0.0356, wR_2 = 0.0837	R_1 = 0.0331, wR_2 = 0.0754	R_1 = 0.0328, wR_2 = 0.0756
Final R indexes [all data]	R_1 = 0.0505, wR_2 = 0.0864	R_1 = 0.0481, wR_2 = 0.0899	R_1 = 0.0483, wR_2 = 0.0821	R_1 = 0.0453, wR_2 = 0.0812
Largest diff. peak/hole / e Å^{-3}	0.20/-0.28	0.70/-0.70	0.22/-0.30	0.23/-0.30

Table S3.2 continued - Crystal data and structure refinement for Polymorph **D** variable temperature.

Identification code	200(2) K	175(2) K	150(2) K	125(2) K
Empirical formula	$C_{26}H_{20}FeN_{14}S_2$	$C_{26}H_{20}FeN_{14}S_2$	$C_{26}H_{20}FeN_{14}S_2$	$C_{26}H_{20}FeN_{14}S_2$
Formula weight	648.53	648.53	648.53	648.53
Temperature/K	200(2)	175(2)	150(2)	125(2)
Crystal system	monoclinic	monoclinic	monoclinic	monoclinic
Space group	$P2_1/c$	$P2_1/c$	$P2_1/c$	$P2_1/c$
a/Å	10.7828(3)	10.7833(3)	10.7982(4)	10.8057(3)
b/Å	15.8845(5)	15.8575(5)	15.8008(5)	15.7552(5)
c/Å	17.3213(5)	17.2623(5)	17.1570(6)	17.0726(5)
α/°	90	90	90	90
β/°	106.8280(10)	106.9690(10)	107.3830(10)	107.6380(10)
γ/°	90	90	90	90
Volume/Å^3	2839.74(15)	2823.27(14)	2793.64(17)	2769.90(14)
Z	4	4	4	4
ρ_{calc}g/cm^3	1.517	1.526	1.542	1.555
μ/mm^{-1}	0.724	0.728	0.736	0.742
F(000)	1328.0	1328.0	1328.0	1328.0
Crystal size/mm^3	0.4 × 0.24 × 0.16	0.4 × 0.24 × 0.16	0.4 × 0.24 × 0.16	0.4 × 0.24 × 0.16
Radiation	MoKα (λ = 0.71073)	MoKα (λ = 0.71073)	MoKα (λ = 0.71073)	MoKα (λ = 0.71073)
2θ range for data collection/°	3.55 to 52.738	3.562 to 52.734	3.582 to 52.74	3.598 to 52.742
Index ranges	-13 ≤ h ≤ 13, -19 ≤ k ≤ 19, -21 ≤ l ≤ 17	-13 ≤ h ≤ 13, -19 ≤ k ≤ 19, -17 ≤ l ≤ 21	-13 ≤ h ≤ 13, -19 ≤ k ≤ 19, -21 ≤ l ≤ 21	-13 ≤ h ≤ 13, -19 ≤ k ≤ 19, -17 ≤ l ≤ 21
Reflections collected	17015	16896	27288	16506
Independent reflections	5804 [R_{int} = 0.0306, R_{sigma} = 0.0333]	5775 [R_{int} = 0.0299, R_{sigma} = 0.0326]	5709 [R_{int} = 0.0323, R_{sigma} = 0.0241]	5660 [R_{int} = 0.0303, R_{sigma} = 0.0332]
Data/restraints/parameters	5804/7/407	5775/1/407	5709/7/407	5660/1/407
Goodness-of-fit on F^2	1.028	1.020	1.024	1.022
Final R indexes [I>=2σ (I)]	R_1 = 0.0334, wR_2 = 0.0760	R_1 = 0.0315, wR_2 = 0.0732	R_1 = 0.0285, wR_2 = 0.0683	R_1 = 0.0312, wR_2 = 0.0701
Final R indexes [all data]	R_1 = 0.0460, wR_2 = 0.0819	R_1 = 0.0434, wR_2 = 0.0787	R_1 = 0.0363, wR_2 = 0.0720	R_1 = 0.0410, wR_2 = 0.0738
Largest diff. peak/hole / e Å^{-3}	0.21/-0.36	0.30/-0.33	0.26/-0.36	0.31/-0.41

Table S3.2 continued - Crystal data and structure refinement for Polymorph **D** variable temperature.

Identification code	100(2) K	75(2) K	50(2) K	30(2) K
Empirical formula	$C_{26}H_{20}FeN_{14}S_2$	$C_{26}H_{20}FeN_{14}S_2$	$C_{26}H_{20}FeN_{14}S_2$	$C_{26}H_{20}FeN_{14}S_2$
Formula weight	648.53	648.53	648.53	648.53
Temperature/K	100(2)	75(2)	50(2)	30(2)
Crystal system	monoclinic	monoclinic	monoclinic	monoclinic
Space group	$P2_1/c$	$P2_1/c$	$P2_1/c$	$P2_1/c$
a/Å	10.8090(3)	10.8076(3)	10.8072(4)	10.8082(4)
b/Å	15.7339(5)	15.7173(5)	15.7062(6)	15.6979(5)
c/Å	17.0294(5)	17.0045(5)	16.9907(7)	16.9850(6)
α/°	90	90	90	90
β/°	107.6660(10)	107.6570(10)	107.6310(10)	107.6180(10)
γ/°	90	90	90	90
Volume/Å^3	2759.57(14)	2752.41(14)	2748.53(19)	2746.61(17)
Z	4	4	4	4
ρ_{calc}g/cm^3	1.561	1.565	1.567	1.568
μ/mm^{-1}	0.745	0.747	0.748	0.749
F(000)	1328.0	1328.0	1328.0	1328.0
Crystal size/mm^3	0.4 × 0.24 × 0.16	0.4 × 0.24 × 0.16	0.4 × 0.24 × 0.16	0.4 × 0.24 × 0.16
Radiation	MoKα (λ = 0.71073)	MoKα (λ = 0.71073)	MoKα (λ = 0.71073)	MoKα (λ = 0.71073)
2θ range for data collection/°	3.606 to 52.744	3.61 to 52.742	3.612 to 52.744	3.614 to 52.734
Index ranges	-13 ≤ h ≤ 13, -19 ≤ k ≤ 19, -21 ≤ l ≤ 21	-10 ≤ h ≤ 13, -19 ≤ k ≤ 19, -21 ≤ l ≤ 18	-11 ≤ h ≤ 13, -19 ≤ k ≤ 19, -21 ≤ l ≤ 21	-13 ≤ h ≤ 13, -19 ≤ k ≤ 19, -21 ≤ l ≤ 21
Reflections collected	31337	16384	18564	31139
Independent reflections	5646 [R_{int} = 0.0334, R_{sigma} = 0.0223]	5631 [R_{int} = 0.0289, R_{sigma} = 0.0321]	5622 [R_{int} = 0.0332, R_{sigma} = 0.0336]	5621 [R_{int} = 0.0363, R_{sigma} = 0.0245]
Data/restraints/parameters	5646/1/407	5631/0/403	5622/0/403	5621/0/403
Goodness-of-fit on F^2	1.024	1.027	1.042	1.039
Final R indexes [I>=2σ (I)]	R_1 = 0.0266, wR_2 = 0.0636	R_1 = 0.0296, wR_2 = 0.0693	R_1 = 0.0302, wR_2 = 0.0695	R_1 = 0.0279, wR_2 = 0.0646
Final R indexes [all data]	R_1 = 0.0326, wR_2 = 0.0664	R_1 = 0.0377, wR_2 = 0.0729	R_1 = 0.0393, wR_2 = 0.0730	R_1 = 0.0336, wR_2 = 0.0673
Largest diff. peak/hole / e Å^{-3}	0.33/-0.39	0.34/-0.38	0.32/-0.39	0.34/-0.45

Table S3.2 continued - Crystal data and structure refinement for Polymorph **D** variable temperature.

Identification code	30(2) K LIESST
Empirical formula	$C_{26}H_{20}FeN_{14}S_2$
Formula weight	648.53
Temperature/K	30(2)
Crystal system	monoclinic
Space group	$P2_1/c$
a/Å	10.7016(4)
b/Å	15.9017(6)
c/Å	17.1557(6)
α/°	90
β/°	106.0400(10)
γ/°	90
Volume/Å^3	2805.79(18)
Z	4
ρ_{calc}g/cm^3	1.535
μ/mm^{-1}	0.733
F(000)	1328.0
Crystal size/mm^3	0.4 × 0.24 × 0.16
Radiation	MoKα (λ = 0.71073)
2θ range for data collection/°	3.558 to 52.742
Index ranges	-12 ≤ h ≤ 13, -19 ≤ k ≤ 19, -21 ≤ l ≤ 21
Reflections collected	22558
Independent reflections	5744 [R_{int} = 0.0357, R_{sigma} = 0.0312]
Data/restraints/parameters	5744/0/403
Goodness-of-fit on F^2	1.029
Final R indexes [I>=2σ (I)]	R_1 = 0.0293, wR_2 = 0.0682
Final R indexes [all data]	R_1 = 0.0379, wR_2 = 0.0719
Largest diff. peak/hole / e Å^{-3}	0.36/-0.38

Table S3.3 - Crystal data and structure refinement for Polymorph **D** variable pressure.

Identification code	Ambient start	1.8(2) kbar	7.5(2) kbar	9.6(2) kbar
Empirical formula	$C_{26}H_{20}N_{14}S_2Fe$	$C_{26}H_{20}N_{14}S_2Fe$	$C_{26}H_{20}N_{14}S_2Fe$	$C_{26}H_{20}N_{14}S_2Fe$
Formula weight	648.53	648.53	648.53	648.53
Temperature/K	296.15	296.15	296.15	296.15
Crystal system	monoclinic	monoclinic	monoclinic	monoclinic
Space group	$P2_1/c$	$P2_1/c$	$P2_1/c$	$P2_1/c$
a/Å	10.7819(15)	10.760(2)	10.7361(7)	10.6923(8)
b/Å	15.870(4)	15.808(6)	15.4827(17)	15.3683(18)
c/Å	17.415(3)	17.253(4)	16.6888(11)	16.4865(12)
α/°	90	90	90	90
β/°	106.875(10)	106.721(12)	107.567(4)	107.682(4)
γ/°	90	90	90	90
Volume/Å^3	2851.7(9)	2810.5(14)	2644.7(4)	2581.1(4)
Z	4	4	4	4
ρ_{calc}g/cm^3	1.511	1.533	1.629	1.669
μ/mm^{-1}	0.377	0.382	0.409	0.416
F(000)	1328.0	1328.0	1328.0	1328.0
Crystal size/mm^3	0.18 × 0.14 × 0.12	0.18 × 0.14 × 0.12	0.18 × 0.14 × 0.12	0.18 × 0.14 × 0.12
Radiation	AgKα (λ = 0.56086)	AgKα (λ = 0.56086)	AgKα (λ = 0.56086)	AgKα (λ = 0.56086)
2θ range for data collection/°	2.796 to 39.206	3.118 to 39.072	2.896 to 39.048	2.926 to 39.064
Index ranges	-12 ≤ h ≤ 12, -14 ≤ k ≤ 15, -19 ≤ l ≤ 19	-12 ≤ h ≤ 12, -13 ≤ k ≤ 13, -19 ≤ l ≤ 18	-12 ≤ h ≤ 12, -14 ≤ k ≤ 14, -17 ≤ l ≤ 19	-12 ≤ h ≤ 12, -14 ≤ k ≤ 14, -17 ≤ l ≤ 19
Reflections collected	15847	23079	23039	22491
Independent reflections	2524 [R_{int} = 0.0858, R_{sigma} = 0.0948]	2717 [R_{int} = 0.0567, R_{sigma} = 0.0436]	2697 [R_{int} = 0.0562, R_{sigma} = 0.0426]	2669 [R_{int} = 0.0599, R_{sigma} = 0.0403]
Data/restraints/parameters	2524/346/403	2717/351/407	2697/346/403	2669/346/403
Goodness-of-fit on F^2	1.047	1.059	1.100	1.084
Final R indexes [I>=2σ (I)]	R_1 = 0.0821, wR_2 = 0.1916	R_1 = 0.0396, wR_2 = 0.0925	R_1 = 0.0467, wR_2 = 0.1124	R_1 = 0.0498, wR_2 = 0.1220
Final R indexes [all data]	R_1 = 0.1318, wR_2 = 0.2231	R_1 = 0.0604, wR_2 = 0.1028	R_1 = 0.0649, wR_2 = 0.1234	R_1 = 0.0705, wR_2 = 0.1343
Largest diff. peak/hole / e Å^{-3}	0.48/-0.42	0.26/-0.24	0.28/-0.27	0.31/-0.34

Table S3.3 continued - Crystal data and structure refinement for Polymorph **D** variable pressure.

Identification code	12.0(2) kbar	15.0(2) kbar	Ambient end
Empirical formula	$C_{26}H_{20}FeN_{14}S_2$	$C_{26}H_{20}N_{14}S_2Fe$	$C_{26}H_{20}N_{14}S_2Fe$
Formula weight	648.53	648.53	648.53
Temperature/K	296.15	296.15	296.15
Crystal system	monoclinic	monoclinic	monoclinic
Space group	$P2_1/c$	$P2_1/c$	$P2_1/c$
a/Å	10.6433(7)	10.4607(17)	10.777(2)
b/Å	15.3285(16)	15.203(4)	15.859(5)
c/Å	16.4392(11)	16.348(3)	17.450(5)
α/°	90	90	90
β/°	107.475(4)	105.886(11)	106.734(12)
γ/°	90	90	90
Volume/Å^3	2558.2(4)	2500.7(9)	2856.2(13)
Z	4	4	4
ρ_{calc}g/cm^3	1.684	1.723	1.508
μ/mm^{-1}	0.420	0.430	0.376
F(000)	1328.0	1328.0	1328.0
Crystal size/mm^3	0.18 × 0.14 × 0.12	0.18 × 0.14 × 0.12	0.18 × 0.14 × 0.12
Radiation	AgKα (λ = 0.56086)	AgKα (λ = 0.56086)	AgKα (λ = 0.56086)
2θ range for data collection/°	2.932 to 39.018	2.94 to 39.182	2.794 to 38.994
Index ranges	-12 ≤ h ≤ 12, -14 ≤ k ≤ 14, -18 ≤ l ≤ 17	-12 ≤ h ≤ 12, -14 ≤ k ≤ 14, -16 ≤ l ≤ 16	-12 ≤ h ≤ 12, -16 ≤ k ≤ 15, -18 ≤ l ≤ 18
Reflections collected	22284	13610	24875
Independent reflections	2601 [R_{int} = 0.0545, R_{sigma} = 0.0352]	2354 [R_{int} = 0.0727, R_{sigma} = 0.0687]	2832 [R_{int} = 0.0610, R_{sigma} = 0.0428]
Data/restraints/parameters	2601/346/393	2354/346/393	2832/350/407
Goodness-of-fit on F^2	1.112	1.085	1.063
Final R indexes [I>=2σ (I)]	R_1 = 0.0466, wR_2 = 0.1111	R_1 = 0.0735, wR_2 = 0.1762	R_1 = 0.0455, wR_2 = 0.1204
Final R indexes [all data]	R_1 = 0.0642, wR_2 = 0.1213	R_1 = 0.1088, wR_2 = 0.1986	R_1 = 0.0700, wR_2 = 0.1354
Largest diff. peak/hole / e Å^{-3}	0.30/-0.27	0.46/-0.52	0.23/-0.28

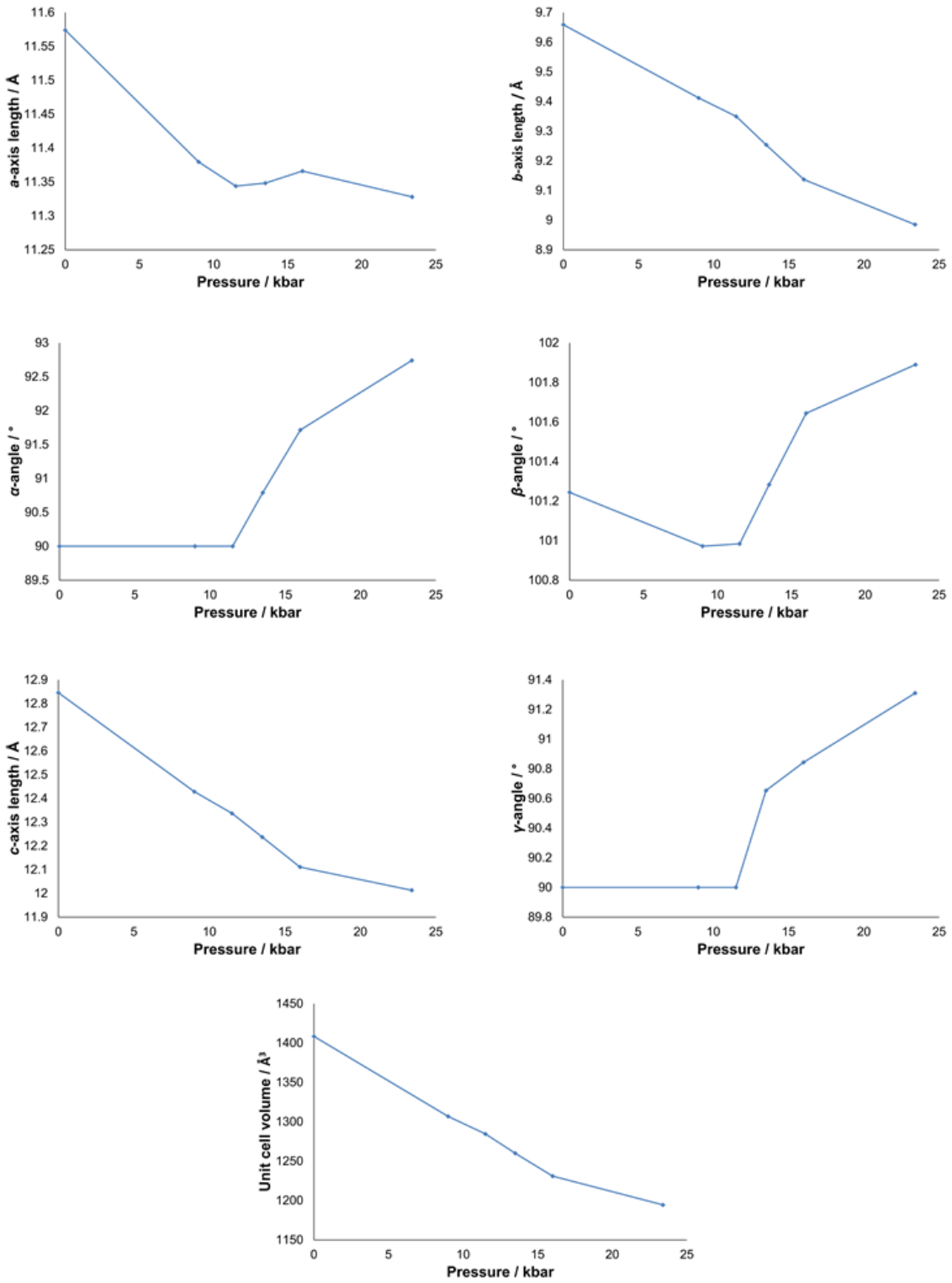

Figure S3.1 – Polymorph **B** effect of pressure on the unit cell parameters. Note that to allow direct comparison with the original monoclinic cell *a* and *b* and alpha and beta on the conventional triclinic cell have been switched for these plots.

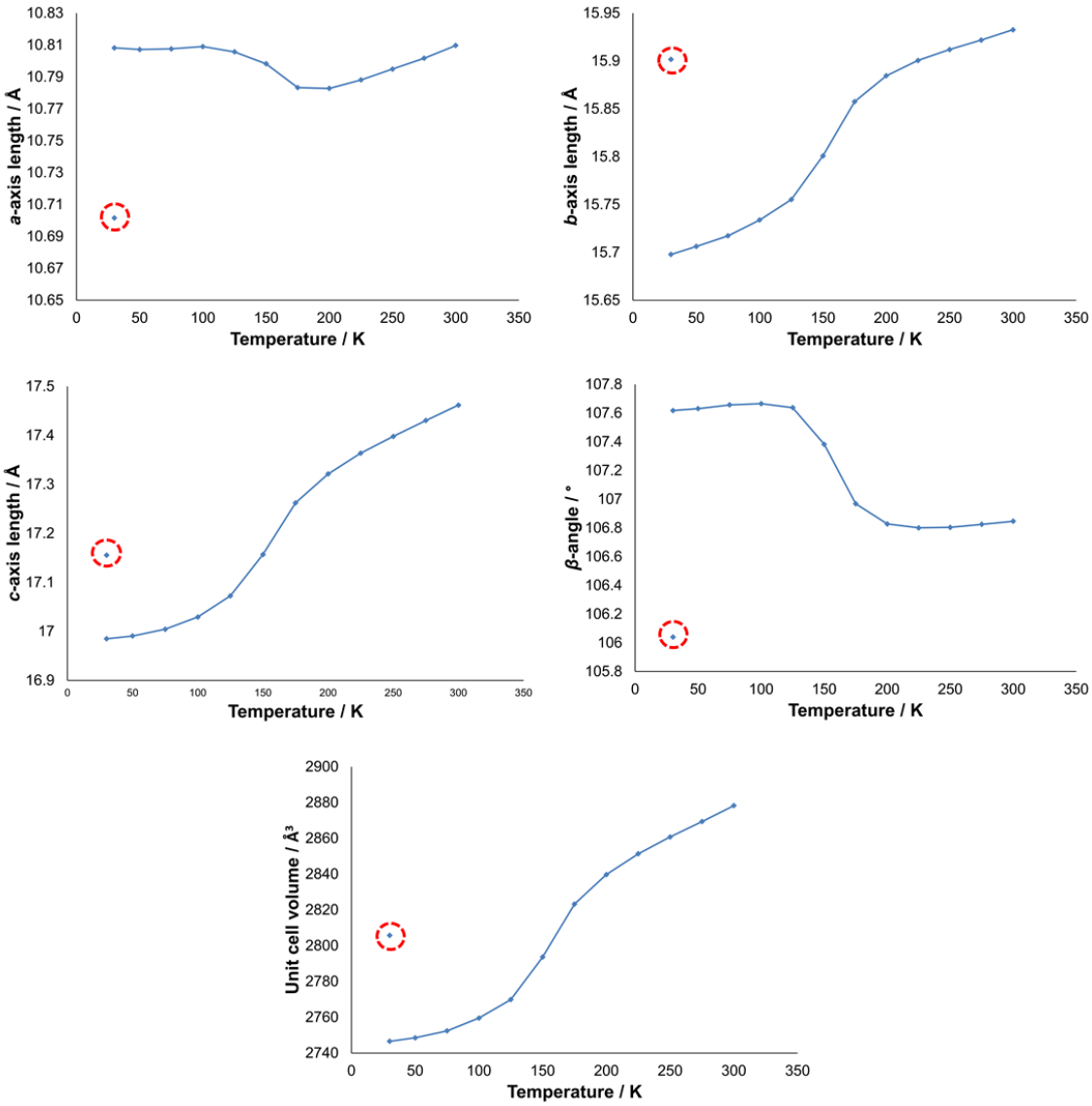

Figure S3.2 - Polymorph **D** effect of temperature on unit cell parameters. Point shown in red dashed circle is the LIESST structure.

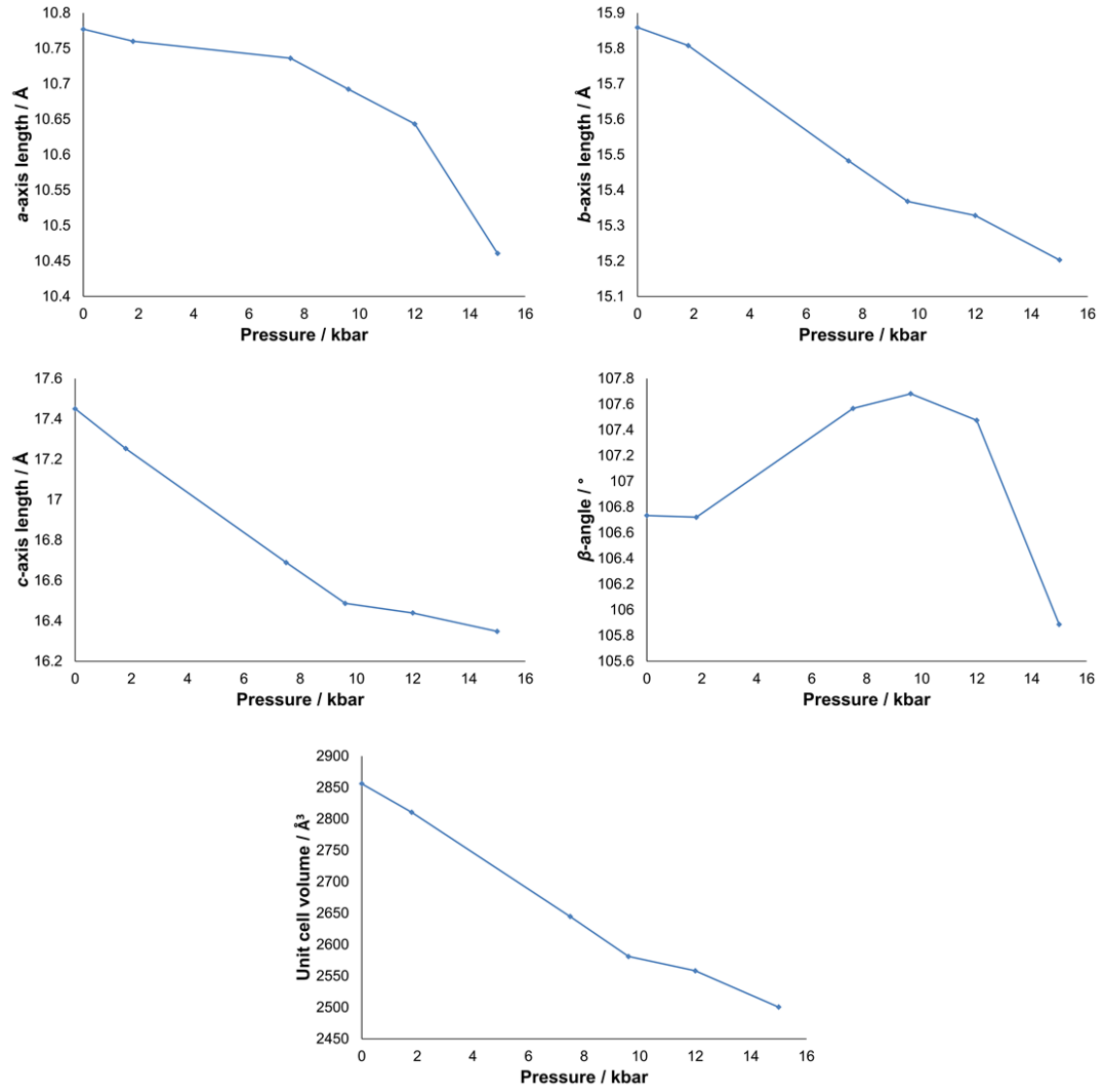

Figure S3.3 – Polymorph **D** effect of pressure on unit cell parameters.

Appendix 4

$[Fe(abpt)_2(NCSe)_2]$ polymorph A: Structural studies into the spin crossover behaviour

Helen E. Mason, Michelle L. Hamilton, Judith A. K. Howard and Hazel A. Sparkes

Published *New Journal of Chemistry*, 2018, **42(22)**, 18028-18037, doi 10.1039/C8NJ03627F.

Table S4.1 - Crystal data and refinement results for **A** at 50 K, 75 K, 100 K and 108 K.

Identification code	50(2) K	75(2) K	100(2) K	108(2) K
Empirical formula	$C_{26}H_{20}FeN_{14}Se_2$	$C_{26}H_{20}FeN_{14}Se_2$	$C_{26}H_{20}FeN_{14}Se_2$	$C_{26}H_{20}FeN_{14}Se_2$
Formula weight	742.33	742.33	742.33	742.33
Temperature / K	50(2)	75(2)	100(2)	108(2)
Crystal system	monoclinic	monoclinic	monoclinic	monoclinic
Space group	$P2_1/n$	$P2_1/n$	$P2_1/n$	$P2_1/n$
a / Å	8.4368(5)	8.4405(5)	8.4499(6)	8.4550(6)
b / Å	9.9497(6)	9.9558(6)	9.9648(6)	9.9691(7)
c / Å	16.3497(10)	16.3563(9)	16.3673(10)	16.3559(11)
β / °	93.1257(13)	93.1270(10)	93.1342(13)	93.0618(13)
V / Å^3	1370.41(14)	1372.40(14)	1376.09(15)	1376.65(17)
Z	2	2	2	2
ρ_{calc} / (g/cm^3)	1.799	1.796	1.792	1.791
μ / mm^{-1}	3.254	3.249	3.240	3.239
F(000)	736.0	736.0	736.0	736.0
Radiation	MoKα (λ = 0.71073)	MoKα (λ = 0.71073)	MoKα (λ = 0.71073)	MoKα (λ = 0.71073)
2θ range for data collection / °	4.794 to 56.55	4.792 to 56.56	4.788 to 56.552	4.788 to 56.562
Index ranges	-11 ≤ h ≤ 10, -12 ≤ k ≤ 13, -21 ≤ l ≤ 19	-11 ≤ h ≤ 11, -13 ≤ k ≤ 13, -21 ≤ l ≤ 21	-11 ≤ h ≤ 10, -12 ≤ k ≤ 13, -21 ≤ l ≤ 19	-11 ≤ h ≤ 11, -13 ≤ k ≤ 11, -20 ≤ l ≤ 21
Reflections collected	9150	21905	9170	11504
R_{int} / R_{sigma}	0.0328 / 0.0397	0.0388 / 0.0245	0.0322 / 0.0386	0.0306 / 0.0313
Data/restraints/parameters	3380/0/202	3400/0/202	3399/0/202	3424/0/202
Goodness-of-fit on F^2	1.070	1.091	1.047	1.075
Final R indexes [I>=2σ (I)]	R_1 = 0.0352, wR_2 = 0.0742	R_1 = 0.0320, wR_2 = 0.0696	R_1 = 0.0356, wR_2 = 0.0753	R_1 = 0.0321, wR_2 = 0.0662
Final R indexes [all data]	R_1 = 0.0437, wR_2 = 0.0769	R_1 = 0.0385, wR_2 = 0.0719	R_1 = 0.0454, wR_2 = 0.0785	R_1 = 0.0397, wR_2 = 0.0687
Largest diff. peak/hole / (e Å^{-3})	0.81/-0.65	0.86/-0.69	0.93/-0.61	0.72/-0.66

Table S4.1 continued - Crystal data and refinement results for **A** at 125 K,150 K, 175 K and 200 K.

Identification code	125(2) K	150(2) K	175(2) K	200(2) K
Empirical formula	$C_{26}H_{20}FeN_{14}Se_2$	$C_{26}H_{20}FeN_{14}Se_2$	$C_{26}H_{20}FeN_{14}Se_2$	$C_{26}H_{20}FeN_{14}Se_2$
Formula weight	742.33	742.33	742.33	742.33
Temperature / K	125(2)	150(2)	175(2)	200(2)
Crystal system	monoclinic	monoclinic	monoclinic	monoclinic
Space group	$P2_1/n$	$P2_1/n$	$P2_1/n$	$P2_1/n$
a / Å	8.4560(3)	8.4649(4)	8.4815(4)	8.4971(3)
b / Å	9.9693(4)	9.9787(5)	9.9987(5)	10.0240(4)
c / Å	16.3570(7)	16.3697(8)	16.3984(9)	16.4110(6)
β / °	93.0825(7)	93.0951(9)	93.1310(10)	93.1650(7)
V / Å^3	1376.91(9)	1380.71(12)	1388.57(12)	1395.67(9)
Z	2	2	2	2
ρ_{calc} / (g/cm^3)	1.790	1.786	1.775	1.766
μ / mm^{-1}	3.239	3.230	3.211	3.195
F(000)	736.0	736.0	736.0	736.0
Radiation	Mo$K\alpha$ (λ = 0.71073)	Mo$K\alpha$ (λ = 0.71073)	Mo$K\alpha$ (λ = 0.71073)	Mo$K\alpha$ (λ = 0.71073)
2θ range for data collection / °	4.786 to 56.532	4.782 to 55.748	4.774 to 56.556	4.764 to 52.736
Index ranges	-11 ≤ h ≤ 11, -13 ≤ k ≤ 13, -20 ≤ l ≤ 21	-11 ≤ h ≤ 11, -13 ≤ k ≤ 8, -16 ≤ l ≤ 21	-11 ≤ h ≤ 11, -13 ≤ k ≤ 8, -21 ≤ l ≤ 16	-10 ≤ h ≤ 10, -12 ≤ k ≤ 12, -20 ≤ l ≤ 20
Reflections collected	15248	9538	9355	15588
R_{int} / R_{sigma}	0.0336 / 0.0279	0.0287 / 0.0329	0.0303 / 0.0364	0.0329 / 0.0223
Data/restraints/parameters	3421/0/202	3282/0/202	3444/1/202	2861/0/202
Goodness-of-fit on F^2	1.093	1.079	1.050	1.101
Final R indexes [I>=2σ (I)]	R_1 = 0.0311, wR_2 = 0.0655	R_1 = 0.0325, wR_2 = 0.0671	R_1 = 0.0341, wR_2 = 0.0697	R_1 = 0.0295, wR_2 = 0.0633
Final R indexes [all data]	R_1 = 0.0384, wR_2 = 0.0679	R_1 = 0.0416, wR_2 = 0.0702	R_1 = 0.0461, wR_2 = 0.0739	R_1 = 0.0351, wR_2 = 0.0649
Largest diff. peak/hole / (e Å^{-3})	0.66/-0.63	0.73/-0.69	0.75/-0.64	0.64/-0.51

Table S4.1 continued - Crystal data and refinement results for **A** at 225 K, 250 K, 275 K and 300 K.

Identification code	225(2) K	250(2) K	275(2) K	300(2) K
Empirical formula	$C_{26}H_{20}FeN_{14}Se_2$	$C_{26}H_{20}FeN_{14}Se_2$	$C_{26}H_{20}FeN_{14}Se_2$	$C_{26}H_{20}FeN_{14}Se_2$
Formula weight	742.33	742.33	742.33	742.33
Temperature / K	225(2)	250(2)	275(2)	300(2)
Crystal system	monoclinic	monoclinic	monoclinic	monoclinic
Space group	$P2_1/n$	$P2_1/n$	$P2_1/n$	$P2_1/n$
a / Å	8.5401(5)	8.5815(4)	8.6022(3)	8.6181(4)
b / Å	10.0947(5)	10.1622(5)	10.1941(4)	10.2163(4)
c / Å	16.4597(9)	16.5208(9)	16.5527(6)	16.5785(7)
β / °	93.2083(10)	93.2926(10)	93.3872(7)	93.4701(9)
V / Å^3	1416.76(13)	1438.35(13)	1449.00(9)	1456.98(11)
Z	2	2	2	2
ρ_{calc} / (g/cm^3)	1.740	1.714	1.701	1.692
μ / mm^{-1}	3.147	3.100	3.077	3.061
F(000)	736.0	736.0	736.0	736.0
Radiation	Mo$K\alpha$ (λ = 0.71073)	MoKα (λ = 0.71073)	Mo$K\alpha$ (λ = 0.71073)	MoKα (λ = 0.71073)
2θ range for data collection / °	4.736 to 56.546	4.708 to 52.734	4.694 to 52.744	4.686 to 52.728
Index ranges	-11 ≤ h ≤ 11, -13 ≤ k ≤ 8, -16 ≤ l ≤ 21	-10 ≤ h ≤ 10, -12 ≤ k ≤ 8, -16 ≤ l ≤ 20	-10 ≤ h ≤ 10, -12 ≤ k ≤ 12, -20 ≤ l ≤ 20	-10 ≤ h ≤ 10, -12 ≤ k ≤ 12, -19 ≤ l ≤ 20
Reflections collected	10118	8953	16262	11766
R_{int} / R_{sigma}	0.0330 / 0.0390	0.0314 / 0.0343	0.0373 / 0.0255	0.0347 / 0.0314
Data/restraints/parameters	3517/0/202	2938/0/202	2963/0/202	2977/0/202
Goodness-of-fit on F^2	1.050	1.070	1.091	1.057
Final R indexes [I>=2σ (I)]	R_1 = 0.0391, wR_2 = 0.0760	R_1 = 0.0373, wR_2 = 0.0815	R_1 = 0.0358, wR_2 = 0.0812	R_1 = 0.0377, wR_2 = 0.0849
Final R indexes [all data]	R_1 = 0.0585, wR_2 = 0.0821	R_1 = 0.0514, wR_2 = 0.0870	R_1 = 0.0475, wR_2 = 0.0855	R_1 = 0.0577, wR_2 = 0.0930
Largest diff. peak/hole / (e Å^{-3})	0.79/-0.63	0.72/-0.56	0.76/-0.58	0.90/-0.60

Table S4.1 continued - Crystal data and refinement results for **A** at 325 K and 350 K.

Identification code	325(2) K	350(2) K
Empirical formula	$C_{26}H_{20}FeN_{14}Se_2$	$C_{26}H_{20}FeN_{14}Se_2$
Formula weight	742.33	742.33
Temperature / K	325(2)	350(2)
Crystal system	monoclinic	monoclinic
Space group	$P2_1/n$	$P2_1/n$
a / Å	8.6327(5)	8.6423(4)
b / Å	10.2367(6)	10.2507(4)
c / Å	16.6049(10)	16.6132(7)
β / °	93.4981(11)	93.5248(9)
V / Å^3	1464.65(15)	1468.97(11)
Z	2	2
ρ_{calc} / (g/cm^3)	1.683	1.678
μ / mm^{-1}	3.045	3.036
F(000)	736.0	736.0
Radiation	Mo*Kα* (λ = 0.71073)	MoKα (λ = 0.71073)
2θ range for data collection / °	4.676 to 52.734	4.672 to 52.746
Index ranges	-10 ≤ h ≤ 10, -12 ≤ k ≤ 8, -20 ≤ l ≤ 16	-10 ≤ h ≤ 10, -12 ≤ k ≤ 12, -19 ≤ l ≤ 20
Reflections collected	8669	14266
R_{int} / R_{sigma}	0.0338 / 0.0394	0.0379 / 0.0306
Data/restraints/parameters	2992/0/202	3004/0/202
Goodness-of-fit on F^2	1.045	1.070
Final R indexes [I>=2σ (I)]	R_1 = 0.0406, wR_2 = 0.0894	R_1 = 0.0408, wR_2 = 0.0900
Final R indexes [all data]	R_1 = 0.0720, wR_2 = 0.1041	R_1 = 0.0657, wR_2 = 0.1013
Largest diff. peak/hole / (e Å^{-3})	0.87/-0.61	0.93/-0.64

Table S4.2 - Unit cell and structural parameters for $[Fe(abpt)_2(NCSe)_2]$ polymorph **A** collected at 225 K ($\sim T_{1/2}$) during cooling (↓) and warming (↑) cycles.

Temperature	225(2) K (↓)	225(2) K (↑)
Empirical formula	$FeC_{26}H_{20}N_{14}Se_2$	$FeC_{26}H_{20}N_{14}Se_2$
Crystal system	Monoclinic	Monoclinic
Space group	*P* $2_1/n$	*P* $2_1/n$
a / Å	8.5401(5)	8.5410(5)
b / Å	10.0947(5)	10.0946(5)
c / Å	16.4597(9)	16.4604(9)
α / °	90	90
β / °	93.2083(10)	93.2069(11)
γ / °	90	90
V / Å^3	1416.76(13)	1416.96(13)
Z, Z'	2, 0.5	2, 0.5
Fe1-N7 / Å	2.032(3)	2.030(3)
Fe1-N1 / Å	2.096(2)	2.094(3)
Fe1-N2 / Å	2.027(2)	2.029(3)
V_{poly} / Å^3	11.234(8)	11.224(9)
Σ / °	59.0(6)	58.8(7)
Θ / °	229.4(11)	228.6(12)

Table S4.3 - Fe-N bond lengths for all structures, along with the distortion parameter, Σ, and the volume of the Fe octahedron, V_p.

	50(2) K	75(2) K	100(2) K	108(2) K	200(2) K	250(2) K
Fe1-N1 / Å	1.949(2)	1.951(2)	1.950(2)	1.952(2)	1.973(2)	2.098(3)
Fe1-N2 / Å	2.014(2)	2.016(2)	2.014(2)	2.015(2)	2.032(2)	2.168(3)
Fe1-N3 / Å	1.957(2)	1.957(2)	1.955(2)	1.957(2)	1.974(2)	2.086(3)
Σ[a] / º	49.6(6)	49.8(6)	49.9(6)	49.6(5)	52.3(5)	65.5(7)
V_p[b] / Å^3	10.075(7)	10.090(7)	10.067(7)	10.090(6)	10.358(7)	12.259(10)

[a] Σ, the angle distortion parameter, is the sum of the absolute value of the deviation of all 12 *cis* N-Fe-N angles from 90°. [b] V_p is the volume of the Fe octahedron calculated in Olex2.

Table S4.3 continued - Fe-N bond lengths for all structures, along with the distortion parameter, Σ, and the volume of the Fe octahedron, V_p.

	300(2) K	350(2) K
Fe1-N1 / Å	2.133(3)	2.142(4)
Fe1-N2 / Å	2.207(3)	2.213(3)
Fe1-N3 / Å	2.119(3)	2.124(3)
Σ[a] / º	69.4(7)	70.0(8)
V_p[b] / Å^3	12.839(10)	12.946(12)

[a] Σ, the angle distortion parameter, is the sum of the absolute value of the deviation of all 12 *cis* N-Fe-N angles from 90°. [b] V_p is the volume of the Fe octahedron calculated in Olex2.

Table S4.4 - Summary of the hydrogen bonding parameters in **A** as a function of temperature.

Temperature	D-H···A	D-H / Å	H···A / Å	D···A / Å	<D-H···A /°
375(2) K	N6-H6B···N7	0.87(5)	2.16(5)	2.860(5)	137(4)
	C2-H2···N4^{i}	0.93	2.80	3.580(6)	143
	N6-H6A···Se1^{ii}	0.98(5)	2.76(5)	3.563(4)	140(4)
350(2) K	N6-H6B···N7	0.86(5)	2.17(5)	2.856(5)	137(4)
	C2-H2···N4^{i}	0.93	2.79	3.575(5)	142
	N6-H6A···Se1^{ii}	1.00(5)	2.75(4)	3.554(4)	137(3)
325(2) K	N6-H6B···N7	0.89(5)	2.13(5)	2.856(5)	139(4)
	C2-H2···N4^{i}	0.93	2.79	3.571(5)	142
	N6-H6A···Se1^{ii}	0.97(5)	2.75(5)	3.547(4)	139(3)
300(2) K	N6-H6B···N7	0.84(4)	2.18(4)	2.860(4)	138(4)
	C2-H2···N4^{i}	0.93	2.78	3.559(5)	142
	N6-H6A···Se1^{ii}	1.00(4)	2.68(4)	3.541(4)	144(3)
275(2) K	N6-H6B···N7	0.86(4)	2.15(4)	2.855(4)	140(3)
	C2-H2···N4^{i}	0.93	2.75	3.530(4)	142
	N6-H6A···Se1^{ii}	0.99(4)	2.71(4)	3.535(3)	141(3)
250(2) K	N6-H6B···N7	0.85(4)	2.15(4)	2.860(4)	140(3)
	C2-H2···N4^{i}	0.94	2.69	3.477(4)	142
	N6-H6A···Se1^{ii}	1.05(4)	2.65(4)	3.519(3)	141(3)
225(2) K	N6-H6B···N7	0.86(4)	2.16(4)	2.858(4)	137(3)
	C2-H2···N4^{i}	0.93	2.54	3.313(4)	141
	N6-H6A···Se1^{ii}	0.97(4)	2.72(4)	3.502(3)	138(3)
200(2) K	N6-H6B···N7	0.90(3)	2.12(3)	2.852(3)	137(3)
	C2-H2···N4^{i}	0.95	2.39	3.181(3)	140
	N6-H6A···Se1^{ii}	1.00(3)	2.66(3)	3.490(3)	141(2)
175(2) K	N6-H6B···N7	0.90(3)	2.14(3)	2.856(3)	136(3)
	C2-H2···N4^{i}	0.95	2.36	3.145(3)	140
	N6-H6A···Se1^{ii}	0.97(2)	2.66(2)	3.484(3)	143(2)
150(2) K	N6-H6B···N7	0.92(3)	2.11(3)	2.850(3)	137(3)
	C2-H2···N4^{i}	0.95	2.35	3.136(3)	140
	N6-H6A···Se1^{ii}	0.99(3)	2.65(3)	3.479(3)	142(2)
125(2) K	N6-H6B···N7	0.94(3)	2.09(3)	2.853(3)	138(2)
	C2-H2···N4^{i}	0.95	2.35	3.132(3)	140
	N6-H6A···Se1^{ii}	0.96(5)	2.65(5)	3.476(2)	145(2)
108(2) K	N6-H6B···N7	0.90(3)	2.12(3)	2.855(3)	139(3)
	C2-H2···N4^{i}	0.95	2.35	3.134(3)	140
	N6-H6A···Se1^{ii}	0.95(3)	2.69(3)	3.476(2)	141(2)
100(2) K	N6-H6B···N7	0.92(4)	2.10(3)	2.852(4)	139(3)
	C2-H2···N4^{i}	0.95	2.34	3.135(4)	140
	N6-H6A···Se1^{ii}	0.94(3)	2.68(3)	3.470(3)	142(3)
75(2) K	N6-H6B···N7	0.93(3)	2.11(3)	2.851(3)	136(3)
	C2-H2···N4^{i}	0.95	2.34	3.132(3)	140
	N6-H6A···Se1^{ii}	0.97(3)	2.67(3)	3.469(2)	140(2)
50(2) K	N6-H6B···N7	0.92(4)	2.10(3)	2.853(3)	137(3)
	C2-H2···N4^{i}	0.95	2.35	3.134(3)	140
	N6-H6A···Se1^{ii}	0.96(3)	2.66(3)	3.465(3)	141(3)
30(2) K	N6-H6B···N7	0.91(4)	2.14(3)	2.855(4)	135(3)
	C2-H2···N4^{i}	0.95	2.35	3.133(4)	140
	N6-H6A···Se1^{ii}	0.95(4)	2.65(4)	3.467(3)	144(3)
30(2) K	N6-H6B···N7	0.91(5)	2.13(4)	2.853(4)	136(4)
LIESST HS*	C2-H2···N4^{i}	0.93	2.73	3.506(5)	142
	N6-H6A···Se1^{ii}	0.98(5)	2.69(5)	3.503(3)	140(3)

(i) 1-*x*, 1-*y*, 1-*z*; (ii) 1/2+*x*, 3/2-*y*, 1/2+*z*.

Table S4.5 - Summary of the π-π contacts in **A**.

Temperature	Plane 1	Plane 2	Centroid-centroid distance / Å	Offset / Å
375(2) K	(N2, C2-C6)	(N7, C9-C13)^{i}	3.725(2)	1.366(7)
350(2) K	(N2, C2-C6)	(N7, C9-C13)^{i}	3.710(2)	1.354(7)
325(2) K	(N2, C2-C6)	(N7, C9-C13)^{i}	3.698(2)	1.344(7)
300(2) K	(N2, C2-C6)	(N7, C9-C13)^{i}	3.688(2)	1.338(6)
275(2) K	(N2, C2-C6)	(N7, C9-C13)^{i}	3.679(2)	1.338(5)
250(2) K	(N2, C2-C6)	(N7, C9-C13)^{i}	3.678(2)	1.354(6)
225(2) K	(N2, C2-C6)	(N7, C9-C13)^{i}	3.693(2)	1.403(5)
200(2) K	(N2, C2-C6)	(N7, C9-C13)^{i}	3.707(2)	1.449(4)
175(2) K	(N2, C2-C6)	(N7, C9-C13)^{i}	3.703(2)	1.448(4)
150(2) K	(N2, C2-C6)	(N7, C9-C13)^{i}	3.692(1)	1.443(4)
125(2) K	(N2, C2-C6)	(N7, C9-C13)^{i}	3.684(1)	1.432(4)
108(2) K	(N2, C2-C6)	(N7, C9-C13)^{i}	3.682(1)	1.434(4)
100(2) K	(N2, C2-C6)	(N7, C9-C13)^{i}	3.678(2)	1.432(4)
75(2) K	(N2, C2-C6)	(N7, C9-C13)^{i}	3.670(2)	1.423(4)
50(2) K	(N2, C2-C6)	(N7, C9-C13)^{i}	3.664(2)	1.415(4)
30(2) K	(N2, C2-C6)	(N7, C9-C13)^{i}	3.663(2)	1.417(4)
30(2) K LIESST HS*	(N2, C2-C6)	(N7, C9-C13)^{i}	3.591(2)	1.263(5)

(i) 1-*x*, 2-*y*, 1-*z*;

Appendix 5

$Co(abpt)_2(NCS)_2$ and $Ni(abpt)_2(NCS)_2$: Structural Characterisation of Polymorphs A and B

Helen E. Mason, Judith A. K. Howard and Hazel A. Sparkes

Published *Acta Crystallographica C*, 2021, in publication, doi.org/10.1107/S2053229621010251.

Table S5.1 Crystal data and structure refinement for $Co(abpt)_2(NCS)_2$ Polymorphs **A** and **B** at 300(2) K.

	$Co(abpt)_2(NCS)_2$	
Identification code	Polymorph **A**	Polymorph **B**
Empirical formula	$C_{26}H_{20}CoN_{14}S_2$	$C_{26}H_{20}CoN_{14}S_2$
Formula weight	651.61	651.61
Temperature/K	300(2)	300(2)
Crystal system	monoclinic	monoclinic
Space group	$P2_1/n$	$P2_1/n$
a/Å	8.487(5)	11.5855(6)
b/Å	10.249(6)	9.5998(5)
c/Å	16.539(10)	12.8411(6)
α/°	90	90
β/°	93.419(13)	101.3000(10)
γ/°	90	90
Volume/Å^3	1435.9(14)	1400.48(12)
Z	2	2
ρ_{calc}g/cm^3	1.507	1.545
μ/mm^{-1}	0.788	0.808
F(000)	666.0	666.0
Crystal size/mm^3	0.24 × 0.16 × 0.12	0.48 × 0.22 × 0.1
Radiation	MoKα (λ = 0.71073)	MoKα (λ = 0.71073)
2Θ range for data collection/°	4.678 to 50.684	4.332 to 50.696
Index ranges	-9 ≤ h ≤ 10, -11 ≤ k ≤ 12, -19 ≤ l ≤ 14	-13 ≤ h ≤ 13, -11 ≤ k ≤ 10, -9 ≤ l ≤ 15
Reflections collected	7130	7562
Independent reflections	2605 [R_{int} = 0.0872, R_{sigma} = 0.0967]	2565 [R_{int} = 0.0311, R_{sigma} = 0.0345]
Data/restraints/parameters	2605/0/202	2565/0/202
Goodness-of-fit on F^2	1.024	1.030
Final R indexes [I>=2σ (I)]	R_1 = 0.0593, wR_2 = 0.1397	R_1 = 0.0335, wR_2 = 0.0735
Final R indexes [all data]	R_1 = 0.1258, wR_2 = 0.1660	R_1 = 0.0486, wR_2 = 0.0791
Largest diff. peak/hole / e Å^{-3}	0.36/-0.47	0.22/-0.27

Appendix 6

No Appendix for Chapter 6.

Appendix 7

Structural studies of *N*-(methoxysalicylidene)-fluoroaniline, *N*-(methoxysalicylidene)-chloroaniline and *N*-(methoxysalicylidene)-bromoaniline derivatives

Helen E. Mason, Jane L. R. Yates, Rachael J. Potts, Matthias J. Gutmann, Judith A. K. Howard and Hazel A. Sparkes

Published *Acta Crystallographica B*, 2021, in publication, doi.org/10.1107/S2052520621009835.

Table S7.1 - Crystal data and structure refinement for **1-F** to **9-F**.

Identification code	**1-F**	**2-F**	**3-F**	**4-F**
Empirical formula	$C_{14}H_{12}FNO_2$	$C_{14}H_{12}FNO_2$	$C_{14}H_{12}FNO_2$	$C_{14}H_{12}FNO_2$
Formula weight	245.25	245.25	245.25	245.25
Temperature/K	120(2)	120(2)	120(2)	120.15
Crystal system	orthorhombic	orthorhombic	monoclinic	orthorhombic
Space group	$P2_12_12_1$	$Pbca$	$P2_1/c$	$Pna2_1$
a/Å	5.0834(2)	6.2970(8)	20.3838(10)	19.3411(12)
b/Å	12.4697(5)	25.465(3)	4.6633(2)	4.9865(3)
c/Å	18.1059(8)	14.3055(14)	12.6117(6)	12.2219(8)
α/°	90	90	90	90
β/°	90	90	106.7470(10)	90
γ/°	90	90	90	90
Volume/Å^3	1147.71(8)	2294.0(5)	1147.97(9)	1178.73(13)
Z	4	8	4	4
ρ_{calc}g/cm^3	1.419	1.420	1.419	1.382
μ/mm^{-1}	0.106	0.106	0.106	0.103
F(000)	512.0	1024.0	512.0	512.0
Crystal size/mm^3	0.4 × 0.26 × 0.2	0.41 × 0.28 × 0.03	0.44 × 0.3 × 0.16	0.46 × 0.26 × 0.14
Radiation	MoKα (λ = 0.71073)	MoKα (λ = 0.71073)	MoKα (λ = 0.71073)	MoKα (λ = 0.71073)
2θ range for data collection/°	3.966 to 56.55	5.696 to 51.364	4.174 to 56.564	4.212 to 56.564
Index ranges	-6 ≤ h ≤ 6, -16 ≤ k ≤ 16, -24 ≤ l ≤ 24	-7 ≤ h ≤ 7, -31 ≤ k ≤ 29, -17 ≤ l ≤ 17	-27 ≤ h ≤ 27, -6 ≤ k ≤ 6, -16 ≤ l ≤ 16	-25 ≤ h ≤ 25, -6 ≤ k ≤ 6, -16 ≤ l ≤ 16
Reflections collected	15619	8769	12140	12283
Independent reflections	2845 [R_{int} = 0.0381, R_{sigma} = 0.0259]	2179 [R_{int} = 0.1099, R_{sigma} = 0.1057]	2834 [R_{int} = 0.0291, R_{sigma} = 0.0238]	2930 [R_{int} = 0.0267, R_{sigma} = 0.0217]
Data/restraints/parameters	2845/0/168	2179/0/168	2834/0/168	2930/1/168
Goodness-of-fit on F^2	1.036	1.110	1.065	1.044
Final R indexes [I>=2σ (I)]	R_1 = 0.0337, wR_2 = 0.0835	R_1 = 0.0845, wR_2 = 0.1122	R_1 = 0.0383, wR_2 = 0.0985	R_1 = 0.0302, wR_2 = 0.0747
Final R indexes [all data]	R_1 = 0.0427, wR_2 = 0.0900	R_1 = 0.1369, wR_2 = 0.1289	R_1 = 0.0499, wR_2 = 0.1043	R_1 = 0.0351, wR_2 = 0.0776
Largest diff. peak/hole / e Å^{-3}	0.20/-0.16	0.27/-0.28	0.25/-0.21	0.18/-0.18

Table S7.1 continued - Crystal data and structure refinement for **1-F** to **9-F**.

Identification code	**5-F**	**6-F**	**7-F**	**8-F**
Empirical formula	$C_{14}H_{12}FNO_2$	$C_{14}H_{12}FNO_2$	$C_{14}H_{12}FNO_2$	$C_{14}H_{12}FNO_2$
Formula weight	245.25	245.25	245.25	245.25
Temperature/K	120(2)	120(2)	120(2)	120(2)
Crystal system	monoclinic	monoclinic	monoclinic	monoclinic
Space group	$P2_1/c$	$P2_1/c$	$P2_1/c$	$P2_1/c$
a/Å	3.8058(3)	13.1230(9)	11.3352(7)	3.8354(3)
b/Å	10.6818(8)	13.2386(9)	12.0366(7)	10.6493(7)
c/Å	27.574(2)	6.8116(4)	9.3002(6)	27.9772(19)
α/°	90	90	90	90
β/°	91.609(2)	103.690(2)	114.1750(10)	90.8060(10)
γ/°	90	90	90	90
Volume/Å^3	1120.53(15)	1149.76(13)	1157.61(12)	1142.60(14)
Z	4	4	4	4
ρ_{calc}g/cm^3	1.454	1.417	1.407	1.426
μ/mm^{-1}	0.109	0.106	0.105	0.107
F(000)	512.0	512.0	512.0	512.0
Crystal size/mm^3	0.2 × 0.16 × 0.06	0.38 × 0.24 × 0.18	0.4 × 0.3 × 0.26	0.46 × 0.14 × 0.12
Radiation	MoKα (λ = 0.71073)	MoKα (λ = 0.71073)	MoKα (λ = 0.71073)	MoKα (λ = 0.71073)
2θ range for data collection/°	2.956 to 51.362	3.194 to 51.354	3.938 to 56.564	2.912 to 52.744
Index ranges	-4 ≤ h ≤ 4, -13 ≤ k ≤ 13, -33 ≤ l ≤ 33	-16 ≤ h ≤ 15, -14 ≤ k ≤ 16, -6 ≤ l ≤ 8	-15 ≤ h ≤ 15, -16 ≤ k ≤ 16, -12 ≤ l ≤ 12	-4 ≤ h ≤ 4, -13 ≤ k ≤ 13, -34 ≤ l ≤ 34
Reflections collected	10327	6467	12782	10926
Independent reflections	2129 [R_{int} = 0.0653, R_{sigma} = 0.0519]	2183 [R_{int} = 0.0359, R_{sigma} = 0.1086]	2872 [R_{int} = 0.0891, R_{sigma} = 0.0525]	2336 [R_{int} = 0.0443, R_{sigma} = 0.0354]
Data/restraints/parameters	2129/0/168	2183/0/174	2872/0/168	2336/0/168
Goodness-of-fit on F^2	1.025	1.075	1.043	1.035
Final R indexes [I>=2σ (I)]	R_1 = 0.0514, wR_2 = 0.1096	R_1 = 0.0472, wR_2 = 0.1310	R_1 = 0.0445, wR_2 = 0.1136	R_1 = 0.0499, wR_2 = 0.1097
Final R indexes [all data]	R_1 = 0.0916, wR_2 = 0.1262	R_1 = 0.0708, wR_2 = 0.1486	R_1 = 0.0642, wR_2 = 0.1249	R_1 = 0.0723, wR_2 = 0.1182
Largest diff. peak/hole / e Å^{-3}	0.23/-0.21	0.15/-0.24	0.40/-0.20	0.18/-0.22

Table S7.1 continued - Crystal data and structure refinement for **1-F** to **9-F**.

Identification code	**9-F**
Empirical formula	$C_{14}H_{12}FNO_2$
Formula weight	245.25
Temperature/K	120(2)
Crystal system	monoclinic
Space group	*C*2/*c*
a/Å	28.1425(12)
b/Å	6.9311(3)
c/Å	12.8535(5)
α/°	90
β/°	113.2170(10)
γ/°	90
Volume/Å^3	2304.15(17)
Z	8
ρ_{calc}g/cm^3	1.414
μ/mm^{-1}	0.106
F(000)	1024.0
Crystal size/mm^3	0.42 × 0.32 × 0.3
Radiation	MoKα (λ = 0.71073)
2θ range for data collection/°	3.15 to 56.562
Index ranges	-37 ≤ h ≤ 37, -9 ≤ k ≤ 8, -16 ≤ l ≤ 17
Reflections collected	12612
Independent reflections	2865 [R_{int} = 0.0333, R_{sigma} = 0.0259]
Data/restraints/parameters	2865/0/168
Goodness-of-fit on F^2	1.039
Final R indexes [I>=2σ (I)]	R_1 = 0.0408, wR_2 = 0.1044
Final R indexes [all data]	R_1 = 0.0553, wR_2 = 0.1130
Largest diff. peak/hole / e Å^{-3}	0.26/-0.18

Table S7.2 - Crystal data and structure refinement for **1-Cl** to **9-Cl**.

Identification code	**1-Cl**	**2-Cl**	**3-Cl**	**4-Cl**
Empirical formula	$C_{14}H_{12}ClNO_2$	$C_{14}H_{12}ClNO_2$	$C_{14}H_{12}ClNO_2$	$C_{14}H_{12}ClNO_2$
Formula weight	261.70	261.70	261.70	261.70
Temperature/K	120(2)	120(2)	120(2)	100(2)
Crystal system	orthorhombic	monoclinic	monoclinic	orthorhombic
Space group	$Pna2_1$	$C2/c$	$P2_1/c$	$P2_12_12_1$
a/Å	6.4045(2)	22.2996(14)	13.1915(3)	4.9119(2)
b/Å	14.5211(4)	7.2002(5)	8.2973(2)	12.4251(5)
c/Å	12.9892(3)	16.4795(11)	11.9180(2)	19.5142(7)
α/°	90	90	90	90
β/°	90	113.2315(9)	112.5479(12)	90
γ/°	90	90	90	90
Volume/Å^3	1208.00(6)	2431.4(3)	1204.76(5)	1190.97(8)
Z	4	8	4	4
ρ_{calc}g/cm^3	1.439	1.430	1.443	1.460
μ/mm^{-1}	0.308	0.306	0.309	0.313
F(000)	544.0	1088.0	544.0	544.0
Crystal size/mm^3	0.44 × 0.28 × 0.19	0.42 × 0.41 × 0.32	0.35 × 0.34 × 0.22	0.25 × 0.2 × 0.15
Radiation	MoKα (λ = 0.71073)	MoKα (λ = 0.71073)	MoKα (λ = 0.71073)	MoKα (λ = 0.71073)
2θ range for data collection/°	4.208 to 56.08	3.976 to 56.176	3.342 to 56.134	3.886 to 56.376
Index ranges	-7 ≤ h ≤ 8, -19 ≤ k ≤ 19, -17 ≤ l ≤ 17	-29 ≤ h ≤ 29, -9 ≤ k ≤ 5, -21 ≤ l ≤ 21	-17 ≤ h ≤ 14, -10 ≤ k ≤ 10, -14 ≤ l ≤ 15	-6 ≤ h ≤ 6, -15 ≤ k ≤ 16, -25 ≤ l ≤ 25
Reflections collected	15606	10887	10548	10919
Independent reflections	2912 [R_{int} = 0.0289, R_{sigma} = 0.0224]	2956 [R_{int} = 0.0174, R_{sigma} = 0.0162]	2920 [R_{int} = 0.0271, R_{sigma} = 0.0272]	2927 [R_{int} = 0.0315, R_{sigma} = 0.0309]
Data/restraints/parameters	2912/1/168	2956/0/168	2920/0/168	2927/0/169
Goodness-of-fit on F^2	1.053	1.037	1.045	1.046
Final R indexes [I>=2σ (I)]	R_1 = 0.0249, wR_2 = 0.0600	R_1 = 0.0296, wR_2 = 0.0788	R_1 = 0.0292, wR_2 = 0.0754	R_1 = 0.0294, wR_2 = 0.0676
Final R indexes [all data]	R_1 = 0.0273, wR_2 = 0.0612	R_1 = 0.0343, wR_2 = 0.0823	R_1 = 0.0368, wR_2 = 0.0788	R_1 = 0.0352, wR_2 = 0.0697
Largest diff. peak/hole / e Å^{-3}	0.21/-0.15	0.31/-0.22	0.32/-0.20	0.22/-0.22
Flack parameter	0.028(17)	-	-	0.26(7)

Table S7.2 continued - Crystal data and structure refinement for **1-Cl** to **9-Cl**.

Identification code	**5-Cl**	**6-Cl**	**7-Cl**	**8-Cl**
Empirical formula	$C_{14}H_{12}ClNO_2$	$C_{14}H_{12}ClNO_2$	$C_{14}H_{12}NO_2Cl$	$C_{14}H_{12}NO_2Cl$
Formula weight	261.70	261.70	261.70	261.70
Temperature/K	150(2)	100(2)	120(2)	120(2)
Crystal system	monoclinic	monoclinic	monoclinic	monoclinic
Space group	*C*2/*c*	*Pc*	$P2_1/c$	$P2_1/c$
a/Å	14.1997(4)	12.5233(5)	4.8166(4)	5.5216(11)
b/Å	6.5840(2)	4.4479(2)	21.3693(16)	8.8865(18)
c/Å	26.2190(7)	11.8828(6)	23.8639(16)	25.127(5)
α/°	90	90	90	90
β/°	102.2648(19)	113.577(3)	92.844(3)	95.001(5)
γ/°	90	90	90	90
Volume/Å^3	2395.29(12)	606.65(5)	2453.2(3)	1228.2(4)
Z	8	2	8	4
ρ_{calc}g/cm^3	1.451	1.433	1.417	1.415
μ/mm^{-1}	0.311	0.307	0.304	0.303
F(000)	1088.0	272.0	1088.0	544.0
Crystal size/mm^3	0.67 × 0.49 × 0.20	0.25 × 0.18 × 0.12	0.48 × 0.28 × 0.08	0.28 × 0.08 × 0.03
Radiation	MoKα (λ = 0.71073)	MoKα (λ = 0.71073)	MoKα (λ = 0.71073)	MoKα (λ = 0.71073)
2θ range for data collection/°	3.18 to 56.016	6.88 to 56.01	2.56 to 52.74	3.254 to 50.06
Index ranges	-16 ≤ h ≤ 18, -8 ≤ k ≤ 8, -34 ≤ l ≤ 34	-15 ≤ h ≤ 16, -5 ≤ k ≤ 5, -15 ≤ l ≤ 11	-5 ≤ h ≤ 6, -26 ≤ k ≤ 26, -29 ≤ l ≤ 29	-6 ≤ h ≤ 6, -10 ≤ k ≤ 10, -29 ≤ l ≤ 29
Reflections collected	10346	5290	24571	11727
Independent reflections	2895 [R_{int} = 0.0256, R_{sigma} = 0.0248]	2268 [R_{int} = 0.0247, R_{sigma} = 0.0325]	4976 [R_{int} = 0.0512, R_{sigma} = 0.0409]	2175 [R_{int} = 0.0686, R_{sigma} = 0.0574]
Data/restraints/parameters	2895/0/168	2268/2/168	4976/0/335	2175/0/168
Goodness-of-fit on F^2	1.051	1.049	1.067	1.074
Final R indexes [I>=2σ (I)]	R_1 = 0.0352, wR_2 = 0.0856	R_1 = 0.0298, wR_2 = 0.0680	R_1 = 0.0439, wR_2 = 0.0842	R_1 = 0.0648, wR_2 = 0.1683
Final R indexes [all data]	R_1 = 0.0477, wR_2 = 0.0916	R_1 = 0.0344, wR_2 = 0.0704	R_1 = 0.0619, wR_2 = 0.0892	R_1 = 0.0872, wR_2 = 0.1846
Largest diff. peak/hole / e Å^{-3}	0.32/-0.22	0.23/-0.19	0.25/-0.25	0.56/-0.36
Flack parameter	-	0.13(4)	-	-

Table S7.2 continued - Crystal data and structure refinement for **1-Cl** to **9-Cl**.

Identification code	**9-Cl**
Empirical formula	$C_{14}H_{12}NO_2Cl$
Formula weight	261.70
Temperature/K	120(2)
Crystal system	monoclinic
Space group	$P2_1/c$
a/Å	21.2023(12)
b/Å	4.6591(3)
c/Å	12.1240(7)
α/°	90
β/°	93.615(2)
γ/°	90
Volume/Å^3	1195.27(12)
Z	4
ρ_{calc}g/cm^3	1.454
μ/mm^{-1}	0.312
F(000)	544.0
Crystal size/mm^3	0.33 × 0.11 × 0.08
Radiation	MoKα (λ = 0.71073)
2θ range for data collection/°	3.85 to 52.744
Index ranges	-26 ≤ h ≤ 23, -5 ≤ k ≤ 5, -15 ≤ l ≤ 15
Reflections collected	7498
Independent reflections	2429 [R_{int} = 0.0277, R_{sigma} = 0.0299]
Data/restraints/parameters	2429/0/168
Goodness-of-fit on F^2	1.076
Final R indexes [I>=2σ (I)]	R_1 = 0.0379, wR_2 = 0.0985
Final R indexes [all data]	R_1 = 0.0472, wR_2 = 0.1063
Largest diff. peak/hole / e Å^{-3}	0.33/-0.21

Table S7.3 - Crystal data and structure refinement for **1-Br** to **9-Br**.

Identification code	**1-Br**	**2-Br**	**3-Br**	**4-Br**
Empirical formula	$C_{14}H_{12}NO_2Br$	$C_{14}H_{12}NO_2Br$	$C_{14}H_{12}NO_2Br$	$C_{14}H_{12}NO_2Br$
Formula weight	306.16	306.16	306.16	306.16
Temperature/K	120(2)	120(2)	120(2)	120(2)
Crystal system	orthorhombic	monoclinic	monoclinic	monoclinic
Space group	*Pna*2$_1$	*C*2/*c*	*P*2$_1$/*c*	*P*2$_1$/*c*
a/Å	6.2974(11)	22.351(3)	13.290(2)	12.538(2)
b/Å	14.718(2)	7.3950(11)	8.5162(13)	4.8315(9)
c/Å	13.367(2)	16.267(3)	11.9068(18)	21.010(4)
α/°	90	90	90	90
β/°	90	112.973(2)	113.514(3)	103.043(3)
γ/°	90	90	90	90
Volume/Å^3	1239.0(4)	2475.4(6)	1235.7(3)	1239.9(4)
Z	4	8	4	4
ρ_{calc}g/cm^3	1.641	1.643	1.646	1.640
μ/mm^{-1}	3.310	3.314	3.319	3.308
F(000)	616.0	1232.0	616.0	616.0
Crystal size/mm^3	0.26 × 0.18 × 0.07	0.35 × 0.24 × 0.14	0.3 × 0.2 × 0.06	0.45 × 0.13 × 0.1
Radiation	MoKα (λ = 0.71073)	MoKα (λ = 0.71073)	MoKα (λ = 0.71073)	MoKα (λ = 0.71073)
2θ range for data collection/°	4.116 to 56.56	3.958 to 54.192	3.342 to 54.204	3.334 to 54.196
Index ranges	-8 ≤ h ≤ 8, -19 ≤ k ≤ 15, -12 ≤ l ≤ 17	-28 ≤ h ≤ 28, -9 ≤ k ≤ 9, -20 ≤ l ≤ 19	-17 ≤ h ≤ 15, -10 ≤ k ≤ 7, -14 ≤ l ≤ 15	-16 ≤ h ≤ 16, -6 ≤ k ≤ 6, -26 ≤ l ≤ 26
Reflections collected	7921	12177	7467	11740
Independent reflections	2339 [R_{int} = 0.0423, R_{sigma} = 0.0483]	2729 [R_{int} = 0.0349, R_{sigma} = 0.0286]	2717 [R_{int} = 0.0356, R_{sigma} = 0.0418]	2732 [R_{int} = 0.0440, R_{sigma} = 0.0370]
Data/restraints/parameters	2339/1/169	2729/0/168	2717/0/168	2732/0/168
Goodness-of-fit on F^2	1.023	1.030	1.026	1.075
Final R indexes [I>=2σ (I)]	R_1 = 0.0291, wR_2 = 0.0552	R_1 = 0.0250, wR_2 = 0.0543	R_1 = 0.0290, wR_2 = 0.0625	R_1 = 0.0311, wR_2 = 0.0638
Final R indexes [all data]	R_1 = 0.0407, wR_2 = 0.0589	R_1 = 0.0358, wR_2 = 0.0576	R_1 = 0.0412, wR_2 = 0.0669	R_1 = 0.0475, wR_2 = 0.0685
Largest diff. peak/hole / e Å^{-3}	0.35/-0.33	0.36/-0.38	0.36/-0.37	0.45/-0.48

Table S7.3 continued - Crystal data and structure refinement for **1-Br** to **9-Br**.

Identification code	**5-Br**	**6-Br**	**7-Br**	**8-Br**
Empirical formula	$C_{14}H_{12}NO_2Br$	$C_{14}H_{12}BrNO_2$	$C_{14}H_{12}BrNO_2$	$C_{14}H_{12}NO_2Br$
Formula weight	306.16	306.16	306.16	306.16
Temperature/K	120(2)	120(2)	120(2)	120(2)
Crystal system	orthorhombic	monoclinic	orthorhombic	orthorhombic
Space group	$Pca2_1$	Pc	$P2_12_12_1$	$Pna2_1$
a/Å	13.823(4)	12.547(4)	4.8326(10)	6.1895(12)
b/Å	14.140(4)	4.4109(16)	12.544(3)	7.0146(13)
c/Å	6.3118(18)	11.895(4)	20.346(4)	28.557(5)
α/°	90	90	90	90
β/°	90	113.687(5)	90	90
γ/°	90	90	90	90
Volume/Å^3	1233.7(6)	602.9(4)	1233.4(4)	1239.9(4)
Z	4	2	4	4
ρ_{calc}g/cm^3	1.648	1.687	1.649	1.640
μ/mm^{-1}	3.324	3.402	3.325	3.308
F(000)	616.0	308.0	616.0	616.0
Crystal size/mm^3	0.3 × 0.08 × 0.03	0.22 × 0.09 × 0.04	0.32 × 0.06 × 0.02	0.4 × 0.31 × 0.18
Radiation	MoKα (λ = 0.71073)	MoKα (λ = 0.71073)	MoKα (λ = 0.71073)	MoKα (λ = 0.71073)
2θ range for data collection/°	2.88 to 54.166	3.544 to 51.354	3.814 to 51.362	5.706 to 52.734
Index ranges	-17 ≤ h ≤ 16, -11 ≤ k ≤ 18, -8 ≤ l ≤ 7	-15 ≤ h ≤ 15, -5 ≤ k ≤ 5, -14 ≤ l ≤ 14	-5 ≤ h ≤ 5, -15 ≤ k ≤ 15, -24 ≤ l ≤ 24	-7 ≤ h ≤ 7, -8 ≤ k ≤ 8, -34 ≤ l ≤ 34
Reflections collected	7073	4965	11274	10666
Independent reflections	2474 [R_{int} = 0.0567, R_{sigma} = 0.0738]	2292 [R_{int} = 0.0596, R_{sigma} = 0.0872]	2345 [R_{int} = 0.0796, R_{sigma} = 0.0669]	2444 [R_{int} = 0.0283, R_{sigma} = 0.0361]
Data/restraints/parameters	2474/1/166	2292/2/166	2345/0/169	2444/1/169
Goodness-of-fit on F^2	1.008	1.082	1.104	1.089
Final R indexes [I>=2σ (I)]	R_1 = 0.0382, wR_2 = 0.0720	R_1 = 0.0558, wR_2 = 0.1267	R_1 = 0.0418, wR_2 = 0.0721	R_1 = 0.0188, wR_2 = 0.0422
Final R indexes [all data]	R_1 = 0.0669, wR_2 = 0.0827	R_1 = 0.0670, wR_2 = 0.1327	R_1 = 0.0632, wR_2 = 0.0779	R_1 = 0.0212, wR_2 = 0.0431
Largest diff. peak/hole / e Å^{-3}	0.52/-0.43	2.10/-1.70	0.48/-0.85	0.31/-0.31

Table S7.3 continued - Crystal data and structure refinement for **1-Br** to **9-Br**.

Identification code	**9-Br 220 K**	**9-Br 120 K**
Empirical formula	$C_{14}H_{12}BrNO_2$	$C_{14}H_{12}NO_2Br$
Formula weight	306.16	306.16
Temperature/K	220(2)	120(2)
Crystal system	monoclinic	monoclinic
Space group	*Pc*	*Cc*
a/Å	14.077(3)	27.874(5)
b/Å	6.8915(15)	6.8640(12)
c/Å	6.5365(13)	6.4840(12)
α/°	90	90
β/°	98.320(4)	95.091(4)
γ/°	90	90
Volume/Å^3	627.5(2)	1235.7(4)
Z	2	4
ρ_{calc}g/cm^3	1.620	1.646
μ/mm^{-1}	3.268	3.319
F(000)	308.0	616.0
Crystal size/mm^3	0.16 × 0.1 × 0.08	0.16 × 0.1 × 0.08
Radiation	MoKα (λ = 0.71073)	MoKα (λ = 0.71073)
2θ range for data collection/°	5.85 to 54.202	2.934 to 52.726
Index ranges	-13 ≤ h ≤ 18, -8 ≤ k ≤ 8, -8 ≤ l ≤ 5	-19 ≤ h ≤ 34, -8 ≤ k ≤ 8, -7 ≤ l ≤ 8
Reflections collected	3788	3511
Independent reflections	1818 [R_{int} = 0.0485, R_{sigma} = 0.0791]	1623 [R_{int} = 0.0479, R_{sigma} = 0.0708]
Data/restraints/parameters	1818/2/169	1623/2/169
Goodness-of-fit on F^2	1.015	1.119
Final R indexes [I>=2σ (I)]	R_1 = 0.0370, wR_2 = 0.0694	R_1 = 0.0418, wR_2 = 0.0922
Final R indexes [all data]	R_1 = 0.0642, wR_2 = 0.0781	R_1 = 0.0492, wR_2 = 0.0960
Largest diff. peak/hole / e Å^{-3}	0.43/-0.46	1.00/-0.57

Table S7.4 - C-H···O interactions in **1-F** to **9-F**.

Compound	Interaction	H···O(Å)	C···O (Å)	C-H···O (°)
1-**F**	C13-H13···O1^{i}	2.494	3.329(3)	147
2-**F**	C12-H12···O1^{ii}	2.490	3.438(5)	176
	C14-H14···O2^{iii}	2.572	3.405(4)	147
3-**F**	C1-H1B···O1^{iv}	2.516	3.471(2)	165
	C6-H6···O2^{v}	2.624	3.487(2)	151
4-**F**	C6-H6···O1^{vi}	2.690	3.470(3)	140
	C8-H8···O1^{vi}	2.665	3.436(2)	139
5-**F**	C1-H1B···O1^{vii}	2.608	3.490(3)	150
6-**F**	C1-H1B···O2^{viii}	2.621	3.537(2)	156
	C10-H10···O2^{ix}	2.533	3.383(2)	149
	C12-H12···O1^{x}	2.383	3.310(3)	165
7-**F**	C13-H13···O1^{xi}	2.486	3.400(2)	161
	C13-H13···O2^{xi}	2.671	3.257(2)	120
	C14-H14···O2^{xi}	2.698	3.282(2)	120
8-**F**	C1-H1A···O1^{xii}	2.641	3.531(3)	151
9-**F**	C10-H10···O2^{xiii}	2.605	3.500(2)	157
	C13-H13···O1^{xiv}	2.555	3.432(2)	154

(i) 1-x, -½+y, 3/2-z, (ii) 3/2-x, -½+y, +z, (iii) 1+x, +y, +z, (iv) 1-x, -½+y, 3/2-z, (v) +x, -½-y, ½+z, (vi) 3/2-x, ½+y, ½+z, (vii) –x, -y, 1-z, (viii) –x, 1-y, 1-z, (ix) +x, +y, -1+z, (x) 1+x, +y, +z, (xi) –x, 1-y, -z, (xii) 1-x, 1-y, -z, (xiii) +x, -1+y, +z, (xiv) –½+x, ½-y, -½+z

Table S7.5 - C-H···O interactions in **1-Cl** to **9-Cl**.

Compound	Interaction	H···O(Å)	C···O (Å)	C-H···O (°)
1-**Cl**	C13-H13···O1^{i}	2.576	3.497 (3)	164
	C13-H13···O2^{i}	2.639	3.379(3)	135
2-**Cl**	C3-H3···O2^{ii}	2.756	3.705(2)	177
	C5-H5···O1^{iii}	2.710	3.481(2)	139
	C11-H11···O1^{iv}	2.752	3.564(2)	144
3-**Cl**	C8-H8···O2^{v}	2.520	3.458(1)	169
	C14-H14···O2^{v}	2.628	3.443(1)	144
	C12-H12···O1^{vi}	2.704	3.242(2)	117
4-**Cl**	C1-H1A···O2^{vii}	2.606	3.445(3)	146
	C13-H13···O1^{viii}	2.596	3.324(3)	135
5-**Cl**	C1-H1C···O1^{ix}	2.624	3.350(2)	131
6-**Cl**	C6-H6···O2^{x}	2.712	3.476(3)	138
	C8-H8···O2^{x}	2.476	3.289(3)	144
7-**Cl**	C6-H6···O3^{xi}	2.718	3.596(3)	154
	C10-H10···O4^{xii}	2.578	3.199(3)	123
	C11-H11···O4^{xii}	2.630	3.220(3)	121
	C25-H25···O1^{xiii}	2.561	3.476(3)	162
8-**Cl**	C1-H1C···O1^{xiv}	2.653	3.431(5)	137
	C11-H11···O2^{xv}	2.613	3.336(5)	133
9-**Cl**	C1-H1B···O1^{xvi}	2.485	3.432(2)	162
	C3-H3···O1^{xvii}	2.633	3.449(2)	144
	C6-H6···O2^{xviii}	2.612	3.431(2)	145
	C8-H8···O2^{xviii}	2.567	3.398(2)	146

(i) 2-x, 1-y, -½+z, (ii) 1-x, -y, 1-z, (iii) ½-x, ½+y, ½-z, (iv) ½+x, ½+y, +z, (v) +x, 3/2-y, -½+z, (vi) -1+x, 3/2-y, -½+z, (vii) -1+x, +y, +z, (viii) 1-x, -½+y, ½-z, (ix) ½-x, 3/2-y, 1-z, (x) +x, 1-y, -½+z, (xi) 2-x, 1-y, 1-z, (xii) 1-x, 1-y, 1-z (xiii) 1-x, -½+y, 3/2-z, (xiv) 2-x, 1-y, 1-z, (xv) –x, -½+y, 3/2-z, (xvi) –x, -½+y, ½-z, (xvii) x, -½-y, ½+z, (xviii) x, ½-y, -½+z

Table S7.6 - C-H···O interactions in **1-Br** to **9-Br**.

Compound	Interaction	H···O(Å)	C···O (Å)	C-H···O (°)
1-**Br**	C13-H13···O1^{i}	2.587	3.498(5)	161
	C13-H13···O2^{i}	2.647	3.413(5)	138
2-**Br**	C5-H5···O1^{ii}	2.674	3.447(2)	139
3-**Br**	C8-H8···O2^{iii}	2.517	3.457(3)	170
4-**Br**	C13-H13···O1^{iv}	2.692	3.219(3)	116
5-**Br**	C14-H14···O2^{v}	2.611	3.523(7)	161
6-**Br**	C6-H6···O2^{vi}	2.711	3.326(13)	144
	C8-H8···O2^{vi}	2.508	3.322(13)	144
7-**Br**	C1-H1A···O2^{vii}	2.654	3.437(9)	137
	C11-H11···O1^{viii}	2.428	3.296(9)	152
8-**Br**	C1-H1A···O1^{ix}	2.704	3.488(4)	137
9-**Br**	C10-H10···O2^{x}	2.421	3.247(11)	145

(i) 1-x, 1-y, ½+z, (ii) 3/2-x, -½+y, ½-z, (iii) +x, ½-y, -½+z, (iv) 1-x, 1-y, -z, (v) +x, +y, 1+z, (vi) x, -y, ½+z, (vii) -1+x, +y, +z, (viii) 1-x, ½+y, 3/2-z, (iv) ½+x. ½-y, +z, (x) +x, +y, -1+z

Table S7.7 - C-H···F short contacts in **1-F** to **9-F**.

Compound	Interaction	H···F(Å)	C···F (Å)	C-H···F (°)
1-F	C5-H5···F1^{i}	2.590	3.250(2)	127
2-F	C11-H11···F1^{ii}	2.557	3.500(4)	172
	C5-H5···F1^{iii}	2.583	3.395(4)	144
3-F	C14-H14···F1^{iv}	2.586	3.063(1)	111
4-F	C13-H13···F1^{v}	2.639	3.398(3)	137
5-F	C1-H1C···F1^{vi}	2.460	3.439(3)	177
	C12-H12···F1^{vii}	2.627	3.449(3)	145
6-F Disordered F	C1-H1C···F1B^{viii}	2.430	3.106(3)	127
	C14-H14···F1A^{ix}	2.579	3.243(3)	127
7-F	C4-H4···F1^{x}	2.472	3.421(2)	178
8-F	C13-H13···F1^{xi}	2.634	3.310(2)	130
9-F	C4-H4···F1^{xii}	2.612	3.513(2)	159
	C1-H1C···F1B^{xiii}	2.582	3.321(2)	132

(i) 2-x, -½+y, 3/2-z, (ii) 1-x, 1-y, 1-z, (iii) ½+x, 3/2-y, 1-z, (iv) +x, ½-y, ½+z, (v) 1-x, 3-y, ½+z, (vi) –x, ½+y, ½-z, (vii) 1-x, -y, -z, (viii) -1+x, +y, -1+z, (ix) +x, +y, 1+z, (x) 1+x, 3/2-y, 3/2+z , (xi) 2-x, 1-y, 1-z, (xii) ½+x, ½-y, ½+z, (xiii) ½+x, -½-y, ½+z.

Table S7.8 - π-π interactions identified within the 27 compounds studied.

Compound	Plane 1	Plane 2	Centroid-centroid distance (Å)	Shift distance (Å)
5-F	C2-C7	C2-C7^{i}	3.806	1.626
	C9-C14	C9-C14^{i}	3.806	1.699
6-F	C2-C7	C2-C7^{ii}	3.804	1.537
	C9-C14	C9-C14^{iii}	3.957	1.996
8-F	C2-C7	C2-C7^{i}	3.835	1.683
	C9-C14	C9-C14^{i}	3.835	1.658
1-Cl	C2-C7	C9-C14^{iv}	3.641	1.263
3-Cl	C2-C7	C2-C7^{iii}	3.825	1.789
5-Cl	C2-C7	C9-C14^{v}	3.750	1.339
1-Br	C2-C7	C9-C14^{iv}	3.672	1.471
3-Br	C2-C7	C2-C7^{vi}	3.808	1.676
5-Br	C2-C7	C9-C14^{vii}	3.867	1.314

(i) -1+x, +y, +z and 1+x, +y, +z, (ii) –x, 1-y, 1-z, (iii) 1-x, 1-y, 1-z, (iv) -1+x, +y, +z, (v) 1-x, +y, ½-z, (vi) 2-x, -y, 1-z, (vii) 1-x, 1-y, -½+z

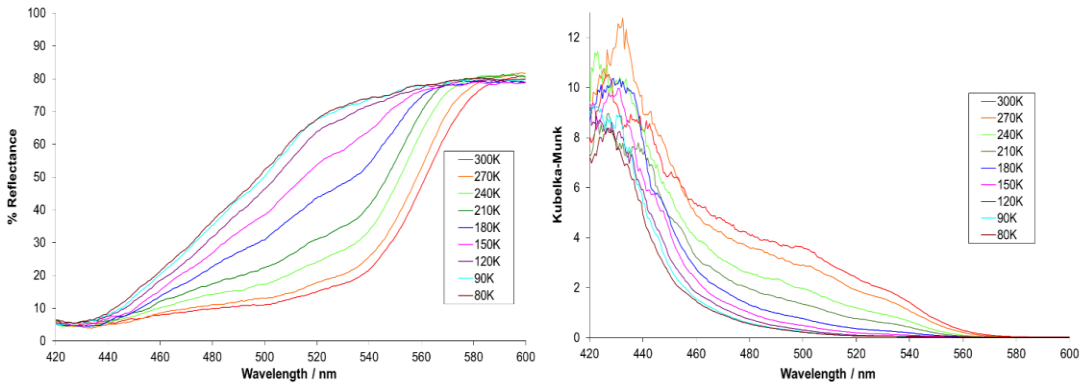

Figure S7.1 - Variable temperature diffuse reflectance spectra between 300 and 80K for **1-Br**, illustrated as wavelength versus (left) % reflectance and (right) the Kubelka-Munk function.

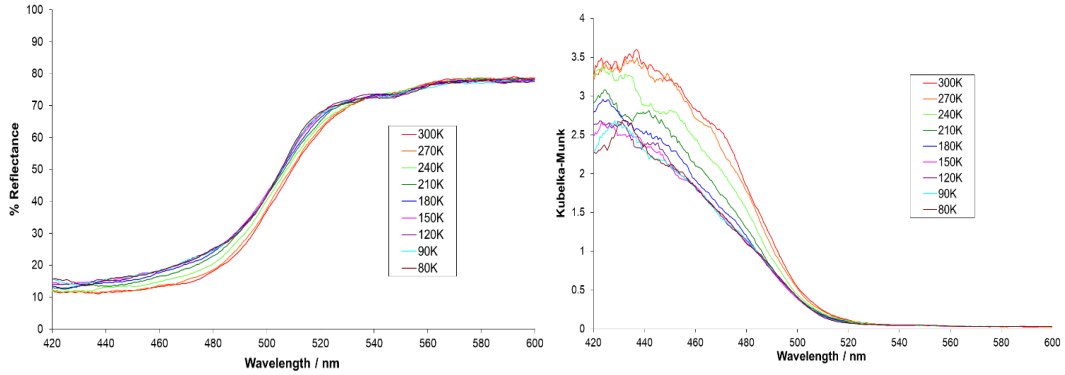

Figure S7.2 - Variable temperature diffuse reflectance spectra between 300 and 80K for **2-Br**, illustrated as wavelength versus (left) % reflectance and (right) the Kubelka-Munk function.

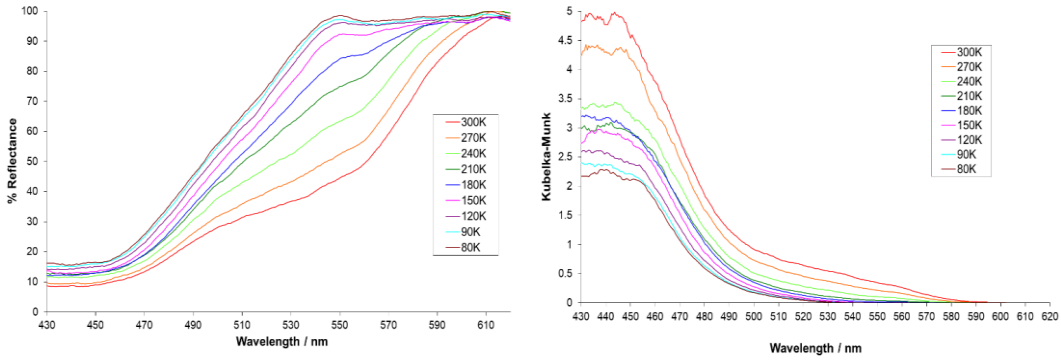

Figure S7.3 - Variable temperature diffuse reflectance spectra between 300 and 80K for **3-Br**, illustrated as wavelength versus (left) % reflectance and (right) the Kubelka-Munk function.

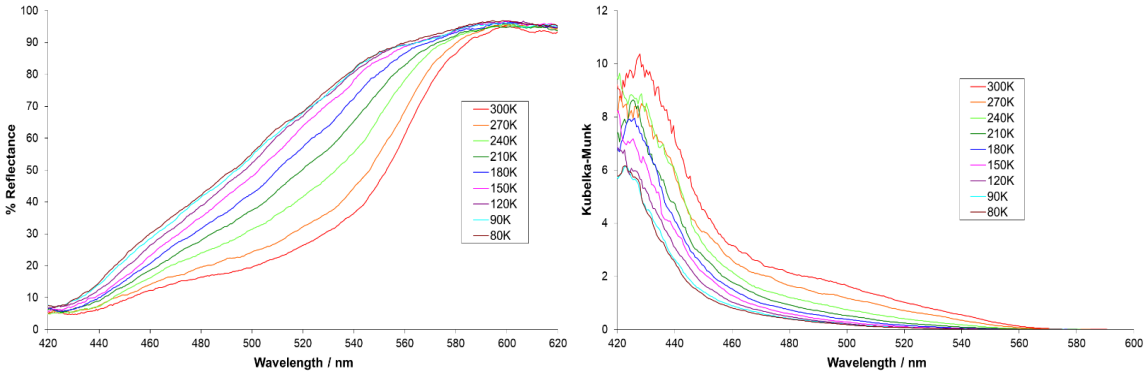

Figure S7.4 - Variable temperature diffuse reflectance spectra between 300 and 80K for **4-Br**, illustrated as wavelength versus (left) % reflectance and (right) the Kubelka-Munk function.

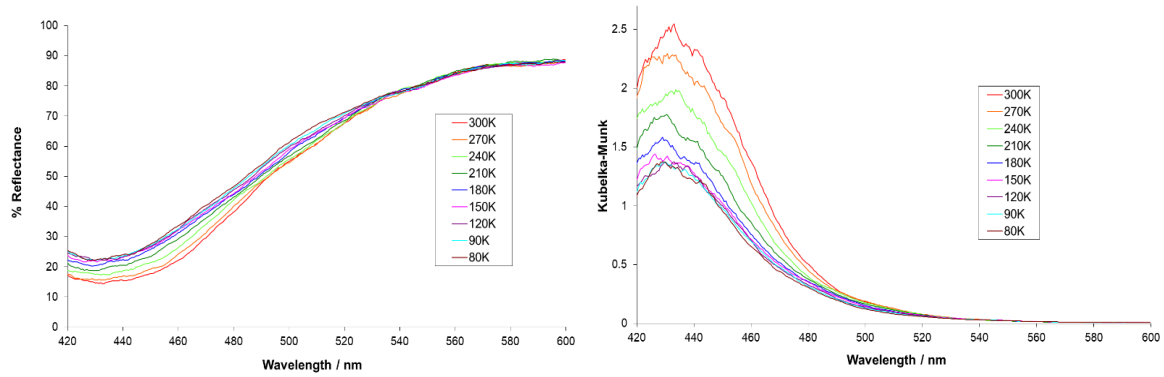

Figure S7.5 - Variable temperature diffuse reflectance spectra between 300 and 80K for **5-Br**, illustrated as wavelength versus (left) % reflectance and (right) the Kubelka-Munk function.

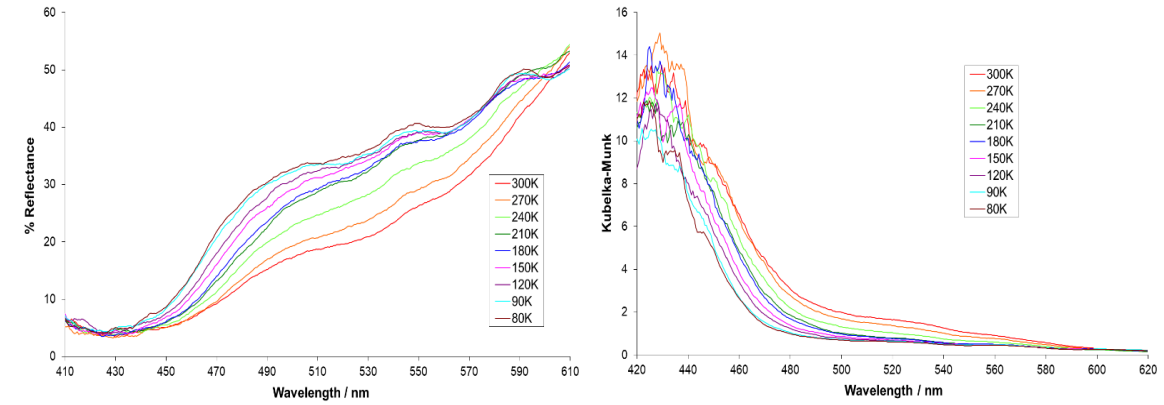

Figure S7.6 - Variable temperature diffuse reflectance spectra between 300 and 80K for **6-Br**, illustrated as wavelength versus (left) % reflectance and (right) the Kubelka-Munk function.

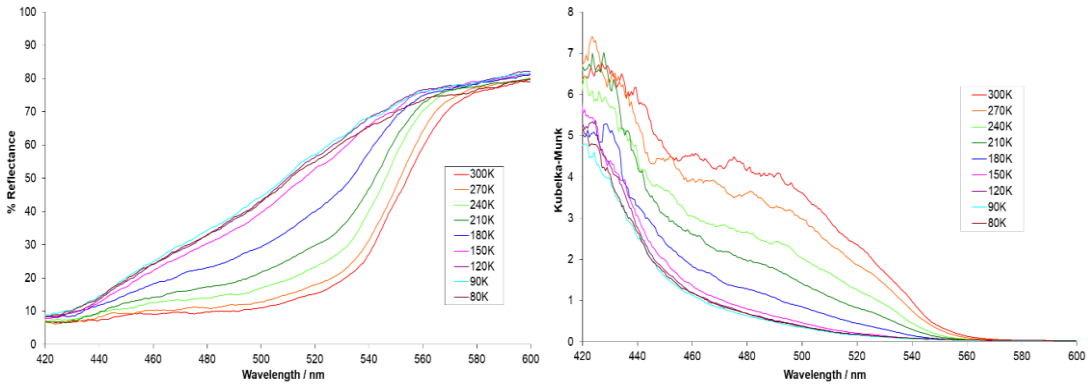

Figure S7.7 - Variable temperature diffuse reflectance spectra between 300 and 80K for **7-Br**, illustrated as wavelength versus (left) % reflectance and (right) the Kubelka-Munk function.

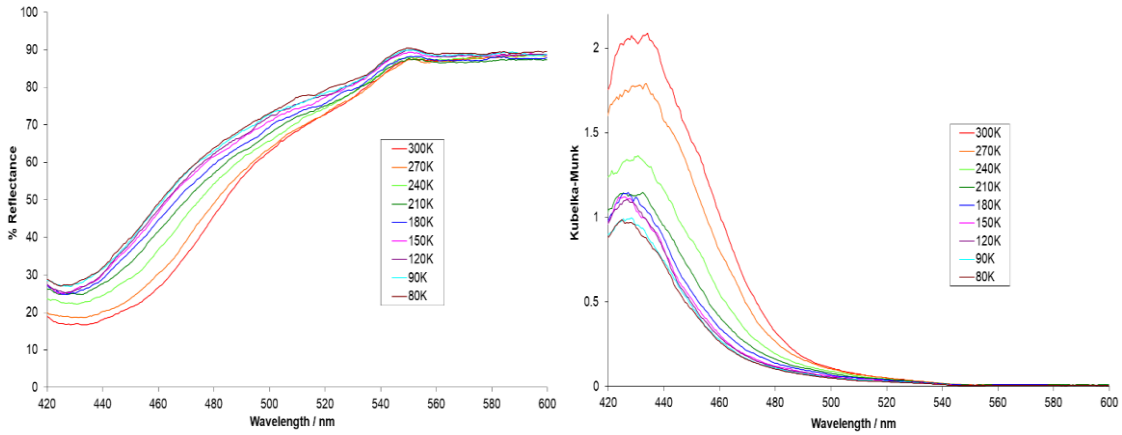

Figure S7.8 - Variable temperature diffuse reflectance spectra between 300 and 80K for **8-Br**, illustrated as wavelength versus (left) % reflectance and (right) the Kubelka-Munk function.

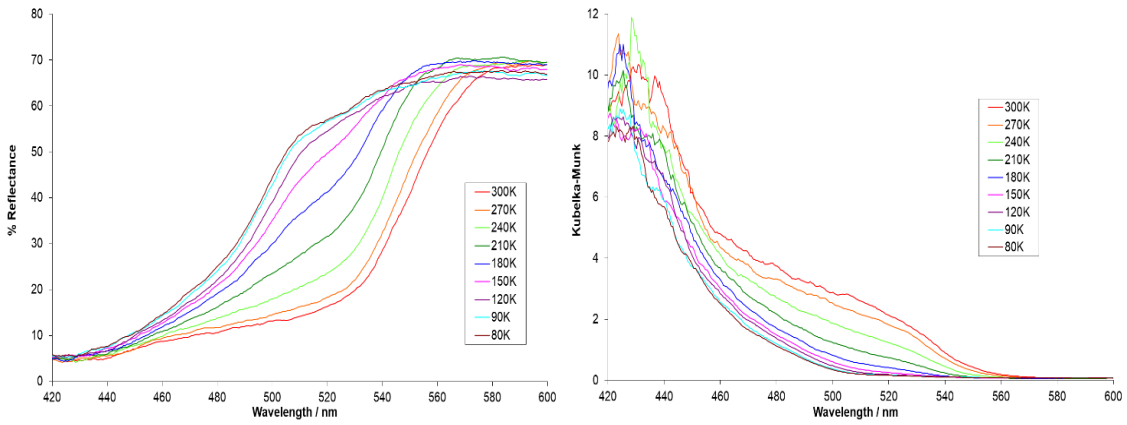

Figure S7.9 - Variable temperature diffuse reflectance spectra between 300 and 80K for **9-Br**, illustrated as wavelength versus (left) % reflectance and (right) the Kubelka-Munk function.

Appendix 8

Selected solid state behaviour of three di-tertiary butyl substituted *N*-salicylideneaniline derivatives: temperature induced phase transitions and chromic behaviour

Helen E. Mason, Judith A. K. Howard and Hazel A. Sparkes

Published *Acta Crystallographica*, 2021, **C77**, 659-667, doi.org/10.1107/S2053229621008780.

S8.1 Characterisation

S8.1.1 (E)-2,4-di-tert-butyl-6-(((4-fluorophenyl)imino)methyl)phenol, 1

Compound **1** was obtained in a yield of 92% (0.378 g). *Elemental Analysis, actual% (predicted%):* C= 76.39(77.03); H= 7.92 (8.00); N= 4.20 (4.28).

S8.1.2 (E)-2,4-di-tert-butyl-6-(((4-chlorophenyl)imino)methyl)phenol, 2

Compound **2** was obtained in a yield of 97% (0.837 g). *Elemental analysis, actual % (predicted %):* C = 73.42 (73.35); H = 7.60 (7.62); N = 3.89 (4.07).

S8.1.3 (E)-2,4-di-tert-butyl-6-(((4-bromophenyl)imino)methyl)phenol, 3

Compound **3** was obtained in a yield of 87% (0.422 g). *Elemental Analysis, actual% (predicted%):* C= 64.84(64.95); H= 6.75(6.75); N= 3.61 (3.61).

Table S8.1 Crystal data and structure refinement for **2** and **3**.

Identification code	**2** 300(2) K	**2** 250(2) K	**2** 200(2) K	**2** 150(2) K
Empirical formula	$C_{21}H_{26}ClNO$	$C_{21}H_{26}ClNO$	$C_{21}H_{26}ClNO$	$C_{21}H_{26}ClNO$
Formula weight	343.88	343.88	343.88	343.88
Temperature/K	300(2)	250(2)	200(2)	150(2)
Crystal system	monoclinic	monoclinic	monoclinic	monoclinic
Space group	$P2_1/c$	$P2_1/c$	$P2_1/c$	$P2_1/c$
a/Å	17.9412(17)	17.8739(13)	17.8132(12)	17.7326(13)
b/Å	10.5067(7)	10.4846(7)	10.4564(6)	10.4696(7)
c/Å	10.3890(7)	10.3312(6)	10.2814(6)	10.2385(7)
α/°	90	90	90	90
β/°	92.719(7)	92.296(5)	91.965(5)	91.536(6)
γ/°	90	90	90	90
Volume/Å^3	1956.2(3)	1934.5(2)	1913.9(2)	1900.1(2)
Z	4	4	4	4
ρ_{calc}g/cm^3	1.168	1.181	1.193	1.202
μ/mm^{-1}	0.202	0.204	0.206	0.208
F(000)	736.0	736.0	736.0	736.0
Crystal size/mm^3	0.33 × 0.28 × 0.10			
Radiation	MoKα (λ = 0.71073)			
2θ range for data collection/°	5.518 to 43.932	5.538 to 45.97	5.558 to 47.064	5.566 to 50.694
Index ranges	-18 ≤ h ≤ 17, -10 ≤ k ≤ 11, -10 ≤ l ≤ 10	-19 ≤ h ≤ 19, -7 ≤ k ≤ 11, -8 ≤ l ≤ 11	-20 ≤ h ≤ 20, -11 ≤ k ≤ 11, -11 ≤ l ≤ 11	-21 ≤ h ≤ 17, -8 ≤ k ≤ 12, -12 ≤ l ≤ 11
Reflections collected	5532	5874	11973	8155
Independent reflections	2382 [R_{int} = 0.0499, R_{sigma} = 0.0753]	2688 [R_{int} = 0.0475, R_{sigma} = 0.0789]	2833 [R_{int} = 0.0550, R_{sigma} = 0.0440]	3481 [R_{int} = 0.0534, R_{sigma} = 0.0805]
Data/restraints/parameters	2382/169/277	2688/181/277	2833/163/277	3481/151/289
Goodness-of-fit on F^2	1.019	1.061	1.029	1.075
Final R indexes [I>=2σ (I)]	R_1 = 0.0560, wR_2 = 0.1118	R_1 = 0.0623, wR_2 = 0.1214	R_1 = 0.0509, wR_2 = 0.1105	R_1 = 0.0632, wR_2 = 0.1207
Final R indexes [all data]	R_1 = 0.0983, wR_2 = 0.1325	R_1 = 0.1080, wR_2 = 0.1445	R_1 = 0.0695, wR_2 = 0.1196	R_1 = 0.1005, wR_2 = 0.1383
Largest diff. peak/hole / e Å^{-3}	0.16/-0.15	0.16/-0.19	0.26/-0.23	0.25/-0.30

Table S8.1 Crystal data and structure refinement for **2** and **3** continued.

Identification code	**2** 120(2) K	**3** 300(2) K	**3** 250(2) K	**3** 200(2) K
Empirical formula	$C_{21}H_{26}NOCl$	$C_{21}H_{26}BrNO$	$C_{21}H_{26}BrNO$	$C_{21}H_{26}BrNO$
Formula weight	343.88	388.34	388.34	388.34
Temperature/K	120.15	300(2)	250(2)	200(2)
Crystal system	monoclinic	monoclinic	monoclinic	monoclinic
Space group	$P2_1/c$	$P2_1/c$	$P2_1/c$	$P2_1/c$
a/Å	17.3654(7)	18.0356(7)	17.9642(4)	17.8944(4)
b/Å	10.6721(4)	10.5891(3)	10.5593(2)	10.54749(18)
c/Å	10.1549(6)	10.3641(3)	10.3153(2)	10.2693(2)
α/°	90.00	90	90	90
β/°	89.924(4)	92.894(3)	92.535(2)	92.1529(18)
γ/°	90.00	90	90	90
Volume/Å^3	1881.96(15)	1976.82(11)	1954.79(8)	1936.88(6)
Z	4	4	4	4
ρ_{calc}g/cm^3	1.214	1.305	1.320	1.332
μ/mm^{-1}	0.210	2.086	2.110	2.129
F(000)	736.0	808.0	808.0	808.0
Crystal size/mm^3	0.35 × 0.31 × 0.10	0.3 × 0.05 × 0.05		
Radiation	Mo Kα (λ = 0.71073)			
2θ range for data collection/°	5.54 to 52.74	5.874 to 48.806	5.906 to 55.738	5.932 to 55.74
Index ranges	-21 ≤ h ≤ 21, -13 ≤ k ≤ 12, -12 ≤ l ≤ 12	-20 ≤ h ≤ 20, -12 ≤ k ≤ 12, -9 ≤ l ≤ 12	-23 ≤ h ≤ 23, -9 ≤ k ≤ 13, -13 ≤ l ≤ 13	-23 ≤ h ≤ 23, -9 ≤ k ≤ 13, -13 ≤ l ≤ 13
Reflections collected	14145	13771	29546	29301
Independent reflections	3863 [R_{int} = 0.0796, R_{sigma} = 0.0705]	3195 [R_{int} = 0.0359, R_{sigma} = 0.0300]	4650 [R_{int} = 0.0480, R_{sigma} = 0.0370]	4612 [R_{int} = 0.0433, R_{sigma} = 0.0327]
Data/restraints/parameters	3863/0/226	3195/181/278	4650/181/278	4612/175/290
Goodness-of-fit on F^2	1.072	1.051	1.017	1.018
Final R indexes [I>=2σ (I)]	R_1 = 0.0724, wR_2 = 0.1725	R_1 = 0.0443, wR_2 = 0.1055	R_1 = 0.0394, wR_2 = 0.0888	R_1 = 0.0352, wR_2 = 0.0747
Final R indexes [all data]	R_1 = 0.0994, wR_2 = 0.1923	R_1 = 0.0639, wR_2 = 0.1175	R_1 = 0.0746, wR_2 = 0.1011	R_1 = 0.0601, wR_2 = 0.0830
Largest diff. peak/hole / e Å^{-3}	0.84/-0.44	0.35/-0.42	0.33/-0.36	0.37/-0.32

Table S8.1 Crystal data and structure refinement for **2** and **3** continued.

Identification code	**3** 150(2) K	**3** 120(2) K
Empirical formula	$C_{21}H_{26}BrNO$	$C_{21}H_{26}BrNO$
Formula weight	388.34	388.34
Temperature/K	150(2)	120(2)
Crystal system	monoclinic	monoclinic
Space group	$P2_1/c$	$P2_1/c$
a/Å	17.8028(3)	17.5364(3)
b/Å	10.55679(16)	10.65933(19)
c/Å	10.21910(18)	10.1718(2)
α/°	90	90
β/°	91.6950(16)	90.6047(16)
γ/°	90	90
Volume/Å^3	1919.74(6)	1901.26(6)
Z	4	4
ρ_{calc}g/cm^3	1.344	1.357
μ/mm^{-1}	2.148	2.169
F(000)	808.0	808.0
Crystal size/mm^3	0.3 × 0.05 × 0.05	
Radiation	Mo Kα (λ = 0.71073)	
2θ range for data collection/°	5.958 to 55.746	5.988 to 55.756
Index ranges	-23 ≤ h ≤ 23, -9 ≤ k ≤ 13, -13 ≤ l ≤ 13	-23 ≤ h ≤ 23, -10 ≤ k ≤ 14, -13 ≤ l ≤ 13
Reflections collected	28980	44888
Independent reflections	4570 [R_{int} = 0.0396, R_{sigma} = 0.0291]	4509 [R_{int} = 0.0450, R_{sigma} = 0.0273]
Data/restraints/parameters	4570/67/258	4509/103/258
Goodness-of-fit on F^2	1.030	1.046
Final R indexes [I>=2σ (I)]	R_1 = 0.0309, wR_2 = 0.0671	R_1 = 0.0319, wR_2 = 0.0684
Final R indexes [all data]	R_1 = 0.0473, wR_2 = 0.0727	R_1 = 0.0458, wR_2 = 0.0739
Largest diff. peak/hole / e Å^{-3}	0.45/-0.36	0.47/-0.42

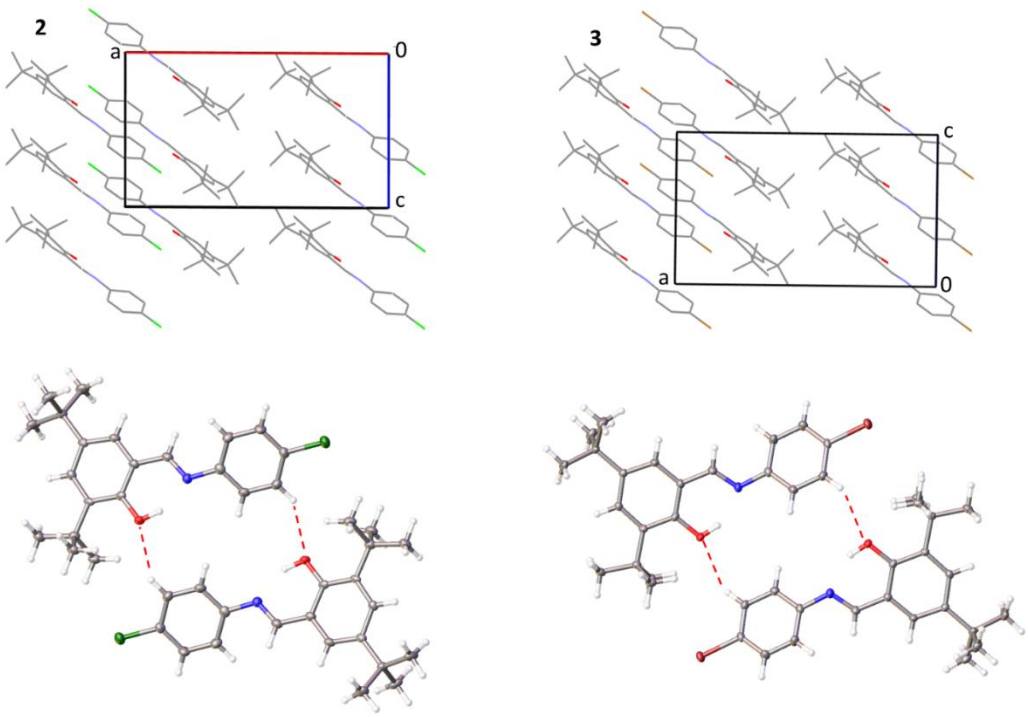

Figure S8.1 - Illustration of (top) the packing of **2** and **3** at 100(2) K looking down the b axis. Hydrogen atoms omitted for clarity. (bottom) C-H···O interactions.

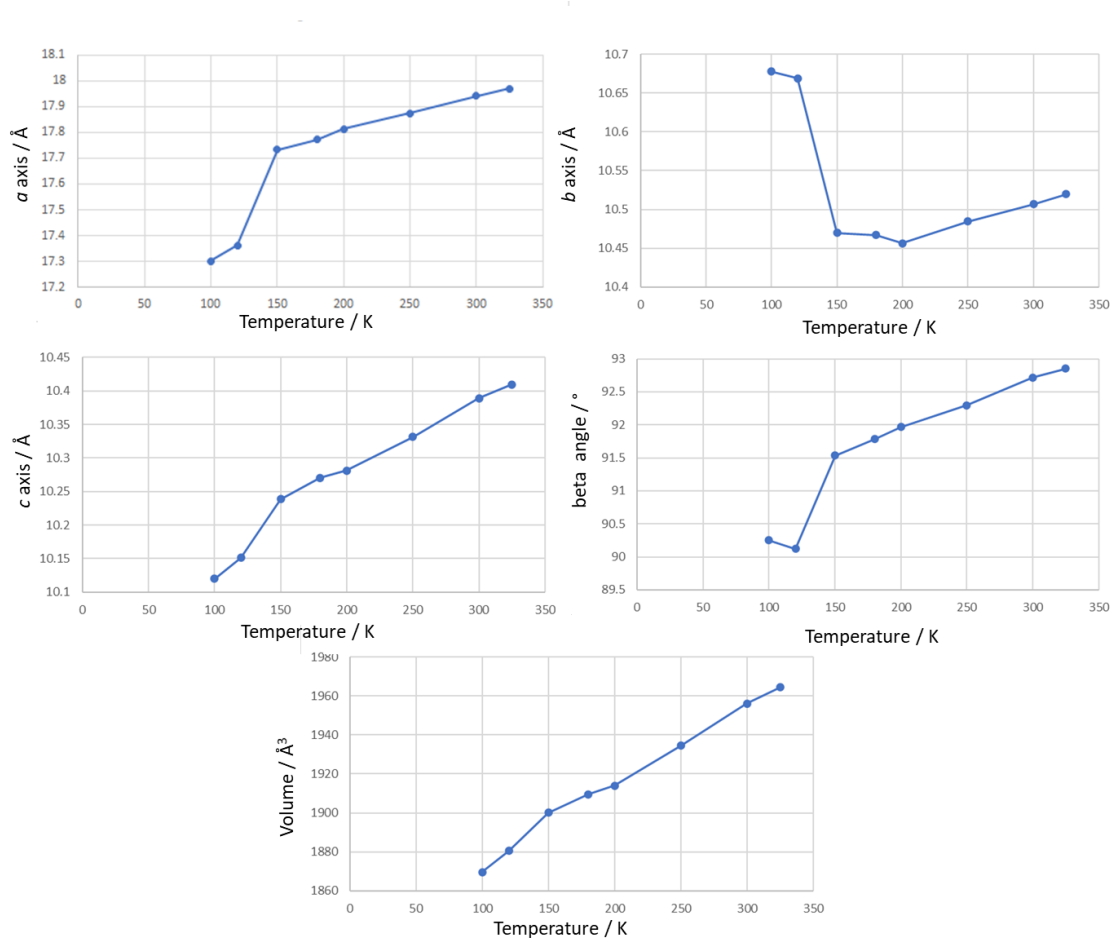

Figure S8.2 - Change in cell parameters for **2** as a function of temperature.

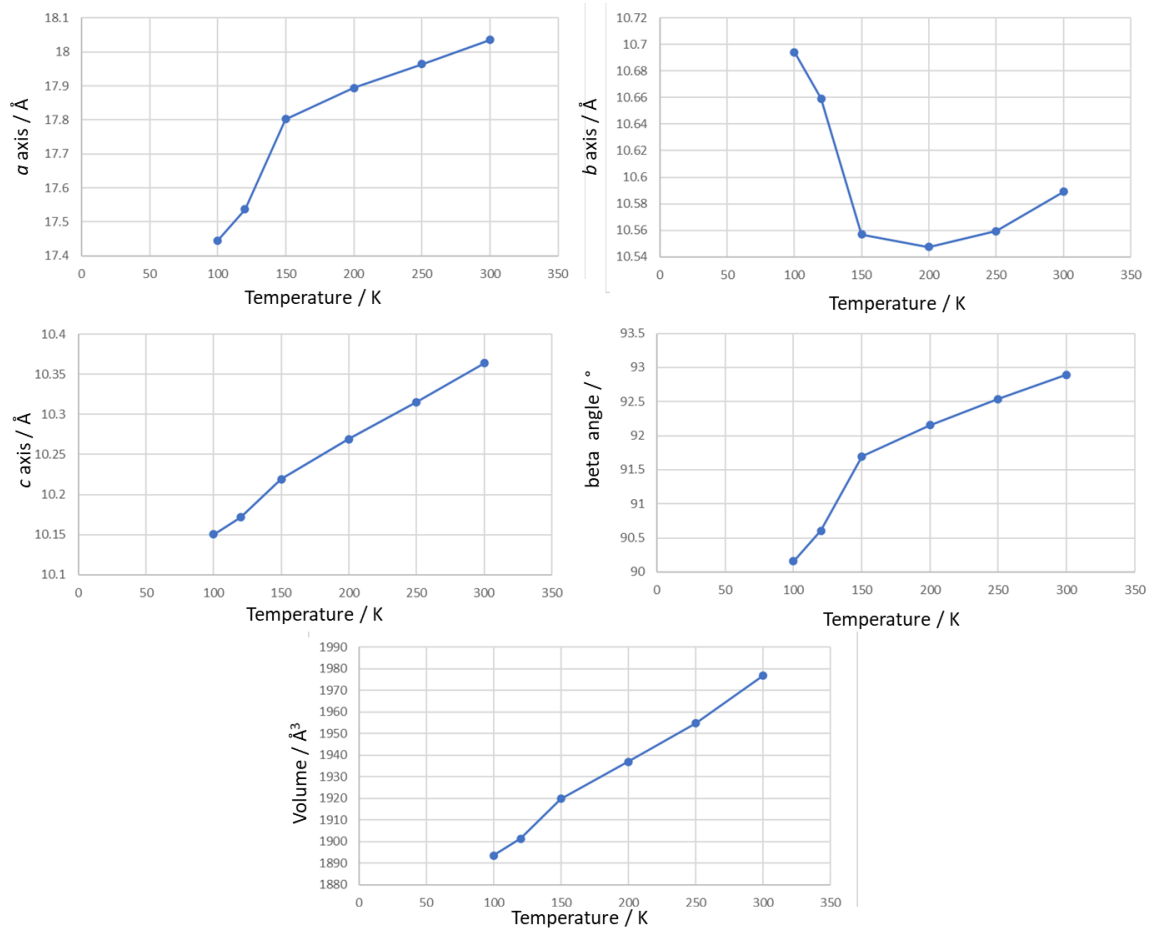

Figure S8.3 - Change in cell parameters for **3** as a function of temperature.

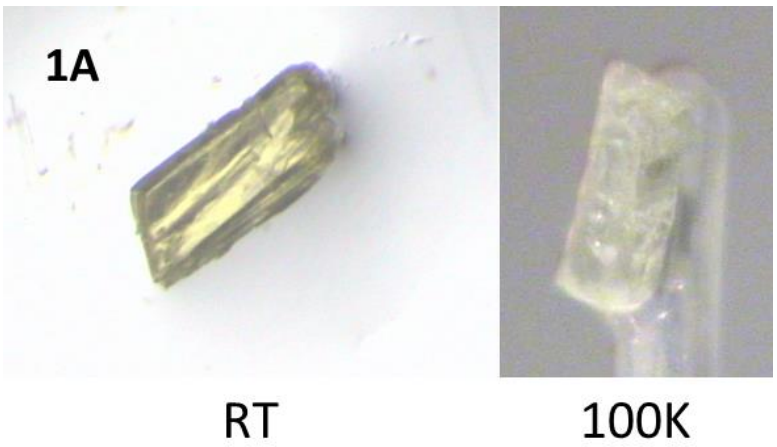

Figure S8.4 - Colour of **1A** at room temperature (RT) and 100(2) K.

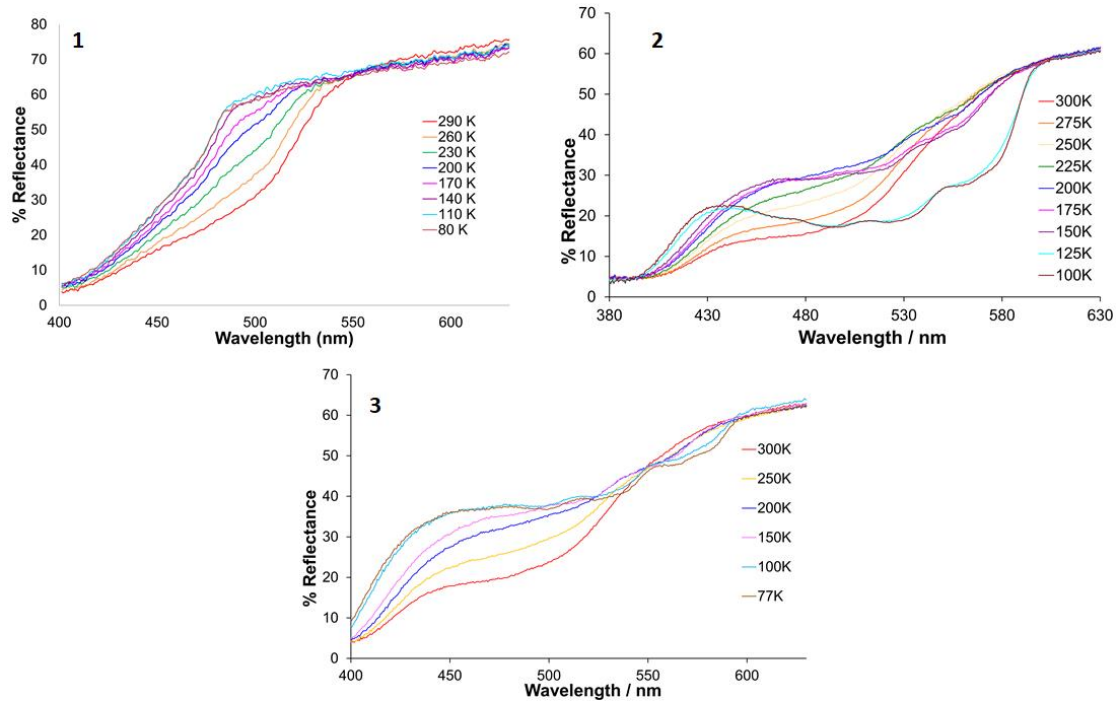

Figure S8.5 - Diffuse reflectance spectra for **1** (likely to be a mixture of both polymorphs), **2** and **3**, displayed as reflectance versus wavelength.

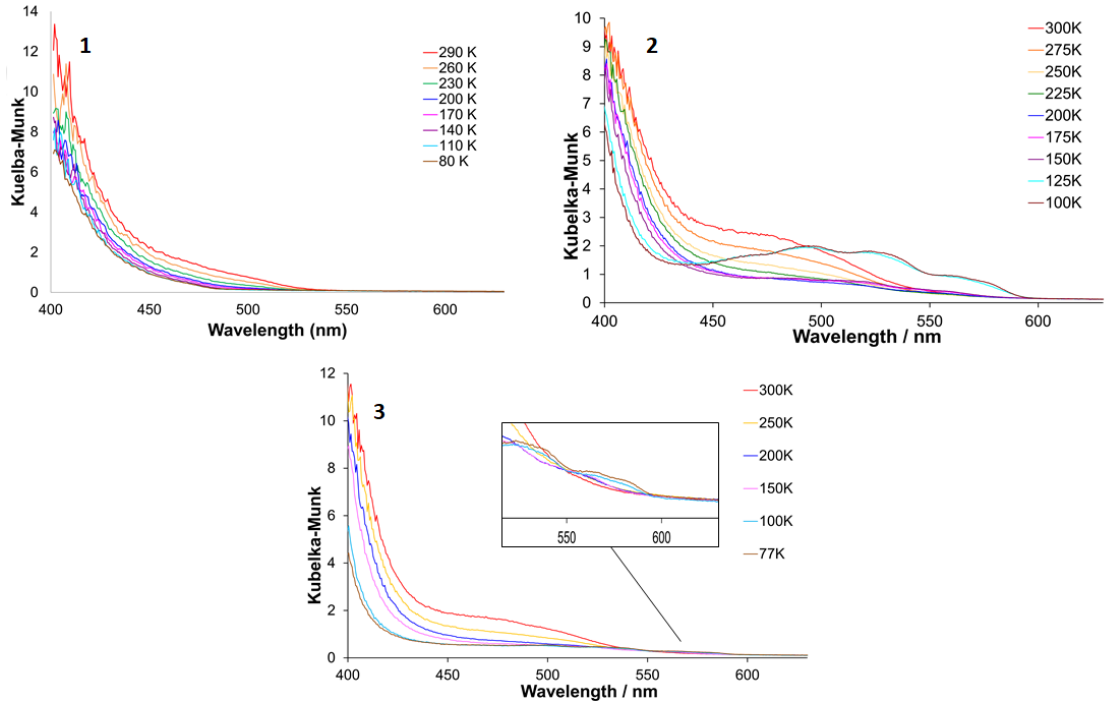

Figure S8.6 - Diffuse reflectance spectra for **1** (likely to be a mixture of both polymorphs), **2** and **3**, displayed as Kubelka-Munk versus wavelength.

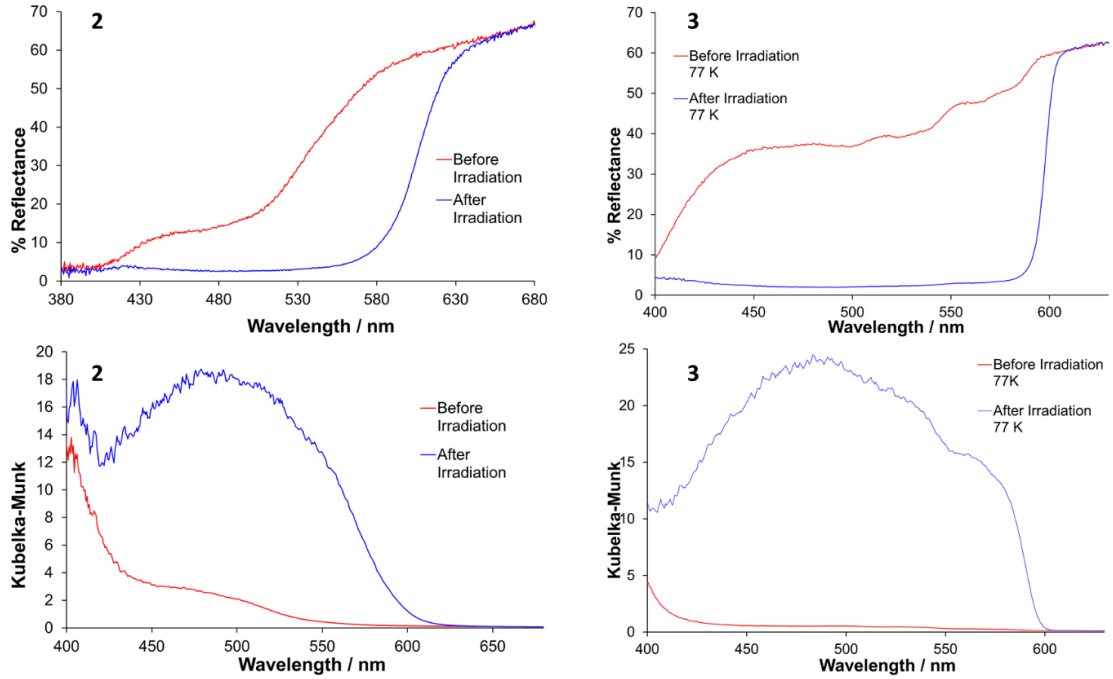

Figure S8.7 - Reflectance spectra for (left) **2** at 298 K and (right) **3** at 77 K before and after irradiation, presented as (top) % reflectance versus wavelength and (bottom) Kubelka-Munk versus wavelength.

Appendix 9

Synthesis and structures of three isoxazole containing Schiff bases

Helen E. Mason, Judith A. K. Howard and Hazel A. Sparkes

Published *Acta Crystallographica*, 2020, **C76**, 927-931, doi.org/10.1107/S2053229620010530.

S9.1 Characterisation

S9.1.1 (E)-2-((isoxazol-3-ylimino)methyl)phenol (1)

Compound **1** was obtained in a yield of 93% (0.875 g). *Elemental analysis, actual % (predicted %):* C = 62.02 (63.83); H = 4.29 (4.28); N = 15.62 (14.89). *Mass spectrometry [$C_{10}H_8N_2O_2$], actual m/z (predicted m/z):* ES+ spectrum shows one main $[M+H]^+$ peak; $[M+H]^+$ = 189.5 (189.2).

S9.1.2 (E)-2-(((5-methylisoxazol-3-yl)imino)methyl)phenol (2)

Compound **2** was obtained in a yield of 94% (0.947 g). *Elemental analysis, actual % (predicted %):* C = 64.70 (65.34); H = 4.98 (4.98); N = 13.82 (13.85). *Mass spectrometry [$C_{11}H_{10}N_2O_2$], actual m/z (predicted m/z):* ES+ spectrum shows one main $[M+H]^+$ peak; $[M+H]^+$ = 202.9 (203.2).

S9.1.3 (E)-2,4-di-tert-butyl-6-((isoxazol-3-ylimino)methyl)phenol (3)

Compound **3** was obtained in a yield of 94% (1.407 g). *Elemental analysis, actual % (predicted %):* C = 66.73 (71.97); H = 7.99 (8.06); N = 9.42 (9.33). *Mass spectrometry [$C_{18}H_{24}N_2O_2$], actual m/z (predicted m/z):* ES+ spectrum shows one main $[M+H]^+$ peak; $[M+H]^+$ = 301.3 (301.4).

Appendix 10

No Appendix for Chapter 10.